

The Telecommunications and Data Acquisition Progress Report 42-90

April-June 1987

E. C. Posner
Editor

(NASA-CR-181286) THE TELECOMMUNICATIONS AND
DATA ACQUISITION REPORT Progress Report,
Apr. - Jun. 1987 (Jet Propulsion Lab.) 163
P Avail: NTIS HC A08/EF A01 CSCL 17B

N87-28775
--THRU--
N87-28794
Unclass
G3/32 C093312

August 15, 1987



National Aeronautics and
Space Administration

Jet Propulsion Laboratory
California Institute of Technology
Pasadena, California

The Telecommunications and Data Acquisition Progress Report 42-90

April-June 1987

E. C. Posner
Editor

August 15, 1987



National Aeronautics and
Space Administration

Jet Propulsion Laboratory
California Institute of Technology
Pasadena, California

The research described in this publication was carried out by the Jet Propulsion Laboratory, California Institute of Technology, under a contract with the National Aeronautics and Space Administration.

Reference herein to any specific commercial product, process, or service by trade name, trademark, manufacturer, or otherwise, does not constitute or imply its endorsement by the United States Government or the Jet Propulsion Laboratory, California Institute of Technology.

Preface

This quarterly publication provides archival reports on developments in programs managed by JPL's Office of Telecommunications and Data Acquisition (TDA). In space communications, radio navigation, radio science, and ground-based radio astronomy, it reports on activities of the Deep Space Network (DSN) and its associated Ground Communications Facility (GCF) in planning, in supporting research and technology, in implementation, and in operations. Also included is TDA-funded activity at JPL on data and information systems and reimbursable DSN work performed for other space agencies through NASA. The preceding work is all performed for NASA's Office of Space Tracking and Data Systems (OSTDS).

In geodynamics, the publication reports on the application of radio interferometry at microwave frequencies for geodynamic measurements. In the search for extraterrestrial intelligence (SETI), it reports on implementation and operations for searching the microwave spectrum. The latter two programs are performed for NASA's Office of Space Science and Applications (OSSA).

Finally, tasks funded under the JPL Director's Discretionary Fund and the Caltech President's Fund which involve the TDA Office are included.

This and each succeeding issue of the TDA Progress Report will present material in some, but not necessarily all, of the following categories:

OSTDS Tasks:

- DSN Advanced Systems
 - Tracking and Ground-Based Navigation
 - Communications, Spacecraft-Ground
 - Station Control and System Technology
 - Network Data Processing and Productivity
- DSN Systems Implementation
 - Capabilities for Existing Projects
 - Capabilities for New Projects
 - New Initiatives
 - Network Upgrade and Sustaining
- DSN Operations
 - Network Operations and Operations Support
 - Mission Interface and Support
 - TDA Program Management and Analysis
- GCF Implementation and Operations
- Data and Information Systems

OSSA Tasks:

- Search for Extraterrestrial Intelligence
- Geodynamics
 - Geodetic Instrument Development
 - Geodynamic Science

Discretionary Funded Tasks

Contents

OSTDS TASKS DSN Advanced Systems TRACKING AND GROUND-BASED NAVIGATION

Power Supply Conditioning Circuit	1
L. E. Primas and R. Loveland	
NASA Code 310-10-62-16-00	
A High-Performance Single-Mode Fiber-Optic Isolator Assembly	8
G. Lutes	
NASA Code 310-10-62-16-00	

COMMUNICATIONS, SPACECRAFT-GROUND

Calculated 70-Meter Antenna Performance for Offset L-Band and C-Band Feeds	12
D. Hoppe and P. Stanton	
NASA Code 310-20-64-80-02	
Sorption Compressor/Mechanical Expander Hybrid Refrigeration	21
J. A. Jones and M. Britcliffe	
NASA Code 310-20-66-53-00	
Reduction of Ground Noise in the Transmitter Crowbar Instrumentation System by the Use of Baluns and Other Noise Rejection Methods	27
J. Daeges and A. Bhanji	
NASA Code 310-20-64-15-00	

STATION CONTROL AND SYSTEM TECHNOLOGY

Image Statistics Decoding for Convolutional Codes	32
G. H. Pitt, III, L. Swanson, and J. H. Yuen	
NASA Code 310-30-71-83-04	
Constructions for Finite-State Codes	42
F. Pollara, R. J. McEliece and K. Abdel-Ghaffar	
NASA Code 310-30-71-83-02	
Systolic Arrays and Stack Decoding	50
M. Shahshahani	
NASA Code 310-30-71-83-02	
Survey of Current Correlators and Applications	54
C. R. Lahmeyer and S. S. Brokl	
NASA Code 310-30-70-87-02	
A Comparison of VLSI Architecture of Finite Field Multipliers Using Dual, Normal or Standard Basis	63
I. S. Hsu, T. K. Truong, H. M. Shao,	
L. J. Deutsch, and I. S. Reed	
NASA Code 310-30-70-84-08	
Soft-Decision Decoding of Some Block Codes	76
F. Pollara	
NASA Code 310-30-71-83-02	

DSN Systems Implementation CAPABILITIES FOR NEW PROJECTS

Compound-Taper Feedhorn for the DSN 70-Meter Antennas	81
F. Manshadi and R. Hartop	
NASA Code 314-30-56-44-18	
X-Band Phase Calibration Generator Coupler	89
P. H. Stanton	
NASA Code 314-30-50-57-27	
State Transition Storyboards: A Tool for Designing the Goldstone Solar System Radar Data Acquisition System User Interface Software	94
S. D. Howard	
NASA Code 314-40-53-31-01	
DSS 63 64-Meter Antenna S- and X-Band Efficiency and System Noise Temperature Calibrations, July 1986	103
S. D. Slobin	
NASA Code 314-40-56-04-14	
DSS 43 64-Meter Antenna S- and X-Band Efficiency and System Noise Temperature Calibrations, January 1987	116
S. D. Slobin	
NASA Code 314-40-56-04-14	
DSS 43 Antenna Gain Analysis for Voyager Uranus Encounter: 8.45-GHz Radio Science Data Correction	127
S. D. Slobin and W.A. Imbriale	
NASA Code 314-40-56-04-14	

NETWORK UPGRADE AND SUSTAINING

A New Linear Quadratic Optimal Controller for the 34-Meter High Efficiency Antenna Position Loop	136
J. A. Nickerson	
NASA Code 314-40-41-82-09	
A Method for Using a Time Interval Counter to Measure Frequency Stability	149
C. A. Greenhall	
NASA Code 314-40-41-82-07	
Referees	157

ORIGINAL PAGE IS
OF POOR QUALITY

Power Supply Conditioning Circuit

L. E. Primas and R. Loveland
Communications Systems Research Section

This article describes a power supply conditioning circuit that can reduce Periodic And Random Deviations (PARD) on the output voltages of DC power supplies to -150 dBV (32 nanovolts/ $\sqrt{\text{Hz}}$) from DC to several KHz with no measurable periodic deviations. The PARD for a typical commercial low noise power supply is -74 dBV (200 microvolts/ $\sqrt{\text{Hz}}$) for frequencies above 20 Hz and is often much worse at frequencies below 20 Hz. The power supply conditioning circuit described in this article relies on the large differences in the dynamic impedances of a constant current diode and a zener diode to establish a DC voltage with low PARD. Power supplies with low PARD are especially important in circuitry involving ultrastable frequencies for the DSN.

Introduction

Often DC power supplies are characterized by the PARD on their output voltages. The PARD is the periodic and random variation of a DC voltage or current from its average value, over a specified bandwidth, with all influence and control quantities maintained constant. A bandwidth commonly used to specify PARD is 20 Hz to 20 MHz.

The PARD on the output voltage of a power supply used to power RF circuitry results in undesired amplitude and phase modulation of the RF signal being processed or generated. This problem is especially significant when using ultrastable frequencies generated by modern atomic frequency standards (e.g., σ_y [100 seconds] = 8.5×10^{-13} for cesium). In order to minimize the spurious AM and PM modulation of ultrastable frequencies, the PARD on the associated power supply voltages must be minimized. Most commercial power supplies do not reduce the periodic variations, predominately at 60 Hz and its harmonics, to a low enough level to use in ultrastable RF

circuitry. These periodic variations should be reduced below the level of random deviation (noise). The need for a power supply conditioner came about when the phase noise of a low noise voltage controlled oscillator was measured and found to exceed the specification for spurious signals. It was determined that PARD from the power supply was modulating the RF output signal.

Sidebands that are generated in frequency multiplier circuits as a result of PARD on the power supply voltage are of particular concern because the power in sidebands, P_{sb} , is increased by,

$$P_{sb} = 20 \log (f_2/f_1) \quad (1)$$

where f_1 is the input frequency and f_2 is the output frequency of the multiplier. For example, if a 5 MHz reference frequency is multiplied to 10 GHz the sidebands will increase by 66 dB. This increase in sideband power will often degrade the stability of the desired high frequency signal to an unacceptable level.

The power supply conditioning circuit described in this article takes advantage of the large difference in dynamic impedance of constant current diodes and low voltage avalanche zener diodes. This design uses the reference voltage established by a constant current diode and a zener diode to generate a DC output voltage with low PARD.

II. Design

The circuit in Fig. 1 is capable of providing a DC reference voltage having extremely low PARD for frequencies ranging from DC to several KHz. The constant current diode (D_1) and zener diode (D_2) in series form a voltage divider having a very large division ratio for AC signals. Using the voltage divider equation, the deviation, e_o , of the output voltage caused by a deviation in the input voltage, e_i , will be,

$$e_o = \frac{r_z}{r_c + r_z} e_i \quad (2)$$

where

r_z = dynamic impedance of the zener diode, and

r_c = dynamic impedance of the constant current diode.

The dynamic impedance of the constant current diode can be greater than 100 Kohms and the dynamic impedance of the zener diode can be less than 10 ohms. If Eq. (1) is evaluated for $r_c = 100$ Kohms and $r_z = 10$ ohms the rejection ratio, e_o/e_i , will be 10^{-4} or -80 dB. Thus, the large dynamic impedance of the constant current diode and the small dynamic impedance of the zener diode, cause any deviation of the DC voltage applied to the input of the voltage reference circuit to be greatly reduced at the output of the circuit.

For the best results this circuit requires the use of a constant current diode with the highest possible dynamic impedance and a zener diode with the lowest possible dynamic impedance. [1]. However, certain compromises must be made in designing the circuit. The dynamic impedances of constant current diodes have an inverse relationship to the current rating. As the current ratings of constant current diodes go down, the dynamic impedances go up. This makes it necessary to use a zener diode which is designed to have a low impedance at a low current so that the highest possible impedance ratio consistent with good zener regulation can be obtained. Low voltage avalanche zener diodes meet this requirement and have low noise as well.

Since one of the requirements for achieving a maximum rejection ratio in this circuit is to use the lowest possible current, this circuit can only be used as a voltage reference.

The design described below uses additional circuitry to obtain an output voltage with low PARD and to increase output current.

In the field effect transistor (FET) circuit (Fig. 2) reference is reproduced at the output using feedback operational amplifier (op amp), U_1 , used in conjunction with a field effect transistor, Q_1 , increases the current capability. The output voltage of the op amp controls the current through Q_1 in such a manner as to reproduce the reference voltage at the circuit output. Fluctuations on the drain voltage are reproduced at the source due to the high impedance between the drain and source.

For most applications the rejection ratio provided by this circuit is sufficient, but if even more rejection is required, the rejection ratio can be increased by connecting two stages in series (Fig. 3).

III. Small Signal Analysis

A theoretical rejection ratio for this circuit can be determined using a small signal analysis. This analysis illustrates which parameters limit the performance of the circuit. The PARD is represented by an AC voltage source. Superposition may be used to determine the effect of this source, by applying the source to different points in the model. In this analysis the AC source is first applied to the anode of the constant current diode and then to the drain of the FET (Figs. 4 and 5).

The rejection ratios are defined in dB to be

$$Rr_1 = 20 \log \left[\frac{V_{out_1}}{V_{in}} \right]$$

$$Rr_2 = 20 \log \left[\frac{V_{out_2}}{V_{in}} \right]$$

and

$$Rr_t = 20 \log \left[10 \exp \left(\frac{Rr_1}{20} \right) + 10 \exp \left(\frac{Rr_2}{20} \right) \right]$$

where

Rr_1 = rejection ratio with the AC source connected to the anode of the constant current diode,

Rr_2 = rejection ratio with the AC source connected to the drain of the FET,

Rr_t = total rejection ratio,

V_{out_1} = AC output voltage with the AC source connected to the anode of the constant current diode,

V_{out_2} = AC output voltage with the AC source connected to the drain of the FET,

V_{in} = AC input voltage.

As shown in Eq. (5), the overall rejection ratio of this circuit is approximately equal to the poorer of the two independent rejection ratios.

IV. Analysis of FET Circuit

For purposes of analysis, the FET circuit was simplified by removing the bypass capacitor. The analysis of the model (Fig. 4) with the AC source connected to the anode of the constant current diode, shows this rejection ratio to be largely determined by the dynamic impedances of the constant current diode and the zener diode. The following equations may be arrived at from the model [2].

$$\frac{V_2 - V_{in}}{R_c} + \frac{V_2}{R_z} + \frac{V_2 - V_{out_1}}{R_{in}} = 0 \quad (6)$$

$$\frac{V_{out_1} - V_2}{R_{in}} = g_m V_{gs} - \frac{V_{out_1}}{R_{eq}} \quad (7)$$

$$V_g = A (V_2 - V_{out_1}) \quad (8)$$

$$V_s = V_{out_1} \quad (9)$$

$$V_{gs} = A V_2 - (A + 1) V_{out_1} \quad (10)$$

where

R_{in} = input impedance of operational amplifier

R_{out} = output impedance of operational amplifier

A = gain of operational amplifier

$R_{eq} = R_{ld} // R_o$

R_{ld} = load resistance

R_o = drain source resistance

V_g = AC gate voltage

V_s = AC source voltage

V_{gs} = AC gate to source voltage

g_m = transconductance of the MOSFET

In the above, as well as throughout the remainder of this article, the symbol $R_1 // R_2$ represents the lumped resistance due to R_1 and R_2 being in parallel. In other words

$$R_1 // R_2 = \frac{1}{\frac{1}{R_1} + \frac{1}{R_2}}$$

Combining Eqs. (6), (7), and (10) leads to

$$\frac{V_{out_1}}{V_{in}} = \frac{R_{eq}(R_a)(1 + g_m A R_{in})}{R_c \left[R_{eq} + R_{in} + g_m R_{in} R_{eq} (A + 1) - \left(\frac{1}{R_{in}} + g_m A \right) R_{eq} (R_a) \right]} \quad (11)$$

where $R_a = R_c // R_z // R_{in}$

With the assumptions

$$A \gg 1$$

$$R_c \gg R_z$$

$$R_{in} \gg R_z$$

$$R_o \gg R_{ld}$$

Eq. (11) reduces to

$$\frac{V_{out_1}}{V_{in}} = \frac{R_z}{R_c} \quad (12)$$

The analysis of the model (Fig. 5) with the AC source connected to the drain of the MOSFET shows this rejection ratio to be largely determined by the transconductance and drain to source resistance of the MOSFET, and the gain of the op amp. The following equations may be derived from the model.

$$\frac{V_{out_2}}{R_{ld}} + \frac{V_{out_2}}{(R_c // R_z) + R_{in}} = g_m V_{gs} + \frac{V_{in} - V_{out_2}}{R_o} \quad (13)$$

$$\frac{V_2}{R_c} + \frac{V_2}{R_z} = \frac{V_{out_2} - V_2}{R_{in}} \quad (14)$$

$$V_g = A (V_2 - V_{out_2}) \quad (15)$$

$$V_s = V_{out_2} \quad (16)$$

$$V_{gs} = A V_2 - (A + 1) V_{out_2} \quad (17)$$

Combining Eqs. (13), (14), and (17) leads to

$$\frac{V_{out_2}}{V_{in}} = \frac{\frac{1}{R_o}}{\frac{1}{R_{ld}} + \frac{1}{R_b} + \frac{1}{R_o} + g_m(A + 1) - \frac{g_m A (R_a)}{R_{in}}} \quad (18)$$

where

$$R_a = R_c // R_z // R_{in}$$

and

$$R_b = (R_c // R_z) + R_{in}$$

With the assumptions

$$A \gg 1$$

$$R_c \gg R_z$$

$$R_{in} \gg R_z$$

$$R_o \gg 1$$

$$R_{ld} > 1$$

Eq. (18) reduces to

$$\frac{V_{out_2}}{V_{in}} = \frac{1}{g_m A R_o} \quad (19)$$

A component listing for an FET circuit (Fig. 6) that was tested is given below.

D_1	1N5314	4.7 mA constant current diode
-------	--------	-------------------------------

D_2, D_3, D_4	LVA351A	5.1 V zener diode
U_1	OP-27	Low noise precision op amp (PMI)
Q_1	VN88AF	N-channel enhancement MOSFET
R_x		1 Kohm resistor
R_{ld}		30 ohm resistor
C_1		1uF capacitor

The rejection ratio of this circuit was determined by adding an AC voltage to the DC supply and measuring the AC voltage present at the output of the power supply conditioner. A -10 dBV AC signal was added to the input and rejection ratios near -70 dB were measured for frequencies ranging from 1 Hz to 10 KHz (Fig. 7). The input voltage was 22.0 V and the output voltage 15.3 V, with an output current of 0.5A.

Equations (12) and (19) were used to compare this result with the theoretical results, using values

$$A = 10^{-6}$$

$$g_m = 195 \times 10^{-3} \text{ siemens}$$

$$R_o = 3 \text{ Kohms}$$

$$R_c = 50 \text{ Kohms}$$

$$R_z = 15 \text{ ohms}$$

The theoretical rejection ratio due to the constant current diode and the zener diode is -70 dB, while that due to the MOSFET is -175 dB. Thus in this case, the dynamic impedances of the constant current zener diodes limit the rejection ratio to -70 dB.

V. Conclusion

The power supply conditioner described above provides a simple and effective way to reduce the PARD found on the output voltages of power supplies. A low noise voltage reference, consisting of a constant current diode and a low noise zener diode connected in series, provides the basis for this design. The rejection ratio of this design is determined by the ratio of the dynamic impedances of the constant current diode and the zener diode, and can be improved by increasing this ratio and using lower noise zener diodes. Further improvements can be made by connecting two stages in series. An additional advantage of this power supply conditioner is that it provides large current capabilities, making it a practical addition to systems requiring power supplies with low PARD down to DC.

References

- [1] G. F. Lutes, "Stable Low Noise Voltage Source," *JPL DSN Progress Report 42-47*, vol. July and August 1978, pp. 89-93, Jet Propulsion Laboratory, Pasadena, Calif., Oct. 15, 1978.
- [2] R. A. Colclaser, D. A. Neamen, and C. F. Hawkins, *Electronic Circuit Analysis Basic Principles*, John Wiley & Sons, Inc., USA, pp. 339-392, 1984.

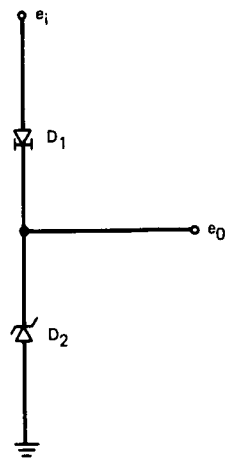


Fig. 1. Voltage reference circuit

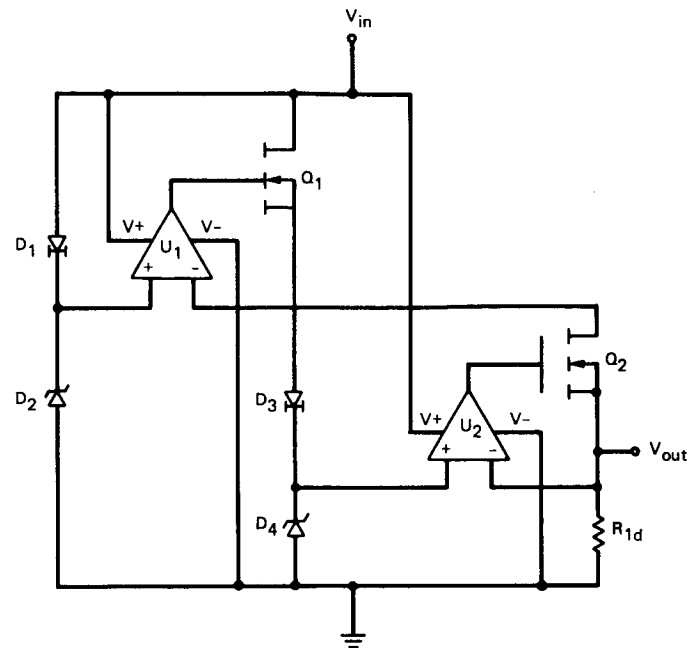


Fig. 3. Two staged FET circuit

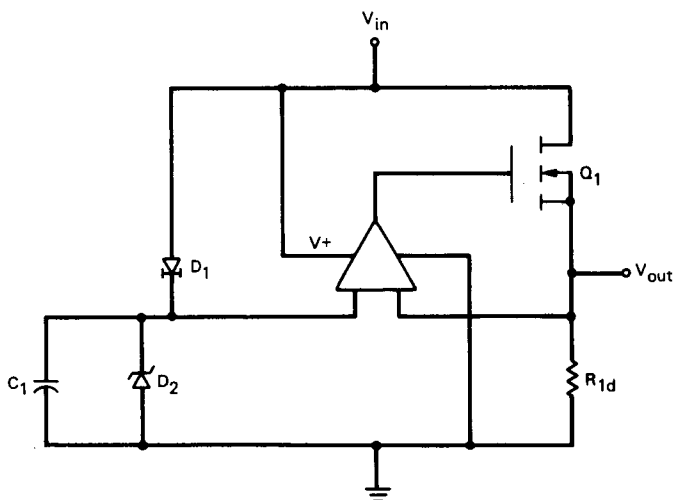


Fig. 2. FET circuit

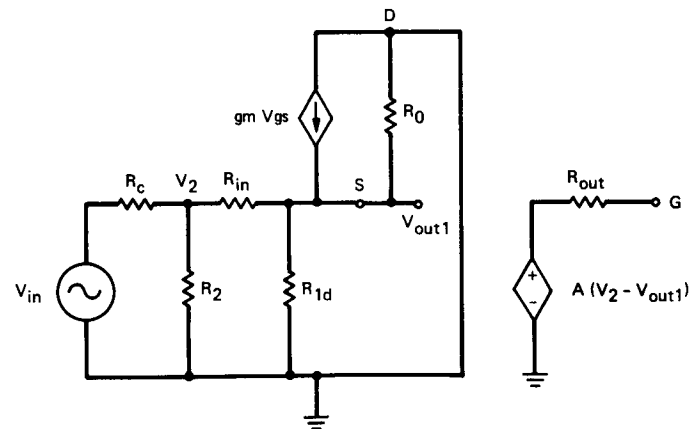


Fig. 4. Small signal model with AC source on anode of constant diode (R_c)

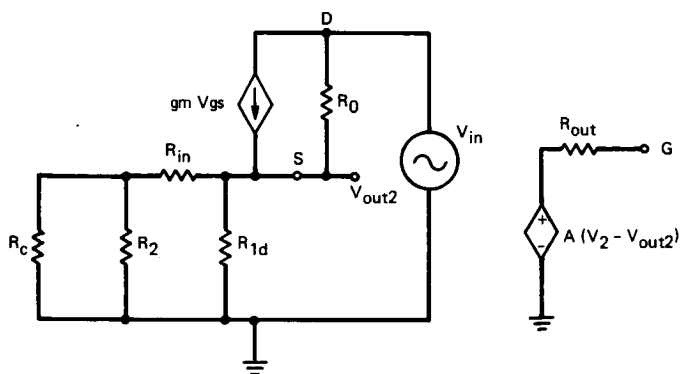


Fig. 5. Small signal model with AC source on drain of FET

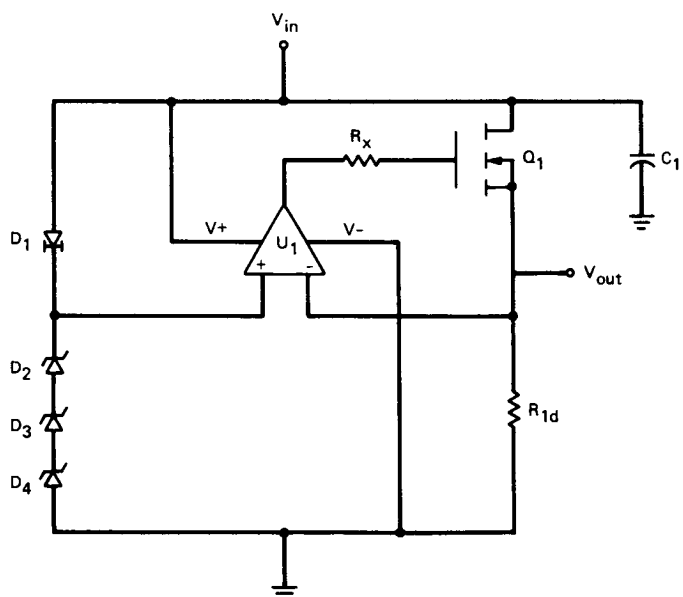


Fig. 6. Example FET circuit

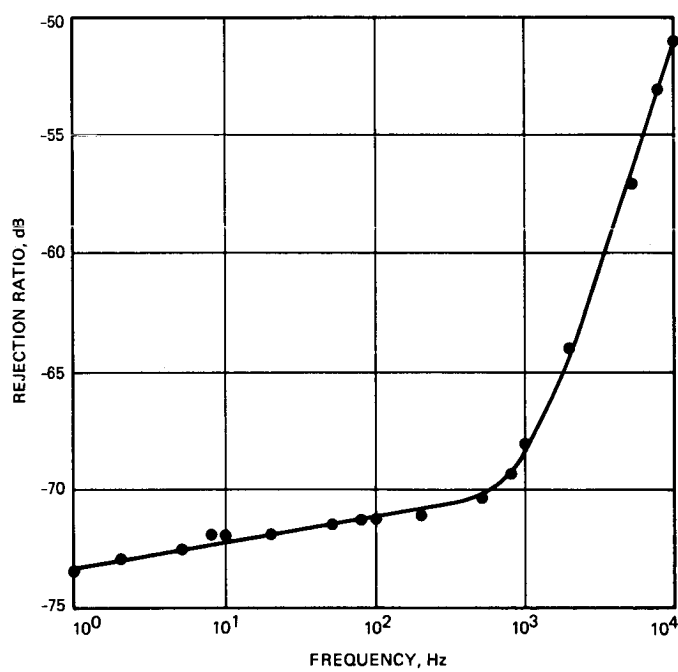


Fig. 7. Measured rejection ratio vs. frequency for FET circuit

A High-Performance Single-Mode Fiber-Optic Isolator Assembly

G. Lutes

Communications Systems Research Section

A high-isolation single-mode fiber-optic isolator assembly has been designed and fabricated by the Time and Frequency Systems Research Group. The measured forward loss is 2.6 dB and the reverse loss (isolation) is greater than 70 dB. This is a 30-dB higher isolation than the isolation of the best fiber-optic isolator previously reported. This isolator provides isolation between the semiconductor laser diode and the optical fiber in a precise reference frequency transmission system. The isolation of the laser greatly reduces the system's sensitivity to microphonics.

I. Introduction

Reflections cause intolerable instabilities in fiber-optic systems used in some precision applications, such as the precise reference frequency distribution system being developed by the Time and Frequency Systems Research Group. These reflections have the same effect on the semiconductor laser as an unstable external cavity and result in changes in the laser's output wavelength and amplitude. External reflections must be reduced by 60 dB or more before the resulting instabilities are reduced to tolerable levels.

Optical isolators are currently used to alleviate this problem. However, the best single-mode fiber-optic isolators which have been reported have losses of 3 or 4 dB and isolation of 30 to 40 dB [1], [2], [3]. It is necessary to use two such isolators in series to obtain the isolation of greater than 60 dB required in some fiber-optic systems such as those used for precise reference frequency or microwave frequency distribution. There are two disadvantages in doing this: Good optical isolators are very expensive (around \$3,000 each), and the forward

loss is increased. This article describes a single-mode fiber-optic isolator assembly that provides less than a 3-dB loss in the forward direction and greater than 70 dB of isolation.

II. Fiber-Optic Isolator

The fiber-optic isolator described in this article and shown in Fig. 1 is an assembly consisting of a commercial optical isolator, an expanded-beam single-mode fiber-optic connector, and single-mode fiber pigtails.

The optical isolator used in this assembly is manufactured by Optics For Research in Caldwell, New Jersey [4]. They manufacture a variety of optical isolators using the Faraday rotator principle (see, for example, [5]). The model used in this system, IO-4-IR, is designed for use at 1300 nm operation and has an aperture of 4 mm. Isolation is specified as greater than 30 dB, and the manufacturer has stated that they have not seen one better than about 40 dB. Forward loss is specified to be less than 0.5 dB.

We have assembled the isolator with a lens system which consists of two Lamdek expanded-beam single-mode fiber connectors. These connectors permit light to be transmitted with low loss from one single-mode optical fiber to another with a gap of several centimeters between them. A plot of the optical loss as a function of the distance between connectors is shown in Fig. 2.

In this assembly the connectors mounted on single-mode fiber pigtailed are placed facing each other and are separated by the appropriate distance; the optical isolator is installed between them.

III. Results

The Optics For Research isolators have much greater isolation potential than reported previously. The isolation, however, is limited by scattering due to internal reflections. The polarization of this scattered light at various locations within the isolator is not in the direction required for high attenuation. A secondary problem is presented by the nonuniformity of the polarizers across their diameters. The polarizers have a higher extinction ratio when the optical beam size is smaller because they are more uniform across a small area.

Fortunately the scattered light, which limits the isolation, is not parallel to the axis of the isolator when it exits the unit. Therefore, it can be virtually eliminated by collecting the optical output using a lens system with a small aperture and small acceptance angle.

The Lamdek expanded beam connector (data available from [6]) can provide the small aperture and small acceptance angle needed for high isolation. These connectors, when used on both sides of the isolator, set the optical beam diameter to

about 1.5 mm and present a 1.5-mm-diameter aperture at the receiving fiber. The transmission loss in dB of optical power at the receiving connector is related to the offset angle of a light beam or ray by,¹

$$\text{Loss} = 10 \log \left[e^{-(f \tan \Theta / n \omega_o)^2} \right]$$

where

f = the focal length of the lens = 7 mm

Θ = the offset angle (radians)

n = the index of refraction = 1.4995

ω_o = 1/2 the mode field diameter = 0.00523 mm

A plot of the transmission loss as a function of the offset angle is shown in Fig. 3. At an angle of 0.0045 radians the loss is 70 dB. This accounts for the extremely large rejection of scattered light coming out of the optical isolator.

IV. Conclusion

A single-mode fiber-optic isolator has been assembled and measured for loss (2.6 dB) and isolation (greater than 70 dB). These results were achieved using commercially available components. The availability of such high-quality single-mode fiber-optic isolator assemblies will make it possible to achieve substantial improvements in precision fiber-optic systems such as those used for stable reference frequency distribution and microwave frequency transmission.

¹Fredrick B. Messbauer of Lamdek Fiber-Optics, private communication, April 1987.

Acknowledgments

The author would like to thank Fred Messbauer of Lamdek Corporation and Jay Van Delden of Optics For Research for information used in this article and Lori Primas of the Time and Frequency Systems Research Group for her help in making the measurements and plotting the data used.

References

- [1] K. Okamoto, H. Miyazawa, J. Noda, and M. Saruwatari, "Novel Optical Isolator Consisting of a YIG Spherical Lens and PANDA-Fiber Polarizers," *Electron. Lett.*, Vol. 21, pp. 36-38, 1985.
- [2] A. E. Green and G. Georgiou, "Compact Bulk Optical Isolator With Monomode Fiber Pigtailes For Use at 1.3 μ ," *Electron. Lett.*, Vol. 22, pp. 1045-1046, 1986.
- [3] D. J. Gauthier, P. Narum, and R. W. Boyd, "Simple, Compact, High-Performance Permanent-Magnet Faraday Isolator," *Optics Letters*, Vol. II, pp. 623-625, 1986.
- [4] Data sheet obtained from Optics For Research, P. O. Box 82, Caldwell, New Jersey, 07006.
- [5] E. B. Brown, *Modern Optics*. New York: Reinhold Publ. Co. 1965, p. 125.
- [6] Lamdek Fiber-Optics, 901 Elmgrove Road, Rochester, New York, 14650.

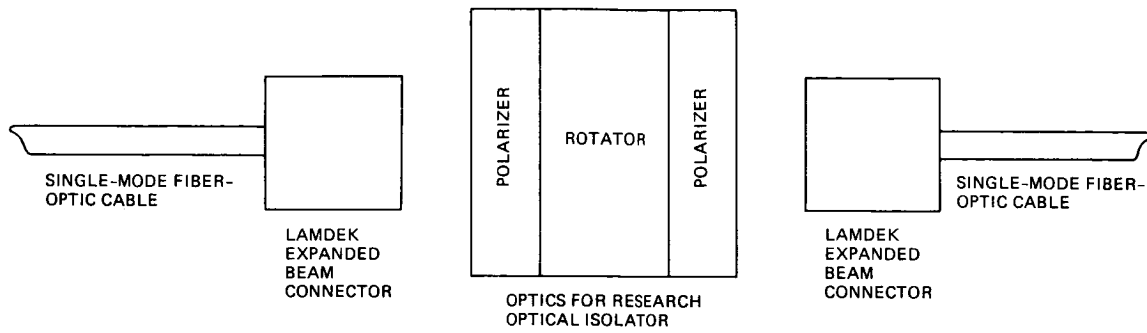


Fig. 1. Optical isolator block diagram

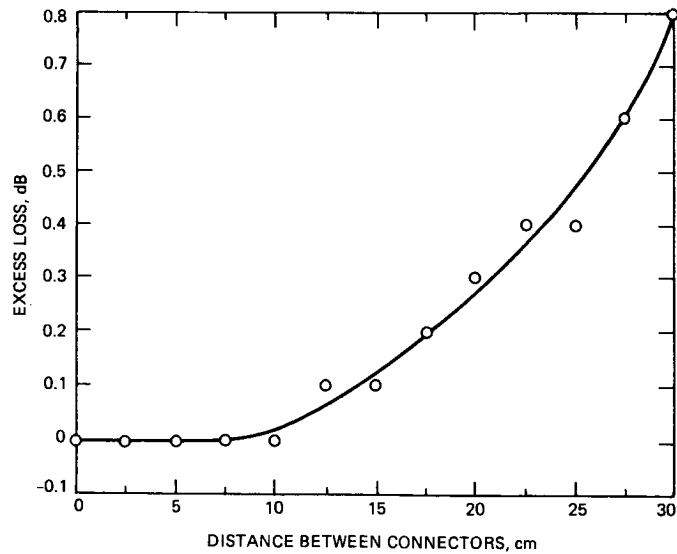


Fig. 2. Excess coupling loss as a function of the distance between the Lamdek connectors

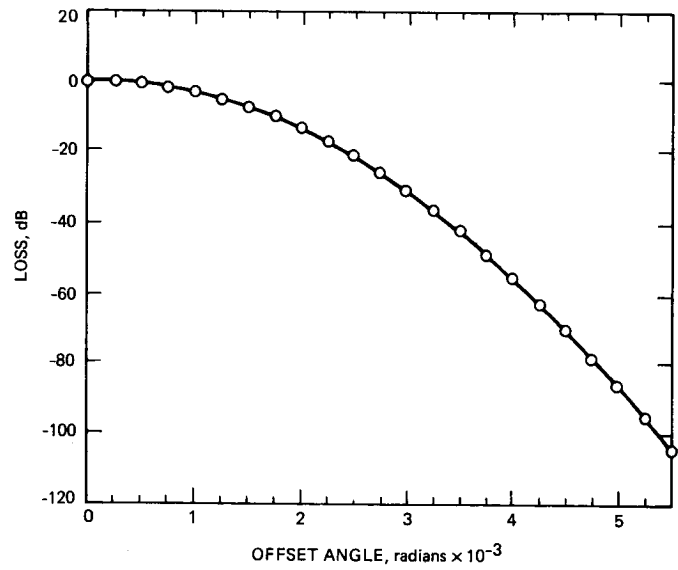


Fig. 3. Connector coupling loss as a function of the angular offset

Calculated 70-Meter Antenna Performance for Offset L-Band and C-Band Feeds

D. Hoppe and P. Stanton

Radio Frequency and Microwave Subsystems Section

This article summarizes a series of calculations that were carried out in order to determine the performance of the new dual-shaped 70-m antenna for feeds that are displaced from the focal ring. Calculations were carried out at 1.68 GHz (L-band) and 5.0 GHz (C-band) for a number of feed/subreflector configurations. The effects of feed displacement, feed pointing angle, subreflector tilt, and lateral subreflector movement are summarized. Of specific interest are gain, beam squint, and spillover noise temperature for each of the feed/subreflector configurations described above.

I. Introduction

In order to support the Soviet Mars Orbiter/Phobos Lander mission with an uplink as well as a downlink capability, a 5-GHz (C-band) transmit feed will be added to the existing 1.68-GHz (L-band) receive feed at DSS 14. Due to lack of focal ring space, the L-band feed is radially displaced from the ring, causing a slight drop in gain and a small beam squint. In order for the transmit and receive beams to be coincident, the C-band feed's phase center should coincide with that of the L-band feed. Unfortunately, the rather large radial displacement (in terms of wavelengths) at C-band causes a significant drop in gain. Existing computer programs (T. Veruttipong, D. Rochblatt, W. A. Imbriale and V. Galindo, *Dual-Shaped and Conic GTD/Jacobi-Bessel Analysis Programs: A User Manual*, JPL Internal Document D-2583, Jet Propulsion Laboratory, Pasadena, California) were used to determine the C-band and L-band gain loss, and to determine beam squint as a function of radial feed displacement for the upgraded dual-shaped 70-m antenna system (A. G. Cha and W. A. Imbriale, *Computer Programs for the Synthesis and Interpolation of 70M Antenna Reflector Surfaces*, JPL Internal Document D-1843, Jet Propulsion Laboratory, Pasadena, California, November 1984).

In an effort to retrieve some of the gain loss, the effects of feed pointing, subreflector tilt, and lateral subreflector movement were examined. The results of these parameter sweeps are summarized, and spillover noise temperatures and antenna patterns are presented for a few cases. The next section compares the antenna performance for feeds placed at the present L-band location (henceforth called the nominal configuration) to that which could be obtained for feeds placed on the focal ring. Subsequent sections present results for the parameter sweeps described above.

II. Nominal Configuration

The geometry of the dual-shaped 70-m system is shown in Fig. 1. Point N represents the position of the phase center for a feed location on the focal ring. The pointing angle of such a feed with respect to the main reflector axis is shown as $\theta_N = 5.73722$ degrees. Also shown is the location of the phase center for the offset L-band feed, point L . This point is displaced radially about 24 inches from the focal ring and displaced about 3 inches toward the subreflector from point N . The L-band pointing angle, $\theta_L = 8.617$ degrees, is also shown. For

The calculation of antenna gain, the same feed pattern was used for both frequencies—that of a 22.4-dB corrugated horn. It is assumed to be a good representation of both the dual-mode L-band horn near its center frequency and the C-band feed that is yet to be developed.

Table 1 summarizes calculated dual-reflector gain and beam position for both frequencies at both feed locations. The first line, labeled directivity, represents the calculated gain from the dual-reflector analysis program. This gain value is modified due to quadripod blockage, VSWR, surface tolerance, and horn and waveguide loss. Pointing loss at C-band assumes a 0.005 degree pointing accuracy, and pointing loss at L-band assumes a 0.005 degree pointing accuracy and L-band squint relative to C-band. Calculated beam position for the four cases is also shown in the table. Far-field patterns (asymmetric plane) are shown for the offset feed position at L-band and C-band in Figs. 2 and 3.

As can be seen from the first line of Table 1, a severe gain loss of over 2.7 dB is suffered when the C-band feed is displaced from the focal ring, while the L-band loss is a tolerable 0.42 dB. Examination of the main reflector current indicates that a severe phase error is responsible for the gain loss. The phase error is, of course, a function of the feed displacement in terms of wavelengths. The beam position is about 0.19 degrees for the offset feed at both frequencies. Figures 2 and 3 show the coma lobes generated by the offset feeds—about -12.5 dB at L-band and -10 dB at C-band. Due to the large gain loss incurred by displacing the feed, particularly at C-band, some investigations were carried out to determine the effects of feed angle and subreflector position on this gain loss. The next few sections summarize the calculations made to determine these effects.

III. Feed Displacement

Antenna gain and beam position were calculated as a function of purely radial feed displacement for both frequencies of interest. The geometry is depicted in Fig. 4. The radial feed displacement (ΔR) was varied with a fixed feed angle of $\theta_F = 5.73722$ degrees. Calculated antenna directivity (line 1 of Table 1) is plotted as a function of ΔR for L-band in Fig. 5 and C-band in Fig. 6. The calculated beam position is essentially identical for both frequencies and is plotted in Fig. 7.

From Fig. 6, we see that at 5-GHz a gain loss of about 0.5 dB occurs for an 8-inch offset, and about 1 dB for a 12-inch offset. On this plot, the current L-band feed location is well represented by a 24-inch offset and a gain loss of 2.7 dB, even though the feed angle used for this plot is 5.7 degrees as opposed to 8.6 degrees. Feed angle has only a small

influence on antenna gain, and these effects are described next. Figure 7 shows that beam position is essentially a linear function of feed displacement.

IV. Feed Angle

Feed pointing angle effects were examined for a fixed feed position. The position chosen was an offset of 14 inches ($\Delta R = 14$ inches). This distance represents the minimum distance the phase center of the L-band feed must be from the focal ring due to mechanical considerations. Gain versus feed angle is plotted in Fig. 8 for L-band and in Fig. 9 for C-band. Beam position is insensitive to feed angle and is essentially constant at 0.121 degrees. These figures indicate that gain is a weak function of feed angle (note the scale of 0.05 dB per division). We will later show that spillover noise temperature is affected significantly by this parameter. From Fig. 9, we note that the optimum feed angle (in terms of gain) for a 14-inch offset is very nearly the focal ring feed angle of 5.7 degrees.

V. Subreflector Tilt

For a study of subreflector tilt, the feed was placed at the present L-band location with a pointing angle of 5.73722 degrees. The geometry for subreflector tilt is depicted in Fig. 10. The subreflector system was rotated through an angle ($\theta' - \theta_0$) about the point B , which is located at $Z_m = 644$ inches. This particular rotation point was chosen since excellent results have been obtained using this point when analyzing a similar problem [1]. Also, following the results of [1], the nominal angle of rotation was taken to be one-half the difference between the offset feed location and the focal ring location. Gain at L-band and C-band for several subreflector tilt angles near the optimum point is shown in Figs. 11 and 12. The corresponding beam position, identical for both frequencies, is shown in Fig. 13.

As was previously reported [1], these calculations indicate that nearly all of the gain lost due to displacing the feed can be recovered by tilting the subreflector. For approximately 1.2 degrees of subreflector tilt, all but 0.13 dB of the gain lost at C-band is recovered, and all but 0.11 dB at L-band. Unfortunately, the mechanical controls required to tilt the subreflector between tracks are not part of the present design.

VI. Lateral Subreflector Movement

As an alternative to subreflector tilt, the effect of lateral subreflector movement on antenna gain was investigated. Unlike subreflector tilt, the mechanical controls required for lateral subreflector movement are part of the present design.

For these calculations, a feed located at the present L-band position and pointed at the present L-band feed angle (8.617 degrees) was used. The subreflector was moved in a purely ($-X_m$) direction (see Fig. 10). Gain at L-band and C-band for subreflector displacements up to 5 inches is shown in Figs. 14 and 15, with the corresponding beam position shown in Fig. 16. Figures 17 and 18 show antenna patterns for a subreflector displacement of 5 inches.

Again, a substantial increase in gain, particularly at C-band, can be obtained for offset feeds by a lateral displacement of the subreflector. For a 3-inch subreflector movement, the gain lost relative to that for a feed on the focal ring is about 1 dB, and about 0.5 dB for a 5-inch subreflector movement. These losses should be compared to 2.7 dB for a non-displaced subreflector. For L-band, all but about 0.1 dB of the gain loss is recovered for a subreflector offset of 3 inches. Figures 17 and 18 show how the pattern symmetry is improved and the comma lobe is reduced for a 5-inch subreflector displacement.

VII. Spillover Noise Temperature

Since lateral displacement of the subreflector appears to be a reasonable method of obtaining acceptable gain loss for offset C-band and L-band feeds, spillover noise temperature was calculated as a function of subreflector displacement. Computer programs used in the analysis are described elsewhere (A. G. Cha, *Physical Optics Analysis of NASA/JPL*

Deep Space Network Antennas, JPL Internal Document D-1853, Jet Propulsion Laboratory, Pasadena, California, November 1984) and the results are summarized in Table 2. For both frequencies, spillover noise is reduced for larger subreflector displacements. Therefore, both increased gain and reduced noise can be obtained by laterally displacing the subreflector.

Finally, the influence of feed tilt angle on spillover noise was examined for the case of a 5-inch lateral subreflector displacement. Spillover noise at L-band versus feed tilt angle is plotted in Fig. 19. At the present feed angle (8.617 degrees), spillover noise is about 4.8 K, but could be reduced to about 2.0 K if the feed were repointed to an angle between 3 degrees and 5.5 degrees.

VIII. Conclusion

The results of calculations of gain for the 70-m dual-shaped antenna for several different feed and subreflector configurations at L-band and C-band have been presented. For a C-band feed located at the current L-band location, a severe gain loss of 2.7 dB occurs. Tilting the subreflector can reduce this loss to about 0.1 dB. A lateral displacement of the subreflector of 3 inches can reduce the loss from 2.7 dB to about 1 dB. Feed pointing angle was shown to have only a small effect on antenna gain, but a larger effect on spillover noise temperature.

Acknowledgements

The authors would like to acknowledge the assistance of the Antenna and Microwave Development Group, particularly Dr. T. Veruttipong, throughout this study.

References

- [1] T. Veruttipong, V. Galindo-Israel and W. A. Imbriale, "Low Loss Off-Axis Feeds for Symmetric Dual-Reflector Antennas," *TDA Progress Report 42-84*, vol. Oct.-Dec. 1985, pp. 35-59, Jet Propulsion Laboratory, Pasadena, Calif., February 15, 1986.

Table 1. 70-m theoretical performance

Parameter	5-GHz (C-Band)		1.68-GHz (L-Band)	
	N	L	N	L
Feed location (Fig. 1)				
Directivity	70.85	68.11	61.29	60.87
Quad (0.922)	-0.35	-0.35	-0.35	-0.35
VSWR (1.2)	-0.04	-0.04	-0.04	-0.04
Surface tolerance (0.0208 in.)	-0.05	-0.05	-0.01	-0.01
Horn loss	-0.22	-0.22	-0.10	-0.10
Waveguide loss	-0.18	-0.18	-0.07	-0.07
Pointing loss	-0.07	-0.07	-0.01	-0.08
Gain (dBi) at system η	69.94	67.20	60.71	60.22
$\eta\%$	72.7	38.7	77.8	69.5
Gain (dBi) at 100% η	71.32	71.32	61.80	61.80
Beam position, deg	0.0	0.186	0.0	0.194

Table 2. Spillover noise temperatures

Subreflector Displacement, in.	Spillover Noise (C-Band), K	Spillover Noise (L-Band), K
0	11.7	9.4
3	8.7	7.6
5	5.9	4.8

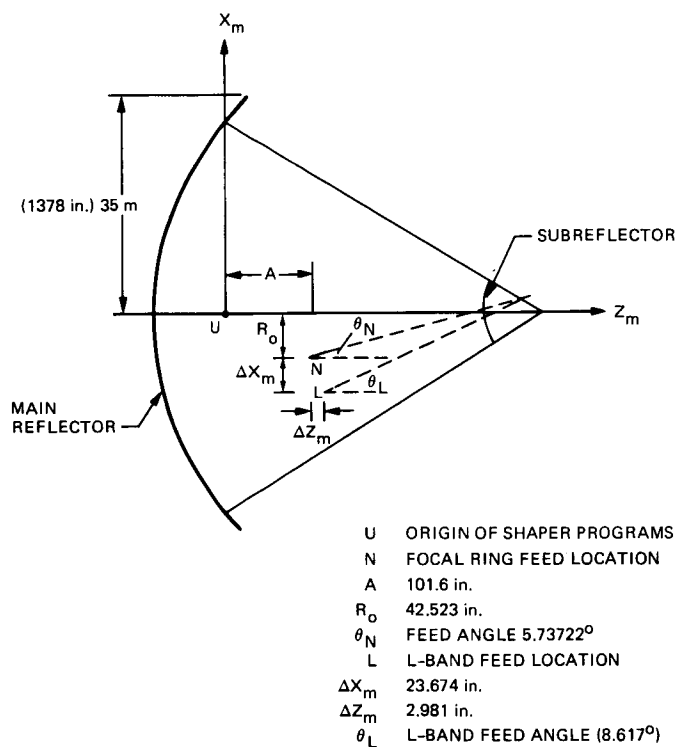


Fig. 1. 70-m antenna geometry

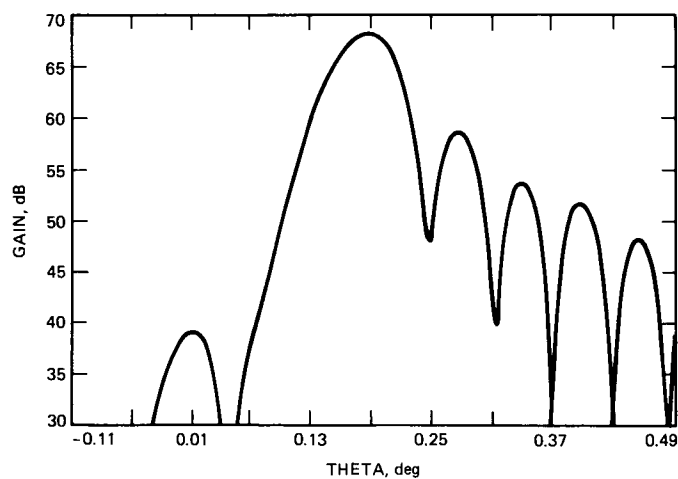


Fig. 2. C-band pattern, present L-band feed location

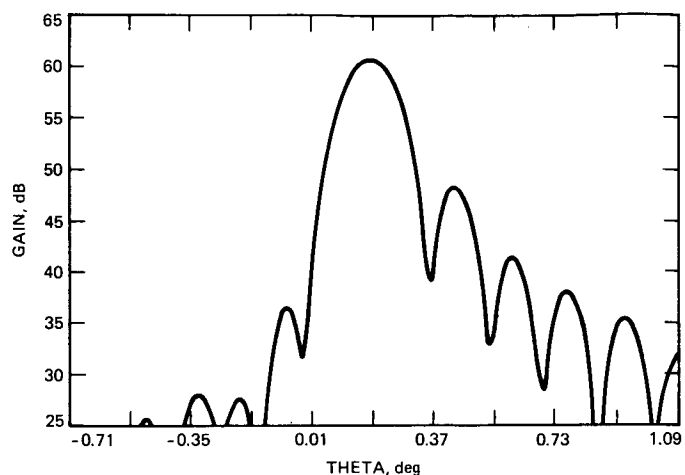


Fig. 3. L-band pattern, present L-band feed location

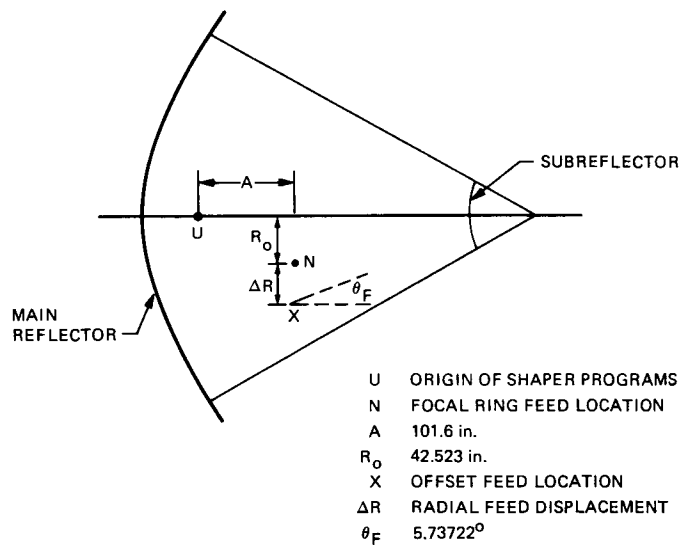


Fig. 4. Geometry for radial feed displacement

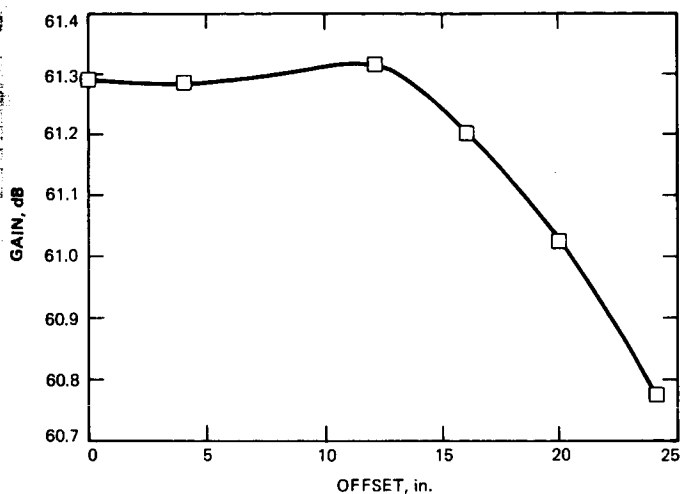


Fig. 5. Gain vs. radial feed displacement (L-band)

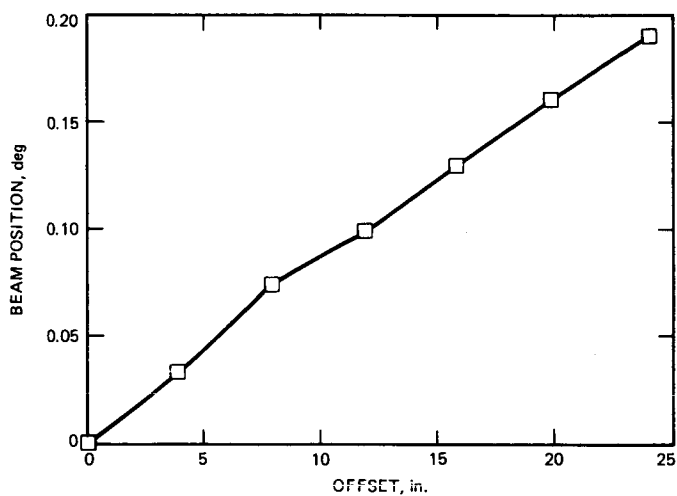


Fig. 7. Beam position vs radial feed displacement

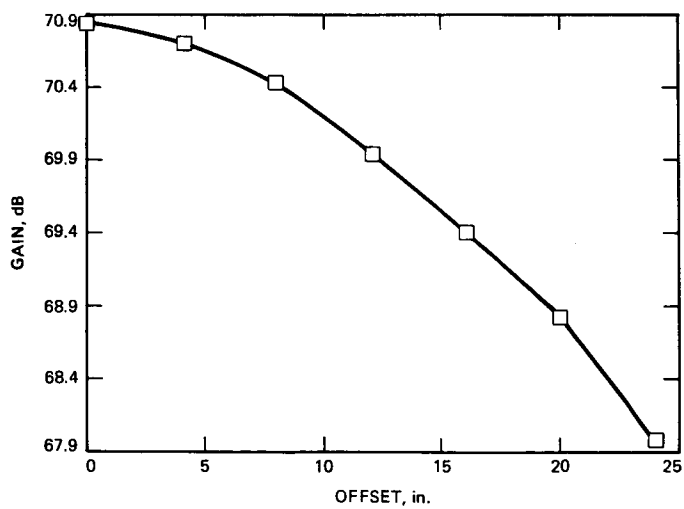


Fig. 6. Gain vs. radial feed displacement (C-band)

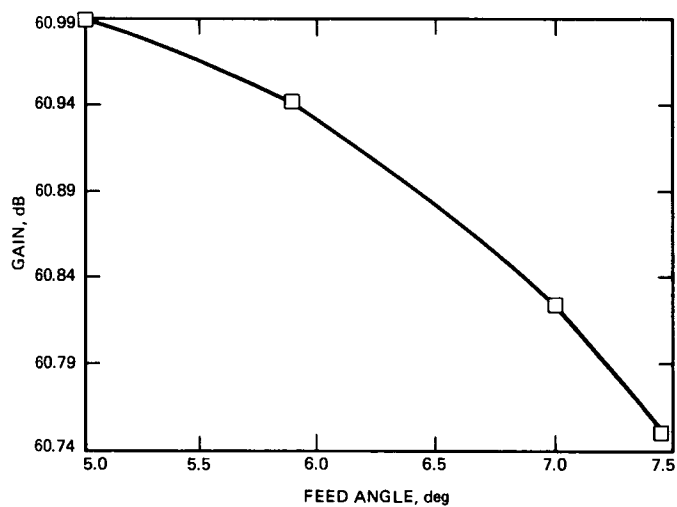


Fig. 8. Gain vs. feed angle (L-band)

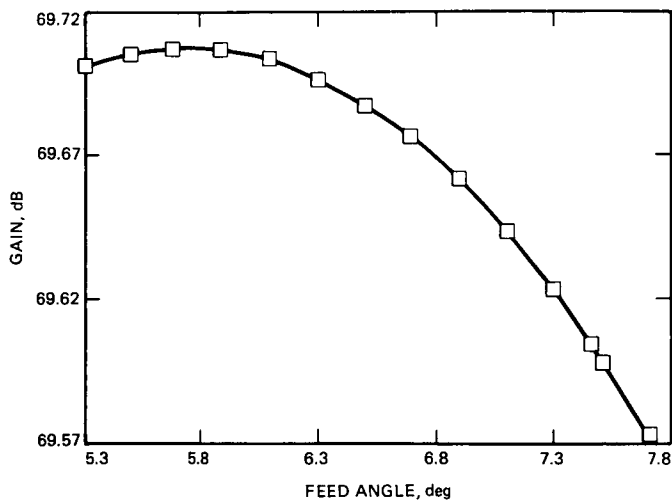


Fig. 9. Gain vs. feed angle (C-band)

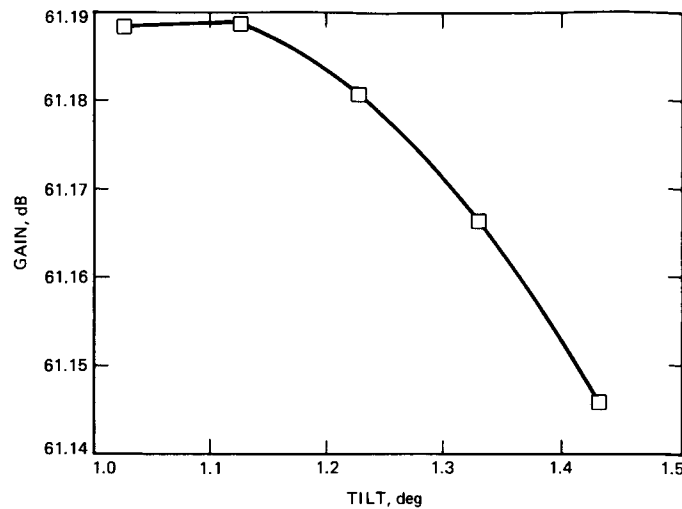


Fig. 11. Gain vs. subreflector tilt (L-band)

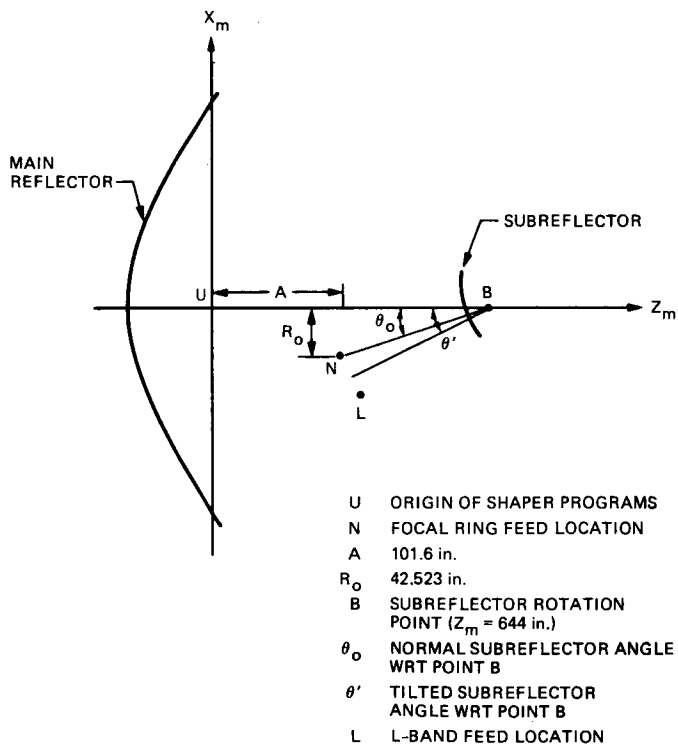


Fig. 10. Geometry for subreflector tilt

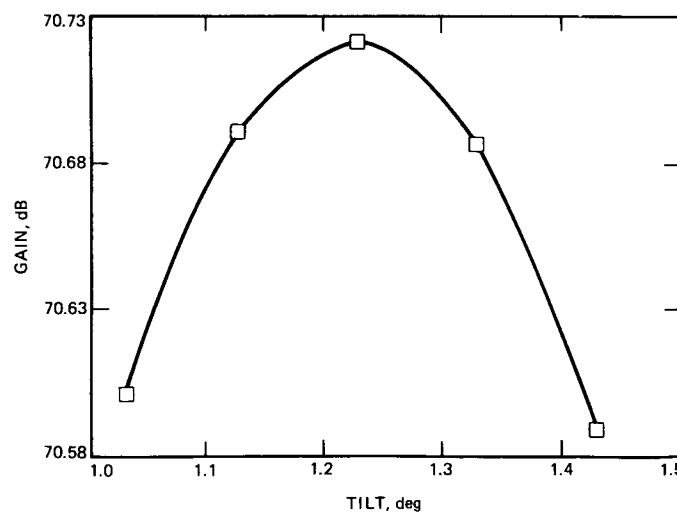


Fig. 12. Gain vs. subreflector tilt (C-band)

ORIGINAL PAGE IS
OF POOR QUALITY

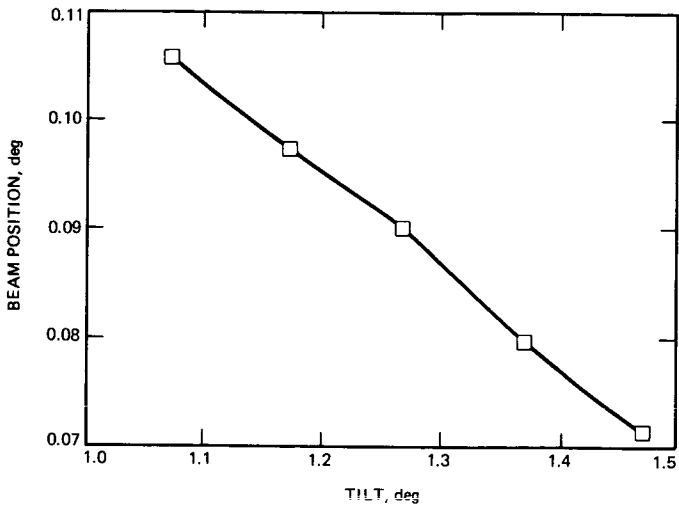


Fig. 13. Beam position vs subreflector tilt

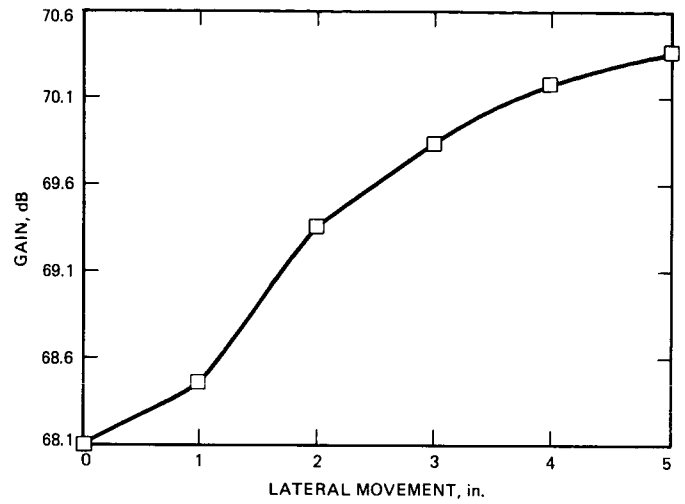


Fig. 15. Gain vs. lateral subreflector movement (C-band)

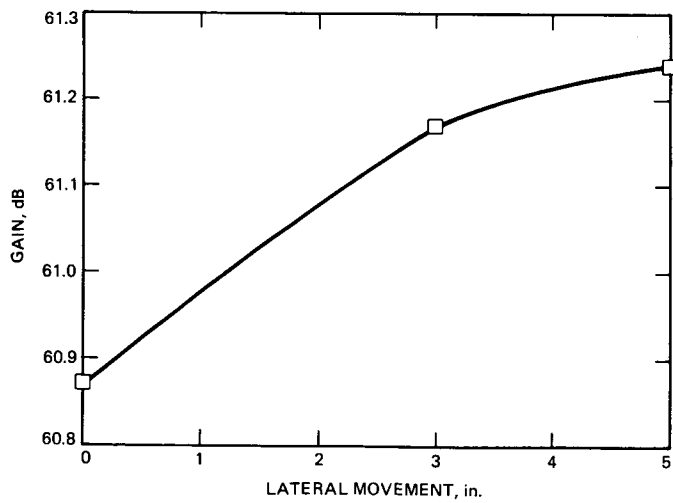


Fig. 14. Gain vs. lateral subreflector movement (L-band)

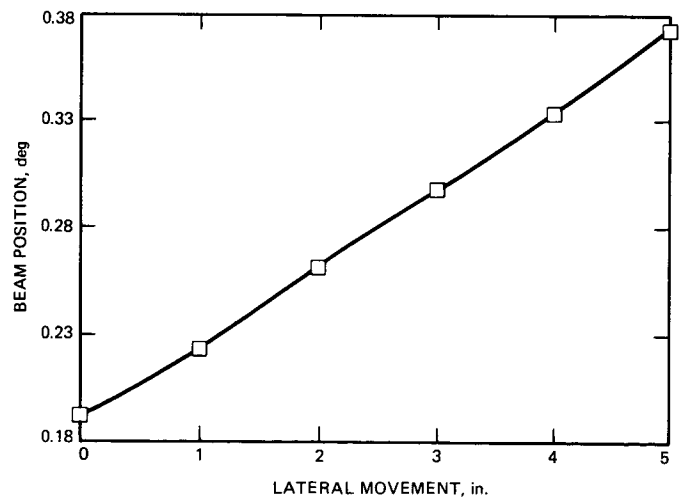


Fig. 16. Beam position vs. lateral subreflector movement

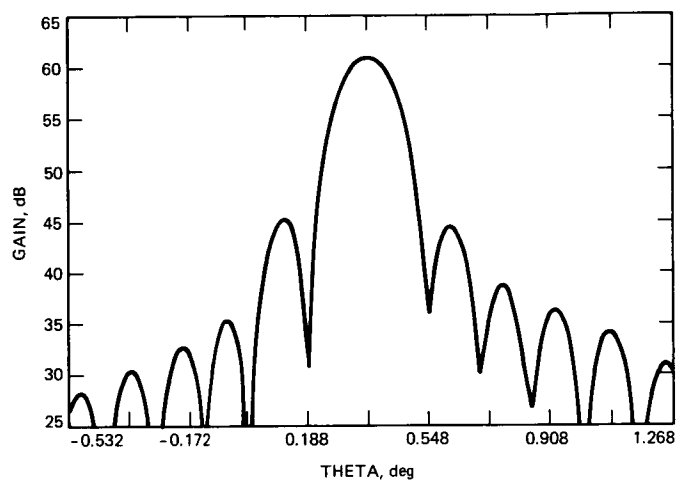


Fig. 17. L-band pattern 5-inch subreflector offset

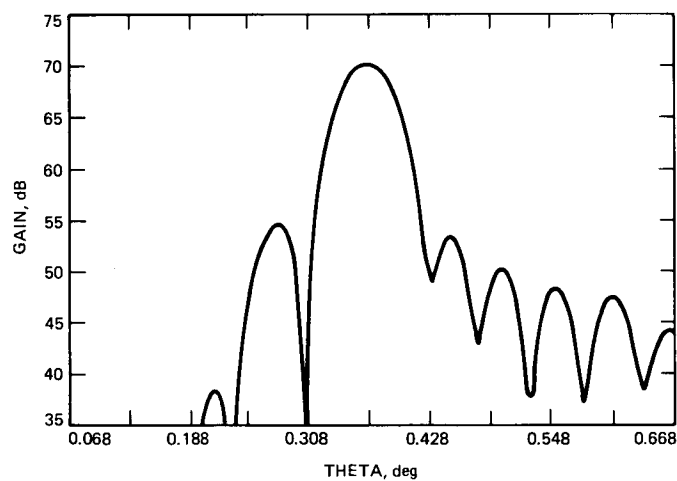


Fig. 18. C-band pattern 5-inch subreflector offset

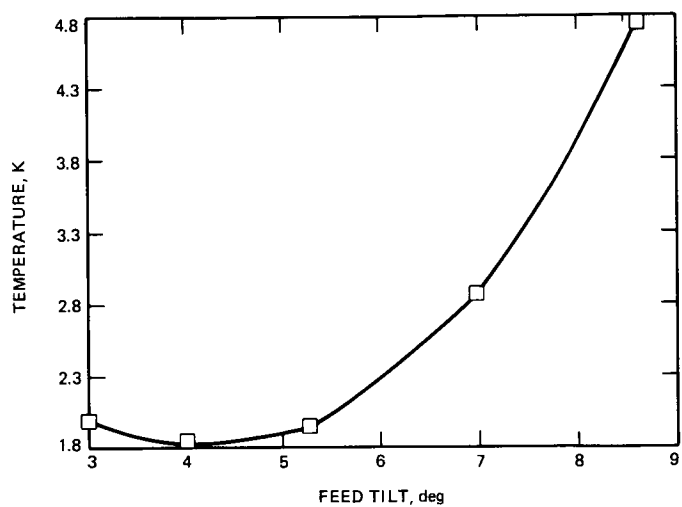


Fig. 19. Spillover noise temperature vs. feed tilt angle

Sorption Compressor/Mechanical Expander Hybrid Refrigeration

J. A. Jones

Applied Technologies Section

M. Britcliffe

Radio Frequency and Microwave Subsystems Section

Experience with DSN ground-based cryogenic refrigerators has proved the reliability of the basic two-stage Gifford-McMahon helium refrigerator. A very long life cryogenic refrigeration system appears possible by combining this expansion system or a turbo expansion system with a hydride sorption compressor, in place of the usual motor-driven piston compressor. To test the feasibility of this system, a commercial Gifford-McMahon refrigerator was tested using hydrogen gas as the working fluid. Although no attempt was made to optimize the system for hydrogen operation, the refrigerator developed 1.3 W at 30 K and 6.6 W at 60 K. The results of this test and of theoretical performances of the hydrid compressor are presented, coupled to these expansion systems.

I. Introduction

Sorption refrigeration is a method of cooling wherein gas is compressed by means of physical surface adsorption or chemical internal absorption, and then passed through an expansion device such as a Joule-Thomson (J-T) expansion valve, thus creating net cooling. For example, hydrogen is chemically absorbed into certain rare Earth metallic compounds such as LaNi_5 . At room temperature, the partial pressure of hydrogen on LaNi_5 is about 2 atm, while at 373 K, the LaNi_5 hydride decomposes and the hydrogen is released at 40 atm. By heating and cooling a series of such canisters [1], a continuous flow of high-pressure hydrogen gas can be generated, and this gas can be expanded to provide cooling to liquid hydrogen temperatures (14 K to 33 K). A somewhat

similar process occurs between charcoal and nitrogen, except that the nitrogen is physically adsorbed onto the solid charcoal surface rather than chemically adsorbed. Cooling to about 80 K or above can be obtained with this method. Charcoal adsorption tends to occur best at temperatures below 250 K and desorption occurs best above 400 K.

Both physical and chemical sorption cooling have recently been demonstrated [2], [3], and [4], and the results are most encouraging in terms of extending the life of both ground-based and flight-borne refrigeration systems to 10 years or more. Since sorption systems have virtually no wear-related moving parts except for very long life, room temperature, low frequency valves, they have a potential life expectancy of

many decades. Recent tests have demonstrated hydride sorption compressor operation for 5800 h [2], hydride cryogenic systems operation between 14 K and 29 K for over 1000 h [2] and feasibility testing of charcoal/nitrogen cryogenic systems between 100 K and 120 K [4].

Since sorption systems are powered by low-grade heat (above approximately 400 K), space-borne systems are particularly attractive applications. Direct solar heat can be used or even waste heat from a radioactive thermoelectric generator. Unfortunately, sorption refrigeration also has its disadvantages. Although hydrogen is absorbed at temperatures above 300 K, nitrogen requires adsorption temperatures generally below 250 K. In a low Earth orbit, this temperature requires fairly large and heavy radiators, unless a fluid loop is used to reject the heat at varying levels, e.g., 400 K, 300 K, 250 K, etc.

An alternative to nitrogen physical adsorption for cooling in the 65 K to 100 K region is an oxygen chemisorption J-T refrigeration system. This system, which is still in an experimental phase at JPL (NASA patent pending), may eventually prove to be very efficient both in terms of power and weight.

For the present, however, alternatives to J-T expansion of sorbed gas are Gifford-McMahon (G-M) expansion or turbo-expansion. These alternative expansion systems would allow hydride compressors to function as the gas supplier for a first-stage refrigeration system (65 K to 100 K). Due to the high inversion temperature (about 200 K) of hydrogen gas, a first-stage refrigeration system is necessary to precool the gas before it is expanded in a J-T system. The G-M or turbo-expanded hydride system could then serve as a first stage for a hydride J-T system.

As mentioned, the hydride compressor itself has virtually no wear-related moving parts and is thus expected to last at least 10 years [2]. Present G-M expanders typically have a 20,000 h to 30,000 h mean time between maintenance (MTBM) [5], and they are lightweight as well as highly reliable. A 9 kg expander can provide about 15 W of cooling at 70 K. For the past two decades, G-M expanders have been used as the primary means of cooling for almost all ground-based cryogenic radio antenna systems. Furthermore, their failure mode in the presence of trace contamination is in the form of gradual deterioration of performance, as opposed to catastrophic failure, as is the case with most other mechanical expanders. Lightweight redundancy or multiple units with lower duty cycles are clearly possible. Furthermore, systems research can likely increase the present single-unit G-M maintenance-free life to 40,000 to 50,000 h (P. Kerney, private communication, CTI Cryogenic, Waltham, MA, 1985, 1986 and R. Longworth, private communication, Air Products Corp., Allentown, PA,

1986). Gas-bearing turbo-expanders, by contrast, have no wear-related moving parts and can thus be expected to last at least 10 years. They also are very lightweight (less than 1 kg for 15 W of cooling at 70 K).

The following section describes data obtained by running a G-M expander with hydrogen and helium gas. Based on these measurements, as well as predictions of turbo-expander hydrogen performance, various system performance estimates are made for hydride-driven G-M and turbo-expansion refrigerators.

II. Gifford-McMahon Expansion

A. Test Results

A series of tests was performed with an unmodified stock CTI Model 21 two-stage G-M refrigerator, using both helium and hydrogen as the working fluid. The data for both first- and second-stage performance for helium are shown in Fig. 1. With no power on the second stage, the refrigerator first-stage performance varied from 2 W at 40 K to 6 W at 70 K. Alternatively, with no power on the first stage, the second-stage performance varied from 1 W at 15 K to 2.75 W at 30 K. The helium flow rate was measured as 7.5 SCFM (0.587 gm/sec) when the pressure ratio was set at 18.2×10^5 Pa/ 6.89×10^5 Pa (18.0 atm/6.8 atm). (Note that 1 atm = 1.0133×10^5 Pa.) In general, these values are all quite close to those predicted by CTI for the Model 21.

The performance of an open-cycle hydrogen G-M system operating off of bottled hydrogen gas was generally somewhat higher for the first stage, but lower for the second stage. A variety of pressure ratios were tested in order to determine how overall system performance varied (Fig. 2). With a pressure ratio of 18.69 atm/6.78 atm and a flow rate of 9.7 SCFM hydrogen (0.381 gm/sec), approximately 6.6 W of power was obtained at 60 K with no second-stage load. When the pressure ratio was increased to about 18.7 atm/2.4 atm, the cooling power increased to about 9.3 W at 60 K with 11.4 SCFM (0.446 gm/sec) hydrogen. This compares with the helium measured cooling rate of about 4.7 W at 60 K with 7.5 SCFM (0.587 gm/sec) helium.

With no load on the first stage, the second-stage hydrogen performance was severely degraded compared to the helium performance. Even with a very high pressure ratio (18.7 atm/2.7 atm), the refrigerator produced only about 1.3 W at 30 K, compared to about 2.75 W at 30 K for helium at 18.0 atm/6.8 atm. The lower second-stage hydrogen performance is likely due to partial liquefaction of the hydrogen gas, which has a saturation temperature of about 24 K at 2.7 atm. Partial liquefaction in the regenerator could cause thermal "short-

circuits" and greatly reduce overall second-stage regenerator performance. It should be mentioned that the G-M test unit was not optimized for specific use with hydrogen, and therefore this data should not be used to make a final comparison between helium and hydrogen operation. The actual unit tested was designed for use with helium, as are all present G-M units, and thus some improvement may be expected if the regenerator, rpm rate, etc., are specifically designed for hydrogen gas.

B. Analysis

Based on the test data, a plot of usable cooling power at 65 K vs hydrogen pressure ratio is shown in Fig. 3. The first-stage regenerator effectiveness, ϵ , for a G-M refrigerator may be considered to vary from about 99.57 percent [6] to 98.5 percent [7]. For the analytical calculations, a regenerator effectiveness of 99.0 percent is assumed. For ground operations, a 300 K heat sink is reasonable, while for Earth orbital low power operations, 200 K is attainable by means of direct passive radiators for high Earth orbits, or by thermoelectric coolers for low Earth orbits.

A computer program has been developed at JPL for predicting hydride refrigerator performance [8]. The program agrees well with hydride J-T test data, and has shown that high-pressure ratio hydride compressor systems take only slightly more power to operate than do low-pressure ratio hydride compressor systems, because most of the energy input to a hydride compressor is used to liberate the hydrogen gas, while a much smaller part is used to compress the gas, or increase the overall thermal capacity of the system.

Based on the values shown in Fig. 3, approximately 8.2 ± 0.5 kW of power is necessary to generate 11.4 SCFM of hydrogen gas in the pressure range of $0.1 < P_L/P_H < 0.6$. Thus, the required specific power of a hydride-powered G-M system can be considered to vary from about 1000 W/W at $P_L/P_H = 0.36$ and 300 K heat sink to as little as 645 W/W at $P_L/P_H = 0.1$ and 200-K heat sink ($\epsilon = 99.0$ percent). A summary of the required hydride compressor specific powers is given in Table 1.

III. Turbo Expansion

Based on calculations made by Walter Swift of Creare, Inc., Hanover, NH (private communication, 1986) a turbo expander for hydrogen gas can be made as small as about 1/8-in. diameter for a 5-W load at 65 K. With a pressure ratio of 2 atm/0.2 atm, a turbo expander can be expected to have up to about 40 percent of ideal expansion (isentropic) efficiency. Significantly larger turbo-expanders, e.g., 100 W at 65 K, can be expected to have efficiencies as high as 80 per-

cent of isentropic expansion. Unfortunately, virtually no test data presently exist for miniature hydrogen turbo expanders, although miniature helium turbo expanders have generally ranged in the 30 to 60 percent isentropic efficiency range (W. Swift, private communication, Creare, Inc., Hanover, NH, 1986).

A sorption computer program was used to compute the necessary power to generate turbo-expanded cooling, at 65 K, assuming a counterflow heat exchanger effectiveness of 98 percent, a pressure ratio of 2 atm/0.2 atm, and an isentropic expansion efficiency of 40 percent. For a 300 K initial hydrogen temperature, the required specific power was 326 W/W, and for a 200 K heat sink, the required specific power was 259 W/W. When the isentropic expansion efficiency was increased to 80 percent, as would be the case for a larger turbo expansion system, the required specific powers were then cut by more than half. A summary of the results of the turbo expansion analyses is shown in Table 2.

IV. Summary and Conclusions

The hydrogen/G-M test results and the analyses of the hydride/G-M and hydride/turbo expansion refrigerators indicate that both systems use significantly more power than other developmental long-life refrigeration systems. In general, small developmental mechanical systems require between 40 W/W to 100 W/W for 65 K cooling [9] while the small hydride/G-M system can be expected to require about 1000 W/W for ground applications (300 K heat sink), or 645 W/W for space applications (200 K heat sink). The hydride/turbo expander is also predicted to require a high amount of power (although somewhat lower than the hydride/G-M system). For ground applications, calculations have predicted that small coolers require about 326 W/W, and space coolers require about 260 W/W. Large hydrogen turbo or G-M expansion systems, e.g., 100 W at 65 K, are likely to require less than half as much specific power.

Although these first-stage sorption refrigeration systems require considerably more power than their mechanical refrigeration counterparts, they do have some specific advantages. First, they can be operated directly from low-grade waste heat (e.g., solar or radioactive waste heat) as opposed to electricity. Hydride compressors operate quite satisfactorily with heat source temperatures between 75° C to 100° C. Second, and probably most importantly, they have a very long predicted lifetime (at least 50,000 h MTBM). Due to their simplicity and a minimum of wearing parts, their reliability should be extremely high. Although both first-stage systems are above the air freezing temperature of about 64 K, the G-M system is likely to be somewhat more "forgiving" in regard to gas contamination than the turbo-expanded system. Third,

for the case of the hydride/turbo expansion combination, this refrigerator offers nearly vibrationless operation. The very tiny turbo expander is supported on a thin film of gas and rotates typically at several hundred thousand rpm. The resulting vibration is virtually below the measurement threshold, as is the vibration due to the gas flow in the reversible chemical-hydride compressor. This lack of vibration can be of crucial importance for highly sensitive infrared detector applications. It should be mentioned, however, that the vibration level of

the G-M system can be minimized by counterbalancing with a second G-M unit.

Finally, although these individual first-stage sorption systems require a relatively high amount of power, when used in series with lower-staged sorption refrigeration systems for temperatures below 15 K, the overall power and weight of the multi-staged sorption systems can be significantly less than multi-stage mechanical systems [9].

Acknowledgments

Peter Kerney of CTI, Waltham, MA, assisted in the Gifford-McMahon experimental portion of this report. Walter Swift of Creare, Inc., Hanover, NH, assisted in the analytical prediction of hydrogen/turbo-expander performance.

References

- [1] H. H. Van Mal and A. Mijnheer, "Hydrogen refrigeration for the 20 K region with a LaNi_5 hydride thermal absorption compressor for hydrogen," *Proc 4th Int'l Cryogenic Eng Conf.*, IPC Science & Tech. Press, Surrey, England, pp. 122-125, 1972.
- [2] J. A. Jones and P. M. Golben, "Design, life testing, and future designs of cryogenic hydride refrigeration systems," *Cryogenics*, vol. 25, pp. 212-219, 1985.
- [3] J. A. Jones, "Cryogenic hydride refrigerator results and applications to hydrogen liquefaction," video presentation, *World Hydrogen Energy Conf.*, Toronto, Canada, 1984.
- [4] S. Bard, "Development of an 80-120 K charcoal/nitrogen adsorption cryocooler," *Int'l Cryocooler Conf.*, Annapolis, MD, 1986 (also submitted to *Proc Int'l Cryocooler Conf.*, Annapolis, MD.)
- [5] F. E. F. Chellis, "Comparing closed cycle cryocoolers," *CTI Cryogenics*, Waltham, MA, 1979.
- [6] R. A. Ackermann and W. E. Gifford, "A heat balance analysis of a Gifford-McMahon refrigerator," *Trans. ASME, J. Eng. Ind.*, 91:273, pp. 221-229, 1969.
- [7] D. B. Colyer and R. L. Gessner, "Maintenance cryogenic refrigerator turbomachinery," *Advances in Cryogenic Engineering*, vol. 14, pp. 485-493, Plenum Publishers, NY, 1968.
- [8] K. B. Sigurdson, "A general computer model for predicting the performance of gas sorption refrigerators," *Second Biennial Conference on Refrigeration for Cryogenic Sensors and Electronic Systems, GSFC*, Greenbelt, Maryland, pp. 343-355, Dec. 7-8, 1982.
- [9] J. A. Jones, "Sorption refrigeration comparison study," *Eleventh International Cryogenic Engineering Conference*, West Berlin, West Germany, pp. 393-397, April 22-25, 1986.

**Table 1. Hydride-powered G-M performance estimates
for 10 W at 65 K**

P_L/P_H	Spec Power @ 300 K Heatsink	Spec Power* @ 200 K Heatsink
0.10	1000	645
0.36	1330	720

*These values assume the test regenerator effectiveness was 99.0%.

Table 2. Hydride-powered turbo performance estimates

Cooling Power @ 65 kW	Turbine Efficiency, %	Spec Power @ 300 K Heatsink	Spec Power @ 200 K Heatsink
5	40	326	259
100	80	125	114

Assumptions: $\epsilon_{HX} = 98\%$
 $P_L/P_H = 0.10$

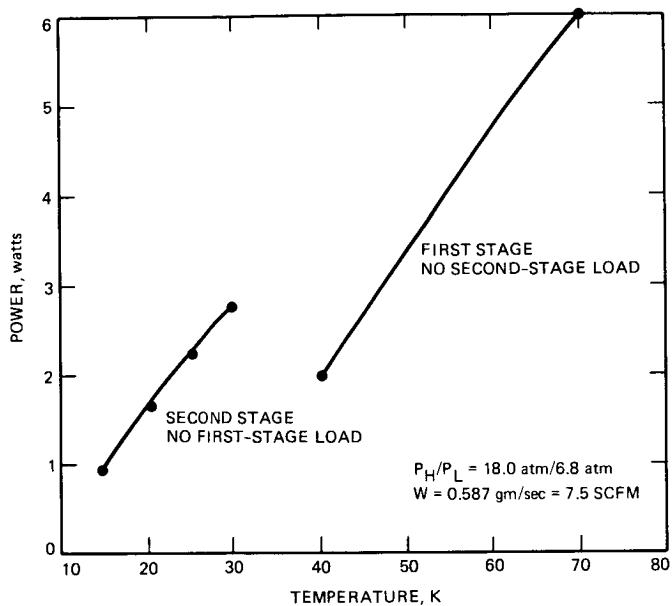


Fig. 1. CTI model 21 G-M performance with helium

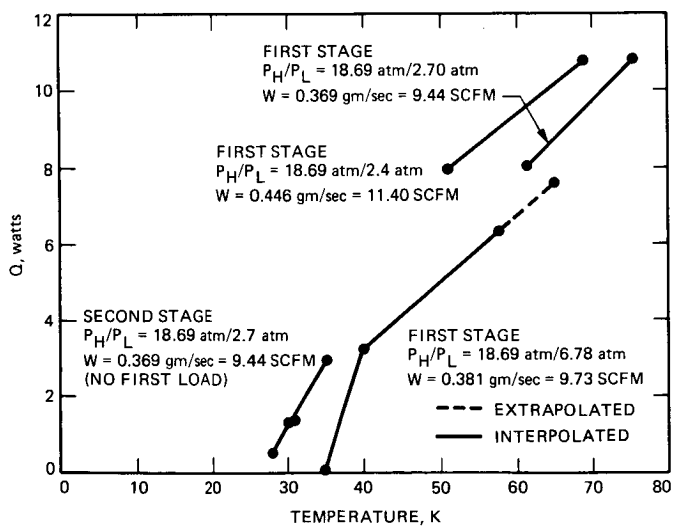


Fig. 2. CTI model 21 G-M performance with hydrogen

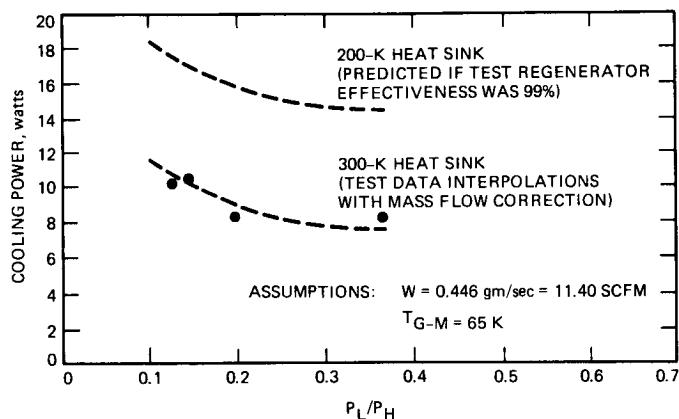


Fig. 3. Hydrogen G-M cooling powers for varying P_L/P_H

Reduction of Ground Noise in the Transmitter Crowbar Instrumentation System by the Use of Baluns and Other Noise Rejection Methods

J. Daeges and A. Bhanji

Radio Frequency and Microwave Subsystems Section

Electrical noise interference in the transmitter crowbar monitoring instrumentation system creates false sensing of crowbar faults during a crowbar firing. One predominant source of noise interference is the conduction of currents in the instrumentation cable shields. Since these circulating ground noise currents produce noise that is similar to the crowbar fault sensing signals, such noise interference reduces the ability to determine true crowbar faults.

Analysis and test data are presented to show that by properly applying baluns (Balancing Units) and other noise rejection methods, the induced ground noise is reduced and proper operation of the crowbar instrumentation system is obtained.

I. Introduction

Modern day high-power transmitters use large and expensive components in the final RF amplifier stage. For example, a klystron may cost as much as \$250,000. The protection of these high-cost items from destructive arcs and overloads is, therefore, of paramount importance. One of the special protection devices in a high-power transmitter is the crowbar unit. When an internal arc in the klystron is sensed, the crowbar is instantly fired and diverts the large stored energy in the power supply system, thus preventing the disaster that would result if the energy were "dumped" into the arc.

The crowbar instrumentation system that senses the faults and commands firing of the crowbar has been integrated into an overall transmitter control console. The console provides

the operator with the overall status of the transmitter. The successful operation of this monitoring and protection system is unfortunately degraded due to electrical noise interference. A conductor or a circuit in a monitor and control system is always subjected to electrical influences from the surroundings. This is pronounced in crowbar systems, where high voltages and high currents arise relative to other circuits or ground. The disturbances thus caused can produce erroneous operation of the circuit, particularly if the circuit is relatively rapid and thus liable to be influenced by high frequency disturbances. Sources of these noise disturbances in monitor and control circuits include stray capacitive coupling, stray inductive coupling, circuits exposed to high voltage and high current gradients, and common impedance (all points connected to reference ground are not equivalent) [1]. Various methods of minimizing and suppressing ground noise have been used and

are described in this article. Baluns were used extensively as an EMC control device (noise suppressor) and played a key role in suppressing noise in the crowbar logic and timing circuits. The noise-suppressing effects of baluns have been investigated and details are presented below.

II. Baluns as an EMC Control Device (Noise Suppressor)

Baluns, as referred to here, are basically small iron-core transformers, bi-filar wound, with an equal number of primary and secondary turns used such that the signal current passes through one winding as it goes to a load and through the other winding as it returns to the source. Although baluns have been widely used by RF designers to connect balanced transmission lines with unbalanced lines or devices, their ability to suppress noise within electronic equipment has not been as fully exploited. A balun, or common-mode choke, is a bi-filar wound, broadband transformer that allows equal and opposite currents to flow through its windings, while suppressing unequal currents, such as those due to ground noise. Because of the bi-filar windings, no net flux is generated in the balun when its two currents are balanced; therefore, balanced signals encounter no inductance when passing through the balun. For unbalanced currents, however, the device acts as an inductance and effectively breaks up the ground current path. Unlike differential amplifiers, which can also be used to suppress ground noise, baluns are not common-mode limited and do not require expensive power supplies. Other advantages over differential amplifiers are lower cost, less distortion, and vastly greater reliability.

Baluns can be applied at either the driving or receiving end of a transmission signal line. Among the driving-end applications are ground isolation, current balancing, and protection of critical analog circuitry. In receiver applications, a balun can provide isolation for digital-circuit grounds, perform noise balancing, or reduce noise associated with single-wire transmission. When used as a receiver for a single-ended line, the balun allows the line to be converted into a balanced line without picking up any ground noise.

An instrumentation system with a coaxial balun at the input of the sensor amplifier is shown in Fig. 1. As stated above, when equal and opposite currents flow through the windings, as in the case of sensor current I_L (Fig. 1), no net flux is generated, and, therefore, no inductance is encountered. If unbalanced currents flow through the windings, as in the case of I_{n1} and I_{n2} , the coaxial balun acts as an inductance. A lumped inductance in series with the sensor amplifier cable shield would not be desirable because the sensor current and noise current would be reduced, thus maintaining a constant signal-to-noise ratio.

The ground noise current, induced cable noise current, and induced cable noise voltage (I_n , I_{n2} , and V_{na} , respectively) can be derived from Kirchhoff's laws by assuming that the amplifier input voltage signal from the sensor, V_{La} , equals zero [2]:

$$I_n = \frac{V_n [R_S + R_L + R_a + j2\pi f (L_s + L_c - 2M)]}{(R_S + R_g + j2\pi f L_s) (R_L + R_a + R_g + j2\pi f L_c) - (R_g + j2\pi f M)^2}$$

$$I_{n2} = \frac{I_n [R_S + j2\pi f (L_s - M)]}{R_S + R_L + R_a + j2\pi f (L_s + L_c - 2M)}$$

$$= \frac{V_n [R_S + j2\pi f (L_s - M)]}{(R_S + R_g + j2\pi f L_s) (R_L + R_a + R_g + j2\pi f L_c) - (R_g + j2\pi f M)^2}$$

$$V_{na} = I_{n2} R_a$$

where

R_a is amplifier input resistance

R_L is sensor resistance

R_S is shield resistance

R_g is ground resistance

L_c is coaxial balun center conductor inductance

L_s is coaxial balun shield inductance

M is coaxial balun mutual inductance

The above equations show that the induced ground noise is minimized when $L_s \gg 0$ and $L_c \gg 0$.

III. Summary of Other Noise Rejection Methods Employed

Although baluns played a key role in reducing ground noise interference in the transmitter crowbar instrumentation system, other simple basic rules were employed to limit ground noise current to inductive and capacitive coupling. These design rules included:

- (1) All circuits sensitive to disturbance of high current crowbar discharges were designed so that their outgoing and return conductors followed each other as closely as possible. The conductors were either a twisted shield pair or coaxial cable.
- (2) In the crowbar cabinet, all the sensing cables (coax and twisted pair) were contained within a conductive conduit to reduce the high frequency ground noise [2].

- (3) The signal grounding system was connected to the ground system at only one point.
- (4) All wiring was carried out radially to prevent conductor loops.
- (5) As much care and attention was given to the "disturbing" circuits as the "disturbed" ones. High voltage corona and current arcing were minimized to reduce EMI.
- (6) Damping and clamping circuits (Zener diodes) were used wherever necessary.

IV. Experimental Results

The transmitter crowbar instrumentation system comprises basically the crowbar logic circuits (i.e., all circuits that monitor various transmitter critical operating parameters such as beam voltages and currents, the klystron body ("fast" body and "slow" body) and klystron magnet currents) and the crowbar timing circuit. When the klystron body currents or magnet current exceed the allowable operating range, the logic circuit senses this false operation and "fires" the crowbar, i.e., removes the beam voltage rapidly (in less than 10 microseconds). At the same time, the crowbar timing circuit measures the time it took to remove the beam voltage and verifies that the crowbar fired properly.

The data recorded in Fig. 2 was measured at DSS 13 before any attempts to apply baluns and other noise rejection methods to the crowbar cabinet and the crowbar instrumentation system were made. Note that when the crowbar was tested, the true fault should have been fast body interlock; however, due to the induced ground noise in the shields (as seen on the analog signals), the true fast body interlock was reset and false interlock signals of slow body and magnet interlocks were set.

The data recorded in Fig. 3 was measured at DSS 13 after the following modifications were made:

- (1) The crowbar logic and timing circuit boards were moved from the crowbar cabinet to local control console (LCC) cabinets, about 30 feet away.
- (2) All signals were carried between the crowbar cabinet and LCC by either coaxial cables or twisted-shield pairs.
- (3) In the crowbar cabinet, attempts were made to reduce EMI created by voltage corona and current arcing, and all signal cables (coaxial and twisted pair) were contained in conduits. All wiring was carried out radially to prevent conductor loops.
- (4) Baluns were applied to all signals arriving and leaving the logic and timing cards by wrapping each coaxial cable or twisted-shield pair around a Ferroxcube 400XT 750 3C8 core.

Due to modification (3) and primarily due to the addition of baluns, the immunity of the crowbar instrumentation system to induced ground noise was greatly increased. The system now operates without giving false indications during a crowbar firing.

V. Conclusions

By using baluns and other noise rejection methods, induced ground noise in the crowbar instrumentation system was reduced considerably, thus preventing false indications and improving reliability and the maintenance reporting feature of the system. Baluns played a key role in reducing induced ground noise without attenuating the sensor signal.

Finally, the problem of noise-rejection in monitor and control circuits in an electrically unfavorable environment, when circuits, subassemblies, or racks have to be interconnected, affects most engineers engaged in electrical design work. It is probably their biggest headache, and it is therefore necessary that noise rejection methods are applied from the start-up of the project, during the electrical and mechanical design phase.

Acknowledgment

The authors acknowledge the efforts of Keith Gwin, who performed various modifications to the crowbar instrumentation system and the crowbar cabinet.

References

- [1] B. Hammerlund, "Noise and Noise-Rejection Methods in Control Circuits, Particularly for High-Voltage Power Stations," 10th IEEE Electromagnetic Compatibility Symposium Records, pp. 216-227, 1968.
- [2] R. S. Burns, "Effects of Shield Impedance, Connector Resistance, and Coaxial Baluns on Ground Noise Interference in Nuclear Reactor Instrumentation System," Session 4A-1, IEEE Electromagnetic Compatibility Conference, pp. 198-203, 1976.

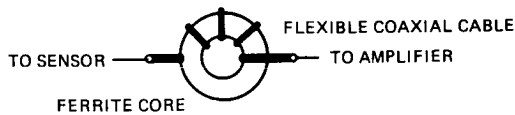
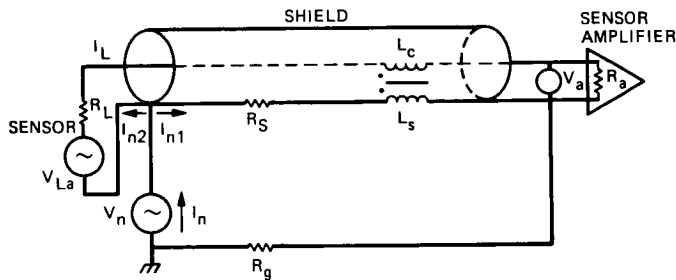


Fig. 1. Coaxial balun placed at the amplifier input

TIMING WAVEFORM DIAGRAM

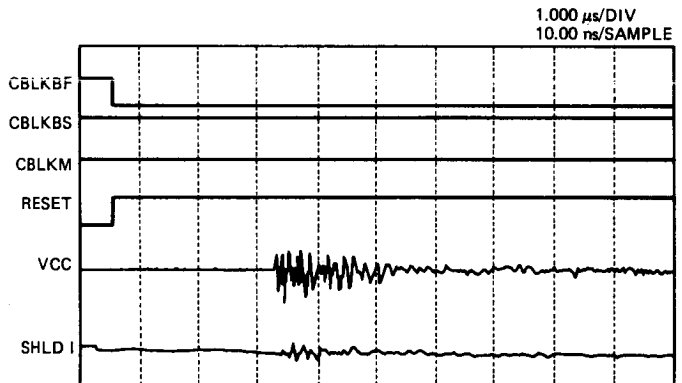


Fig. 3. Crowbar cabinet and instrumentation system noise measurement after improvements

TIMING WAVEFORM DIAGRAM

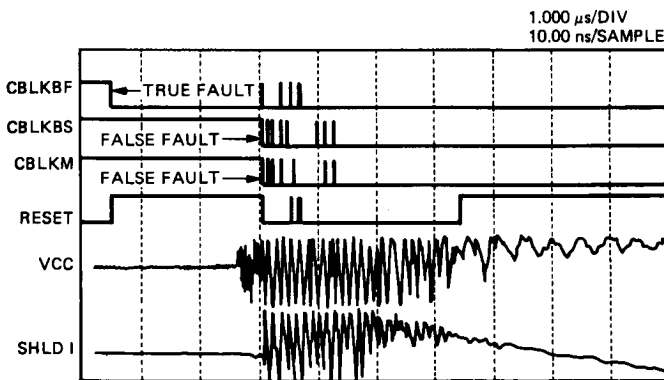


Fig. 2. Crowbar cabinet and instrumentation system noise measurements before improvements

Image Statistics Decoding for Convolutional Codes

G. H. Pitt, III, and L. Swanson
Communications Systems Research Section

J. H. Yuen
Telecommunications Science and Engineering Division

It is a fact that adjacent pixels in a Voyager image are very similar in grey level. This fact can be used in conjunction with the Maximum-Likelihood Convolutional Decoder (MCD) to decrease the error rate when decoding a picture from Voyager. Implementing this idea would require no changes in the Voyager spacecraft and could be used as a backup to the current system without too much expenditure, so the feasibility of it and the possible gains for Voyager were investigated. Simulations have shown that the gain could be as much as 2 dB at certain error rates, and experiments with real data have inspired new ideas on ways to get the most information possible out of the received symbol stream.

I. Introduction

After seeing an image decoded by the MCD recently, it was noticed that many errors in a decoded Voyager image could be detected by eye since pixels in error differ markedly from the image (Fig. 1). It was proposed that an expert look at an image, identify errors, and declare them as erasures for the Reed-Solomon decoder after the MCD. In this way, the Signal-to-Noise Ratio (SNR) could be lowered a bit, allowing even more errors to occur without damaging the chances of receiving a perfect image in the end.

The important facts are as follows:

- (1) Many errors differed markedly from the image.
- (2) The image differs only slightly from itself. This means that pixels that are near each other are usually very similar in value, and ones that are not similar are usually errors.

The Image Statistics Decoder (ISD) that we developed uses fact (2), but inside the convolutional decoder instead of after it, and actually *avoids* many of those errors noticed above. Therefore, in all results so far, the ISD performs better than even the best possible results using the MCD and an expert to declare erasures. In the following, more precise statements of fact (2) will be given in graphs, and the problems faced, the genesis of solutions, and results will be outlined.

II. First Results of Programming the Image Statistics Decoder

A. Feasibility

The first thing to check was how correct fact (2) actually is; how close are adjacent pixels in a Voyager image, and is this closeness fairly constant from image to image? Constant statistics from one image to the next are necessary since we need

to estimate a priori the statistics for each picture before decoding. With b_j defined as the grey level of the j th received pixel in a stream of pixels, the statistic that we decided to use at the beginning of this experiment was $D_j = |b_j - b_{j-1}|$, the absolute difference between the grey levels of two adjacent pixels (pixel values on Voyager range from 0 to 255). Preliminary results using this statistic were reported earlier [1], and some will be repeated here. We computed the theoretical distribution of D assuming independence between adjacent pixels (the MCD assumes independence), and plotted it against the distribution observed in several images. The results may be seen in the chart (Fig. 2).

Three different Voyager images were used for this demonstration: one of dark sky with Titan in the foreground, one of Saturn seen fully in the frame, and one of the rings of Saturn with the planet in the background. These three images seem completely different, but the distributions of D are quite similar for them when compared to the independent case, and quite different from the independent case. Therefore, statistics from any one of these images will be a much better model for another image's statistics than the independent case would be.

B. Theory

Decoders work on a simple principle: find the information bytes that were most likely sent, given that you received symbols $\{r_1, r_2, \dots, r_m\}$. More precisely, if we let B be the event that the information sent was a set of bytes $\{b_1, b_2, \dots, b_n\}$ and R the event that the received symbols¹ were $\{r_1, r_2, \dots, r_m\}$, then we want to find the information bytes $\{b_1, b_2, \dots, b_n\}$ that maximize the probability of B given R . In mathematical notation, we want to maximize $P(B|R)$ over all possible information sets $\{b_1, b_2, \dots, b_n\}$. From probability theory,

$$P(B|R) = \frac{P(B, R)}{P(R)} = \frac{P(R|B) P(B)}{P(R)}$$

where $P(B, R)$ is the probability that B and R both happened.

Let $\{s_1, s_2, \dots, s_m\}$ be the convolutionally encoded symbol stream associated with the information bytes $\{b_1, b_2, \dots, b_n\}$ and S be the event that $\{s_1, s_2, \dots, s_m\}$ was sent. Then S and B are equivalent events.

$$P(B|R) = \frac{P(R|S) P(B)}{P(R)} \quad (1)$$

¹The actual received symbol stream is $\{r_1, r_2, \dots, r_m\}$, so R is an event that actually happened. This is why we are given that R happened.

Over a memoryless Gaussian channel²,

$$P(R|S) = K \exp [-\sum (r_i - s_i)^2 / \sigma^2]$$

where K is a constant, r_i and s_i are described above, and σ^2 is the SNR. Therefore,

$$P(B|R) = K \exp [-\sum (r_i - s_i)^2 / \sigma^2] \frac{P(B)}{P(R)}$$

R and K are fixed, so $P(R)$ and K don't enter into the maximization. Therefore, we have reduced the problem of maximizing $P(B|R)$ over a Gaussian channel to that of maximizing

$$\exp [-\sum (r_i - s_i)^2 / \sigma^2] P(B)$$

We may take the natural log, multiply by -1 and equivalently minimize

$$\sum_i \frac{(r_i - s_i)^2}{\sigma^2} - \ln(P(B)) \quad (2)$$

This is the point where the interdependence of the information bytes makes a difference. If they are completely random and independent, then $P(B)$ is the same for every possible set of information bytes. Thus, $\ln(P(B))$ is constant, and we just have to minimize

$$\sum_i \frac{(r_i - s_i)^2}{\sigma^2} = \frac{1}{\sigma^2} \sum_i (r_i - s_i)^2$$

The SNR, determined by σ^2 , remains constant as we vary $\{b_1, b_2, \dots, b_n\}$, so it may also be removed, leaving

$$\sum_i (r_i - s_i)^2 \quad (3)$$

The MCD minimizes expression (3) over all possible sets $\{s_1, s_2, \dots, s_m\}$. However, as shown in Fig. 2, the information bytes are not independent, so $P(B)$ is not constant and should be used in decoding; we must minimize expression (2). Using the rules of probability again

$$P(B) = P(b_1) \prod_j P(b_j | b_{j-1}, b_{j-2}, \dots, b_1)$$

²The deep space link to Voyager is a memoryless Gaussian channel.

Trying to observe the distribution of $(b_j | b_{j-1}, b_{j-2}, \dots, b_1)$ would be impossible, but it may be possible to approximate it using an almost sufficient statistic like D described above.³ Assuming that D will be used as a sufficient statistic, we may write

$$P(B) \approx P(b_1) \prod_j P(b_j | D_j) \quad (4)$$

where D_j is not hard to calculate, and the distribution of $(b_j | D_j)$ is known (or at least approximated). Therefore we must minimize

$$\begin{aligned} & \sum_i \frac{(r_i - s_i)^2}{\sigma^2} - \ln(P(b_1)) \prod_j P(b_j | D_j) \\ &= \sum_i \frac{(r_i - s_i)^2}{\sigma^2} - \ln(P(b_1)) - \sum_j \ln(P(b_j | D_j)) \end{aligned}$$

Assuming that $P(b_1)$ is constant⁴, we must minimize

$$= \sum_i \frac{(r_i - s_i)^2}{\sigma^2} - \sum_j \ln(P(b_j | D_j)) \quad (5)$$

This is exactly what the original ISD (Image Statistics Decoder) did in the case where $D_j = |X_{j+1} - X_j|$. The SNR is σ^2 , so the SNR must be known or estimated to use the ISD.

C. Programming

The MCD computes the metric associated with the addition of a single bit at a time, requiring each possible state (determined by 6 bits in the Voyager code) to be checked for two possible previous states: those associated with a 1 and a 0 (Fig. 3). The ISD must compute the metric associated with the addition of a whole byte at a time, requiring each state (now determined by 8 bits) to be checked for all 256 possible previous states (Fig. 4). In addition to the regular metric, a special metric, consisting of $\ln(P(b_j | D_j))$, must now be added into each state. The number of computations and comparisons necessary to decode a byte with the ISD has risen by a factor of over 64 over the MCD.

³The first statistic used was D . Later D and M (described below) were used.

⁴That is, assuming that without any prior information, all pixels are equally likely.

Within a few weeks of starting to modify an existing software simulated Viterbi decoder (written by Fabrizio Pollara, Communications Systems Research Section), a working model was finished, but with a major drawback: A picture would be decoded with this software in about 8 months on a dedicated VAX 11/750 computer. This compares with about 7 hours for the existing software simulated Viterbi decoder, and about 20 seconds for the MCD. A decoder as slow as the first ISD was useless even for simulation work, since it would take months just to plot enough points on the error rate curve, especially if it improved these error rates.

Over the remainder of this project, an attempt has been made to increase the speed of the decoder by using all of the available knowledge about its structure and by using different computers. The decoder speed has been increased considerably, so it is now fast enough to obtain some results (Table 1).

III. Simulated Error Rate Results

Figure 5 shows error rates for a normal MCD and for the first ISD used on simulated data over a range of SNRs of interest. Notice that it has a much better error rate for very low SNR, but this rate does not fall off very quickly as the SNR is raised. Theoretically, a decoder should do no worse with the pixel statistics than without them, so we sought an explanation for the poor performance at high SNRs. Even so, there is a gain of about 2.0 dB for a byte error rate of 0.028, and of about 1.0 dB for 0.016. These two error rates are of interest in deep space communications since they translate to failure rates of 10^{-3} and 10^{-6} , respectively, for the Reed-Solomon decoder.⁵

A. The Simulation

Fabrizio Pollara simulated the current MCD in software, thus generating the MCD error rates shown above. The simulation used data from a random number generator and simulated noise, also from a random number generator. We modified these programs to read actual pixel data from a file for decoding, but used the same random noise generator. The modules of the program that generated the input data and the MCD were the only ones that we changed so that the comparisons would be as close as possible.

Two images were necessary to complete the simulation: one image to generate the statistics to use, and one to decode. Using the same image for both purposes would be unrealistic: It would assume that we knew the image's exact statistics

⁵A Reed-Solomon code is used as an outer code on some Voyager data.

before decoding. Therefore, a single Voyager image has been used throughout the simulation for sample statistics: the one of Saturn fully in the frame⁶ (Fig. 6). This image was chosen because Fig. 2 shows that its statistics are closer to random than the other two.

B. A Possible Explanation for the Error Rates

Tools which have been very useful to this project have been a Macintosh and LaserWriter. The final version of the ISD was developed on the Macintosh and images were printed on the LaserWriter. They allowed images to be viewed at high resolution for the first time, making the following problems very obvious (Fig. 7).

A typical Voyager image contains several features which decrease the performance of the ISD. The most prominent of these are limbs and rizzo marks.

1. Limb streaking. Most of a Voyager image is dark sky, but the features of interest are usually the planets and moons, which are not dark, so many Voyager images contain a portion that is much more bright than the background. This creates a limb, the transition from black to white within the span of a few pixels, and then back again. Over the whole image, there are only a few transitions this severe, so this is a rare case according to the statistics. Since the ISD relies on the fact that adjacent pixels are *usually* close in value, it tries to suppress large transitions, and thus causes streaks of errors propagating along a row of the image when a true transition is very large.

2. Rizzo marks. Rizzo marks are the grid of dots put on a Voyager image by the spacecraft for calibration. Within a few pixels the grey level may change from very bright to completely black and back again, creating even more large transitions in an image.

The ISD propagates pixel values along a row of an image, one error causing more after it, so that streaks of pixels in error may be seen in any edge⁷ of the decoded image.

IV. Results With Real Data

With help from Hamil Cooper of JPL's Radio Frequency and Microwave Subsystems Section, we acquired some real

Voyager symbol streams⁸ from the Uranus encounter and decoded them with both the MCD and the ISD.

A. A Fix for a Problem

A problem with the original ISD was that it assumed that the statistics for an image were constant over the whole image, which is not true. Therefore, some method of determining which part of an image is being decoded (an edge, a planet, or black sky) had to be devised.

Just as grey level transitions from one pixel to the next can be predicted in the *horizontal* direction, they can also be predicted in the *vertical* direction (Fig. 8). Therefore, the rows above a given pixel (which have already been decoded) can be used in conjunction with the pixel to its left to predict its grey level.

Three possible schemes were suggested.

1. Averaging grey levels. The grey levels of the pixels above and to the left of the current pixel could be averaged before comparing those levels to the current pixel. In a preliminary experiment, results were disastrous, possibly because errors propagated not only to the right, but down also. The resulting image had massive areas of errors, and not much of the original image left.

2. Regressing edges. The location of an edge could be determined for a few rows previously decoded, and then the edge on the next row could be predicted using a statistical regression technique. The problem with regressing edges is that only true edges would be detected. Rizzo marks and small features like craters in the middle of a planet would not be detected since they only cover a few rows of an image.

3. Dynamically changing statistics. A few pixels directly above the current pixel could be observed to determine whether this is a high transition area, and the statistics could be changed accordingly. The proposed method was to use the difference between the maximum and the minimum of the five pixels directly above the current pixel as an added statistic called M (Fig. 9). The value of M would be large around an edge, medium sized in the middle of a planet, and very small in black sky. The image statistics could then be changed accordingly by observing similar statistics in the Saturn image used above.

After examining the distributions of D when controlled for M (Fig. 10), we decided that this last scheme would be the best

⁶Actually, this image was used as a base for the statistics; the actual statistics used were the result of smoothing the distributions of D observed in this image.

⁷An edge may be caused by a limb, rizzo mark, or even a crater.

⁸That is, Voyager data not yet decoded by the MCD.

to implement, and wrote a 2-way decoder that uses both M and D as sufficient statistics. The decoded images with the 2-way statistics had about one third of the errors that the original ISD had. Areas in planets were still problems for the decoder, but at a greatly reduced error rate; the errors at edges and rizzo marks completely disappeared except on the first decoded row (since there was no previous row to base statistics upon). Perhaps an adjustment of the statistics would be helpful in reducing the rate even more when decoding high pixel-transition areas like planet surfaces.

The actual implementation of the 2-way ISD should be explained briefly. Using the notation of expression (5) above, the 2-way ISD minimizes

$$\sum_i \frac{(r_i - s_i)^2}{\sigma^2} - \sum_j \ln (P(B_j | D_j, M_j)) \quad (6)$$

Changing image statistics for each of the possible values of M described above would require a 256 by 256 array of transition probability cells, creating a problem in determining what should go in each cell of the array.⁹ Therefore, we condensed the values of M into 8 groups, requiring only a 256 by 8 array, but perhaps decreasing the performance of the decoder.

B. Improved Error Rate

As noted before, the ISD is very slow, and now requires much programmer and computer time to decode an image. Only a part of one image, totaling 147 rows of 800 pixels each, has so far been decoded and compared to the image obtained from Glenn Garneau of JPL's Image Processing Applications and Development Section. The part of the image decoded has Miranda covering about 1/4 of the total area, and black sky over the rest. Figure 11 is a fraction of the image decoded by the ISD, zoomed to contain only Miranda.

The software MCD made 176 byte errors over the $147 \times 800 = 117,600$ pixels, an observed error rate of $176/117,600 = 0.0015$. The 2-way ISD made only 68 byte errors over the same area for an observed error rate of $68/117,600 = 0.0006$ at an estimated E_b/N_0 of about 3.0 dB (Fig. 12).

The results are interesting because the original ISD performed worse than the MCD at SNRs this high in simulations. The improvement at low SNR for the 2-way ISD with real data may be even better than that demonstrated in Fig. 6.

⁹Significant results can not be determined for an array of this size with only the 640,000 pixels in a single picture.

Two things should now be mentioned about this particular implementation of the ISD. First the symbols on the tapes acquired during the Uranus flyby are 4-bit quantized instead of real numbers, not necessarily the correct levels for a decoder, so there is some loss in performance for the ISD due to this. The MCD in the DSN uses optimum 3-bit quantization, which represents a very small loss; we don't yet know what the ISD loses, but we assume it is also small, based on past experience. Second, the ISD must know the SNR in order to run, so a module to estimate it was added. This module was written originally in FORTRAN by Gene Rodemich and Vic Vilnrotter of the Communications Systems Research Section, and translated to C in this project.

All of the data obtained is in PB8 format, with IM2 format imbedded in it¹⁰. The ISD as implemented assumes that this is the format of the input data; it will need to be modified to accommodate any other format.

V. Usefulness

A. Low SNR During Neptune Encounter

During Neptune encounter, the SNR could drop to a level where the loss of a fraction of a dB could make an image undecodable to the Reed-Solomon decoder; such a loss may be caused by a cloud passing by the receiver at Goldstone. To help boost the SNR, the VLA in New Mexico will be arrayed with Goldstone to approximately double the SNR. A problem with this strategy is that the VLA drops out for 1.6 milliseconds every 52 milliseconds to find out what time it is [2]. During this dropout, only Goldstone will be receiving, so the SNR will drop to about half its value when both are receiving. Approximately 4 bytes could be lost during this dropout, which could again mean the loss of whole images to the Reed-Solomon decoder depending on the SNR.

The ISD is ideally suited to solving the problem encountered by arraying with the VLA. It can decode even when the SNR is varying over time without significant loss in performance, as shown in Fig. 5. As long as some signal gets through, the ISD can do a better job than the MCD for these very low SNRs, perhaps up to 2 dB better. The speed problem may even be overcome somewhat by using the ISD only in the area around the gap in the SNR, and the MCD over the rest. The ISD would only be on over about 4% of the image, so an image

¹⁰J. Morecroft, *Voyager Flight Data Subsystem Flight Software Description*, 618-236, Rev. A (internal document), Jet Propulsion Laboratory, Pasadena, Calif., August 29, 1980.

could be decoded in about 3 hours on a Sun workstation. Future work planned for the ISD includes development of a decoder that can handle a varying SNR, and tests on data simulated to behave as the Goldstone-VLA array will.

B. Estimated Speed on Various Machines

The ISD is written in C, so it is very portable with only minor modifications. It was mostly developed on a Macintosh with a Hyperdrive 2000, but was ported to several UNIX-based computers with only very minor changes. Therefore the

speed on the different computers in Table 1 are very comparable.

VI. The Future

A simulation of the Goldstone-VLA array and generation of more complete error rate curves for the 2-way ISD are the first priorities. Experiments are needed on the effect of adjusting the statistics used, with the goal of reducing the number of errors in high pixel-transition areas like planet surfaces.

References

- [1] G. H. Pitt and L. Swanson, "Decoding convolutionally encoding images," *The Telecommunications and Data Acquisition Progress Report 42-83*, vol. July-Sept. 1985, pp. 34-38, Jet Propulsion Laboratory, Pasadena, Calif., November 15, 1985.
- [2] L. J. Deutsch, "An update on the use of the VLA for telemetry reception," *The Telecommunications and Data Acquisition Progress Report 42-72*, vol. Oct.-Dec. 1982, pp. 51-60, Jet Propulsion Laboratory, Pasadena, Calif., February 15, 1983.

Table 1. Estimated time to decode one image on several different computers

Computer	Cost, \$	Estimated Time to Decode One Image (640,000 pixels)
Macintosh	2,000	6 weeks
Dedicated VAX 11/750	100,000	3 weeks
Macintosh with a Hyperdrive 2000	4,000	2 weeks
Sun 3/260	30,000	3 days



Fig. 1. Part of an image decoded by the MCD

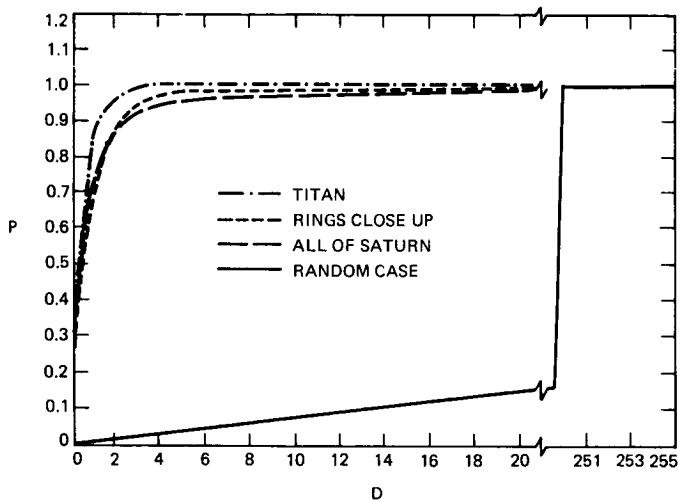


Fig. 2. Distributions of D for 3 different Voyager Images and the random case

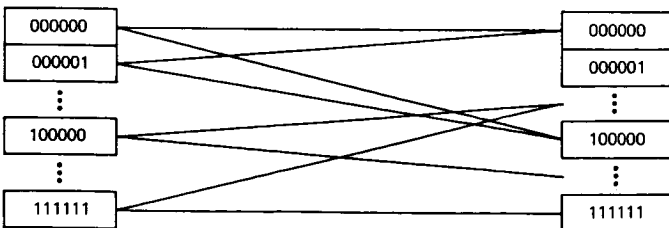


Fig. 3. The state transitions the MCD must check

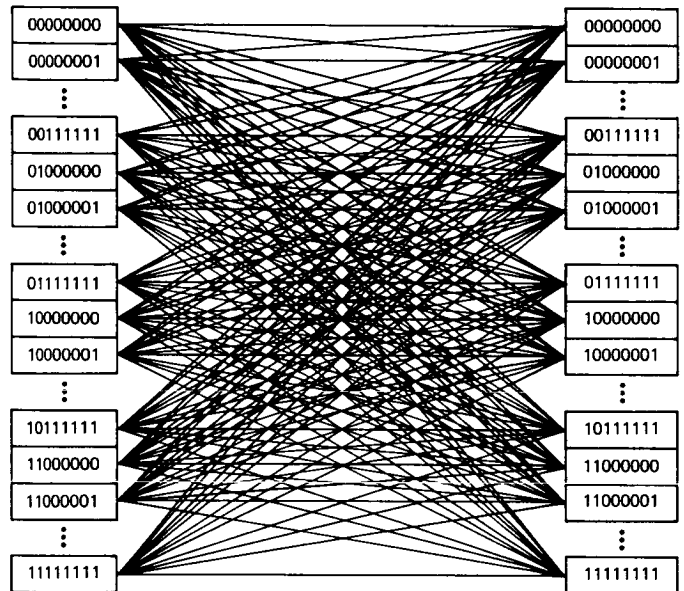


Fig. 4. The state transitions the ISD must check

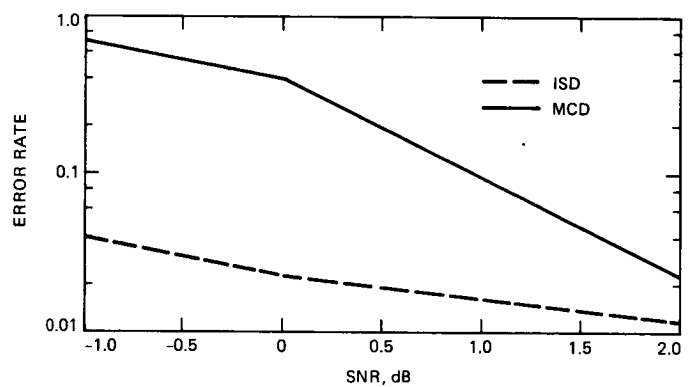


Fig. 5. Byte error rates for the MCD and the ISD

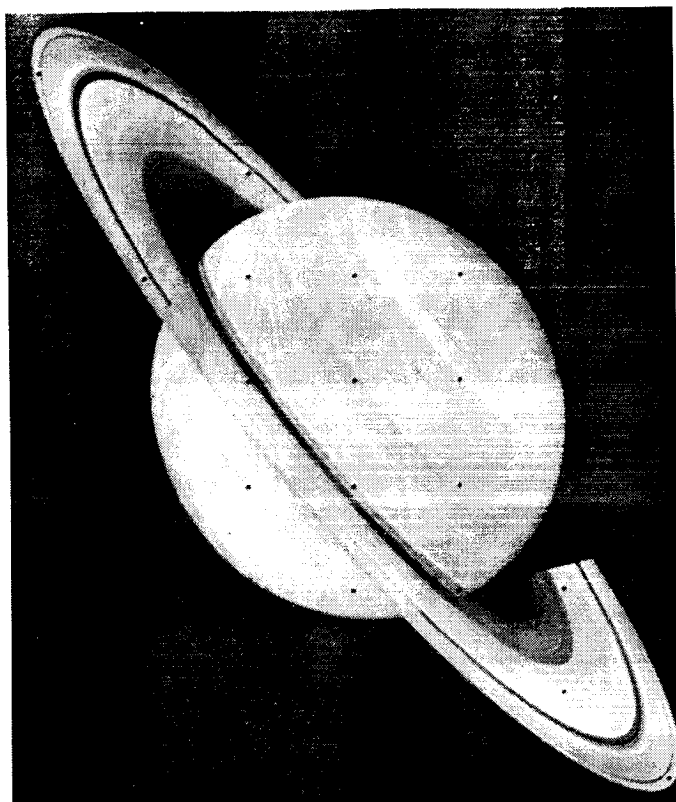


Fig. 6. Most of the image of Saturn close up

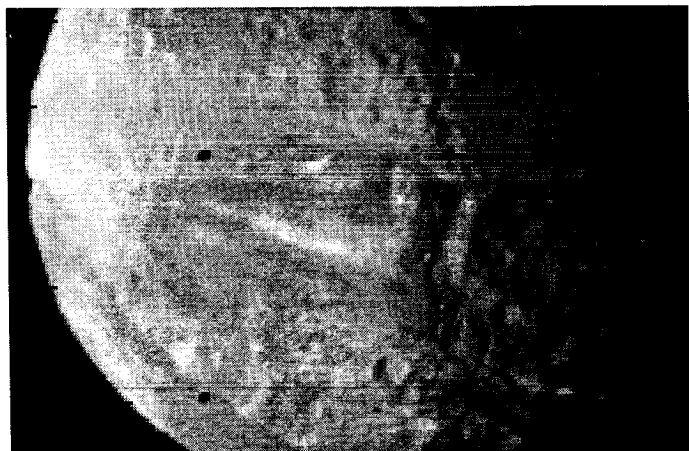


Fig. 7. Same as Fig. 1, decoded by the first ISD

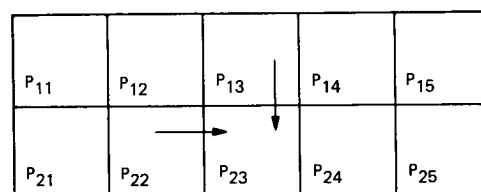


Fig. 8. Two rows of pixels, with arrows indicating which pixels may be used to help decode P_{23}

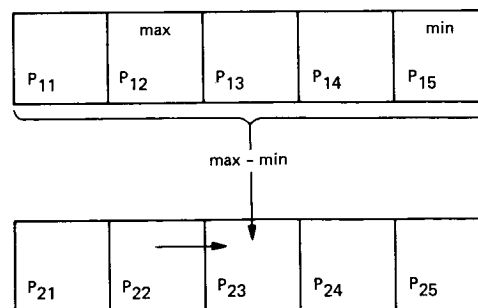


Fig. 9. Demonstrating where D and M come from

ORIGINAL PAGE IS
OF POOR QUALITY

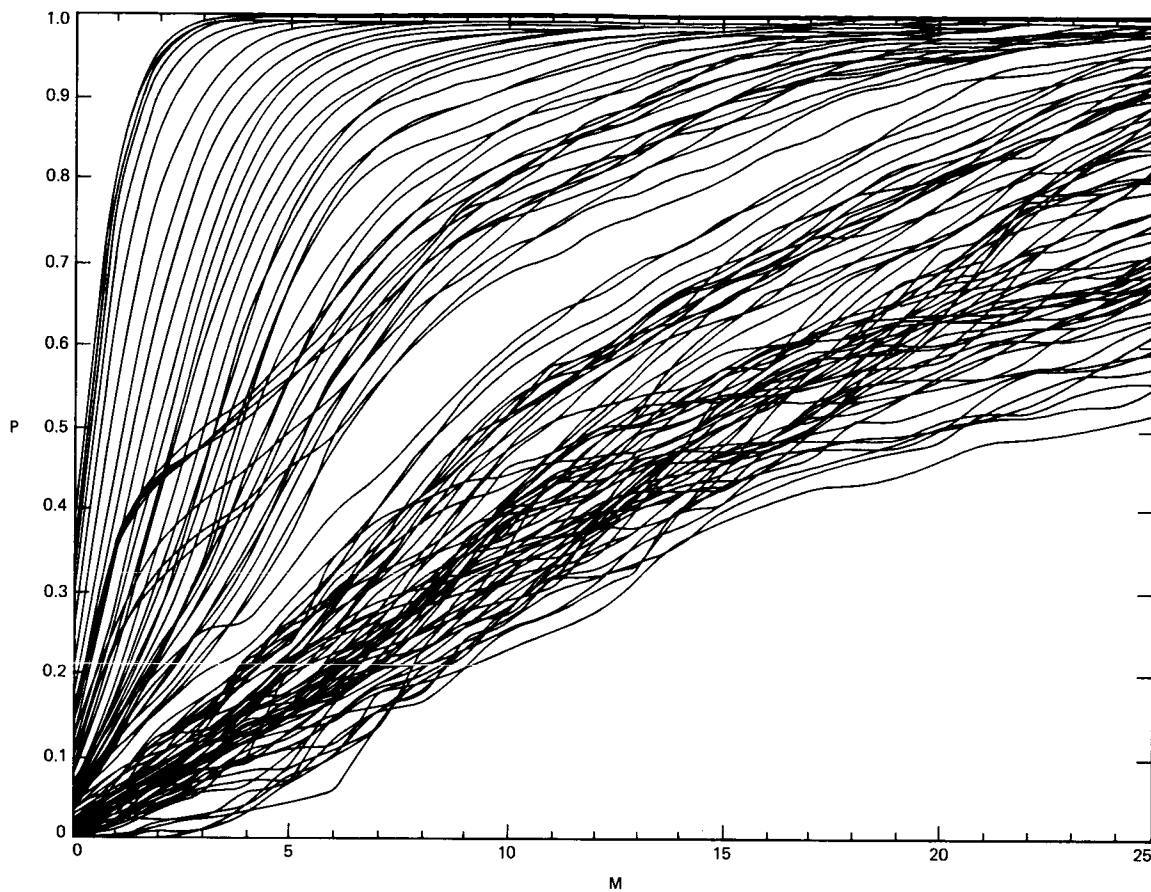


Fig. 10. Distributions of D when controlled for M



Fig. 11. Same as Fig. 1, decoded by the 2-way ISD

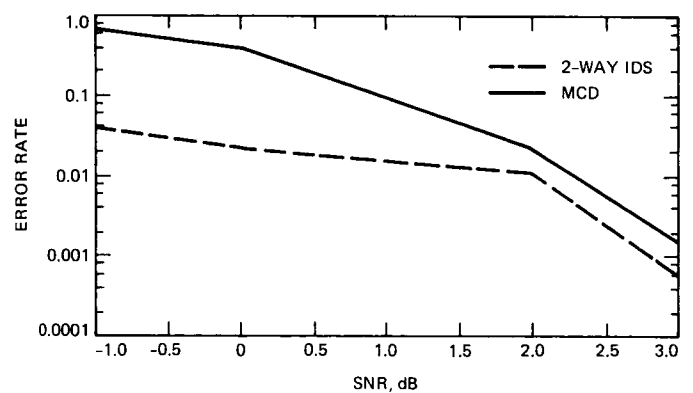


Fig. 12. Same as Fig. 5 with the two new points added at 3 dB

Constructions for Finite-State Codes

F. Pollara

Communications Systems Research Section

R. J. McEliece

California Institute of Technology and
Communications Systems Research Section

K. Abdel-Ghaffar

California Institute of Technology

In this article a class of codes called finite-state (FS) codes is defined and investigated. These codes, which generalize both block and convolutional codes, are defined by their encoders, which are finite-state machines with parallel inputs and outputs. A family of upper bounds on the free distance of a given FS code is derived, from known upper bounds on the minimum distance of block codes. A general construction for FS codes is then given, based on the idea of partitioning a given linear block code into cosets of one of its subcodes, and it is shown that in many cases the FS codes constructed in this way have a d_{free} which is as large as possible. These codes are found without the need for lengthy computer searches, and have potential applications to future deep-space coding systems. The issue of catastrophic error propagation (CEP) for FS codes is also discussed, and it is found that, in order to avoid CEP, one must solve a very interesting problem in graph theory, the problem of finding a noncatastrophic edge-labeling of the state diagram.

I. Introduction

Error-correcting codes are an essential part of all modern reliable and power-efficient deep-space communication systems. In this area of engineering, practice is currently leading theory, and as communication systems evolve, the new codes required must be found by elaborate computer searches. Such searches, although they often result in the discovery of powerful new codes (see e.g. [4]), are not wholly satisfactory for two reasons. First, computer searches are at present costly and time-consuming, and as communications systems evolve and the codes required become more and more complex, these searches may prove to be entirely impractical. Second, once a good new code is found by a search, there is rarely any

guarantee that the best possible candidate has been identified. In this article we begin an attempt to remedy this problem by establishing a new theoretical framework for the simultaneous study of the two major classes of error-correcting codes, block and convolutional codes. It is our belief that this framework will allow researchers to construct provably optimal codes for use in future high-performance deep-space communication systems. The cornerstone of our theory is the notion of a finite state encoder, which we will now describe.

An (n, k, m) FS (finite state) encoder is a q^m -state finite state machine with k parallel inputs and n parallel outputs taken from a q -letter alphabet (Fig. 1). The encoder begins

from a fixed initial state. At each clock pulse, k symbols (the information symbols) are input to the encoder, and in response the encoder changes state and outputs n symbols (the code symbols). Thus if (u_1, u_2, \dots) is a sequence of k -symbol information blocks, then the encoder's output will be a sequence (x_1, x_2, \dots) of n -symbol code blocks, which we call a code sequence. The set of all such code sequences is called the code generated by the FS encoder. A code generated by a (n, k, m) FS encoder will be called an (n, k, m) finite state code. We note that if there is only one state in the encoder, the resulting $(n, k, 0)$ FS code is in fact an ordinary block code. Similarly, a linear convolutional code is just a FS code in which the finite-state machine is a bank of k parallel shift-registers, and each output symbol is a linear combination of the k input symbols and the symbols stored in the shift registers. Thus FS codes include both block and convolutional codes as special cases.

The free distance (d_{free}) of an FS code is defined to be the minimum Hamming distance between all pairs of distinct (infinite) code sequences. If the encoder isn't catastrophic, this is also the minimum Hamming distance between pairs of distinct finite code sequences, i.e., code sequences corresponding to distinct input sequences which lead the encoder from the initial state to the same final state. (If the encoder is catastrophic, it is possible that the smallest Hamming distance between two infinite code sequences could occur for a pair of paths through the encoder's state diagram which begin at the initial state but never again remerge. We will say more about catastrophic and noncatastrophic encoders in Section IV.)

In this article, our concern will be to find bounds on d_{free} in terms of the parameters n, k , and m , and to produce a family of FS codes meeting these bounds in certain cases. In Section II we derive our bounds; in Section III we describe a general construction for (n, k, m) FS codes, using ideas similar to those of Ungerboeck [3]; in Section IV we discuss the issue of catastrophic error propagation, and, using techniques from graph theory, describe an optimal noncatastrophic edge-labeling of the complete 2^m state diagram; and finally in Section V we combine the results of Sections III and IV to construct a class of Reed-Solomon-like FS codes which meet the bounds of Section II whenever $n \leq q$ and $m \leq \min(k-1, n-k-1)$.

II. Bounds on d_{free}

In this section we will derive a family of upper bounds on d_{free} in terms of the parameters n, k , and m . The basic idea is to find subcodes of a given FS code which are block codes, and use the fact that any upper bound on the minimum dis-

tance of the block code is also an upper bound on the free distance of the parent FS code.

Here is some needed notation: let $\Delta(n, k)$ denote the largest possible minimum distance for a block code over a q -letter alphabet with length n , and q^k code words. (We note for future reference the trivial fact that $\Delta(n, k)$ is meaningless for $k \leq 0$.) The following theorem gives a bound on the free distance of a FS code in terms of Δ .

Theorem 1. For any FS code with parameters n, k , and m , the free distance is bounded as follows:

$$d_{\text{free}} \leq \min_{L: Lk > m} \Delta(Ln, Lk - m)$$

Proof: We consider all possible input sequences consisting of L k -symbol input blocks (u_1, u_2, \dots, u_L) . There are q^{Lk} such input sequences. For each of these sequences, the encoder starts in the initial state, and terminates in one of q^m states. It follows from the pigeon-hole principle that there must be at least q^{Lk-m} of these length- L input sequences which have the same final state. The code sequences corresponding to these input sequences can be thought of as a block code with length Ln , with at least q^{Lk-m} code words. The minimum distance of this block code is at most $\Delta(Ln, Lk - m)$, by definition. On the other hand, by the definition given in Section I, the minimum distance of this block code is an upper bound on the d_{free} of the original convolutional code. Since this is true for all L , we apparently have

$$d_{\text{free}} \leq \min_{L \geq 1} \Delta(Ln, Lk - m)$$

However, as we noted above, $\Delta(n, k)$ is meaningless, if $k \leq 0$, and so the minimization can only be taken over those values of L for which $Lk - m > 0$. ■

Corollary 1. The free distance of an (n, k, m) FS code over a q -letter alphabet satisfies

$$\begin{aligned} d_{\text{free}} &\leq \min_{L: Lk > m} (Ln - Lk + m + 1) \\ &= (n - k) \left\lfloor \frac{m}{k} + 1 \right\rfloor + m + 1 \\ &= n - k + 1 + m \quad \text{if } k > m \end{aligned}$$

Proof: This follows from Theorem 1 and the Singleton bound [2, Theorem 1.11], which says that

$$\Delta(n, k) \leq n - k + 1 \quad \blacksquare$$

Corollary 2. The free distance of an FS code also satisfies

$$d_{\text{free}} \leq \min_{L: Lk > m} \left(Ln \frac{q-1}{q} \frac{q^{kL-m}}{q^{kL-m}-1} \right)$$

Proof: This follows from Theorem 1 and the Plotkin bound [1, Theorem 13.49], which says that

$$\Delta(n, k) \leq n \cdot \frac{q-1}{q} \cdot \frac{q^k}{q^k-1} \quad \blacksquare$$

III. Code Constructions

In the last section we derived bounds on d_{free} which apply to arbitrary FS codes. In this section, we will describe a very general construction for a class of FS codes; later in the article, we will find that many of the codes constructed by this technique meet the bounds of Section II.

Our basic idea is to start with an explicit state-transition diagram, and to build a code around this diagram. For definiteness, we will consider only complete q^m -state transition diagrams, in which every pair of states is connected by a directed edge (illustrated in Fig. 2 for $q = 2, m = 2$), but most of our ideas can be generalized to other diagrams.

The FS code is to have parameters n and k . This means that at every clock cycle k symbols go into the encoder and n symbols come out. Of the k input symbols, it is plausible to suppose that m are used to determine the next state of the encoder (recall that there are q^m states altogether) and $k - m$ are used to determine which n symbols are to be output. Thus it is natural to think of the possible n -symbol output blocks associated with a fixed state transition as the words in a $(n, k - m)$ block code. Our basic idea is to assign a $(n, k - m)$ block code to each possible state transition.

Here then is our general construction for an (n, k, m) FS code. We begin with an (n, k_1) block code C_1 , with minimum distance d_1 . We assume that C_1 can be decomposed into the disjoint union of a number of (n, k_2) subcodes, each with minimum distance d_2 . (The easiest way, but not the only way, to arrange this decomposition is for C_1 to be a linear code, with an (n, k_2) , $d_{\min} = d_2$ linear subcode. Then C_1 naturally decomposes into cosets of C_2 . Each one of these cosets is then an (n, k_2) subcode with $d_{\min} = d_2$.) We assign one of the (n, k_2) subcodes to each of the q^{2m} state-transitions in the state transition diagram. We require that all q^m transitions originating at a given state, or terminating at a given state, be assigned a different subcode. This forces us to use at least q^m different subcodes; but in order to avoid catastrophic error

propagation, we will need at least $2q^m$ subcodes, as we will see in Section IV. This requires that the dimensions of the big code C_1 satisfy

$$k_1 \geq k_2 + m + 1$$

The encoder now works as follows. Starting in the initial state, at every clock pulse it accepts $k = m + k_2$ input symbols. The first m of these symbols are used to determine the next state, and the remaining $k - m = k_2$ symbols are used to determine which of the q^{k_2} code words from the subcode corresponding to the state transition is to be output.

In the next theorem, we estimate the d_{free} of the code constructed in this way.

Theorem 2. The free distance of the $(n, m + k_2, m)$ FS code constructed as described above from (n, k_2) , $d_{\min} = d_2$ subcodes of a (n, k_1) , $d_{\min} = d_1$ block code satisfies

$$\min(d_2, 2d_1) \leq d_{\text{free}} \leq d_2$$

Proof: We need to estimate the Hamming distance between pairs of code sequences corresponding to paths in the state diagram which begin and end in the same state. Let us say that these paths both begin in state s_1 and end in state s_K . There are two cases to consider: (1) when the second states in the two paths are the same, and (2) when they are different (see Fig. 3).

In case (1) we look at only the first n -symbol block of each path. These two blocks are distinct code words in the same (n, k_2) subcode, and so they must differ in at least d_2 positions. Thus if case (1) holds, the Hamming distance between the two code sequences is at least d_2 . Furthermore, since d_2 is the minimum distance of each of the subcodes, we know that the Hamming distance between some pair of code sequences is exactly d_2 . Thus $d_{\text{free}} \leq d_2$.

In case (2) the paths must differ in at least two edges: the edges leaving s_1 and the edges next entering a common state (there must be such a common state since the paths both terminate at s_K ; see Fig. 3). The n -symbol blocks corresponding to these pairs of edges are distinct code words in the (n, k_1) parent code, since we have assumed that different subcodes are assigned to all state transitions beginning, or ending in the same state, and so each pair must differ in at least d_1 positions. This means that the two code sequences must differ in at least $2d_1$ positions. Thus if case (2) holds, the Hamming distance between the two code sequences is at least $2d_1$.

Combining cases (1) and (2), we obtain the statement of the theorem. \blacksquare

Example 1: Let $q = 2$ and consider the 4-state diagram of Fig. 2. We choose as the parent code C_1 a $(16, 5)$ first-order Reed-Muller code with $d_1 = 8$. This code contains a $(16, 1)$ linear subcode C_2 (the repetition code) with $d_2 = 16$. There are 16 cosets of C_2 in C_1 , and so it is possible to assign a different coset to each of the 16 state transitions in the state diagram. The result is a $(16, 3, 2)$ code with (according to Theorem 2) $d_{\text{free}} = 16$. On the other hand, by taking $L = 1$ in Corollary 2, we find that the free distance of a $(16, 3, 2)$ code with $q = 2$ is at most 16. Therefore the code constructed this way has the largest possible d_{free} for its given n, k , and m . (This example will be generalized in Example 4 in the next section.)

Example 2: We again take $q = 2$ and use the complete 4-state diagram of Fig. 2, but this time we take as the big code C_1 the $(16, 8)$ $d_{\text{min}} = 6$ nonlinear Nordstrom-Robinson code. It is known ([2], Chapter 15) that this code is the union of 8 cosets of the $(16, 5)$ $d_{\text{min}} = 8$ first-order Reed-Muller code. In the next section we will see that the edge-labeling given in Fig. 2 is noncatastrophic. Thus if we use the edge-labeling described in Fig. 2 to assign these 8 cosets to the 16 state transitions, Theorem 1 tells us that we get a $(16, 7, 2)$ FS code with $d_{\text{free}} = 8$. On the other hand, the bound in Corollary 2 (take $L = 1$) shows that any $(16, 7, 2)$ FS code must have $d_{\text{free}} \leq 8$, and so this code is optimum.

The codes constructed by the techniques of this section are often, as we have seen, quite good if d_{free} is used as the figure of merit. However, they are not yet guaranteed to be noncatastrophic. In the next section, we will address the problem of how to assign subcodes to state transitions to ensure noncatastrophicness.

IV. Noncatastrophic Edge Labelings

In the last section we showed how to construct an (n, k, m) FS code by assigning cosets of a subcode of an (n, k) block code to the edges of a state diagram. However, if the coset-to-edge assignments are not done carefully, the resulting encoder could be catastrophic. In this section, we will see how to make the coset assignment to avoid catastrophicness. We will see that catastrophicness can be avoided only if the number of cosets available is at least $2q^m$, and we will see one way to make a noncatastrophic coset-edge assignment if $2q^m$ cosets are available, and q is a power of 2.

We begin by saying what we mean by a noncatastrophic edge-labeling of a state diagram. If s and t are two states, we denote by $L(s, t)$ the label on the directed edge from s to t . (In our application, the "labels" are cosets.) Let

$$(s_1, s_2, \dots, s_K) \quad \text{and} \quad (t_1, t_2, \dots, t_K)$$

be two sequences of K states. If the two corresponding sequences of labels

$$L(s_1, s_2), L(s_2, s_3), \dots, L(s_{K-1}, s_K)$$

and

$$L(t_1, t_2), L(t_2, t_3), \dots, L(t_{K-1}, t_K)$$

are identical, we call two such state sequences label-indistinguishable.

Definition. An edge labeling of a state diagram is said to be noncatastrophic if and only if there is an integer K_0 such that any two label-indistinguishable state sequences of length $K \geq K_0$ are identical. (Informally, this says that if a state sequence is "long enough," it can be recovered uniquely from its label-sequence.)

A noncatastrophic edge-labeling guarantees that a bad burst of channel noise will never cause the decoder to make an infinite number of decoder errors, i.e., the decoder will not cause catastrophic error propagation. Notice that there exist catastrophic edge-labelings which do not cause catastrophic error propagation, but which also do not meet the condition for Theorem 2.

We can see how a catastrophic edge-labeling may cause catastrophic error propagation as follows. Let (s_1, s_2, \dots) and (t_1, t_2, \dots) be two arbitrarily long label-indistinguishable state sequences. If the encoder follows a state sequence that finishes with the sequence (s_1, s_2, \dots) , it is possible for the channel noise to be such that the decoder will correctly determine the state sequence up to s_1 , but then choose t_1 instead of s_1 . If this happens, the decoder will almost surely never recover, since its metric calculations based on hypothesizing the incorrect state sequence (t_1, t_2, \dots) will be identical to those based on the true state sequence (s_1, s_2, \dots) .

Notice that if all the edge labels are distinct, any state sequence can be uniquely recovered from its label sequence, and so the labeling must be noncatastrophic. (If the state diagram is the complete N -state diagram, this requires N^2 labels.) On the other hand, if all edges in the state diagram have the same label, all pairs of state sequences are label-indistinguishable, and so the labeling must be catastrophic. The basic problem is to find the minimum number of different labels that are needed for a noncatastrophic labeling. For an arbitrary state diagram, we do not know what this number is. However, if we assume that the state diagram is D -regular, i.e., there are exactly D edges coming in to and going out of each

state, the following theorem places a nontrivial lower bound on the required number of distinct labels.

Theorem 3. For a D -regular state diagram with at least two states, at least $2D$ distinct labels are required for a noncatastrophic edge labeling.

Proof: As a first step, note that if we have a labeling L such that $L(s, t) = L(s', t)$, where s and s' are distinct states, the labeling must be catastrophic, since then

$$(s, s_2, s_3, s_4, \dots, s_K) \quad \text{and} \quad (s', s_2, s_3, s_4, \dots, s_K)$$

are label-indistinguishable but not identical state sequences, for any value of K and for $s_2 = t$. Similarly, if $L(s, t) = L(s, t')$, where t and t' are distinct states, the labeling must also be catastrophic, since

$$(s_1, s_2, \dots, s_{K-1}, t) \quad \text{and} \quad (s_1, s_2, \dots, s_{K-1}, t')$$

are label-indistinguishable but not identical state sequences, for any value of K and for $s_{K-1} = s$. Thus we have for any noncatastrophic labeling that

$$L(s, t) \neq L(s', t) \quad \text{if } s \neq s'$$

and

$$L(s, t) \neq L(s, t') \quad \text{if } t \neq t'$$

In other words, if we are given x and $L(x, y)$, we can recover y ; and if we are given y and $L(x, y)$, we can recover x . If the labeling has this property we will say that it is nonsingular. Thus all noncatastrophic labelings are nonsingular, but the converse may not hold.

Next we assume that we are given a noncatastrophic labeling of a D -regular state diagram, but that the labeling uses fewer than $2D$ labels. We will show by induction that this assumption leads to a contradiction, by constructing a pair of arbitrarily long nonidentical but label-indistinguishable state sequences. Since there are $D \times$ (no. of states) edges in the state diagram, but less than $2D$ labels, there must be two distinct edges with the same label. Denote these two edges by (s_1, s_2) and (t_1, t_2) . This is a pair of label-indistinguishable but nonidentical state sequences of length 2. Assume that we have already constructed a pair of nonidentical but label-indistinguishable state sequences of length K , say

$$(s_1, s_2, \dots, s_K) \quad \text{and} \quad (t_1, t_2, \dots, t_K).$$

(We have just seen that we can do this for $K = 2$.) Since the labeling is nonsingular, we know that $s_K \neq t_K$. Now consider

the $2D$ labels of the form $L(s_K, s)$ and $L(t_K, s)$. Since there are fewer than $2D$ labels available, two of these labels must be identical. These identical labels can't be of the form $L(s_K, s)$ and $L(s_K, s')$, or $L(t_K, t)$ and $L(t_K, t')$, since the labeling is nonsingular. Hence we must have $L(s_K, s) = L(t_K, t)$ for some s and t . Thus if we set $s_{K+1} = s$ and $t_{K+1} = t$, then

$$(s_1, s_2, \dots, s_{K+1}) \quad \text{and} \quad (t_1, t_2, \dots, t_{K+1})$$

are nonidentical but label-indistinguishable state sequences of length $K + 1$. This completes the proof that $2D$ labels are necessary in any noncatastrophic edge-labeling. ■

Theorem 3 says that $2D$ labels are necessary for a noncatastrophic labeling of a D -regular state diagram. In the next theorem, we will see that $2D$ labels are sufficient if D is a power of two, and if the state diagram is complete, i.e., every state is connected by a directed edge to every other state.

Theorem 4. The complete 2^m -state diagram can be labeled noncatastrophically with 2^{m+1} labels in such a way that every sequence of m edge labels uniquely identifies the state sequence.

Proof: Let us number the 2^m states with the integers in the set $\{0, 1, \dots, 2^m - 1\}$. We will use the integers in the set $\{0, 1, \dots, 2^{m+1} - 1\}$ as edge labels. Indeed, if x and y are two states, we label the directed edge from x to y with the integer $L(x, y) = y - 2x \bmod 2^{m+1}$. We claim that this labeling is noncatastrophic. As a first step in this direction, we note that this labeling is nonsingular. To see this, note that if we are given x and

$$L = y - 2x \bmod 2^{m+1}$$

then

$$y = L + 2x \bmod 2^{m+1}$$

and if we are given y and L , then

$$x = (y - L)/2$$

or

$$(y - L)/2 + 2^m$$

depending on which of these values is in the range $0 \leq x \leq 2^m - 1$.

Now to see why the labeling is noncatastrophic, let

$$x_0, x_1, \dots, x_m \quad \text{and} \quad y_0, y_1, \dots, y_m$$

be a pair of label-indistinguishable state sequences of length $m + 1$, and let L_i be the common label on the edges $x_{i-1} \rightarrow x_i$ and $y_{i-1} \rightarrow y_i$. Then (all arithmetic is interpreted mod 2^{m+1}) we have

$$L_i = x_i - 2x_{i-1} = y_i - 2y_{i-1} \quad \text{for } i = 1, 2, \dots, m$$

From this we conclude that

$$\begin{aligned} x_1 &= L_1 + 2x_0 \\ x_2 &= L_2 + 2L_1 + 4x_0 \\ &\vdots \\ x_m &= L_m + \dots + 2^{m-1} L_1 + 2^m x_0 \end{aligned}$$

Since $2^m x_0$ must be either 0 or $2^m \pmod{2^{m+1}}$, and exactly one of

$$L_m + \dots + 2^{m-1} L_1$$

and

$$L_m + \dots + 2^{m-1} L_1 + 2^m$$

is in the range $\{0, 1, \dots, 2^m\}$, it follows that x_m can be uniquely calculated from L_1, L_2, \dots, L_m . Since y_m can be computed in exactly the same way, it follows that $x_m = y_m$. Since the labeling is nonsingular, it follows that

$$x_{m-1} = y_{m-1}, \dots, x_1 = y_1$$

and so the two state sequences are identical. This proves that the given labeling is noncatastrophic, and indeed that any state sequence can be identified after at most m labels. ■

Example 3: The edge labels prescribed by the construction of Theorem 4 in the case $2^m = 4$ are given in Fig. 2; and in the case $2^m = 8$ are given in the following 8×8 matrix:

	0	1	2	3	4	5	6	7
0	0	1	2	3	4	5	6	7
1	14	15	0	1	2	3	4	5
2	12	13	14	15	0	1	2	3
3	10	11	12	13	14	15	0	1
4	8	9	10	11	12	13	14	15
5	6	7	8	9	10	11	12	13
6	4	5	6	7	8	9	10	11
7	2	3	4	5	6	7	8	9

where the (x, y) entry of the matrix gives the label on the $x \rightarrow y$ state transition. Notice, for example, that the label sequence (7, 4) is ambiguous (the state sequences (0, 7, 5) and (7, 5, 1) both yield the label sequence (7, 4)), but the label sequence (7, 4, 11) uniquely specifies the state sequence (0, 7, 5, 5).

We can combine Theorems 2 and 4 to give the following general construction for linear FS codes.

Theorem 5. Let q be a power of two, and suppose that C_1 is a (n, k_1) , $d_{\min} = d_1$ block code over $GF(q)$, and C_2 is a (n, k_2) , $d_{\min} = d_2$ subcode. Then there exists a $(n, k_1 - 1, k_1 - k_2 - 1)$ FS code with $\min(d_2, 2d_1) \leq d_{\text{free}} \leq d_2$.

Proof: Using the construction of Section III, we begin with a complete $q^{k_1 - k_2 - 1}$ state diagram. Since there are $q^{k_1 - k_2}$ cosets of C_2 in C_1 , by Theorem 4 (since q is a power of two) it is possible to use these cosets to label the edges of the state diagram noncatastrophically. By Theorem 2 the result is a $(n, k_1 - 1, k_1 - k_2 - 1)$ FS code whose free distance satisfies the bounds given in the statement of the theorem. ■

Example 4 (Cf. Example 1): Let $q = 2$; let C_1 be the $(2^m, m + 1)$, $d_{\min} = 2^{m-1}$ first-order Reed-Muller code, and let C_2 be the $(2^m, 1)$, $d_{\min} = 2^m$ repetition code, which is a subcode of C_1 . Using Theorem 5 we can construct a $(2^m, m, m - 1)$, $d_{\text{free}} = 2^m$ FS code, which by Corollary 2 to Theorem 1 (take $L = 1$) is optimal.

V. Reed-Solomon FS Codes

In this final section we will use the techniques of Sections II, III, and IV to construct a class of FS codes which are Reed-Solomon-like, and which meet the bounds of Section II in many cases.

The ancestors of the FS codes to be constructed are Reed-Solomon codes. We remind the reader that such codes are (n, k) block codes with minimum distance $d = n - k + 1$ (thus achieving the Singleton bound) and that these codes exist for all n and k satisfying $1 \leq k \leq n \leq q$, where q is the alphabet size (see [2], Chapter 10). To simplify the construction, we will assume in what follows that the alphabet size q is a power of two.

Our goal is to use a Reed-Solomon code to construct an (n, k, m) FS code with $d_{\text{free}} = n - k + 1 + m$, which by Corollary 1 is the largest possible value. Following the prescription in Section III, we let C_1 be an $(n, k + 1)$ Reed-Solomon code with $d_1 = n - k$. The subcode C_2 is taken to be an $(n, k - m)$ Reed-Solomon code, with $d_2 = n - k + 1 + m$ (this requires

$m < k$). Thus by Theorem 5, the resulting (n, k, m) code will have

$$\min(2(n-k), n-k+1+m) \leq d_{\text{free}} \leq n-k+1+m$$

If $2(n-k) \geq n-k+1+m$, i.e., $m \leq n-k-1$, this gives $d_{\text{free}} = n-k+1+m$, and by Corollary 1 the free distance cannot be larger than this. Therefore we have proved the following.

Theorem 6. For any parameters n, k, m , and q (q must be a power of 2) satisfying $k \leq n-1 \leq q-1$ and

$$m \leq \min(k-1, n-k-1)$$

there exists a noncatastrophic (n, k, m) FS code whose free distance meets the Singleton bound, viz.

$$d_{\text{free}} = n-k+1+m$$

Example 5: If we start with a $(15, 11)$ RS code over $GF(16)$, a code with $d_{\text{min}} = 5$, (thus $k = 10$ in the construction described above), we can construct $(15, 10, m)$ FS codes, for $0 \leq m \leq 10$. For $m = 0, 1, 2, 3$, and 4 , the codes have $d_{\text{free}} = m + 6$, which agrees with the Singleton bound of Corollary 1, and so these codes are all optimal. For $5 \leq m \leq 10$, however,

the codes constructed all have $d_{\text{free}} = 10$, independent of m , do not meet the Singleton bound, and presumably do not have the largest possible d_{free} 's for their values of n, k , and m .

VI. Conclusion

In this article we have introduced the notion of a finite state code in an attempt to unify the theory of block and convolutional codes and to establish a theoretical framework which will allow researchers to explicitly construct powerful new error-correcting codes for deep-space and other applications. Although the results in this article are highly promising, and some of the codes we have constructed are likely to be useful in some applications, much further work remains to be done. In particular, the specific constructions given in Section III only scratch the surface of the interesting problem of synthesizing good FS codes. The central problem here is to take a good block code and to partition it into a disjoint union of isomorphic good subcodes. Another problem worthy of further research is that of finding good noncatastrophic edge labelings of specific state diagrams. Finally, we have not addressed the important problem of decoding at all. And while it seems that many FS codes can be decoded practically using a combination of Viterbi's algorithm with a corresponding block decoding algorithm, this question certainly needs serious study if FS codes are to be used in practice.

References

- [1] E. R. Berlekamp, *Algebraic Coding Theory* (Revised 1984 ed.). Laguna Hills, Calif.: Aegean Park Press, 1984.
- [2] F. J. MacWilliams and N. J. A. Sloane, *The Theory of Error-Correcting Codes*. Amsterdam: North-Holland, 1977.
- [3] G. Ungerboeck, "Channel coding with multilevel/phase signals," *IEEE Trans. Information Theory*, vol. IT-28, Jan. 1982, pp. 55-67.
- [4] J. H. Yuen and Q. D. Vo, "In search of a 2-dB coding gain," *TDA Progress Report 42-83*, vol. July-Sept. 1985, pp. 26-33, Jet Propulsion Laboratory, Pasadena, Calif., November 15, 1985.

ORIGINAL PAGE IS
OF POOR QUALITY

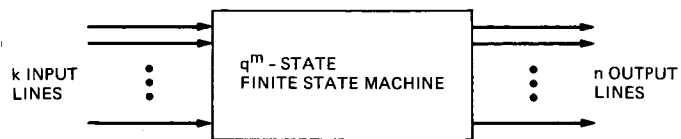


Fig. 1. A Finite-State encoder

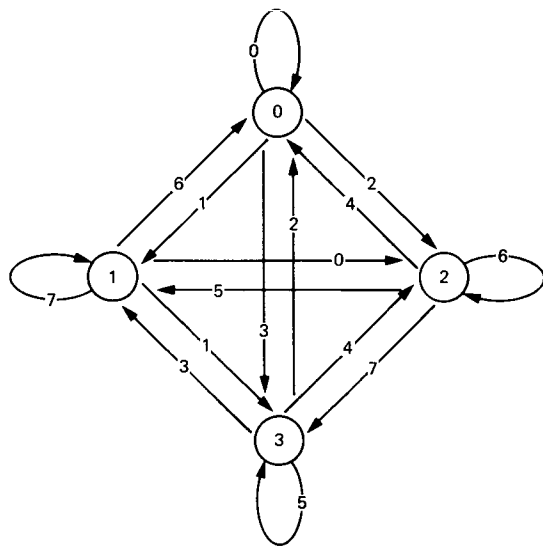
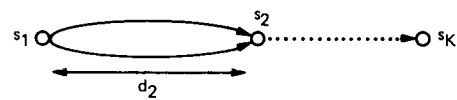
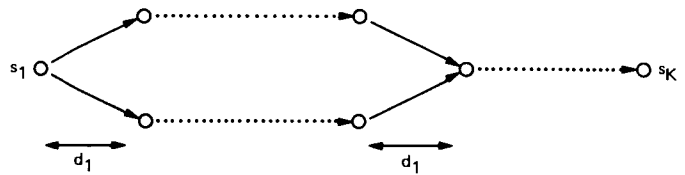


Fig. 2. A complete 4-state diagram. The edge labels are as described in Theorem 4 in Section IV.



CASE 1



CASE 2

Fig. 3. The proof of Theorem 2

ORIGINAL PAGE IS
OF POOR QUALITY

Systolic Arrays and Stack Decoding

M. Shahshahani

Communications Systems Research Section

This article reviews the work of K. Yao and C. Y. Chang on the application of systolic priority queues to the sequential stack decoding algorithm. Using a systolic array architecture, one can significantly improve the performance of such algorithms at high signal-to-noise ratio. However, their applicability at low SNR is doubtful.

I. Introduction

An active area of current research on deep space communications is the development of codes usable at low signal-to-noise ratio. The requirements for such codes are low error probability and the practicality of the decoding algorithm. It is well known that the error probability of convolutional codes decreases with their constraint lengths. However, the complexity of the Viterbi algorithm, which is the standard method for decoding convolutional codes at low SNR, has exponential growth with the code's constraint length. In a report on research conducted under a JPL contract, Yao and Chang suggest that, by using a systolic array architecture, decoding procedures for long constraint length codes can be practically implemented. The viability of the sequential stack algorithm (using systolic arrays) as an alternative to Viterbi's method is the main contention of these authors. This article reports on the scope and limitations of their approach. A serious limitation of their approach is that it may not be useful at the low signal-to-noise ratio for deep space communication.

II. Stack Algorithm

The encoding procedure for a convolutional code can be regarded as a route through the code tree in the usual manner. A received symbol sequence is then a path in the code

tree. To every path, x , is associated a real number $m(x)$ called the Fano metric. Figure 1 is a schematic description of the stack algorithm for decoding (see [1] for further details).

The Fano metric is constructed with the maximum likelihood criterion in mind. In fact, it is a generally accepted theorem that the stack algorithm is a good approximation to maximum likelihood decoding at high SNR.

The simplicity of the stack algorithm, as compared to Viterbi's, is reflected in the design of the hardware for the decoder. The wiring problem for the Viterbi decoder becomes extremely complicated for convolutional codes of constraint length >15 , while the same problem remains fairly simple for the stack algorithm. Exponential growth of the layout area with the constraint length is another serious problem for VLSI design of large constraint length Viterbi decoders. For the stack algorithm, the growth of the layout area is only linear with the constraint length.

In spite of these advantages, the stack algorithm has remained unpopular for several reasons. Most notable are:

- (1) The reordering of paths according to the metric requires a large memory and is very time consuming. This often leads to overflow of the buffer and erasures.

- (2) The performance of the stack algorithm at low SNR is considerably inferior to that of the Viterbi algorithm.

For low data rate and/or two-way communications, erasures (frame deletions) are not a serious problem. However, for application to deep space communication, this effect presents a major obstacle. This problem will be discussed in more detail in section III.

In their articles on the application of systolic priority queues to sequential decoding ([2] and private communication contained in a report "Systolic Array Processing for Stacking Algorithms" which was submitted to Jet Propulsion Laboratory, Pasadena, California as a Second Progress Report), Chang and Yao note that a complete reordering of paths is not necessary for the implementation of the stack algorithm. In fact, the choice of the best path, i.e., the path with the largest Fano metric, is the only requirement and this can be accomplished efficiently by an application of systolic priority queues. Unfortunately, no quantitative measure of the improvement in efficiency is provided by Chang and Yao.

Roughly speaking, systolic arrays, as introduced by Kung [3] and applied by Leiserson to priority queues [4], are a form of parallel processing that has found many applications in VLSI design. Several designs for systolic queues for the determination of the best path are available, viz., random access memory (RAM), shift register scheme (SRS), and ripple register scheme (RRS). A general problem faced by many parallel processing schemes is the necessity of insertion of global controls for proper synchronization of the system. Chang and Yao recommend the RRS since it does not require global controls and maintains the local communication property (private communication contained in a report "Systolic Array Processing for Stacking Algorithms" which was submitted to Jet Propulsion Laboratory, Pasadena, California as a Second Progress Report).

It is also noted by Chang and Yao [5] that the Viterbi algorithm can be regarded as a matrix-vector multiplication (here, matrix entries are from an algebra where multiplication is defined as taking minimum). Therefore, this algorithm lends itself to parallel processing, and systolic priority queues can be used for improvement of the Viterbi decoder. The idea of using parallel processing for VLSI design of the Viterbi decoder is, of course, not new, and substantial work has already been done in this area by researchers at JPL ([6], [7], and [8]).

III. Performance Statistics

It is clear from the description of the stack algorithm that the number of computations necessary to advance one

node in the code tree is a random variable N . At low signal-to-noise ratio, one encounters situations where backtracking is necessary and this effectively increases the mean of the random variable N . The behavior of N has been studied by a number of workers in coding theory. In particular, Jacobs and Berlekamp [9] obtained a lower bound for N . They showed that for fixed error or erasure probability, the distribution of N satisfies the following bound:

$$P(N > t) > t^{-\alpha} (1 + o(t))$$

It is important to note that this bound depends only on the channel error probability and the code rate and is independent of the choice of the method for selection of the best path. The code rate R and the exponent α are functionally dependent. As α tends to 1 from below, the mean of N approaches infinity. The value R_0 of R corresponding to $\alpha = 1$ is called the cut-off rate. Sequential decoding for $R > R_0$ is practically impossible, since the number of computations becomes exceedingly large.

In "A Simulation Study for the Stack Algorithm for Low SNR" (a preprint article submitted to Jet Propulsion Laboratory, Pasadena, California), Chang reports on his simulation results on stack decoding for a (24, 1/4) convolutional code when $\text{SNR} = E_b/N_0$ is between 0.9 and 1.3 dB. As pointed out by the author himself, $R = 1/4$ is greater than the cutoff rate. Therefore, for *a priori* reasons, one cannot draw any optimistic conclusions about the performance of stack decoding on the basis of this work. Moreover, a comparison of this data and those of S. Z. Kalson (JPL Internal Document, Memo 331-86.2-217, November 6, 1986), for a (15, 1/5) convolutional code, shows that the performance of the stack decoder at $\text{SNR} = 0.9$ dB is comparable to that of the Viterbi decoder at $\text{SNR} = 0.4$ dB. This comparison of the Viterbi and stack algorithms did not take into account the overhead due to the short frame length (= 100 bits) adopted by Chang. The loss due to the overhead for a marker of length λ and frame length L is $10 \log(1 + \lambda/L)$, where \log is taken to base 10. Thus, for a 32-bit marker, the loss is about 1.2 dB.

Some of the key parameters chosen by Chang for his study appear to be unrealistic. As pointed out earlier, the code rate 1/4 and the frame length 100 are hardly acceptable choices for these parameters. Chang also gives no indication of the nature of the (24, 1/4) code he is using for his simulation. Special attention must be paid in the choice of the code, since different codes of the same constraint length and rate perform differently under sequential decoding. A discussion of what constitutes a "good" code for sequential decoding appears in [10]. It is also clear that the buffer size affects the error probability and the performance of the stack algorithm. For a conclusive study of the possibilities of the stack algorithm at low SNR, the following points should be kept in mind:

- (1) Experiment with several, much longer (>1000) frame lengths and lower rate codes. This would substantially reduce the overhead and clarify the dependence of the error probability (mainly frame deletion) on the frame length.
- (2) Make sure the chosen code is a "good" one.
- (3) Quantify the dependence of error probability on the buffer size and the computation time. (The latter point is addressed by Chang.)

- (4) The effect of using soft decision on the performance of the stack algorithm should be clarified.

IV. Conclusion

The application of systolic array architecture, as suggested by Chang and Yao, is a significant improvement in the sequential stack decoding techniques at high signal-to-noise ratio. However, it is unlikely that the stack algorithm can serve as a viable alternative to the Viterbi algorithm at low SNR.

References

- [1] G. C. Clark and J. B. Cain, *Error-Correction Coding for Digital Communications*. New York: Plenum Press, 1981.
- [2] C. Y. Chang and K. Yao, "Systolic Array Architecture for the Sequential Stack Algorithm," *SPIE Proc.*, vol. 696, pp. 196-203, August 1986.
- [3] H. T. Kung, "Let's Design Algorithms for VLSI Systems," *Proc. of Caltech Conference on VLSI*, Caltech Comp. Sci. Dept., pp. 65-90, 1979.
- [4] C. E. Leiserson, *Area Efficient VLSI Computation*. Cambridge, Massachusetts: MIT Press, 1983.
- [5] C. Y. Chang and K. Yao, "Systolic Array Processing of the Viterbi Algorithm," *Proc. 23rd Annual Allerton Conference on Comm., Control and Computing*, Sponsored by Co-ordinated Sci. Lab of the Dept. of Electrical Engineering and Comp. Engineering of the U. of Illinois at Urbana-Champaign, pp. 430-439, Oct. 1985, (First Progress Report submitted to JPL, 1986).
- [6] F. Pollara, "Viterbi Algorithm on the Hypercube," *Proc. 23rd Annual Allerton Conference on Comm., Control and Computing*, Sponsored by Co-ordinated Sci. Lab of the Dept. of Electrical Engineering and Comp. Engineering of the U. of Illinois at Urbana-Champaign, pp. 440-449, Oct. 1985.
- [7] F. Polara, "Concurrent Viterbi Algorithm with Traceback," *SPIE Proc.*, vol. 696, pp. 204-209, Aug. 1986.
- [8] I. S. Hsu, T. K. Truong, I. S. Reed, and J. Sun, "A New VLSI Architecture for Viterbi Decoders of Large Constraint Length Convolutional Codes" (preprint), Pacific Rim Conf. Victoria, Canada, IEEE, New York, June 1987.
- [9] I. M. Jacobs and E. R. Berlekamp, "A Lower Bound to the Distribution Computation for Sequential Decoding," *IEEE Trans. Inf. Theory*, IT-13, pp. 167-174, April 1967.
- [10] S. Lin and D. J. Costello, *Error Control Coding*. Englewood Cliffs, NJ: Prentice-Hall, 1983.

ORIGINAL PAGE IS
OF POOR QUALITY

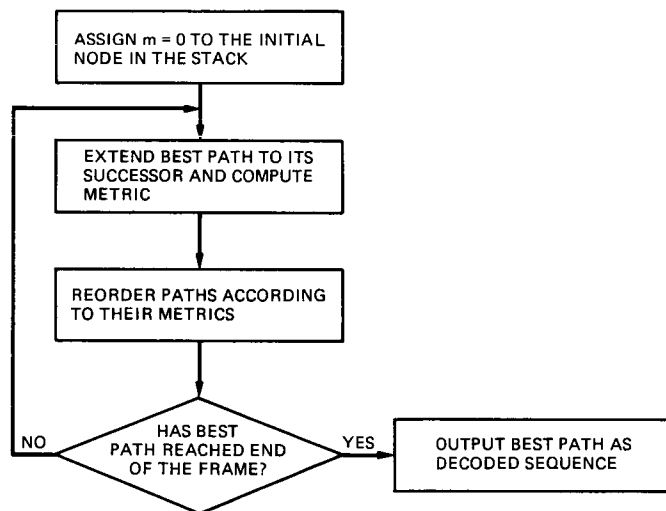


Fig. 1. Flow chart for stack decoding

Survey of Current Correlators and Applications

C. R. Lahmeyer and S. S. Brokl
Communications Systems Research Section

With larger scale integrated circuits becoming available, many new applications are becoming feasible for digital correlators. Numerous projects at JPL and elsewhere now have correlators included in systems. With this survey an attempt was made to contact as many users as possible so as to provide summary data on correlator systems, both in use and planned. Data on currently available VLSI chips and complete systems are included. Also, several planned correlator systems are described and summarized in tabular form. Finally, a description is given of the work being done in the Communications Systems Research Section (JPL Section 331) on VLSI correlator chips and complete correlator systems.

I. Introduction

Modern circuit techniques have permitted the design of much higher performance correlators than was possible a few years ago. Several groups at JPL and elsewhere are planning or already building new correlator systems. Typical areas of application for new correlators are radio and radar astronomy, long distance communications and deep space navigation. This survey was undertaken to determine the nature of the different correlation requirements for the various users with the goal being to examine and compare the different correlation requirements and determine what features they have in common. It was then to be determined if a multipurpose correlator machine might be designed. Also of interest was the structure that a hypothetical multipurpose correlator chip should have.

A brief overview of correlator hardware currently in use is given in Section II. First, the available off-the-shelf correlator chips are surveyed and second, a sample of correlator systems currently in use are described. Tables 1 and 2 summarize these results.

Information on correlators under development and projected future needs was collected from the various groups with correlator requirements. The results are displayed in summary form in Table 3 and are discussed more thoroughly in Section III. This survey is by no means exhaustive but gives a good overview of several typical applications for correlators.

A summary of work being done in the Communications Systems Research Section (Section 331) on VLSI correlator chips and systems is presented in Section IV. This is followed by some suggestions for architectures for implementing large high-performance correlator systems.

II. Devices and Systems Available

The following paragraphs represent a survey of some of the available correlator hardware. First, a description is given of the known VLSI correlator chips. At present there are four organizations known, outside of JPL, who produce VLSI correlator devices. Next, a sampling of correlator systems currently in use is discussed.

A brief definition of the correlation process will be useful for the ensuing discussions. Figure 1 illustrates a single lag cell of a complete correlator, that is, one containing multipliers, accumulators, and two data paths. The function of this i th lag cell is to perform the operation

$$C_i = \sum_{k=1}^N a_k b_{k+i}$$

where N is the duration of the correlation process (limited by the accumulator size). The data quantization (in this case m -bits \times n -bits) is defined as the number of bits per symbol in each data path. Some correlators use a scheme of encoding 3 states (e.g., -1, 0, +1) onto two lines. In this article, such a scheme will be called 1.5-bit quantization. A group of L lag cells connected in series constitutes a complete correlator of lag length L .

A. VLSI Correlator Chips

TRW Corporation has been the most active in the field of custom VLSI correlator chips. They have four different products available: the TDC1004, the TDC1023, the TDC1028, and the TMC2220. The TDC1004 and TDC1023 are both 64-lag correlators with 1×1 (1-bit by 1-bit) data quantization. The TDC1004 outputs an analog voltage from a summing junction, whereas the TDC1023 has digital outputs and a built-in threshold register. The TDC1004 may be clocked at 15 MHz and the TDC1023 operates at 17 MHz. The TDC1028 has only 8 lags but the data quantization is 4×4 and full provisions are made for cascading multiple chips. Its maximum clock rate is 10 MHz. The TMC2220 is four correlators in one package, each with 32 lags and fully programmable digital outputs. It can be clocked at 20 MHz. Also in the planning stage is a new device, designated the TMC2221, which will have 128 lags and a clock rate of 20 MHz. All TRW chips have the disadvantage of not being complete correlators because they do not have accumulators on-board. This means that accumulation must be done by a computer or by external hardware.

Hughes Aircraft has developed a chip called simply the "Digital Correlator" which uses CMOS/SOS technology to make a very fast correlator. This device was designed under the VHSIC (Very High Speed Integrated Circuit) program for DARPA (Defense Advanced Research Project Agency). It is a complete correlator with 12-bit accumulators on-board. It is configured as a 128 lag device with 4×1 quantization and operates at a rate of 25 Megasamples/sec. It is fully cascable with input and output SUM pins.

The Netherlands Foundation for Radio Astronomy (NFRA) has developed a VLSI correlator chip [1] which has 16 lags, 2×2 quantization, 22-bit accumulators and may be clocked at a rate of 55 MHz. This chip is a CMOS gate array device manufactured for NFRA by LSI Logic Corp.

RCA Corporation has a CMOS/SOS correlator chip called the TCS040 which contains two 32-lag correlators. Its outputs are analog voltages and it operates at a rate of 40 Megasamples/sec.

B. Examples of Large Correlator Systems Currently in Use

At the Arecibo Radio Observatory in Puerto Rico [2], interferometry for passive radio astronomy is performed using a correlator system which was developed for the Haystack Observatory by MIT. This machine uses conventional off-the-shelf MSI and LSI chips with ECL (Emitter Coupled Logic) used to perform the higher speed functions and F-TTL (Fast Transistor-Transistor Logic) and CMOS (Complementary MOS logic) to do the rest. This system uses 1.5×1.5 quantization (2-bit, 3 level quantization) and has a total of 2048 lags. It has accumulators 24 bits long and operates at a rate of 80 Megasamples/sec.

In the Communications System Research Section, a project called Goldstone Solar System Radar (GSSR) uses an in-house designed correlator [3]. Its capabilities are a 10 Megasamples/sec data rate with 4×1 quantization, 256 lags and accumulators 28 bits long. This data rate is used for radio astronomy and investigations of Saturn's rings. When the correlator is used for radar astronomy, the data rate is limited to 2.5 Megasamples/sec. The design is based primarily on the TRW TMC1023 chip.

The Very Large Array (VLA) in New Mexico consists of 27 antenna dishes spread over distances of up to 22 miles across the desert. Because of the large number of sources, a very large correlator system is needed [4]. The correlators are configured in arrays of $27 \times 27 = 729$ correlators and 16 different arrays required to perform differing types of correlation. Thus a total of $27 \times 27 \times 16 = 11,664$ individual correlators are required. Each of these operates at a rate of 100 Megasamples/sec and uses recirculation to achieve the equivalent of 32 lags. The data is quantized 2×1.5 and results are summed and stored 24 bits long, as required for their fixed 52 millisecond integrate time. They have no plans for a new correlator system in the near future.

Caltech and JPL jointly operate a correlator system called the Very Long Baseline Interferometry (VLBI) Block I correlator. It has been in existence for several years and was fabri-

cated using medium-scale TTL chips. It has a total of 16 lags, data quantization of 1×1 , accumulators 32 bits long, and correlates at a rate of 500 kilobits/sec. It is used to integrate the signals for periods ranging from 0.2 sec to 20 sec.

III. Planned or Projected Correlator Systems

Interviews were conducted with several parties who have an interest in new correlator systems. Personal visits were used where possible to learn about different types of systems under development and others merely proposed at this time. Table 3 gives a summary of the results of this survey. All of the referenced systems are either in the planning, design, or construction phase. They represent the current thinking about what can be built using the best available and most economical methods from today's technology.

The Arecibo Observatory in Puerto Rico also uses correlators to do planetary radar astronomy [2]. Their current equipment is somewhat old and they are planning to upgrade to a more modern correlator system. Jon Hagen, head of the Electronics Department at Arecibo, says that they would require a correlator with a sample rate of 1 to 4 Megasamples/sec with a lag length of 256 or 512 lags. The correlated pattern is 4095 bits long and they desire 4×1.5 quantization. This suggests an accumulator 16 bits long. Such a correlator is only in the planning stage at present.

In the Tracking Systems and Applications Section at JPL, there is interest in developing a system for spacecraft angular position determination using cross-correlation to perform real-time connected element interferometry. (A similar technique for spacecraft navigation was described by J. B. Thomas in JPL Internal Document, Engineering Memorandum 335-26, Jet Propulsion Laboratory, Pasadena, California, November 11, 1986.) Chad Edwards, a scientist in this section, describes the requirement as a single correlator operating at a rate of 200 Megasamples/sec using 2×2 quantization. Sixty-four lags would be required with each lag having a 26-bit accumulator in order to provide a 0.1 sec integrate time. These requirements are not firm at this time but represent an estimate of the needed performance.

In the Communications Systems Research Section, radar astronomer Ray Jurgens heads a group which performs planetary radar astronomy using the correlator system described in Section II. Future plans call for upgrading to a higher performance correlator system with a 50 Megasample/sec data rate, 4×1 data quantization, lag lengths up to 4096 bits and accumulators 28 bits long.

In the Space Physics and Astrophysics Section, radio astronomer Tom Kuiper performs astronomy using the DSN antennas. He describes a potentially useful correlator system as follows: Two correlators would be required, each operating at a 25 Megahertz bandwidth with 2×2 quantization and 256 to 1024 lags. The correlators should be able to accumulate for 5 to 10 minutes, which implies 40-bit accumulators. This system is a proposal only and is not currently funded.

The Owens Valley Radio Observatory (OVRO) is designing a new millimeter wave interferometer that will use high performance correlators. According to Martin Ewing at Caltech, a total of 15 correlators will be needed to handle the 15 baselines between the six 10-meter dishes being installed at the observatory. A data rate of 250 Megasamples/sec will be needed and the data will be quantized 2×2 . Each correlator will require 512 lags and accumulators 24 bits long. This system is in the early design phase at present.

In the Observational Systems Division, plans are underway to implement an advanced radio astronomy instrument using heterodyne radiometry. Herb Pickett, an instrumentation scientist on this project, describes a system consisting of a 20-meter orbiting dish with surfaces figured to better than one micron. The plans are to cover a multi-gigahertz bandwidth using analog filters. These are expensive, high-precision filters which break the signal into several hundred bands. These bands must then be autocorrelated in order to obtain the noise autocorrelation function. The individual correlators must then operate at a rate of 65 Megasamples/sec with a 2×2 bit quantization. A total of 500 lags will be required for each correlator with accumulators 26 bits long. Since this is a space application, speed-power product is of prime importance and CMOS devices are the logical choice. This project is currently in the planning stage.

The DSN Data Systems Section has need for a correlator for a project called the C-band Uplink. John Smith, a group supervisor in this section, says that this correlator will need to operate at a rate of 2.4 Megasamples/sec and contain 4096 lags with accumulators 24 bits long. The data may be quantized either 1×1 or 1×4 . This project is in the early design stage.

The DSN Data Systems Section also has a requirement for a correlator to perform PN (pseudo-noise) ranging (J. R. Smith, "Capabilities of the Proposed DSN Correlator Chip," JPL Internal Document IOM-3680-86-364/0, Jet Propulsion Laboratory, Pasadena, California, December 8, 1986). The correlator for this application will be required to operate at a rate of 2 to 8 Megasamples/sec with several short lag-length correlators operating in concert, the longest of which is 23 lags long. The data will be quantized 16×1 and accumulators 36 bits long will be needed to allow integration for several

hours at a time. This project is currently in the design phase, with a custom VLSI chip included in the plans.

In the Tracking Systems and Applications Section, Brooks Thomas is designing a high accuracy receiver for the Global Positioning Satellite (GPS) system. His requirements are for a data rate of 15 Megasamples/sec with 1.5-bit quantization. The accumulator needs to be at least 20 bits long. Each receiver will need 3 channels of correlation for each of 8 satellites, thus a total of 24 correlators. Gallium arsenide technology is being considered for this application. Work is presently in the design stage.

The Very Long Baseline Array (VLBA) is a planned series of ten 25-meter radio dishes to be located on U.S. territory from the Virgin Islands to Hawaii [6]. In addition, there are plans to link up to 10 non-VLBA antennas into an array for certain applications, making a total of 20 sources. According to John Romney of the National Radio Astronomy Observatory (NRAO), their approach to this problem is somewhat different than others in that they will perform a Fourier transform on the received signals before correlating them in pairs. First, a 2047-point transform is performed on each signal, then pairs of signals are correlated by performing a single-point multiplication of two 8-bit or 9-bit floating point numbers. The result will then be added to an accumulator of length 35 to 40 bits and accumulated for 10 seconds before dumping to the computer. This method is called the F/X method, where F represents Fourier and X represents correlation, suggesting that a Fourier transform is taken first, then correlation is performed. The data rate required will be about 32 Megasamples/sec and a total of $N(N+1)/2$ baselines will be processed. Since the VLBA needs to process signals from a maximum of $N=20$ antenna sources, processing must be provided for a total of 210 baselines. This system is currently in design and fabrication.

In the radio astronomy group at Caltech, Martin Ewing is supervising the design and construction of the Block II correlator for VLBI (Very Long Baseline Interferometry) applications. The project will consist of 168 correlators, each of which operates at up to 8 Megasamples/sec with a 1×1 quantization and 8 complex lags with 26-bit accumulators. This system is under construction at present and uses gate-array technology and large wire-wrap boards holding nearly 1000 chips each.

IV. VLSI Correlator Developments in the Communications Research Section

Three VLSI correlator chip projects were undertaken in this organization in the past two years which used the same

sub-cells and were intended as dedicated high-speed correlators. These are called SMLCOR, BIGCOR, and RACOR. In addition, a programmable correlator/filter chip has been designed which can be externally reconfigured.

SMLCOR [5] was a proof-of-concept chip to establish that the architecture was valid and allow the design to be extended to a larger scale device. SMLCOR has 4 lags, 4-bit accumulators and 1.5×1.5 bit quantization. It was fabricated using NMOS technology and 4 micron feature size. It operated successfully at speeds up to 6 MHz.

BIGCOR uses an architecture based on SMLCOR but is scaled up to a much larger device of 60,000 transistors. It has 32 complex lags for a total of 64 accumulators, each with 25 bits. It uses 1.5×1.5 quantization but has four data paths to provide for the two real data streams and the real and imaginary parts of a phase rotator vector. A block diagram of the BIGCOR architecture is shown in Fig. 2 and the details of the correlation circuit for each lag are shown in Fig. 3. Each lag has three multipliers and the 25-bit accumulator contains one "overflow" bit which remains set until the end of a correlation cycle when it is cleared by the unload process. Both BIGCOR and SMLCOR use separate correlate and dump cycles so that correlation must be interrupted briefly while the accumulator totals are dumped out. BIGCOR was fabricated using NMOS technology and 3 micron feature size. It operates at frequencies of up to 4 MHz. Further refinements and better fabrication quality are expected to push this rate up to 10 MHz.

A chip designated RACOR (for Radar CORrelator) has been designed using an architecture similar to BIGCOR but with 4×1 quantization and 32-bit accumulators (C. R. Lahmeyer, "Proposal for a VLSI Correlator for Planetary Radar," JPL Internal Document IOM 331-86.3-380, Jet Propulsion Laboratory, Pasadena, California, December 18, 1986). It was originally proposed as a VLSI design to support planetary radar observations, but may have wider application as well. It will also use NMOS technology and 3 micron feature size and has a design speed of 10 MHz. It has not yet been fabricated.

A proposed correlator system was recently described (C. R. Lahmeyer, "A Bandwidth-Multiplying Correlator," JPL Internal Document IOM 331-87.3-014, Jet Propulsion Laboratory, Pasadena, California, February 16, 1987) which incorporates the RACOR chip and a bandwidth-multiplying technique to produce a high performance correlator at a reasonable cost. Figure 4 gives a block diagram view of this design. Two banks of RACOR chips would be used so that

correlation could take place continuously without any interruption to dump the accumulator contents. Each of the two banks consists of 16 RACOR devices wired in a 4-chip by 4-chip configuration. The resulting data rate would be 80 Megasamples/sec with a 4-bit \times 1-bit data quantization. The input shift register would be the only component running at 80 MHz, since the correlator chips are operating in parallel. They would need to operate at 20 MHz, however, which would necessitate their being built with high-performance CMOS technology. While this configuration has 256 lags, the number of lags is easily extendable by connecting several of these modules in series. The data quantization is also extendable by operating modules in parallel and summing the outputs with additional adder chips.

Shalhav Zohar has designed a chip which can produce the cross-correlation of sequences having a wide range of parameters ("Proposal for a Correlator/Filter Chip Based on Distributed Arithmetic," unpublished, Jet Propulsion Laboratory, Pasadena, California, February 5, 1987). Specifically, it can accommodate any system where the total number of bits involved in the computation of one correlation lag is bounded by about 1540. The correlator consists of the special NMOS chip plus a 12-bit TTL accumulator. Augmenting this setup with an external shift register produces absolute precision correlation (no roundoff error). Two extreme examples illustrate the range of possibilities: Using 64-bit input words, this system can produce 132-bit correlations based on 12-term sums at the rate of 50k correlations/sec. At the other extreme, using 1-bit words, it can produce 11-bit correlations based on 1539-term sums at the rate of 6.5M correlations/sec.

V. Conclusions

The question now is whether any commonality exists between the various applications listed. At first glance, the similarities between the applications in Table 3 would seem to be minimal, but closer examination reveals that certain elements in common do exist between the various users. With a few exceptions, the number of lags is in the tens or hundreds. Further, most applications are for data quantizations of 1, 2, or 4 bits. The accumulator sizes required are also rather similar, centering around 25 to 35 bits. The most disparate requirement is the data rate, with values from 1 to 1000 Megasamples per second listed. Even with the great variety of speed requirements it is possible to specify an architecture which utilizes many of the common elements of several of the listed applications. The speed variation could be addressed by building the VLSI correlator chip out of appropriate VLSI technology materials to yield the required performance. For example, ECL (emitter-coupled logic) and GaAs (gallium arsenide) technologies are becoming available for custom and semi-custom chip designs of very high performance.

The bandwidth-multiplying correlator described in Section IV based on the proposed RACOR chip could be used in various combinations to satisfy approximately half of the proposed correlator applications listed in Table 3. Even higher data rates could be processed by using analog bandwidth splitting to divide the incoming signal into several streams of lower bandwidth, then performing correlation separately on each band using separate correlators. This architecture could yield reasonably low-cost correlator systems which could satisfy additional applications in the future.

References

- [1] A. Bos, "The NFRA Correlator Chip," Netherlands Foundation for Radio Astronomy, Internal Technical Report No. 176, Dwingeloo Radio Observatory, Dwingeloo, Netherlands, August 1986.
- [2] J. B. Hagen, "Communications Techniques in Radio Physics and Astronomy," *IEEE Communications Magazine*, vol. 24, no. 10, pp. 16-20, October 1986.
- [3] S. S. Brokl, "Controller and Interface Module for the High-Speed Data Acquisition System Correlator/Accumulator," *TDA Progress Report 42-83*, vol. July-September 1985, pp. 113-124, Jet Propulsion Laboratory, Pasadena, CA, November 15, 1985.
- [4] R. P. Escoffier, "Correlator System Observer's Manual," VLA Technical Report No. 39, National Radio Astronomy Observatory, Charlottesville, VA, October 1979.
- [5] L. J. Deutsch and C. R. Lahmeyer, "A Systolic Architecture for Correlation and Accumulation of Digital Sequences," *TDA Progress Report 42-85*, vol. January-March 1986, pp. 62-68, Jet Propulsion Laboratory, Pasadena, CA, May 15, 1986.
- [6] K. I. Kellerman and A. R. Thompson, "The Very Long Baseline Array," *Science*, vol. 229, no. 4709, pp. 123-130, 12 July 1985.

Table 1. Correlator chips currently available

Manufacturer	Part	Data Rate (MHz)	No. of Lags	Outputs	Accumulator Size (Bits)	Technology
TRW	TDC1004	15	64	Analog	N/A	Bipolar
TRW	TDC1023	17	64	Digital	None	Bipolar
TRW	TDC1028	10	8	Digital	None	Bipolar
TRW	TDC2220	20	128	Digital	None	CMOS
Hughes	—	25	128	Digital	12	CMOS/SOS
NFRA	—	55	16	Digital	22	CMOS
RCA	TCS040	40	64	Analog	N/A	CMOS/SOS

Table 2. Sample of correlator systems currently in use

System	Data Rate (Megasamples/sec)	Quantization (Bits)	No. of Lags	Accumulator Size (Bits)	Number of Correlators
Arecibo	80	1.5×1.5	2048	24	1
Goldstone Solar System Radar	10	4×1	256	28	1
Very Large Array (VLA)	100	2×1.5	32	24	11,664
Very Long Baseline Interferometry (VLBI) Block I	0.5	1×1	16	32	1

Table 3. Survey of planned correlator systems

Application	Cognizant Person	Data Rate (Megasamples/sec)	Quantization (Bits)	Number of Lags	Accumulator Size (Bits)	Number of Correlators	Current Status
Arecibo Radio Observatory, Puerto Rico	John Hagen	1-4	1.5×4	256-512	16	1	Planned
C-Band Uplink, Sec. 368	John Smith	2.4	1×1 or 1×4	4096	24	1	In Design
DSN Radio Astronomy, Sec. 328	Tom Kuiper	50	2×2	256-1024	40	2	Planned
GPS High Accuracy Receiver, Sec. 335	Brooks Thomas	15	1.5×1	8	20	24	In Design
Heterodyne Radiometry, (Radio Astronomy) Sec. 383	Herb Pickett	1000	2×2	200	26	1	In Design
Millimeter-Wave Interferometer Owens Valley Radio Observatory	Martin Ewing	250	2×2	512	24	15	Early Design
PN-Code Spacecraft Ranging, Sec. 368	John Smith	2-8	16×1	23	36	6	In Design
Planetary Radar Astronomy, Sec. 331	Ray Jurgens	50	4×1	4096	28	1	Planned
Spacecraft Navigation, Sec. 335	Chad Edwards	200	2×2	64	26	1	Planned
Very Large Baseline Array (VLBA)	John Romney	32	9×9 (Floating Point)	1	35-40	210	In Design
Very Long Baseline Interferometry (VLBI), Block 2	Martin Ewing	4-8	1×1	8 (Complex)	26	168	Under Construction

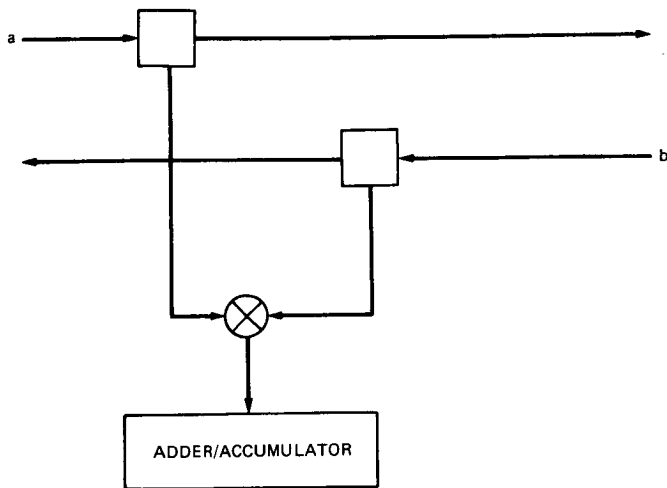


Fig. 1. Single lag cell of a typical correlator

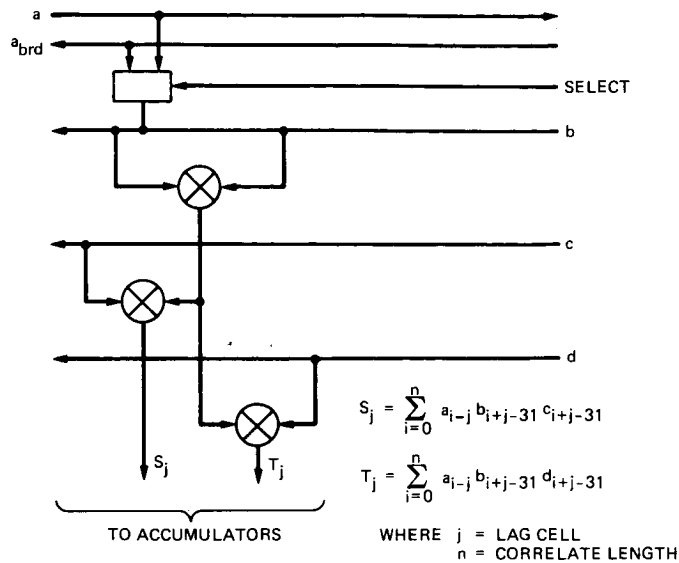


Fig. 3. Detail of BIGCOR lag cell

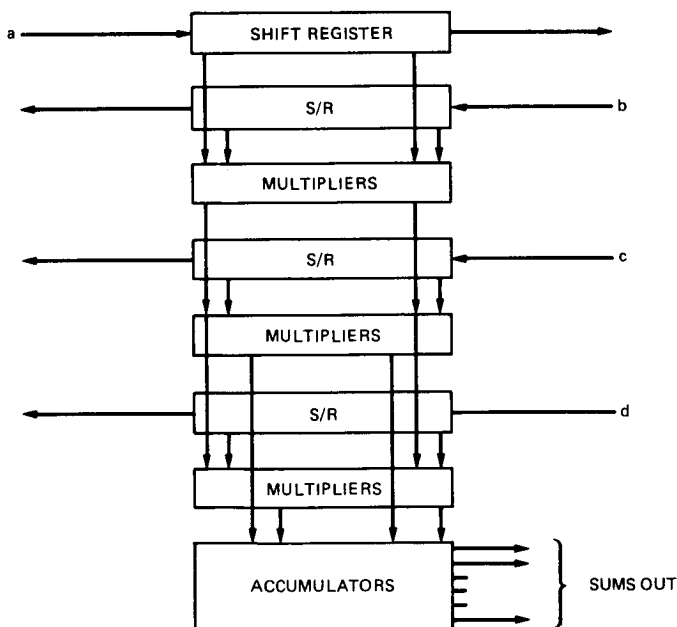


Fig. 2. BIGCOR block diagram

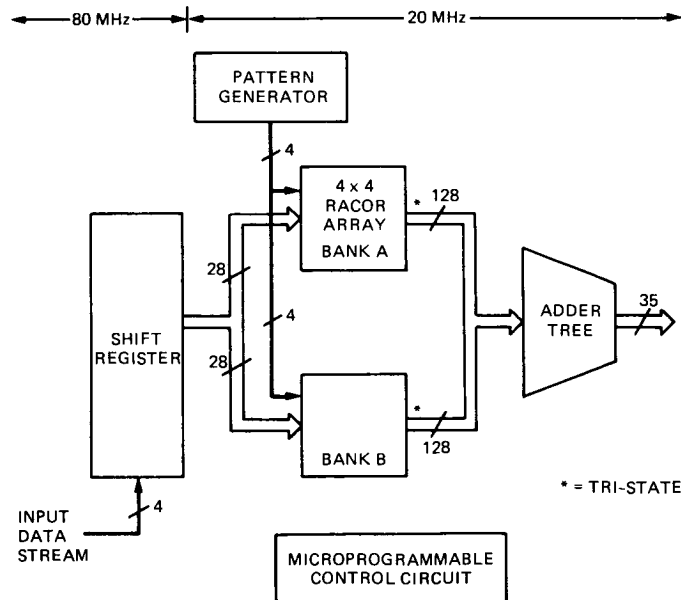


Fig. 4. Proposed VLSI radar correlator using bandwidth multiplication

ORIGINAL PAGE IS
OF POOR QUALITY

A Comparison of VLSI Architecture of Finite Field Multipliers Using Dual, Normal or Standard Basis

I. S. Hsu, T. K. Truong, H. M. Shao, and L. J. Deutsch
Communications Systems Research Section

I. S. Reed
Department of Electrical Engineering
University of Southern California

Three different finite field multipliers are presented: (1) a dual basis multiplier due to Berlekamp, (2) the Massey-Omura normal basis multiplier, and (3) the Scott-Tavares-Peppard standard basis multiplier. These algorithms are chosen because each has its own distinct features which apply most suitably in different areas. Finally, they are implemented on silicon chips with NMOS technology so that the multiplier most desirable for VLSI implementations can readily be ascertained.

I. Introduction

The era of the VLSI digital signal processor has arrived and its impact is evident in many areas of technology. The trend is to put more and more elements on a single silicon chip in order to enhance the performance and reliability of the system.

Recently, finite field arithmetic has found widespread applications. Examples include cryptography, coding theory, and computer arithmetic. Among the finite field arithmetic operations, multiplication is the most complex and time consuming. Already, it is used in a variety of systems, e.g., the VLSI design of Reed-Solomon coder (Refs. 1 and 2). Hence, a small, high performance finite field multiplier is urgently needed. Such a multiplier can also be used as a building block for the design of many large systems which use finite field arithmetic.

In this article, three different finite field multipliers are compared for suitability of VLSI implementation. These include: (1) the dual basis multiplier due to Berlekamp (Ref. 3), (2) the Massey-Omura normal basis multiplier (Ref. 4), and (3) the Scott-Tavares-Peppard standard basis multiplier (Ref. 5). They are chosen for comparison because each has its own distinct features which make them suitable for specific applications.

Different basis representations of field elements are used in these three multipliers. The dual basis multiplier uses the dual basis representation for the multiplicand and standard basis for the multiplier. The product is again in dual basis representation. The Massey-Omura multiplier uses normal basis representations for both the multiplicand and multiplier. The Scott-Tavares-Peppard multiplier uses the standard basis representations for all field elements. The complexity of basis conversion

is heavily dependent on the choice of the primitive irreducible polynomial which generates the field. If the polynomial is chosen adequately, the basis conversion is a simple operation. The algorithms for performing the basis conversions are presented in Appendixes A and B.

It is concluded in this article that the dual basis multiplier needs the least number of gates, which in turn leads to the smallest area required for VLSI implementation. The Massey-Omura multiplier is very effective in performing operations such as finding inverse elements or in performing squaring or exponentiation of a finite field element. The standard basis multiplier does not require basis conversion; hence it is readily matched to any input or output systems. Also, due to its regularity and simplicity, the design and expansion to high order finite fields is easier to realize than in the dual or normal basis multipliers.

Examples of these three multipliers are given in this article for the purpose of illustration. Their 8-bit versions are implemented on a silicon chip. The chip layouts are also presented separately so that their differences can be distinguished without difficulty.

II. The Dual Basis Multiplication Algorithm

Recently, Berlekamp developed a bit-serial multiplier for use in the design of a Reed-Solomon encoder (Ref. 3). Hsu et al. (Ref. 1) used Berlekamp's multiplier to design an 8-bit single chip VLSI (255, 223) Reed-Solomon encoder which has proved to perform well. However, in that design, the multiplicand is a fixed finite field constant which is inconvenient if one desires to change the multiplicand.

In the following, Berlekamp's bit-serial multiplication algorithm is modified and generalized to allow both the multiplicand and multiplier to be variable. Thus, revision of Berlekamp's algorithm is called the dual basis multiplication algorithm in the rest of this article.

In order to understand the dual basis multiplication algorithm, some mathematical preliminaries are needed. Toward this end, the mathematical concepts of the "trace" and a "dual" basis are introduced. For more details and proofs see Refs. 2, 6, and 7.

Definition 1. The trace of an element β belonging to $GF(p^m)$, the Galois field, of p^m elements, is defined as follows:

$$\text{Tr}(\beta) = \sum_{k=0}^{m-1} \beta^{p^k}$$

In particular, for $p = 2$,

$$\text{Tr}(\beta) = \sum_{k=0}^{m-1} \beta^{2^k}$$

A fast algorithm for computing trace values of elements in $GF(2^m)$ is presented in Appendix C. The trace has the following properties which will not be proved here:

$$(1) [\text{Tr}(\beta)]^p = \beta^p + \beta^{p^2} + \dots + \beta^{p^{m-1}} = \text{Tr}(\beta)$$

where $\beta \in GF(p^m)$. This implies that $\text{Tr}(\beta) \in GF(p)$ i.e., the trace is in the ground field $GF(p)$.

$$(2) \text{Tr}(\beta + \gamma) = \text{Tr}(\beta) + \text{Tr}(\gamma), \text{ where } \beta, \gamma \in GF(p).$$

$$(3) \text{Tr}(c\beta) = c\text{Tr}(\beta), \text{ where } c \in GF(p)$$

$$(4) \text{Tr}(1) = m \pmod{p}$$

Definition 2. A basis $\{u_k\}$ in $GF(p^m)$ is a set of m linearly independent elements in $GF(p^m)$.

Definition 3. Two bases $\{u_j\}$ and $\{\lambda_k\}$ are said to be dual of one another if

$$\text{Tr}(u_j \lambda_k) = \begin{cases} 1, & \text{if } j = k \\ 0, & \text{if } j \neq k \end{cases}$$

For convenience, the basis $\{u_j\}$ is sometimes called the original basis, and the basis $\{\lambda_k\}$ is called its dual basis, even though the concept of duality is symmetric.

Theorem. Every basis has a unique dual basis.

Proof. See Ref. 8.

Corollary 1. Let $\{u_j\}$ be a basis of $GF(p^m)$ and let $\{\lambda_k\}$ be its dual basis. Then a field element Z can be expressed in the dual basis $\{\lambda_k\}$ by the expansion

$$Z = \sum_{k=0}^{m-1} z_k \lambda_k$$

where

$$z_k = \text{Tr}(Z \cdot u_k)$$

Proof. Let

$$Z = z_0 \lambda_0 + z_1 \lambda_1 + \dots + z_{m-1} \lambda_{m-1}$$

Multiply both sides by u_k and take the trace. Then by Definition 3 and the property of trace:

$$\text{Tr}(Z \cdot u_k) = \text{Tr} \sum_{i=0}^{m-1} z_i (\lambda_i u_k) = z_k$$

The following corollary is an immediate consequence of Corollary 1.

Corollary 2. Let $\{u_j\}$ be a basis of $GF(p^m)$ and let $\{\lambda_k\}$ be its dual basis. The product $W = ZG$ of two fixed elements in $GF(p^m)$ can be expressed in the dual basis by the expansion

$$W = \sum_{k=0}^{m-1} \text{Tr}(Wu_k) \cdot \lambda_k = \sum_{k=0}^{m-1} \text{Tr}(ZGu_k) \lambda_k$$

where $\text{Tr}(Wu_k)$ is the k th coefficient of the dual basis for the product of two field elements.

These two corollaries provide a theoretical basis for the dual basis finite field multiplier. In the following section, a detailed example is developed to illustrate the dual basis bit-serial multiplication algorithm.

III. An Example of the Dual Basis Multiplication Algorithm

The example is given in $GF(2^4)$ for purposes of illustration; the extension to more general cases is obvious.

Let α be a root of the primitive irreducible polynomial $f(x) = x^4 + x + 1$ over $GF(2)$. Then α satisfies the equation $\alpha^4 + \alpha + 1 = 0$. It is also true that $\alpha^{15} = 1$. Let the standard basis be $\{1, \alpha, \alpha^2, \alpha^3\}$ and its dual basis be $\{\lambda_0, \lambda_1, \lambda_2, \lambda_3\}$. Then, by Definition 3,

$$\text{Tr}(1 \cdot \lambda_0) = 1$$

$$\text{Tr}(\alpha \cdot \lambda_1) = 1$$

$$\text{Tr}(\alpha^2 \cdot \lambda_2) = 1$$

and

$$\text{Tr}(\alpha^3 \cdot \lambda_3) = 1$$

Let

$$Z = \sum_{k=0}^3 z_k \lambda_k$$

be represented in dual basis. Also let

$$G = \sum_{k=0}^3 g_k u_k$$

be represented in standard basis. Then, by Corollary 1,

$$z_k = \text{Tr}(Z\alpha^k)$$

Furthermore, let $W = ZG$ be the product of two elements Z and G . If W is represented in dual basis, then,

$$W = \sum_{k=0}^3 \omega_k \cdot \lambda_k$$

where by Corollary 1,

$$\omega_k = \text{Tr}(W\lambda_k) = \text{Tr}(ZG \cdot \lambda_k)$$

If one defines

$$T^{(k)}(W) = \text{Tr}(ZG \cdot \lambda_k)$$

then

$$T^{(0)}(W) = \text{Tr}(ZG\alpha^0) = \text{Tr}(ZG)$$

$$= \text{Tr}(Z(g_0 \cdot \alpha^0 + g_1 \cdot \alpha + g_2 \cdot \alpha^2 + g_3 \cdot \alpha^3))$$

$$= g_0 z_0 + g_1 z_1 + g_2 z_2 + g_3 z_3 \quad (1)$$

From the definition of $T^{(k)}(W)$, one obtains

$$T^{(k)}(W) = T^{(k-1)}(\alpha ZG \cdot \alpha^{k-1})$$

Therefore, if ZG is replaced by $\alpha \cdot ZG$ in $T^{(k-1)}$, i.e., Z by $\alpha \cdot Z$, $T^{(k)}(W)$ can be obtained from $T^{(k-1)}(W)$. Let

$$Y = \alpha Z = y_0 \lambda_0 + y_1 \lambda_1 + y_2 \lambda_2 + y_3 \lambda_3$$

where

$$y_m = \text{Tr}(Y \cdot \alpha^m) = \text{Tr}(Z \cdot \alpha^{m+1})$$

for each m . Then $T^{(k)}$ is obtained from $T^{(k-1)}$ by replacing

$$z_0 \text{ by } y_0 = \text{Tr}(Z\alpha) = z_1$$

$$z_1 \text{ by } y_1 = \text{Tr}(Z\alpha^2) = z_2$$

$$z_2 \text{ by } y_2 = \text{Tr}(Z\alpha^3) = z_3$$

and

$$z_3 \text{ by } y_3 = \text{Tr}(Z\alpha^4) = z_0 + z_1$$

To reiterate,

$$W = ZG = \sum_{k=0}^3 T^{(k)}(W) \lambda_k$$

can be computed as follows:

- (1) Initially for $k = 0$, compute

$$T^{(0)}(W) \text{ by Eq. (1).}$$

- (2) For $k = 1, 2, 3$, compute $T^{(k)}(W)$ by

$$T^{(k-1)}(W) = T^{(k-1)}(YG)$$

and

$$Y = \alpha Z = y_0 \lambda_0 + y_1 \lambda_1 + y_2 \lambda_2 + y_3 \lambda_3$$

with

$$y_0 = z_1, y_1 = z_2, y_2 = z_3, \text{ and } y_3 = z_0 + z_1 = Z_f$$

where $Z_f = z_0 + z_1$ is the feedback term of the algorithm.

The above algorithm illustrates the dual basis multiplication algorithm. The extension to an 8-bit multiplier is obvious and will not be included here. The primitive irreducible polynomial in the 8-bit design is chosen to be

$$f(x) = x^8 + x^4 + x^3 + x^2 + 1$$

In this case, the feedback term is

$$Z_f = z_4 + z_3 + z_2 + z_0$$

Figure 1 shows the logic diagram of an 8-bit dual basis multiplier. The architecture is composed of four blocks. In Fig. 1, the Z -serial-to-parallel unit performs the serial-to-parallel operation of the input element with dual basis representation. Once all 8 bits of this element are stored in the bottom register, the cyclic operation starts and one bit is fed back from the

feedback logic circuitry. The G -serial-to-parallel unit also performs the serial-to-parallel operation of the input standard basis element. Once all 8 bits of this element are stored in the bottom register, they are latched bitwise so that no further operations are performed on this element as required by the algorithm.

Next, the output bits of these two units are fed into the AND-generation unit. The output consists of the bitwise AND-ed terms. These AND-ed terms again are fed into the XOR-array unit which performs the addition of AND-ed terms. This is needed since the addition of two elements in $GF(2)$ is just an exclusive-OR (XOR) operation. The terms included in this XOR-array are as shown in the following:

$$z_0 g_0 + z_1 g_1 + z_2 g_2 + z_3 g_3 + z_4 g_4 + z_5 g_5 + z_6 g_6 + z_7 g_7$$

The product is then obtained from the output of this XOR-array bit by bit. Figure 2 shows the layout of this dual basis multiplier.

IV. VLSI Architecture for the Massey-Omura Multiplier

Recently, Massey and Omura developed a multiplier which obtains the product of two elements in the finite field $GF(2^m)$. In this invention, they utilize a normal basis of form $\{\alpha, \alpha^2, \alpha^4, \dots, \alpha^{2^{m-1}}\}$ to represent each element in the field, where α is the root of an irreducible polynomial of degree m over $GF(2)$. In this basis, each element in the field $GF(2^m)$ can be represented by m binary digits.

Using the normal basis representation, the squaring of an element in $GF(2^m)$ is readily shown to be a simple cyclic shift of its binary digits (Ref. 4). Multiplication of two elements with a normal basis representation requires the same logic circuitry for every product digit. Adjacent product digit circuits differ only in their inputs which are cyclically shifted versions of one another (Ref. 4).

The conventional method for finding an inverse element in a finite field uses either table look-up or Euclid's algorithm. These methods are not easily realized in a VLSI circuit. However, by using a Massey-Omura multiplier, a recursive, pipeline inversion circuit can be developed (Ref. 4). The details of the Massey-Omura multiplier algorithm are not discussed further here. For a more detailed discussion, see Ref. 4.

The function f as described in (Ref. 4) is chosen to be the following:

$$f(a_0, a_1, a_2, a_3, a_4, a_5, a_6, a_7; b_0, b_1, b_2, b_3, b_4, b_5, b_6, b_7) =$$

$$a_5b_0 + a_6b_0 + a_3b_1 + a_5b_1 + a_4b_2 + a_5b_2 + a_6b_2 + a_7b_2$$

$$+ a_1b_3 + a_4b_3 + a_2b_4 + a_3b_4 + a_0b_5 + a_1b_5 + a_2b_5$$

$$+ a_6b_5 + a_0b_6 + a_2b_6 + a_5b_6 + a_6b_6 + a_2b_7$$

where the primitive irreducible polynomial of this finite field is

$$g(x) = x^8 + x^7 + x^6 + x^1 + 1$$

There are a variety of different possible expressions for the function f ; however, the above one was chosen for the purpose of illustration.¹ Since each term in the above expression represents a conducting line in the AND portion of a PLA (programmable logic array), the fewer the number of terms there are, the smaller the area needed to be used for VLSI implementation.

Figure 3 shows the block diagram of an 8-bit finite field multiplier using the Massey-Omura normal basis algorithm. The architecture of this chip is identical to that of the dual basis multiplier. The differences between these two multipliers are the following:

- (1) The number of terms in the expression of the Massey-Omura multiplier is twenty-one, while in the dual basis multiplier it is only eleven. This means a substantial amount of area is saved in the dual basis multiplier over the normal basis multiplier.
- (2) Both the input serial-to-parallel units are identical in the Massey-Omura multiplier and no feedback is needed. On the other hand, in the dual basis multiplier, the register storing the element with standard basis representation does not need to be cyclically shifted. This field element remains latched in the same position.

Figure 4 shows the layout for the 8-bit Massey-Omura multiplier.

V. VLSI Architecture for the Standard Basis Multiplier

The Scott-Tavares-Peppard multiplication algorithm is serial-in, serial-out, and pipeline in architecture. This algorithm performs multiplication in $GF(2^m)$ with order $O(m)$ in both

computation time and implementation area, but requires $m + 1$ time units between the first-in and first-out of computation. Due to the regularity of this architecture, the expansion to higher order finite fields needs only replicas of a basic cell. Furthermore, the irreducible primitive polynomial which generates the finite field can be changed. This feature makes it more convenient in use. This algorithm performs the finite field multiplication with elements represented in standard basis. As a consequence no basis conversion is needed. This multiplier can be used for applications such as cryptography where m is large. The algorithm is advantageous because of its efficient implementation time and high throughputs. The detailed algorithm will not be discussed further here. For more details, see Ref. 5.

Figure 5 shows the logic diagram of an 8-bit standard basis multiplier by Scott, Tavares, and Peppard. Inputs to this chip are A and B , the two elements to be multiplied, and the irreducible primitive polynomial F . These are fed into the chip serially. The output is the product element P , which is shifted out bit-by-bit.

In Fig. 5, A and F are shifted into their respective registers serially bit-by-bit. Here A is the multiplicand and F is the primitive irreducible polynomial that generates the finite field. The multiplier is denoted by B and the product by P . The register P_i contains the immediate product. Two control signals are required. One is derived from the most significant bit (MSB) of P , and the other from the state of b_i , which is latched with a flip-flop. The left shift is performed by loading the output of cell CELL- i into the product register of cell CELL- $i + 1$. Once the multiplication is completed, the most significant bits of the product register are transferred to the output shift register and shifted out serially.

The circuit diagram of the i th cell CELL- i is shown in Fig. 6. Since the ground field is $GF(2)$, additions are performed by exclusive-OR (XOR) gates. Pass transistors are used to control the data flow. If a "0" is to be added, the input line to the XOR gate is grounded; otherwise A and/or F are passed. The output of the XOR gate is directed to the product register of the next stage so adding and shifting is done in one clock cycle. Figure 7 shows the layout of this 8-bit standard basis finite field multiplier.

VI. Concluding Remarks

Three finite field multipliers are compared here. They are dual basis multiplier, normal basis multiplier, and standard basis multiplier. The dual basis multiplier occupies the smallest amount of chip area in VLSI implementation if the basis conversion is not included. Furthermore, since the dual basis multi-

¹Wang, C. C., "Computer Simulation of Finite Field Multiplications Based on Massey-Omura's Normal Basis Representation of Field Elements," private communication, 1985.

plier performs multiplication by taking the inner product of two elements and then feeds back the sum of certain bits of one element, it is expected that as the order of field goes higher, the dual basis multiplier will outperform the others. The normal basis multiplier is very effective in performing operations such as finding the inverse element or in performing squaring or exponentiation of a finite field element. But the area grows dramatically as the order of field goes up. Also, the f function described in Ref. 4 is to be searched again by

computer as the field is changed, and it is usually very time consuming. The standard basis does not require basis conversion; hence it is readily matched to any input or output system. Also, due to its regularity and simplicity, the design and expansion to high order finite fields are easier to realize than the dual or normal basis multipliers. The irreducible primitive polynomial of the field is changeable in standard basis multiplier. This distinct feature makes it more useful in certain aspects.

References

1. Hsu, I. S., Reed, I. S., Truong, T. K., Wang, K., Yeh, C. S., and Deutsch, L. J., "The VLSI Implementation of a Reed-Solomon Encoder Using Berlekamp's Bit-Serial Multiplier Algorithm," *IEEE Trans. on Computers*, Vol. C-33, No. 10, pp. 906-911, Oct. 1984.
2. Shao, H. M., Truong, T. K., Deutsch, L. J., Yuen, J. H., and Reed, I. S., "A VLSI Design of a Pipeline Reed-Solomon Decoder," *IEEE Trans. on Computers*, Vol. C-34, No. 5, pp. 393-403, May 1985.
3. Berlekamp, E. R., "Bit-Serial Reed-Solomon Encoders," *IEEE Trans. Inform. Theory*, Vol. IT-28, No. 6, pp. 869-874, Nov. 1982.
4. Wang, C. C., Truong, T. K., Shao, H. M., Deutsch, L. J., Omura, J. K., and Reed, I. S., "VLSI Architectures for Computing Multiplications and Inverses in $GF(2^m)$," *IEEE Trans. on Computers*, Vol. C-34, No. 8, pp. 709-717, Aug. 1985.
5. Scott, P. A., Tarvares, S. E., and Peppard, L. E., "A Fast Multiplier for $GF(2^m)$," submitted to *IEEE Trans. on Computers*, 1985.
6. MacWilliams, F. J., and Sloane, N. J. A., *The Theory of Error-Correcting Codes*, North-Holland Publishing Company, New York, N.Y., 1978.
7. Perlman, M., and Lee, J. J., "A Comparison of Conventional Reed-Solomon Encoders and Berlekamp's Architecture," NASA Tech. Brief, No. 3610-81-119, Jet Propulsion Laboratory, Pasadena, Calif., July 10, 1981.
8. Hsu, I. S., "New VLSI Architectures for Coding and Digital Signal Processing," Ph.D. Dissertation, Electrical Engineering Dept., University of Southern California, Los Angeles, Calif., 1985.

ORIGINAL PAGE IS
OF POOR QUALITY

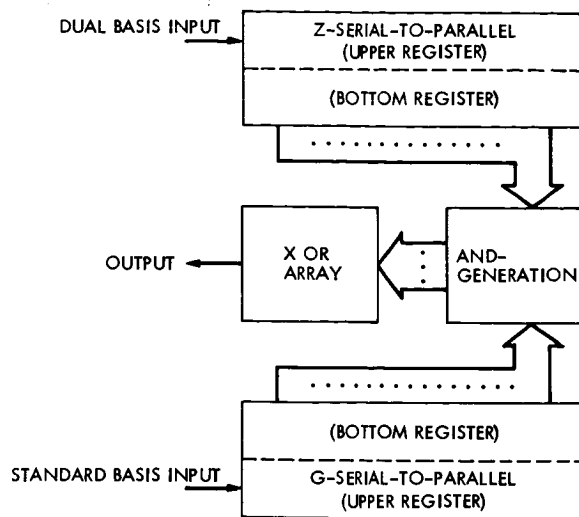


Fig. 1. Logic diagram of an 8-bit dual basis finite field multiplier

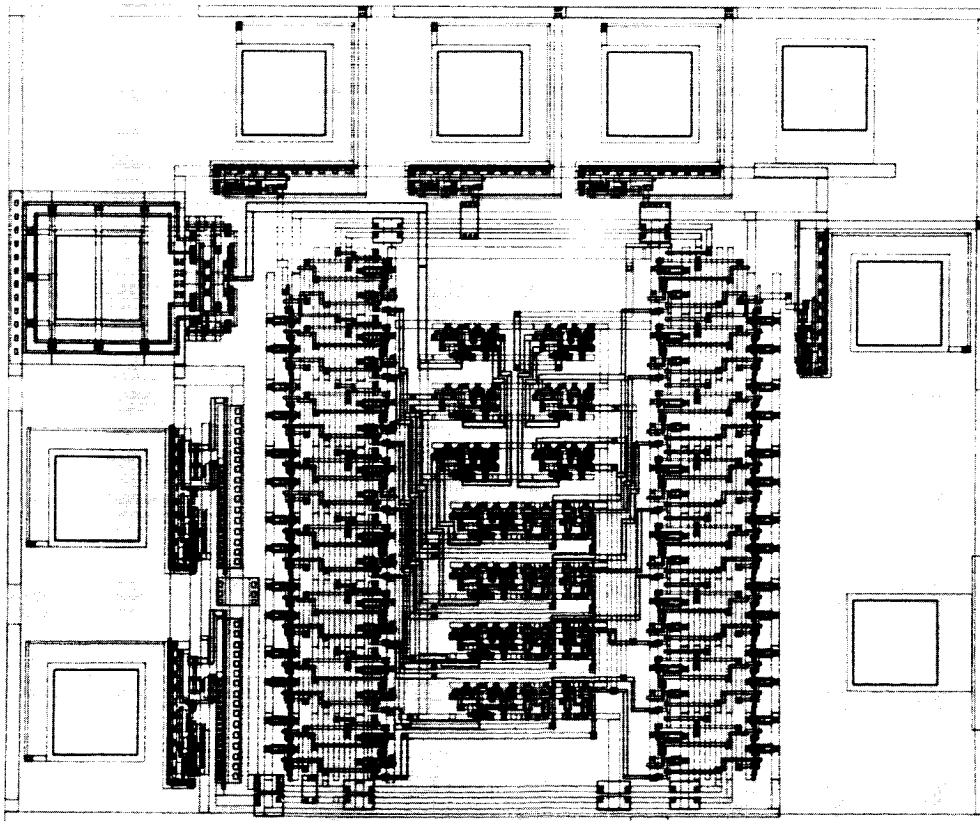


Fig. 2. Layout of an 8-bit dual basis finite field multiplier

ORIGINAL PAGE IS
OF POOR QUALITY

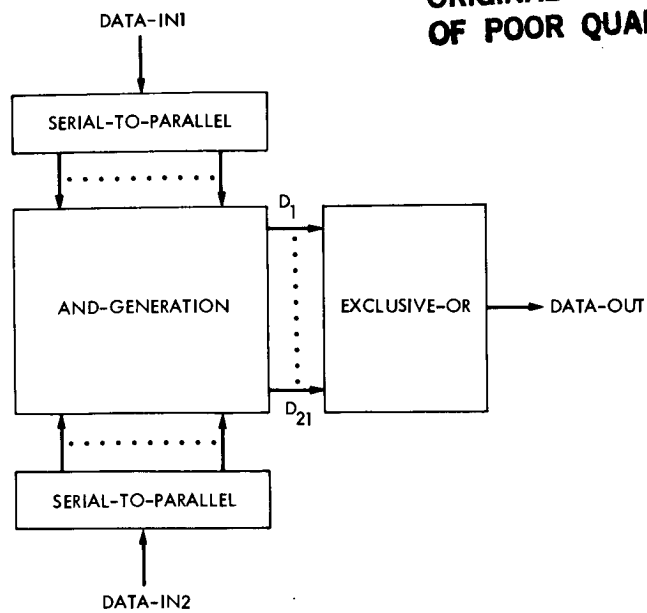


Fig. 3. Block diagram of an 8-bit finite field multiplier using Massey-Omura's normal basis algorithm

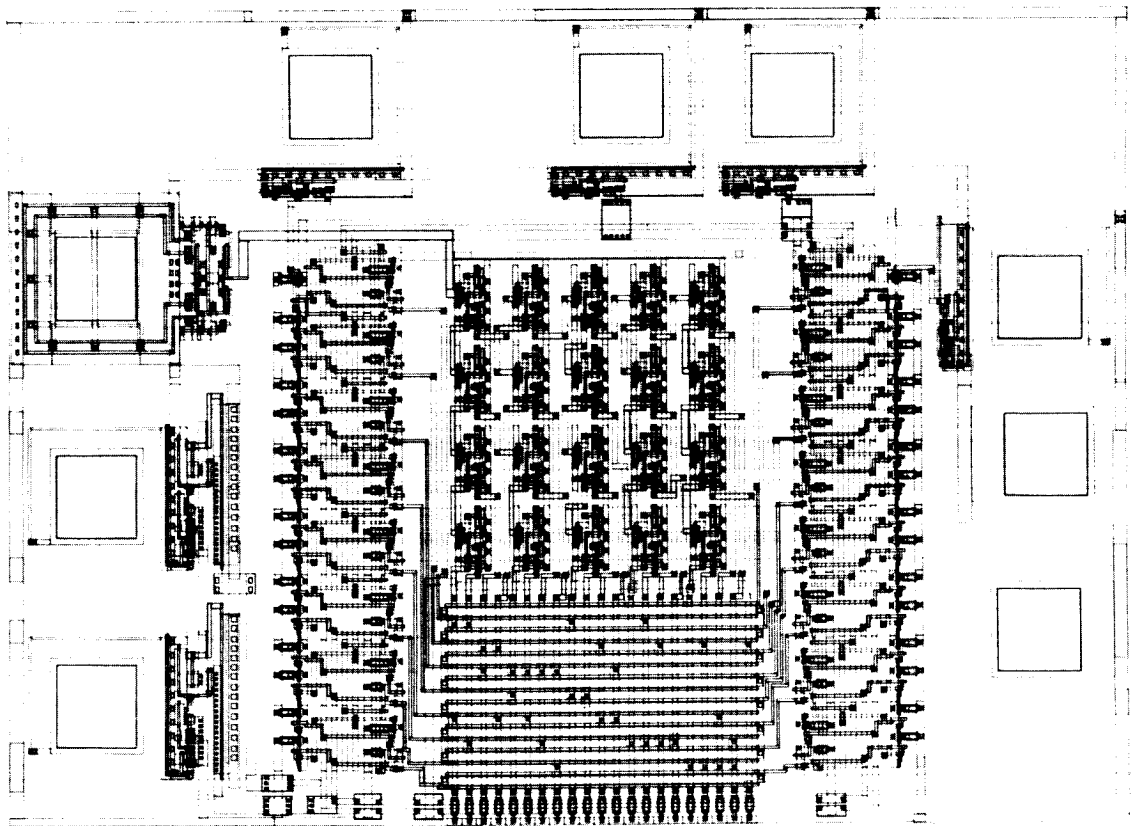


Fig. 4. Layout of an 8-bit Massey-Omura finite field multiplier

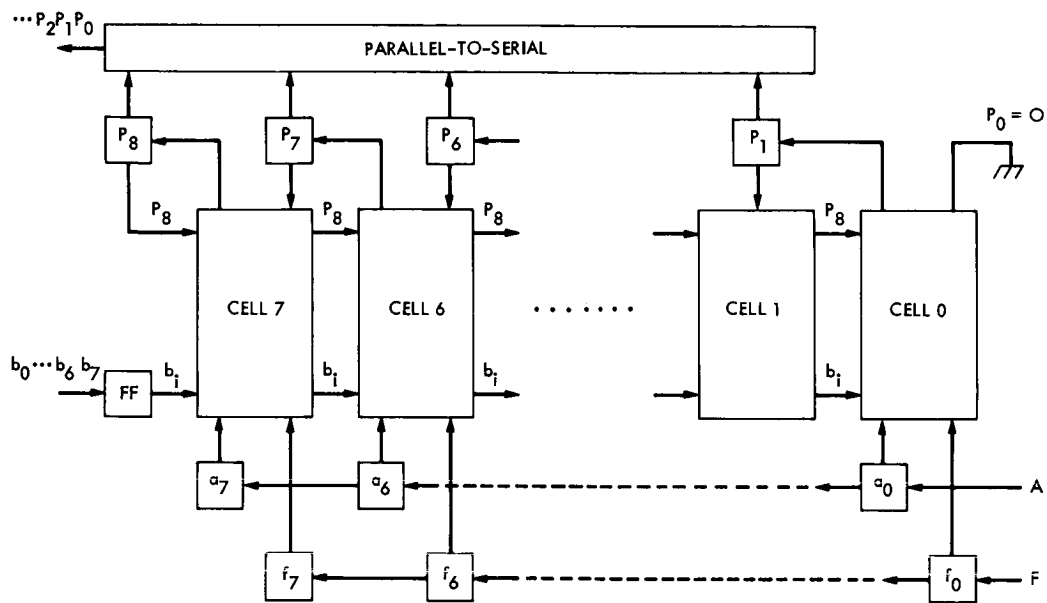


Fig. 5. Logic diagram of an 8-bit standard basis finite multiplier

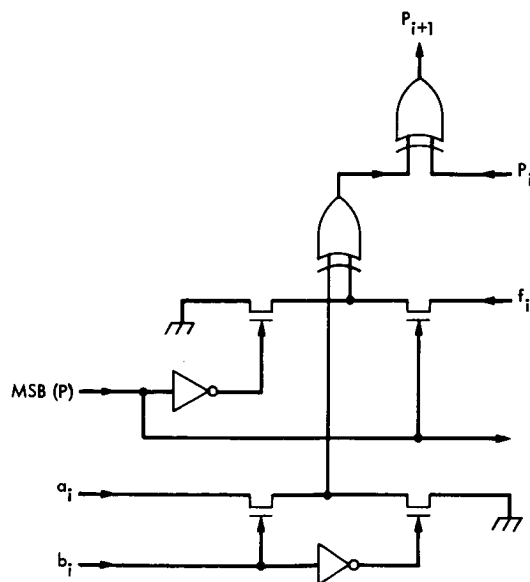


Fig. 6. Circuit diagram of the i th cell as shown in Fig. 5

ORIGINAL PAGE IS
OF POOR QUALITY

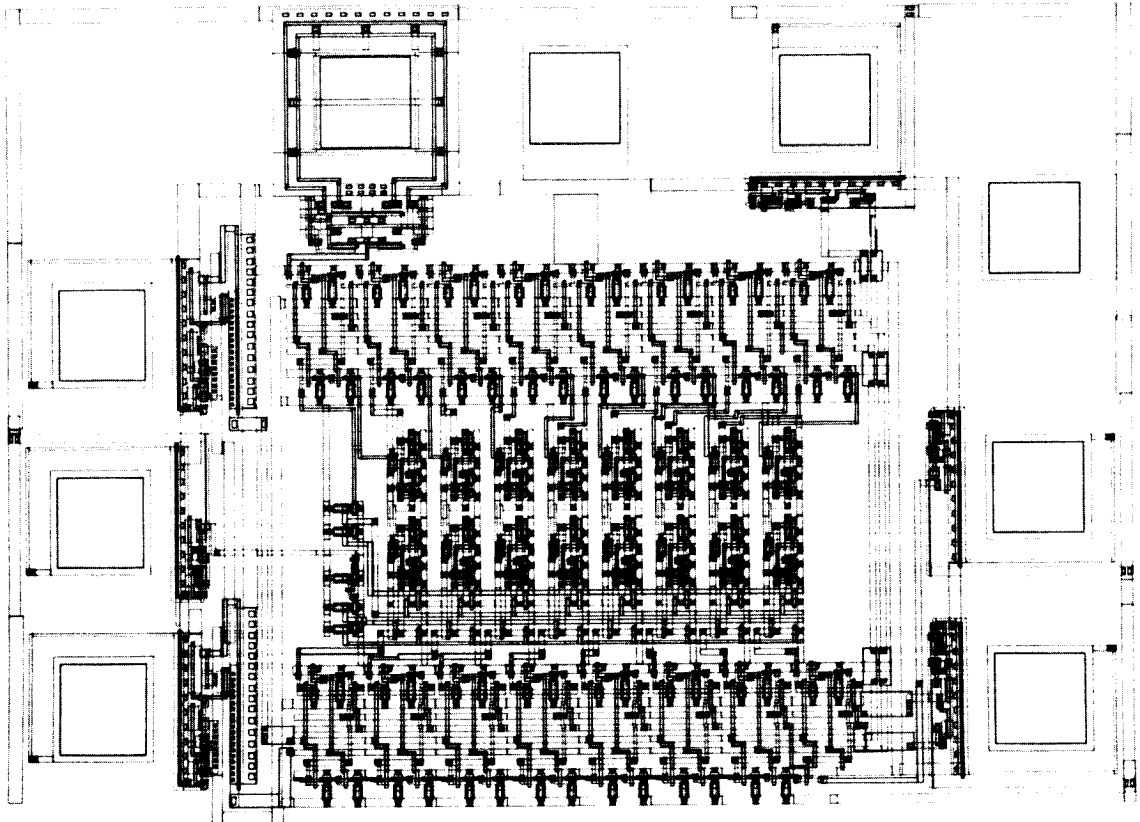


Fig. 7. Layout of an 8-bit standard basis finite field multiplier

Appendix A

A Method for Converting an Element in Standard Basis to Dual Basis

In this appendix, a method for converting an element represented in standard basis to its counterpart in dual basis is described by example. First, let the irreducible primitive polynomial in $GF(2^8)$ be

$$f(X) = x^8 + x^4 + x^3 + x^2 + 1$$

Then, from the definition of trace, one obtains

$$\text{Tr}(1) = 0, \text{Tr}(\alpha) = 0, \text{Tr}(\alpha^2) = 0, \text{Tr}(\alpha^3) = 0,$$

$$\text{Tr}(\alpha^4) = 0, \text{Tr}(\alpha^5) = 1, \text{Tr}(\alpha^6) = 0, \text{Tr}(\alpha^7) = 0$$

where α satisfies the equation $x^8 + x^4 + x^3 + x^2 + 1 = 0$.

An element Z in standard basis is written as

$$Z = \sum_{k=0}^7 z_k \alpha^k$$

In dual basis, it is represented as

$$Z = \sum_{k=0}^7 z'_k \lambda_k$$

where

$$z'_k = \text{Tr}(Z\alpha^k)$$

$$= \text{Tr}((z_0\alpha^0 + z_1\alpha^1 + z_2\alpha^2 + z_3\alpha^3$$

$$+ z_4\alpha^4 + z_5\alpha^5 + z_6\alpha^6 + z_7\alpha^7) \alpha^k)$$

$$= z_0 \text{Tr}(\alpha^k) + z_1 \text{Tr}(\alpha^{k+1}) + z_2 \text{Tr}(\alpha^{k+2})$$

$$+ z_3 \text{Tr}(\alpha^{k+3}) + z_4 \text{Tr}(\alpha^{k+4}) + z_5 \text{Tr}(\alpha^{k+5})$$

$$+ z_6 \text{Tr}(\alpha^{k+6}) + z_7 \text{Tr}(\alpha^{k+7})$$

Therefore, once $\text{Tr}(\alpha^k)$, for $0 \leq k \leq 14$, are known, the basis conversion from standard to dual can be completed.

Appendix B

A Method for Converting an Element in Dual Basis to Standard Basis

This appendix describes a method for converting an element represented in dual basis to standard basis. Again, let an element Z in dual basis be written as

$$Z = \sum_{k=0}^7 z'_k \lambda_k$$

In standard basis let it be represented as

$$Z = \sum_{k=0}^7 z_k \alpha^k$$

From the definition of the trace, one obtains

$$\begin{aligned} z_k &= \text{Tr}(Z \lambda_k) \\ &= \text{Tr}((z'_0 \lambda_0 + z'_1 \lambda_1 + z'_2 \lambda_2 + z'_3 \lambda_3 \\ &\quad + z'_4 \lambda_4 + z'_5 \lambda_5 + z'_6 \lambda_6 + z'_7 \lambda_7) \lambda_k) \\ &= z'_0 \text{Tr}(\lambda_0 \lambda_k) + z'_1 \text{Tr}(\lambda_1 \lambda_k) + z'_2 \text{Tr}(\lambda_2 \lambda_k) \\ &\quad + z'_3 \text{Tr}(\lambda_3 \lambda_k) + z'_4 \text{Tr}(\lambda_4 \lambda_k) + z'_5 \text{Tr}(\lambda_5 \lambda_k) \\ &\quad + z'_6 \text{Tr}(\lambda_6 \lambda_k) + z'_7 \text{Tr}(\lambda_7 \lambda_k) \end{aligned}$$

Hence, if the dual basis is determined and the trace values of the above calculated, the basis conversion from dual basis to standard basis can be completed.

Appendix C

Fast Algorithm for Calculating Trace Values of Elements in $GF(2^m)$

In this appendix, a fast algorithm for calculating the trace values of elements in finite field $GF(2^m)$ is described. From the definition of the trace one has, for $\beta, \beta^2 \in GF(2^m)$:

$$\begin{aligned} \text{Tr}(\beta^2) &= \sum_{k=0}^{m-1} (\beta^2)^{2^k} = \beta^2 + \beta^{2^2} + \dots + \beta^{2^m} = \beta + \beta^2 \\ &+ \dots + \beta^{2^{m-1}} = \text{Tr}(\beta) \end{aligned}$$

Hence, if $\text{Tr}(\beta)$ is obtained, then $\text{Tr}(\beta^2)$ can also be obtained without calculation.

Since every element in $GF(2^m)$ can be represented by the elements which compose the basis, i.e., for $GF(2^m)$, and the

basis is $\{\alpha^0, \alpha^1, \alpha^2, \alpha^3, \alpha^4, \alpha^5, \alpha^6, \alpha^7\}$, then β can be written as

$$\beta = \beta_0 \alpha^0 + \beta_1 \alpha^1 + \beta_2 \alpha^2 + \beta_3 \alpha^3 + \beta_4 \alpha^4 + \beta_5 \alpha^5 + \beta_6 \alpha^6 + \beta_7 \alpha^7$$

From the properties of the trace, one has

$$\text{Tr}(\beta) = \beta_0 \text{Tr}(\alpha^0) + \beta_1 \text{Tr}(\alpha^1) + \beta_2 \text{Tr}(\alpha^2) + \beta_3 \text{Tr}(\alpha^3)$$

$$+ \beta_4 \text{Tr}(\alpha^4) + \beta_5 \text{Tr}(\alpha^5) + \beta_6 \text{Tr}(\alpha^6) + \beta_7 \text{Tr}(\alpha^7)$$

Hence it is only necessary to calculate trace values of $\alpha^0, \alpha^1, \alpha^2, \alpha^3, \alpha^4, \alpha^5, \alpha^6, \alpha^7$, the rest can be obtained easily once it is represented by the basis elements.

Soft-Decision Decoding of Some Block Codes

F. Pollara

Communications Systems Research Section

The performance of certain binary block codes with soft-decision decoding is evaluated by simulation. A construction is proposed to introduce memory on block codes, and simulation results are shown for a trellis code derived from the Nordstrom-Robinson code.

I. Introduction

Recent technological advances make soft-decision decoders, for moderate length block codes, a practical alternative to convolutionally coded systems. In particular, in order to improve the performance of current concatenated coding systems used in deep space communication, it is interesting to find the performance of some block codes, which might be used as inner codes with soft-decision decoders. Soft-decision decoding is mandatory for inner codes to avoid a penalty of approximately 2 dB incurred by hard quantization of channel outputs.

A well-known upper bound on the word error probability P_w of an (n, k) linear binary block code with soft-decision decoder is given by [1]

$$P_w \leq \frac{1}{2} \sum_{m=1}^{M-1} \operatorname{erfc}(\sqrt{R w_m E_b / N_0}) \quad (1)$$

where $M = 2^k$, $R = k/n$, E_b/N_0 is the bit signal-to-noise ratio, and w_m is the weight of the m th code word. This bound is tight for large E_b/N_0 , and the coding gain is proportional to the product $R d_{\min}$, where d_{\min} is the minimum distance of the block code.

Unfortunately, Eq. (1), which is based on the union bound, yields a very loose performance estimate at low E_b/N_0 . Therefore, each binary waveform is obtained by the optimum decision, maximum likelihood performance of some selected binary block codes.

II. Soft-Decision Decoding

We assume a channel with no output quantization. Therefore, each binary waveform is obtained by the optimum demodulator (a matched filter followed by a sampler), and each code word is represented by a sequence of n random variables.

Let E denote the energy of one of these n binary waveforms. Then each binary decision variable can be written as an irrelevant constant, as

$$r_i = \begin{cases} \sqrt{E} + n_i, & \text{if } i\text{th bit} = 1 \\ -\sqrt{E} + n_i, & \text{if } i\text{th bit} = 0 \end{cases}$$

and $i = 0, 1, \dots, n-1$, where the variables n_i are samples of additive white Gaussian noise (AWGN) with zero mean and variance $N_0/2$.

From knowledge of the $M = 2^k$ code words, and upon reception of the sequence r_0, r_1, \dots, r_{n-1} , the decoder computes M squared Euclidean distances

$$d_i^2 = \sum_{j=0}^{n-1} (r_j - \sqrt{E} x_{ij})^2, \quad i = 0, 1, \dots, M-1$$

where $x_{ij} = \pm 1$ corresponds to the j th bit of the i th code word. The decoded code word is the one corresponding to the minimum distance.

III. Simulation Results for Various Block Codes

A few rate $1/2$ binary block codes are considered:

- (a) The extended Golay (24, 12) code with $d_{\min} = 8$.
- (b) The first-order Reed-Muller (8, 4) code with $d_{\min} = 4$.
- (c) The nonlinear (16, 8) Nordstrom-Robinson (N-R) code [2] with $d_{\min} = 6$.

The word error probability P_w of these codes, obtained by simulation, is shown in Fig. 1, in the range of interest for use as inner codes. The results are also compared to the performance of the NASA (7, 1/2) convolutional code, assuming a word length of 8 bits. Care must be exercised in comparing the results, due to different word lengths.

Figure 2 shows the performance of the first-order Reed-Muller (16, 5) code and the (7, 1/3) convolutional code with 8-bit words. Figure 3 shows a similar comparison between the first-order Reed-Muller (32, 6) code and the (14, 1/4) and (14, 1/5) convolutional codes with 10-bit words.

The bit error probabilities of two of the codes considered in Fig. 1, the Golay (24, 12) and the NASA (7, 1/2) codes, are compared in Fig. 4.

In Fig. 1 it appears that the NASA (7, 1/2) code is still the best, except at very low E_b/N_0 , and that longer block codes, longer than those considered here, are necessary to compare favorably. Nevertheless, the simulation of the Nordstrom-Robinson code gave rise to a new approach.

Instead of pursuing the path of longer codes we devised some simple methods to introduce limited memory on a block code. Given that the Nordstrom-Robinson code is composed of a first-order Reed-Muller (16, 5) code and 7 of its cosets [3], we were able to construct a 4-state trellis code by properly assigning these 8 cosets to the branches of the state diagram in Fig. 5. This construction, described in detail and generalized in [4], yields in this case a 4-state (16, 7) code with free distance $d_f = 8$. Notice that even though the product ($Rd_f = 3.5$) for this code is lower than that for the Golay code ($Rd_f = 4$) and for the NASA (7, 1/2) code ($Rd_f = 5$), the code performs better at low E_b/N_0 , and has lower complexity than the Golay code. Figures 6 and 7 show simulation results for the word error probabilities P_w and bit error probabilities P_b respectively, for the three codes just mentioned.

References

- [1] J. G. Proakis, *Digital Communications*. New York: McGraw-Hill, 1983.
- [2] A. W. Nordstrom and J. P. Robinson, "An optimum nonlinear code," *Inform. and Control*, vol. 11, pp. 613-616, 1968.
- [3] F. J. MacWilliams and N. J. Sloane, *The Theory of Error-Correcting Codes*. New York: North-Holland, 1977.
- [4] F. Pollara, R. J. McEliece, and K. Abdel-Ghaffar, "Construction for finite-state codes," *TDA Progress Report 42-90*, vol. April-June 1987 (this issue), Jet Propulsion Laboratory, Pasadena, Calif., August 15, 1987.

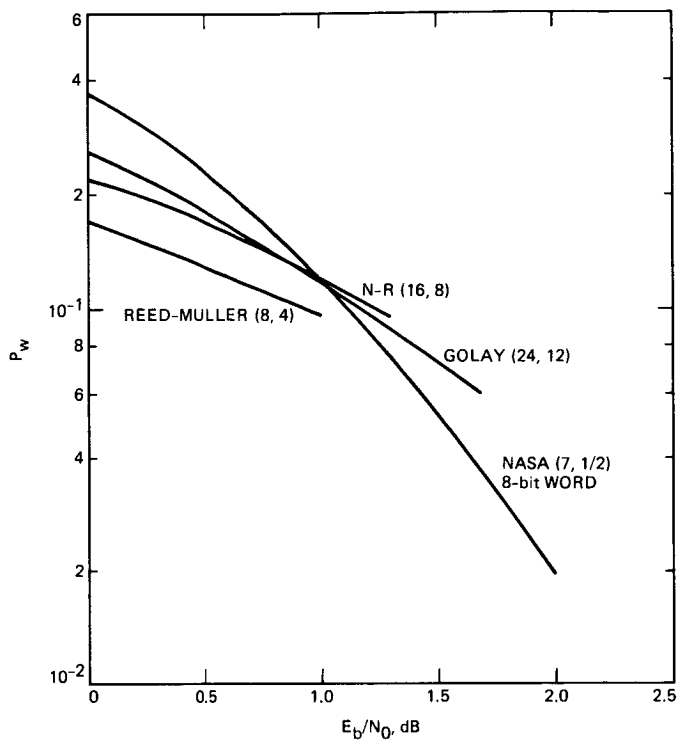


Fig. 1. Soft-decoding performance of three rate 1/2 block codes

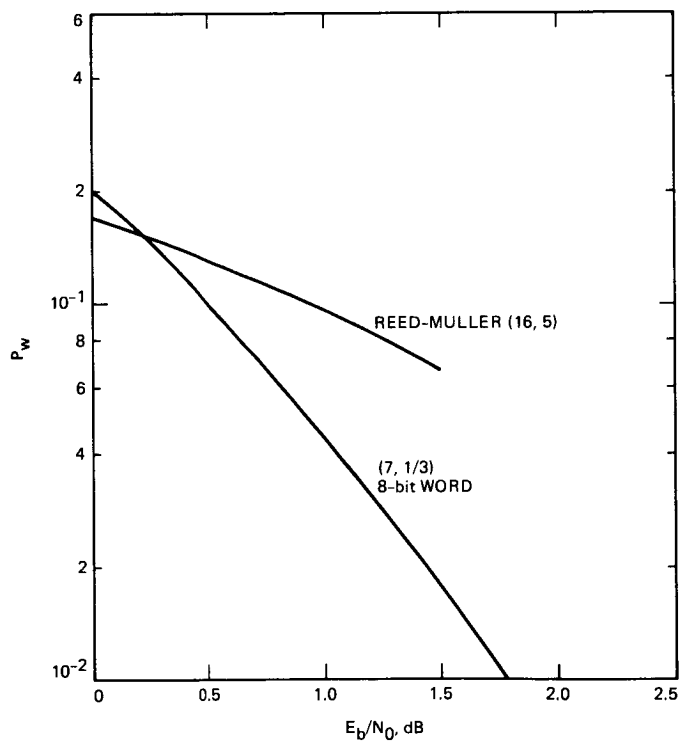


Fig. 2. Soft-decoding performance of first-order Reed-Muller (16, 5) code

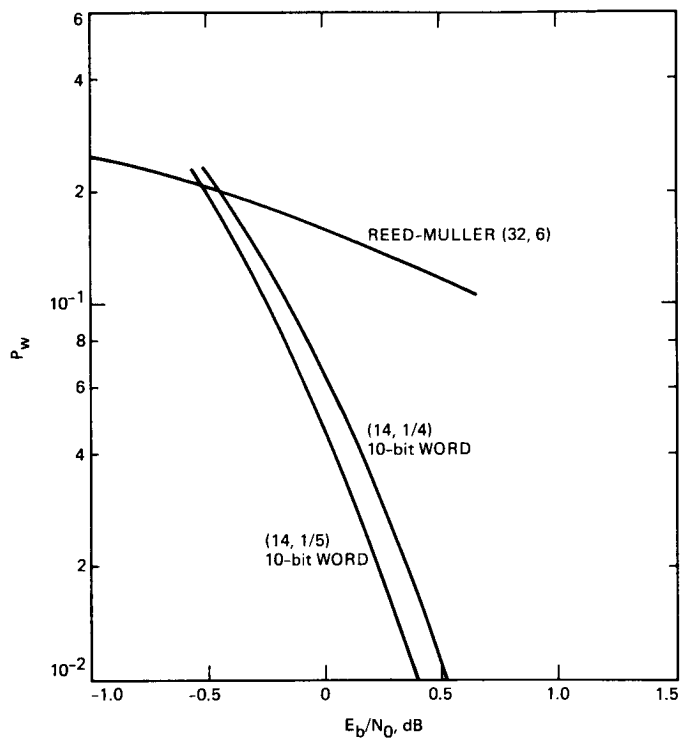


Fig. 3. Soft-decoding performance of first-order Reed-Muller (32, 6) code

ORIGINAL PAGE IS
OF POOR QUALITY

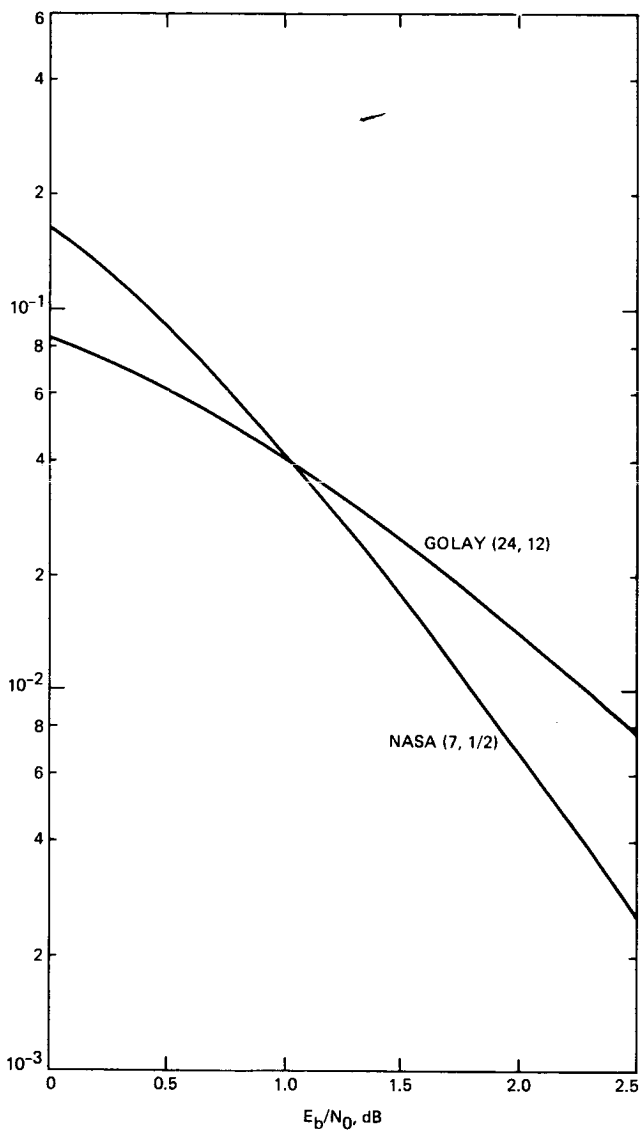


Fig. 4. Bit error probability of Golay code

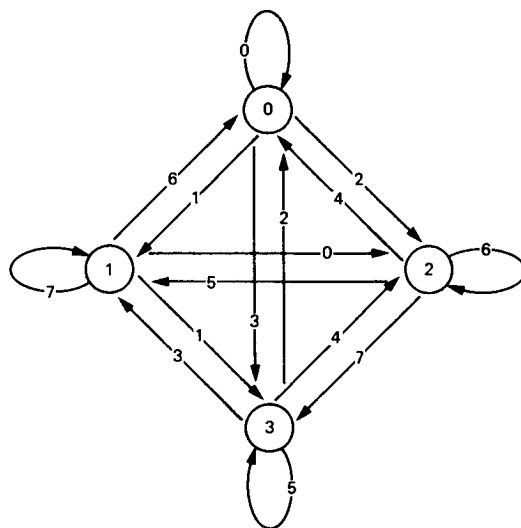


Fig. 5. Diagram of a 4-state trellis

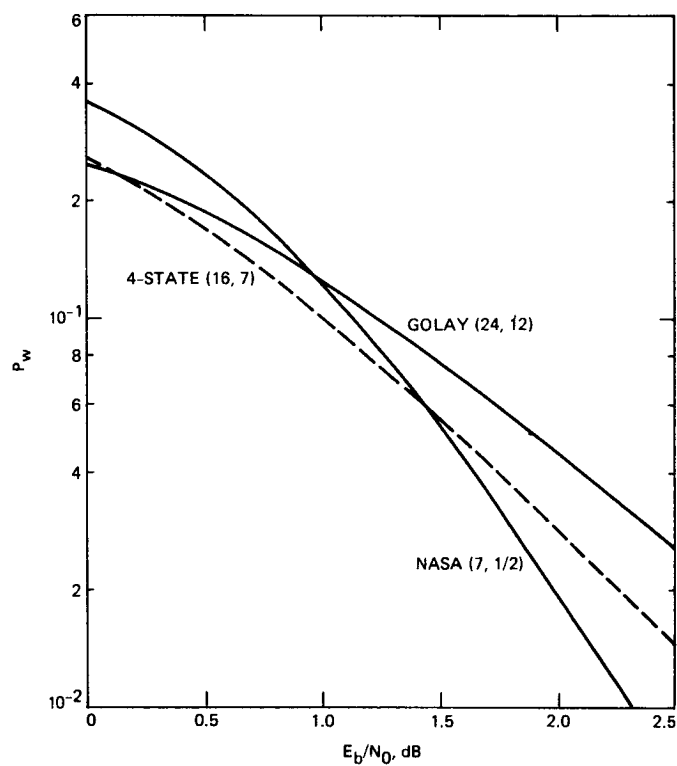


Fig. 6. The P_w of new code compared to Golay and (7, 1/2) codes

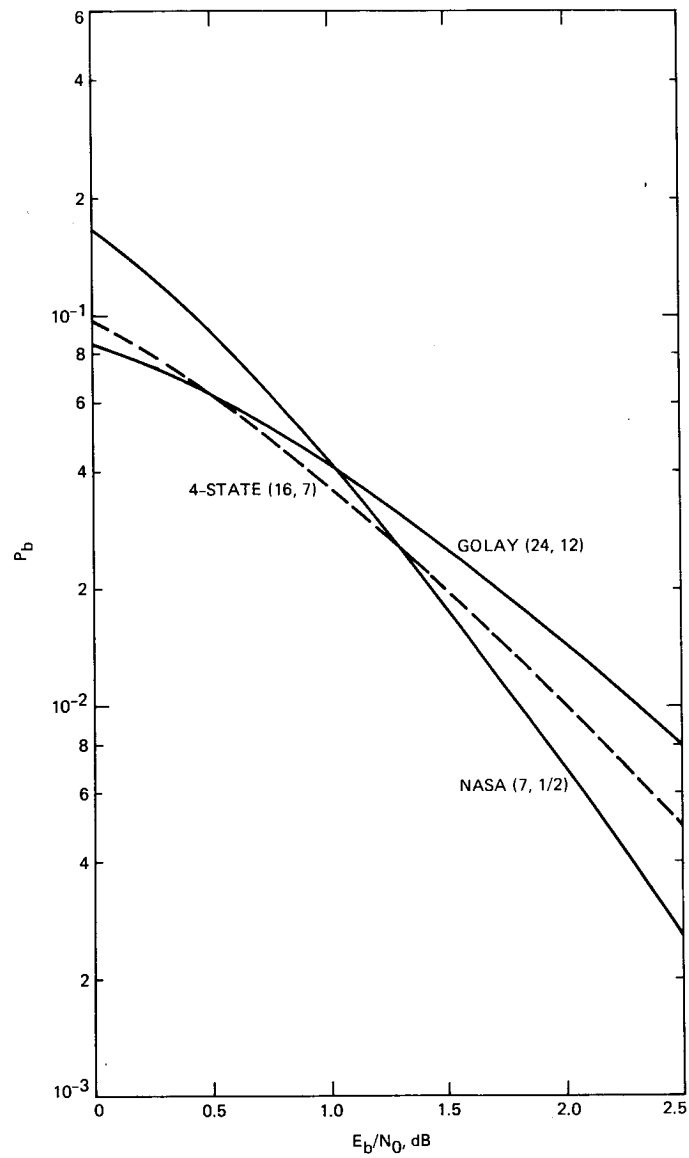


Fig. 7. The P_b of new code compared to Golay and (7, 1/2) codes

ORIGINAL PAGE IS
OF POOR QUALITY

Compound-Taper Feedhorn for the DSN 70-Meter Antennas

F. Manshadi and R. Hartop

Radio Frequency and Microwave Subsystems Section

A novel X-band feedhorn has been designed for the DSN 70-meter antennas. The feedhorn is a compound-taper structure consisting of a corrugated flared section (standard JPL 22-dB feedhorn) and a corrugated straight section (stovepipe). This feedhorn is designed to closely initiate the characteristics of the standard feedhorn, while providing the proper phase center location, without adding any significant loss to the system. The use of an existing feedhorn and the ease of manufacturing the stovepipe have resulted in major overall system cost savings.

I. Introduction

The new DSN 70-meter Cassegrainian antennas are a modification of the old 64-meter antennas at Goldstone, California, Canberra, Australia, and Madrid, Spain. The reflectors of these antennas are shaped to optimize theoretical patterns based on the characteristics of the JPL standard 22-dB feedhorn [1]. However, the standard feedhorn is much shorter than the dual hybrid mode feedhorn [2], [3] of the 64-meter antennas. Therefore, if the standard horn was to replace the dual mode feedhorn, the new phase center would fall far below the proper location considered in the design of the 70-meter antennas. Modifications would entail either elevating all the low noise equipment connected to the feedhorn (for which a rough cost estimate was around \$735K), or extending the length of the feed by adding a piece of circular waveguide to its input section, which would significantly add to the loss of the overall system. A third alternative was to design a new longer feedhorn that would exhibit the same characteristics of the JPL standard feedhorn. To avoid the cost of designing a

whole new feedhorn, it was decided to try a new idea (NASA Technical Brief NPO-16594) of using a straight corrugated section on top of the standard feedhorn in order to move the phase center to the designed location. If this compound-taper feedhorn did not degrade the characteristics of the standard horn significantly, it would be the least expensive solution (rough cost estimate of around \$225K), and would provide a technique for handling all such changes that will be required in the future.

A computer program that originally was developed for cylindrical corrugated waveguides was modified to make it applicable for the analysis of the flared and compound feedhorn. The results from this computer code were extensively validated by checking against measured data and data obtained from other programs used for analyzing corrugated horns. Then the compound feedhorn was designed and its characteristics were compared with the JPL standard feedhorn over a wide range of frequencies.

II. Design Approach

The geometries of the standard JPL feedhorn and the dual hybrid mode feedhorn are shown in Fig. 1 (a and b). The new 70-meter antennas are designed based on the assumption that the standard feedhorn is used in place of the dual hybrid mode feedhorn, but that the location of the phase center would be the same as that of the 64-meter antennas. This means that the new feedhorn must have its phase center at 39.679 inches above the reference plane, which is the plane of the old feedhorn input section. Therefore, if the standard feedhorn is used without any modification, its phase center would fall 16.51 inches below the designed location. In the new antennas, a 4.5-inch-long Phase Calibration Generator (PCG) coupler [4] is added in front of the feedhorn. This will push the phase center 4.5 inches higher and hence, as can be seen in Fig. 1(c), the desired phase center would fall 8.89 inches above the aperture of the standard feedhorn. We will show that the phase center of the standard horn can be moved to the desired point by adding an 8.4-inch stovepipe on the top.

The design tool used is the Scattering Matrix computer code¹ developed at JPL, which is based on a modal field-matching technique by James [5]. In this program, a corrugated structure is modeled as a large number of straight waveguide sections of different radii connected in series. In each section, the fields are expressed in terms of the normal modes of a circular waveguide and are matched at each discontinuity boundary. After the fields are evaluated, a scattering matrix is computed that relates the amplitudes of the reflected and transmitted modes of the structure to the amplitudes of the incident modes. This approach can be summarized by two matrix equations:

$$b_1 = [S_{11}] a_1$$

$$b_2 = [S_{21}] a_1$$

where a_1 contains the input mode amplitudes, b_1 the reflected modes, and b_2 the output modes. The matrices $[S_{11}]$ and $[S_{21}]$ are scattering matrices that are determined by the computer code. The program has been used extensively for corrugated cylindrical waveguides [6], [7], and its results have shown excellent agreement with experimental results and other theoretical methods.

One of the features of this computer code is that the number of modes used for expansion of the fields in each section is proportional to the radius of that section. For the analysis

of feedhorns where the radius of the corrugated sections increases from the input port to the aperture plane, this feature can cause the number of modes to become prohibitively large. Therefore, the program was modified to keep the number of modes between 20 and 30. This was tested and found to be a large enough number of modes for proper convergence of the solution for the standard feedhorn.

The standard JPL feedhorn is made of corrugated sections that are not perpendicular to the axis of the feedhorn and therefore cannot be treated as pieces of cylindrical waveguide. These corrugations were approximated by cylindrical sections (see Fig. 2) that are suitable for the Scattering Matrix program. This new approximate geometry was then used in the computer code, and the far-field patterns of the feedhorn were computed at 8.45 GHz (the center frequency for the receive band). These far-field patterns were compared with the measured patterns and computed patterns using an older JPL computer code called the Hybridhorn program. This program was one of the tools used for design of the JPL standard feedhorn. Figure 3 shows the expanded E-plane pattern of standard feedhorn obtained from the two computer codes and the measurements. As can be seen, there is good agreement between all results. In particular, it seems that the data from the Scattering Matrix program are closer to the measured data than the results from the Hybridhorn program.

To move the phase center of the feedhorn, a section of stovepipe was added to the standard feedhorn. The stovepipe consisted of cylindrical sections with the same corrugation dimensions of the standard horn as shown in Fig. 4. To find the proper length, several lengths of stovepipe section were added to the standard feedhorn, and the variation of the overall phase center location was computed and plotted vs the length of the stovepipe at 8.45 GHz. Figure 5 shows this variation for two values of corrugation depth: one at 0.434 inches, which is the depth of the standard horn corrugation, and the other at 0.350 inches. These plots show the phase center oscillating back and forth about the aperture plane, and that it is possible to select either a positive or a negative location with respect to the aperture. The phase center location for the standard horn alone and with two stovepipes, one 11.76-inches long with a 0.434-inch corrugation depth and the other 5.59-inches long with a 0.350-inch corrugation depth, were measured and are shown by solid circles on the plots of Fig. 5. To find the proper length for the stovepipe that moves the phase center 8.89 inches above the aperture of the standard feedhorn, the data of Fig. 5 was translated to show the phase center location in reference to the aperture of the standard feedhorn. This data is plotted in Fig. 6 vs the length of the stovepipe. It can be seen that for an 8.89-inch movement, the proper length for the stovepipe is about 8.6 inches. Since each cylindrical section in the stovepipe is 0.14 inches long,

¹D. J. Hoppe, "Scattering Matrix Program for Circular Waveguide Junctions," JPL Interoffice Memorandum 3335-84-071 (internal document), Jet Propulsion Laboratory, Pasadena, Calif., Dec. 5, 1984.

ORIGINAL PAGE IS OF POOR QUALITY

a 62-section stovepipe that is 8.68-inches long was required to approximately yield the proper phase center location.

A computer analysis of the compound-taper feedhorn with the 8.68-inch stovepipe showed minor degradation in the cross-polarization and sidelobe levels and about 0.5-dB higher gain. The higher gain, due to the narrower beam generated by the stovepipe, resulted in a lower illumination efficiency of the feedhorn. To remedy this problem, it was decided to reduce the size of the aperture of the stovepipe by reducing its radius. However, changing the radius caused a shift in the phase center. Therefore, the Scattering Matrix program was used and the compound-taper feed was analyzed for different values of radius and length of the stovepipe. The optimum stovepipe, with approximately the same gain and efficiency of the standard feedhorn, was found to be one with a radius of 3.24 inches and a length of 8.4-inches (60 cylindrical sections). The phase center of this feedhorn was computed to be located 0.6 inches in front of the stovepipe aperture. The new compound taper feedhorn had higher sidelobe and cross-polarization levels, but showed higher efficiency, flatter phase pattern, and a more stable phase center. Figure 7 shows one of the compound-taper feedhorns fabricated for the 70-meter antennas.² The 8.45-GHz *E*- and *H*-plane patterns of the compound-taper feedhorn are compared with the standard JPL feedhorn in Figs. 8 and 9. Excellent agreement can be seen for scan angles less than 16 degrees, which is the half-angle subtended by the 70-m antenna subreflector.

III. Analysis

The compound-taper feedhorn and the JPL standard feedhorn have been extensively compared and analyzed by the Scattering Matrix program for several frequencies between 8.2 and 8.7 GHz. Most of the theoretical computations were checked with antenna range measurements, and good agreement was established for all cases.

Table 1 shows the variation of the phase center location of the compound feed and the standard feed, with respect to

their aperture plane, as a function of frequency. As can be seen, the phase center of the new feedhorn is more stable across the frequency range.

Table 2 shows the gain of the two feedhorns as a function of frequency. The gain variations are very similar, showing a slight increase as the frequency is increased, which is expected since the aperture size becomes effectively larger.

The sidelobe and cross-polarization levels for the two feedhorns are shown in Tables 3 and 4, respectively, as a function of frequency. These levels are both higher for the compound feedhorn, which in general is not desirable. However, these sidelobe and cross-polarization levels not only have peaks at angles corresponding to the subreflector's edge, but their absolute values are far below the co-polarized fields. Consequently, the slightly higher sidelobe or cross-polarization levels do not significantly degrade the performance of the overall antenna.

Table 5 shows the overall efficiency of the two feedhorns, over 16 degrees, as a function of frequency. It can be seen that the compound feedhorn and the standard feedhorn are almost equal in efficiency. The efficiency of the compound feed drops slightly at the upper edge of the frequency band due to higher sidelobe and cross-polarization levels.

IV. Summary and Conclusions

A novel technique was used to design a compound-taper feedhorn to replace the dual hybrid mode horn of the 64-meter antennas. The new feedhorn, designed for the 70-meter upgrade of the 64-meter antennas, closely duplicates the characteristics of the JPL standard feedhorn, upon which the shape of the 70-meter antennas are based. The compound feedhorn introduces a phase center in front of its aperture, but in the required location with respect to the subreflector. The new feedhorn has been checked extensively by available computer codes and antenna range measurements over a large band of frequencies. Excellent agreement between theoretical and measured results was established, and the feedhorn was shown to perform as well as the standard feedhorn for all practical purposes. The implementation by this technique, rather than by relocating the traveling wave masers, has resulted in a cost savings to the DSN of one-half million dollars.

²The complete detail geometry of this feedhorn is shown in JPL Drawing 9490170 (internal document), Jet Propulsion Laboratory, Pasadena, Calif.

Acknowledgment

The authors would like to thank W. Folwell and H. Reilly for antenna range measurements, and D. Hoppe for providing the Scattering Matrix program.

References

- [1] R. Hartop, "X-band antenna feedcone assembly," *JPL Technical Report 32-1526*, vol. XIX, Jet Propulsion Laboratory, Pasadena, Calif., Nov. 1973.
- [2] R. Hartop, "New X-band antenna feeds for the DSN 64-meter stations," *DSN Progress Report 42-52*, pp. 71-74, Jet Propulsion Laboratory, Pasadena, Calif., May 1979.
- [3] A. J. Frieley, "Radio frequency performance of DSS 14 64-m antenna at X-band using a dual hybrid mode feed," *DSN Progress Report 42-53*, pp. 132-140, Jet Propulsion Laboratory, Pasadena, Calif., July, 1979.
- [4] P. H. Stanton, "X-band phase calibration generator coupler," *TDA Progress Report 42-90*, vol. April-June 1987, Jet Propulsion Laboratory, Pasadena, Calif., August 15, 1987.
- [5] G. L. James, "Analysis and design of TE_{11} -to- HE_{11} corrugated cylindrical waveguide mode converters," *IEEE Trans. MTT*, vol. 29, No. 10, pp. 1059-1066, Oct. 1981.
- [6] D. J. Hoppe, "Propagation and radiation characteristics of a multimode waveguide feedhorn," *TDA Progress Report 42-82*, vol. April-June 1985, pp. 57-67, Jet Propulsion Laboratory, Pasadena, Calif., August 15, 1985.
- [7] D. Hoppe, W. Imbriale, and A. Bhanji, "The effects of mode impurity on Ka-band system performance," *TDA Progress Report 42-80*, vol. October-December 1984, pp. 12-23, Jet Propulsion Laboratory, Pasadena, Calif., February 15, 1985.

Table 1. Phase center location in reference to the aperture for the standard and compound-tapered feedhorns as a function of frequency^a

Frequency, GHz	Phase Center Location, in.	
	Standard Feedhorn	Compound-Taper Feedhorn
8.2	+2.20	-0.62
8.3	+2.30	-0.59
8.45	+2.52	-0.61
8.6	+2.70	-0.56
8.7	+2.83	-0.52

^aPositive values are for the phase center below the aperture, while negative values are for the phase center above the aperture.

Table 2. Gain of the standard and the compound-taper feedhorns as a function of frequency

Frequency, GHz	Gain, dB	
	Standard Feedhorn	Compound-Taper Feedhorn
8.2	22.2	22.0
8.3	22.3	22.1
8.45	22.5	22.3
8.6	22.6	22.5
8.7	22.7	22.6

Table 3. Sidelobe level of the standard and compound-taper feedhorns as a function of frequency

Frequency, GHz	Sidelobe Level, dB	
	Standard Feedhorn	Compound-Taper Feedhorn
8.2	-25	-22
8.3	-25	-22
8.45	-25	-22
8.6	-25	-22
8.7	-25	-22

Table 4. Cross-polarization levels for the standard and compound feedhorns as a function of frequency

Frequency, GHz	Cross-Polarization Level, dB	
	Standard Feedhorn	Compound-Taper Feedhorn
8.2	-35.0	-33.5
8.3	-34.5	-33.0
8.45	-34.0	-32.0
8.6	-35.0	-32.0
8.7	-34.0	-31.5

Table 5. Overall efficiency of the standard and compound-taper feedhorns as a function of frequency

Frequency, GHz	Overall Efficiency, %	
	Standard Feedhorn	Compound-Taper Feedhorn
8.2	76.4	76.8
8.3	75.8	76.0
8.45	74.4	74.4
8.6	73.2	72.8
8.7	72.3	71.6

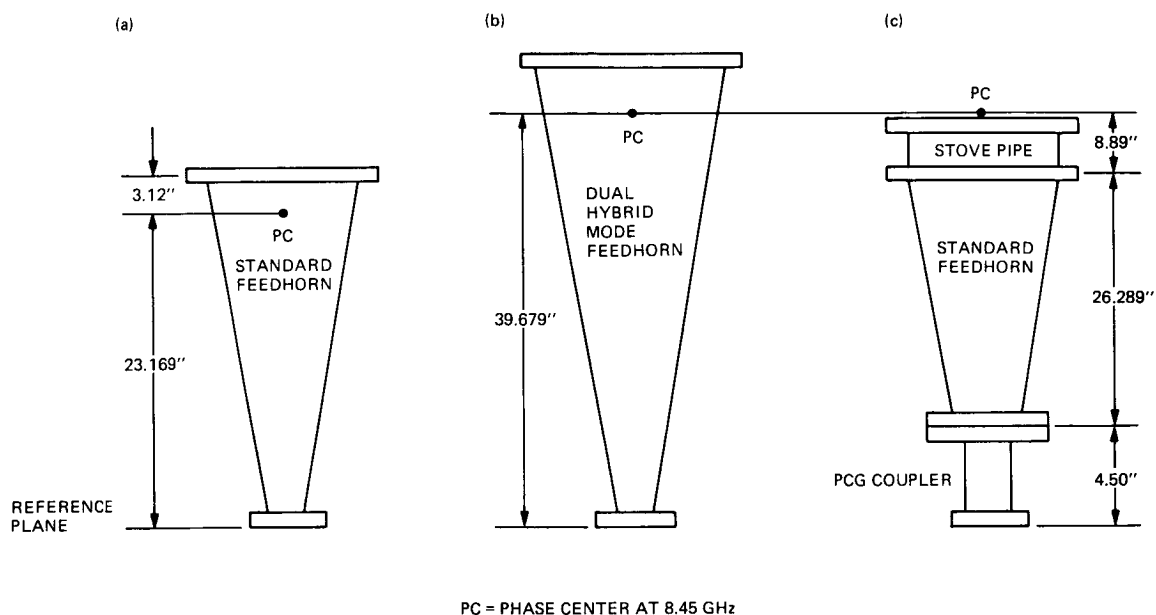


Fig. 1. Comparison of feedhorns and the location of their phase centers: (a) standard JPL 22-dB feedhorn, (b) dual hybrid feedhorn of 64-m antennas, (c) compound-taper feedhorn

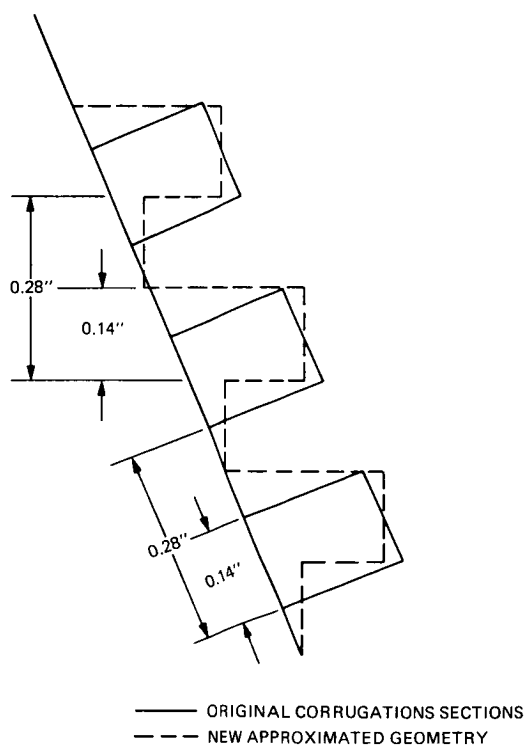


Fig. 2. Approximation of the standard JPL feedhorn corrugations by cylindrical sections

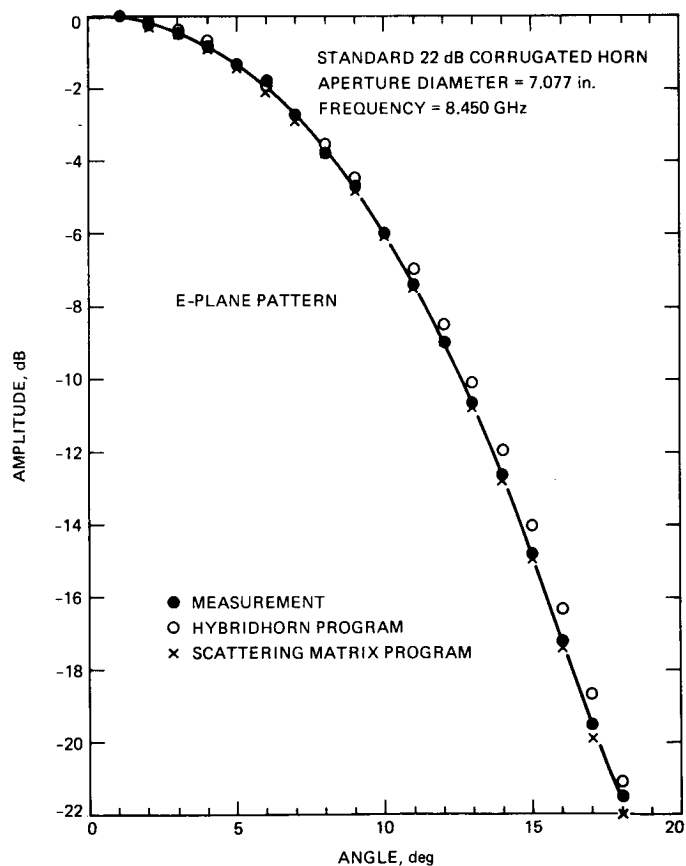


Fig. 3. Expanded E-plane pattern of the JPL standard feedhorn

ORIGINAL PAGE IS
OF POOR QUALITY

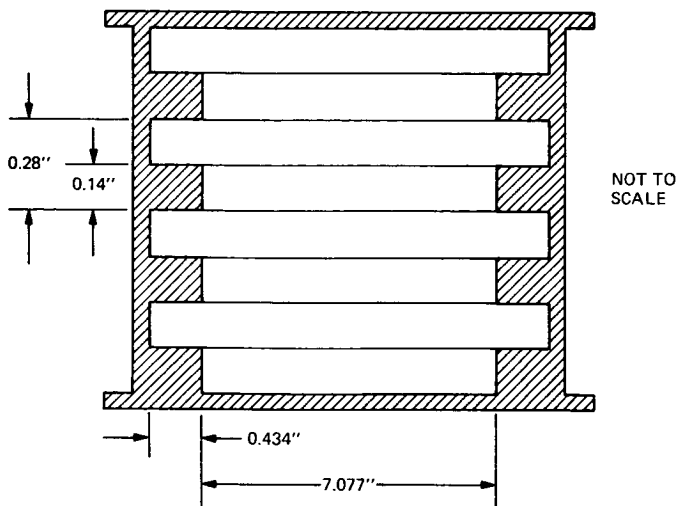


Fig. 4. Cross-section geometry of an eight-section stovepipe with the same corrugation dimensions and radius as the standard feedhorn

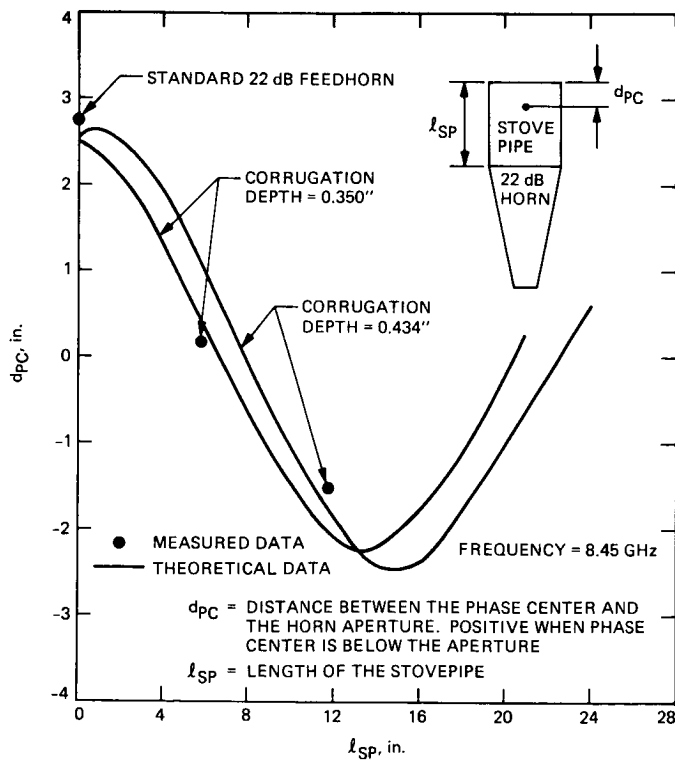


Fig. 5. Variation of phase center location as a function of the stovepipe in a compound feedhorn

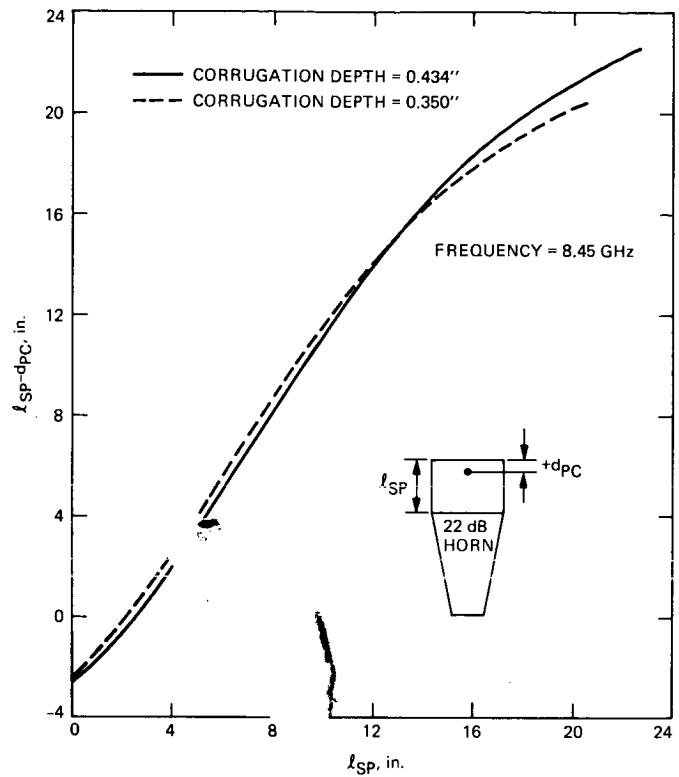


Fig. 6. Phase center location of the compound feedhorn with respect to the standard feedhorn aperture plane

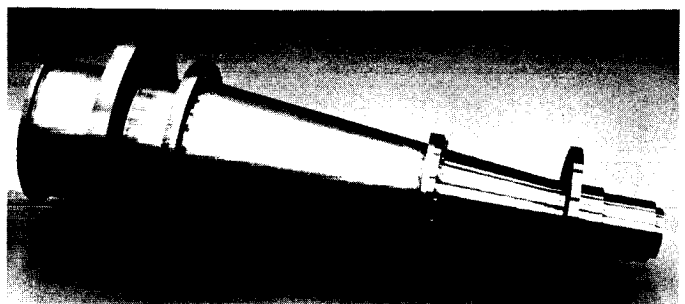


Fig. 7. Compound-taper feedhorn for DSN 70-m antennas

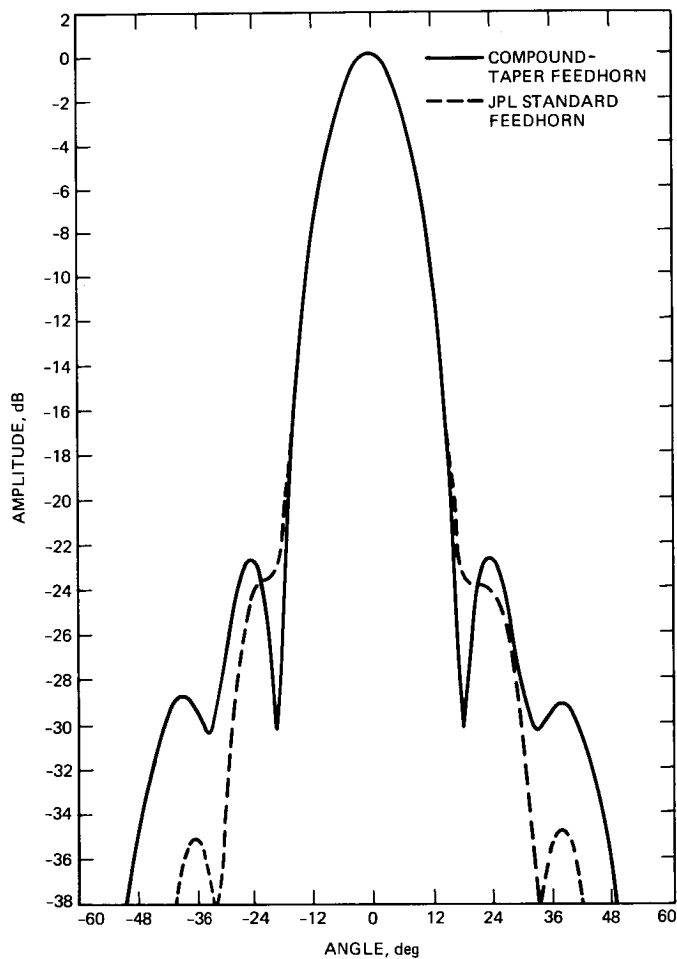


Fig. 8. The *E*-plane patterns of the JPL standard and the compound-taper feedhorns at 8.45 GHz

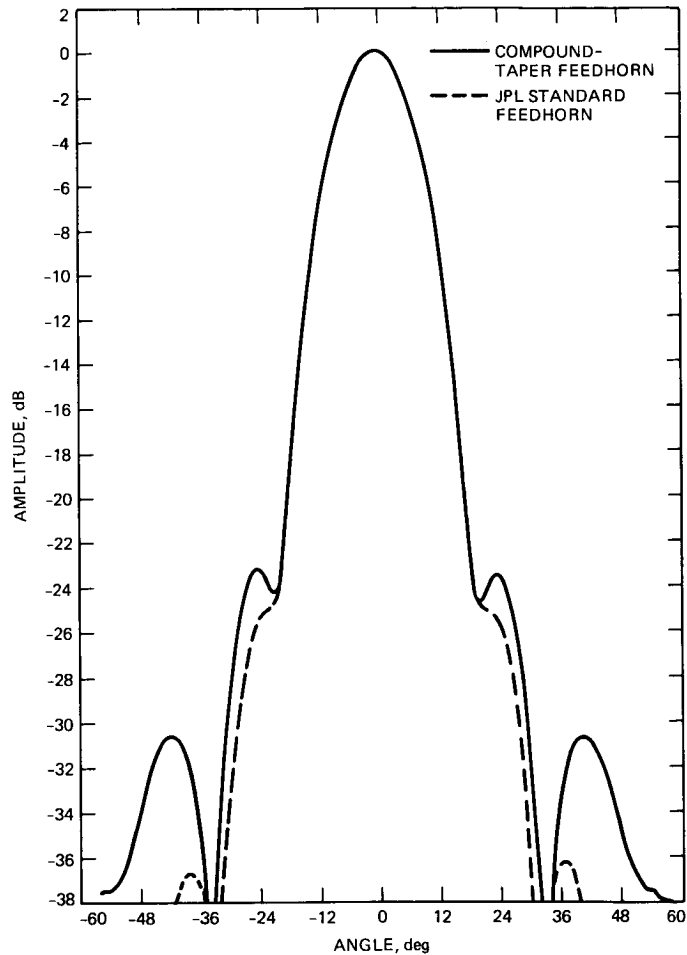


Fig. 9. The *H*-plane patterns of the JPL standard and the compound-taper feedhorns at 8.45 GHz

X-Band Phase Calibration Generator Coupler

P. H. Stanton

Radio Frequency and Microwave Subsystems Section

A new type of phase calibration generator (PCG) coupler has been developed for the DSN X-band antennas that can be located directly behind the feedhorn. The advantage of this is that the calibration includes more of the system. The disadvantage is that the overmoded waveguide at this location must be coupled in a mode-selective manner. Low-power and high-power PCG couplers have been successfully produced, and the RF test results from a PCG coupler are given in this article.

I. Introduction

A phase calibration generator (PCG) coupler was developed for the X-band 34-m high efficiency and the new 70-m antennas. The location selected for this coupler is directly behind the feedhorn, to include as much of the transmission line in the phase calibration path as practical. Two disadvantages of this location are: (1) little available room, requiring compact packaging of the PCG coupler, and (2) an oversized circular waveguide capable of supporting multiple waveguide modes, requiring a design that couples only the desired waveguide mode efficiently. The principal RF requirements are listed in Table 1. Note that the requirement for directivity is not high because the signal going to the feedhorn must be reflected from the subreflector and recaptured by the feedhorn (over 20-dB attenuation) before it can interfere with the desired signal.

II. Design

The Bethe hole coupling technique [1] offered the possibility of minimizing the coupler length while providing moderate directivity and control of unwanted waveguide modes (TM_{01} and TE_{21}). The Bethe coupling technique controls the coupled amplitude of the E - and H -plane fields so that they cancel in the direction of the isolated port and add in the direction of the coupled port (analysis of this coupler is given in [2]). This type of coupling is typically accomplished through a single electrically small (\ll wavelength) aperture between two dominant mode waveguides. For coupling to the TE_{11} mode, the overmoded circular waveguide of these PCG couplers requires a pair of coupling apertures symmetric about the circular waveguide. The E - and H -plane fields coupled to this circular waveguide should be parallel and perpendicular, respectively, to a

plane that includes the waveguide axis and the centers of the two apertures. Figure 1 shows a simplified cutaway diagram of this coupler. A power splitter divides the signal from the phase calibration generator into equal amplitudes. These signals travel along a pair of dominant mode rectangular waveguides (WR 90) to the coupling apertures in the center of the waveguide broadwall, located on either side of the circular waveguide (WC 137). At these apertures, a part of the calibration signal (in this case, <-37 dB) is coupled into the circular waveguide in the direction of the receivers, and a part is coupled in the direction of the horn (in this case, <-58 dB).

The coupling magnitude was controlled by changing the size of the coupling apertures. The coupling aperture shape and the width of the rectangular waveguide in the proximity of the coupling aperture were used to control the directivity. The aperture is in the form of a slot with semicircular ends. Its long dimension is parallel to the axis of the circular waveguide.

The X-band phase calibration coupler (see Fig. 2) has been produced in two configurations. The first was for the 70-m antenna and is a low-power unit. The second was for the 34-m high efficiency antenna and must function properly during 20-kW transmission conditions. This required higher power coupler loads, water cooling, and the addition of a high-pass

(transmitter reject) waveguide filter to the input of the couplers.

III. Results

A high-power model of the PCG coupler was measured and found to meet the requirements specified in Table 1. The result of these measurements are included in Figs. 3 through 7.

Figure 3 shows the measured coupled amplitude of a production high-power PCG coupler from 7.1 to 8.9 GHz. The input high-pass filter attenuates the 20-kW (+73 dBm) transmitter power to a level of approximately 2 microwatts (-27 dBm), which is well under the 0.1-mW (-10 dBm) limit for normal operation. The same curve is shown in Fig. 4, except that it is expanded to show the details in the calibration band of 7.9 to 8.9 GHz. The coupling measures -38.5 dB at 7.9 GHz and increases to -37.5 dB at 8.9 GHz. Taking into account that half of this power goes to each orthogonal arm of the orthomode junction, the coupling to each receiver is -41.5 dB at 7.9 GHz and -40.5 dB at 8.9 GHz, which is within the required -40 dB to -45 dB range. The group delay (Fig. 5) in the receive range shows a smooth decreasing value from 5.6 ns at 7.9 GHz to 4.2 ns at 8.9 GHz. The directivity, shown in Fig. 6, is greater than 22 dB across the receive band. Figure 7 shows the measured VSWR at the coupler input with a peak value of 1.26:1.

References

- [1] H. A. Bethe, "Theory of Diffraction by Small Holes," *Physical Review*, vol. 66, pp. 163-182, 1944.
- [2] R. E. Collin, *Foundations for Microwave Engineering*. New York: McGraw-Hill, 1966.

ORIGINAL PAGE IS
OF POOR QUALITY

Table 1. X-Band PCG coupler requirements

Parameter	Requirement
Coupling frequency range	7.9 to 8.9 GHz
Coupling	40 to 45 dB
Coupled input VSWR	< 1.28:1
Max. coupled transmitter power for normal operation	-10 dBm
Max. coupled transmitter power for no damage	+ 10 dBm
Length	4.5 inches
Directivity	> 14 dB

ORIGINAL PAGE IS
OF POOR QUALITY

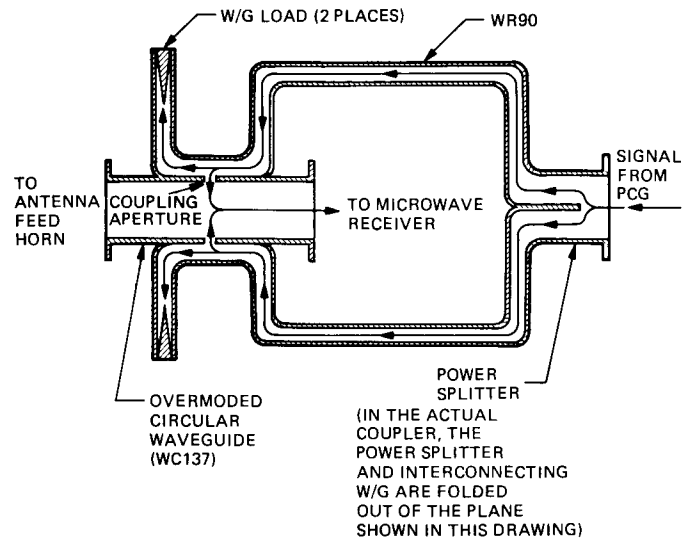


Fig. 1. Cutaway diagram of PCG coupler

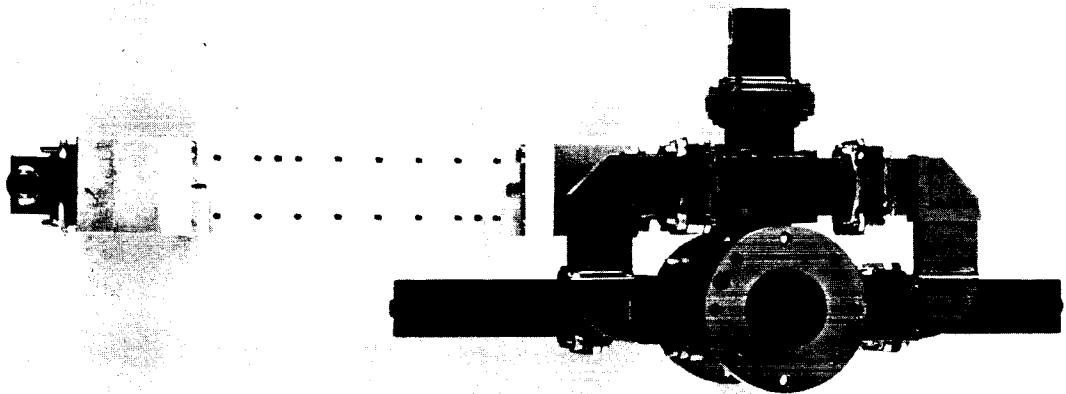


Fig. 2. PCG coupler engineering model

ORIGINAL PAGE IS
OF POOR QUALITY

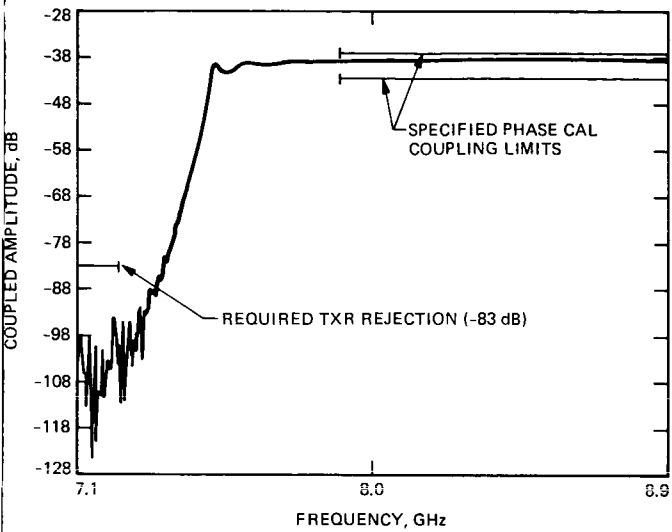


Fig. 3. Coupled amplitude

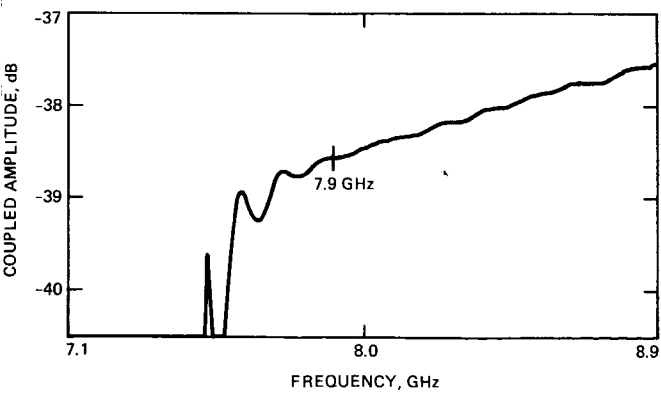


Fig. 4. Coupled amplitude (expanded amplitude scale)

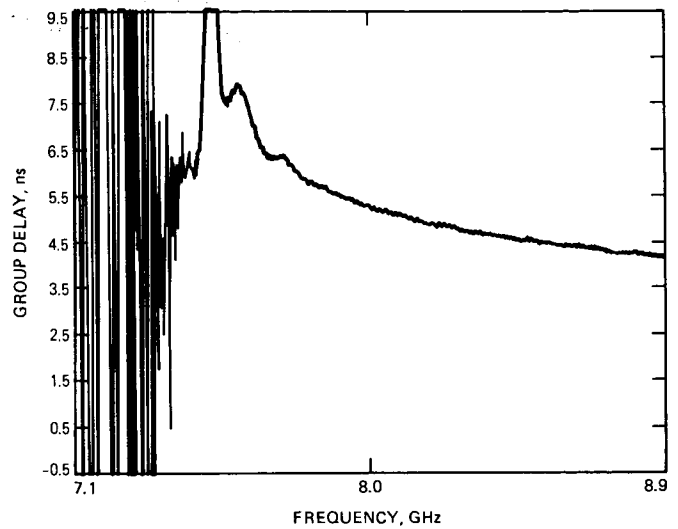


Fig. 5. Coupled group delay

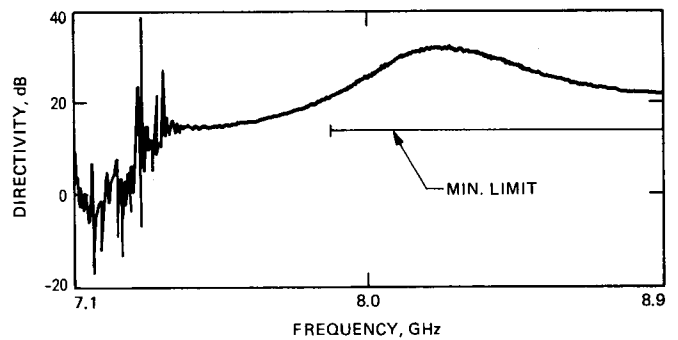


Fig. 6. PCG coupler directivity

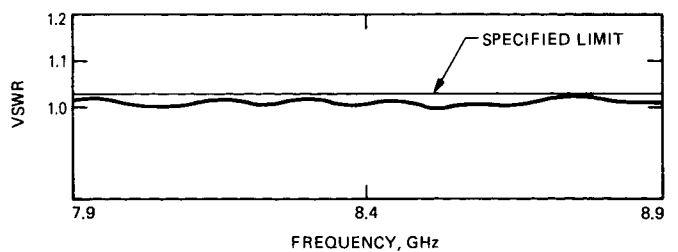


Fig. 7. PCG coupler input VSWR

ORIGINAL PAGE IS
OF POOR QUALITY

State Transition Storyboards: A Tool for Designing the Goldstone Solar System Radar Data Acquisition System User Interface Software

S. D. Howard

Communications Systems Research Section

Effective user interface design in software systems is a complex task that often takes place without adequate modeling tools. By combining state transition diagrams and the storyboard technique of filmmakers, State Transition Storyboards were developed to provide a detailed modeling technique for the Goldstone Solar System Radar Data Acquisition System human-machine interface. Illustrations are included with a description of the modeling technique.

I. Introduction

User interface design presents a unique set of problems to software engineering. After functional specifications have determined which parameters are to be available to the operator, human-machine interface design becomes basically a problem of presentation: having the right information, in the right place, at the right time. The presentation is a communication, usually complex, carefully sequenced, and often highly visual in nature.

This would seem to imply that the user interface should be the easiest part of a software system design to present, to communicate, to previsualize, and to specify. But this has not been the case. The design of the interface is often left either to last minute improvisation or to full prototyping. The prototyping strategy uses the interface itself as a model. In proto-

typing, there is no abstraction; instead, there are cycles of modifications to the full product.

These approaches fail to consider two techniques that have been very useful in software development—step-by-step problem decomposition and the development of an external graphical representation that abstracts important aspects of the system. Stepwise refinement and top-down design [2] are examples of problem decomposition and data flow diagrams [3] are examples of graphical abstractions.

External representations are valuable because they make design reviews (walk-throughs) possible. Members of the design team can then examine and comment on the design, adding new ideas and directing attention to oversights before specifications are written and the design is committed to code.

ORIGINAL PAGE IS OF POOR QUALITY

In most instances, a diagram is more easily modified than a software prototype. The model also forms a record of the evolution of the design as problem decomposition proceeds from a high-level sketch to a final detailed specification.

Problem decomposition in the user interface has a different character than successive refinement in structured programming. For example, if the user interface is indeed another type of human communication, the problem will decompose into the familiar phases of communicating ideas: every interface would be expected to comprise an introduction or orientation, a central functional unit with no more than seven major phases [4], and a conclusion or orderly exit. The orientation might decompose into an introduction screen and a set of "help" screens. Then the general content of each screen can be sketched and later refined to specify string lengths and locations.

State Transition Storyboards were created to provide the Goldstone Solar System Radar (GSSR) Data Acquisition software design team with a modeling tool for developing and specifying the human-machine interface. The technique comprises two ideas. The Yourdon methodology [3] recommends thinking of the user interface as a finite state machine; state transition diagrams describe transitions triggered by user actions. Software designer Paul Heckel [5] describes the creation of a user interface as a communications craft and recommends the storyboarding technique of filmmaking for describing the appearance of the user interface in a sequential manner. Combining these ideas allows a graphical abstraction of the interface presentation as it responds to the operator.

II. Description

State Transition Storyboards are directed graphs composed of nodes, edges, and edge labels. The shape and content of a

node abstracts the screen presentation. Edges indicate the allowable transitions that may take place from that state to other states. Edge labels carry two types of information: (1) the action that causes a transition is summarized above a horizontal line and (2) the steps that effect the transition can be listed below the line. These diagrams are visual in nature, like much of the user interface itself. Figure 1 is given as an illustration.

Transitions can return immediately to the same state. For example, pressing an arrow key on a terminal keyboard might cause a "control G" (bell) and a return to the same screen state. Symbols or icons can be used to represent states that are accessed by many transitions and are therefore graphically difficult to connect. As an example, "help" or information screens are usually accessible from many states. A small labeled screen adjacent to a normal node is used in the manner of an "off-page connector" to indicate that transitions can occur between these states. Figure 2 illustrates these situations.

III. Summary

State Transition Storyboards allow a software designer to sketch and revise interface design ideas quickly to the level of specificity required by the design at that moment. Then, given any state as a precondition and a user action or system update, the postcondition can be determined immediately. Information contained in these diagrams can be easily converted to state transition tables in software for accurate final prototyping. The GSSR Data Acquisition software team is currently exploring extensions to this idea. A draft version of the Goldstone Solar System Radar Data Acquisition System User Interface plans, using the State Transition Storyboard technique, is given in Fig. 3. (The GSSR Data Acquisition System is described in *TDA Progress Report 42-77* [1].)

References

- [1] L. J. Deutsch, R. F. Jurgens, and S. S. Brokl, "Goldstone R/D High Speed Data Acquisition System," *TDA Progress Report 42-77*, vol. January-March 1984, pp. 87-96, Jet Propulsion Laboratory, Pasadena, California, May 15, 1984.
- [2] S. Alagic and M. A. Arbib, *The Design of Well-Structured and Correct Programs*. New York, New York: Springer-Verlag, 1978.
- [3] P. T. Ward and S. J. Mellor, *Structured Development for Real-Time Systems*. New York, New York: Yourdon Press, 1985.
- [4] G. A. Miller, "The Magical Number Seven Plus or Minus Two: Some Limits on Our Capacity for Processing Information," *Psychological Review*, vol. 63, no. 2, pp. 81-97, 1956.
- [5] P. Heckel, *The Elements of Friendly Software Design*. New York, New York: Warner Books, Inc., 1984.

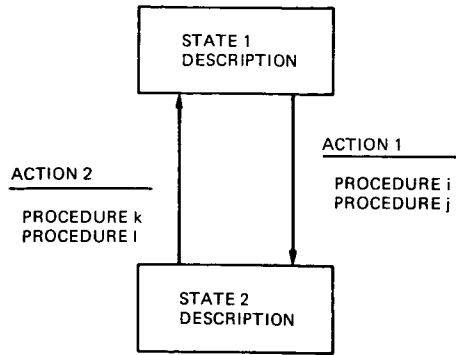


Fig. 1. Basic diagram elements:
edges, nodes, and edge labels

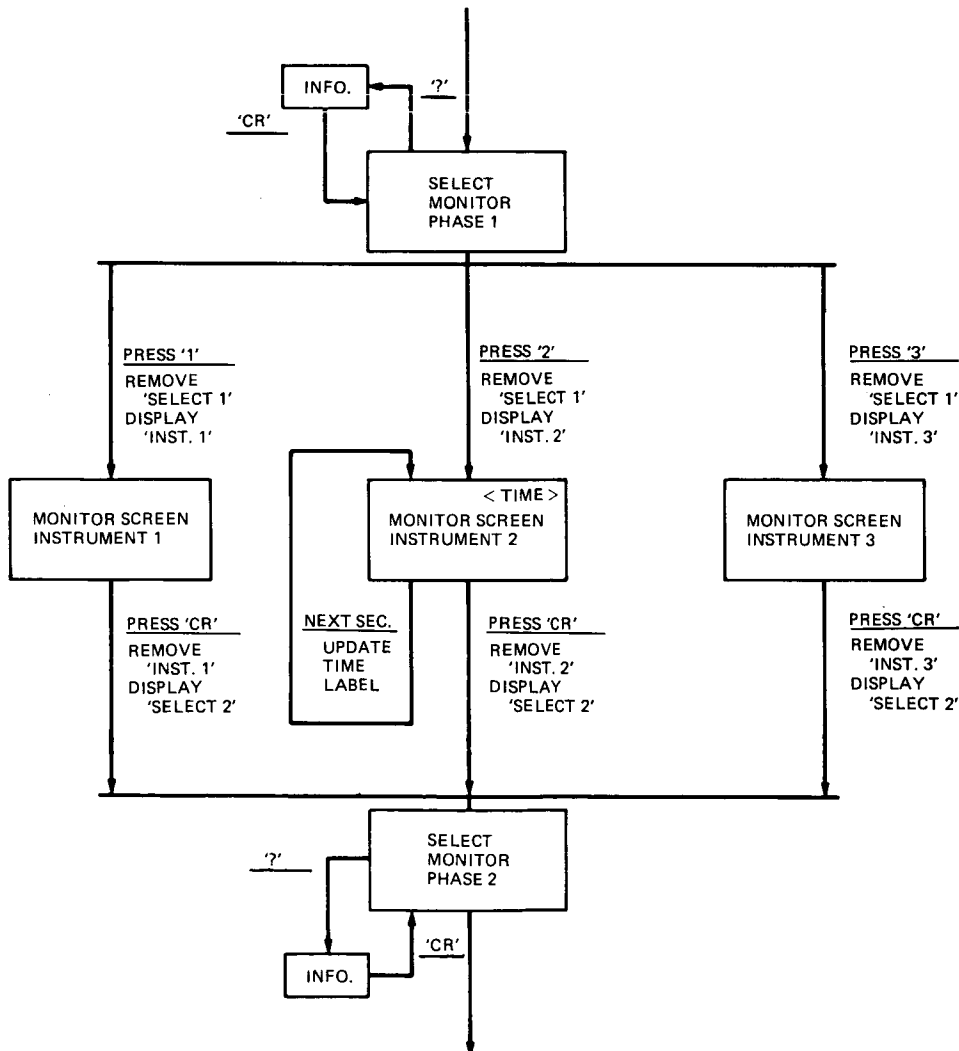


Fig. 2. Special diagramming situations

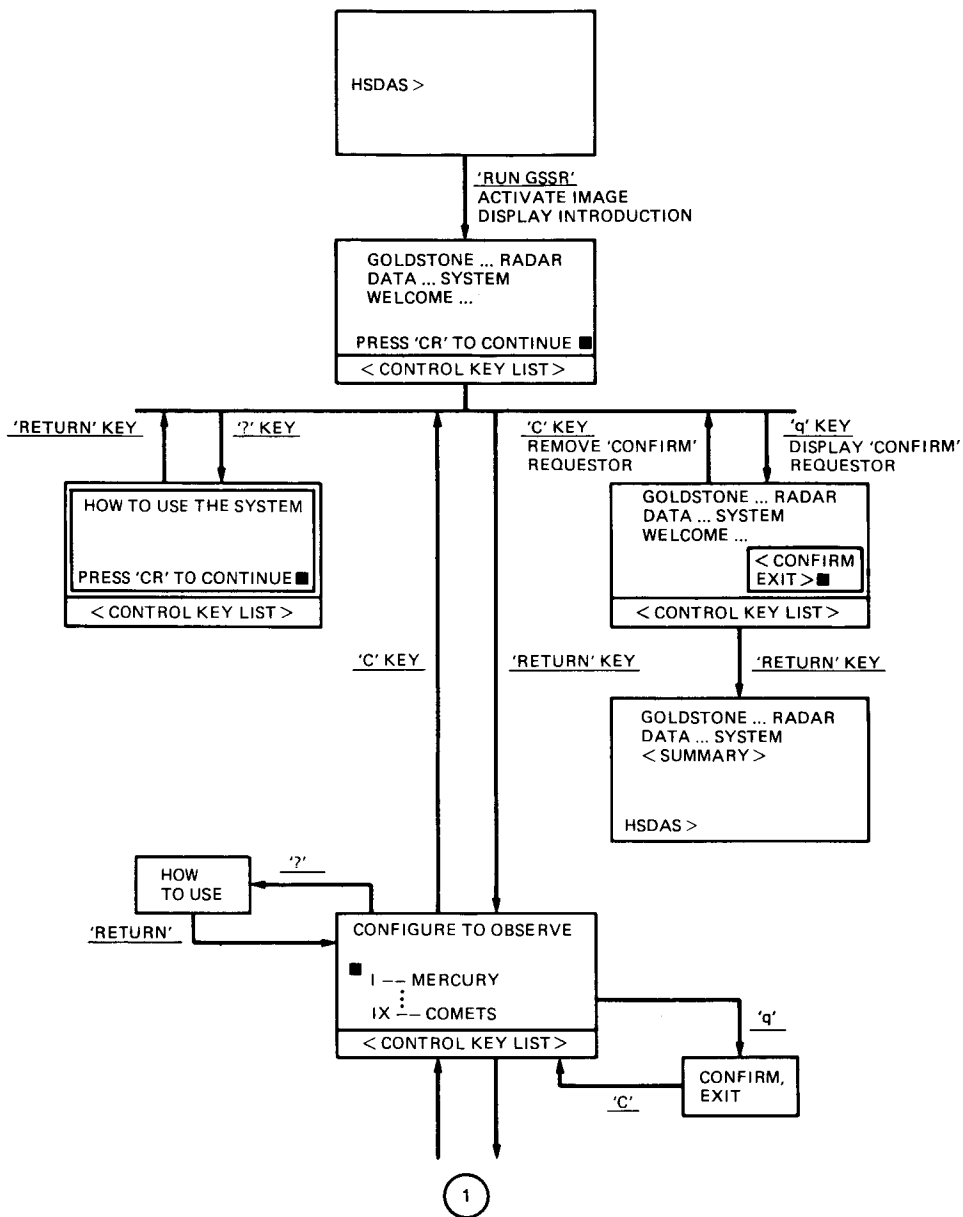


Fig. 3. Goldstone Solar System Radar Data Acquisition System User Interface (draft)

ORIGINAL PAGE IS
OF POOR QUALITY

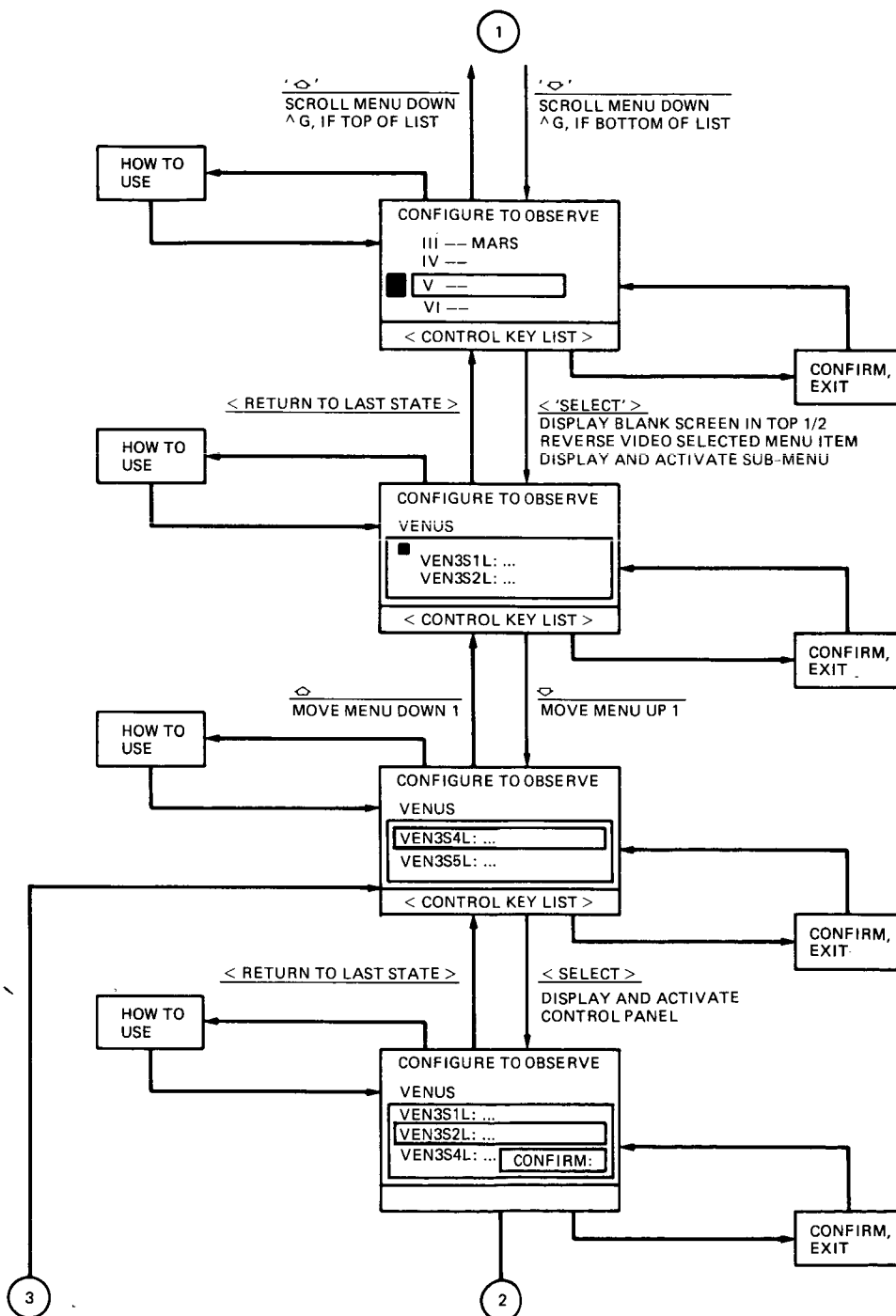


Fig. 3 (contd)

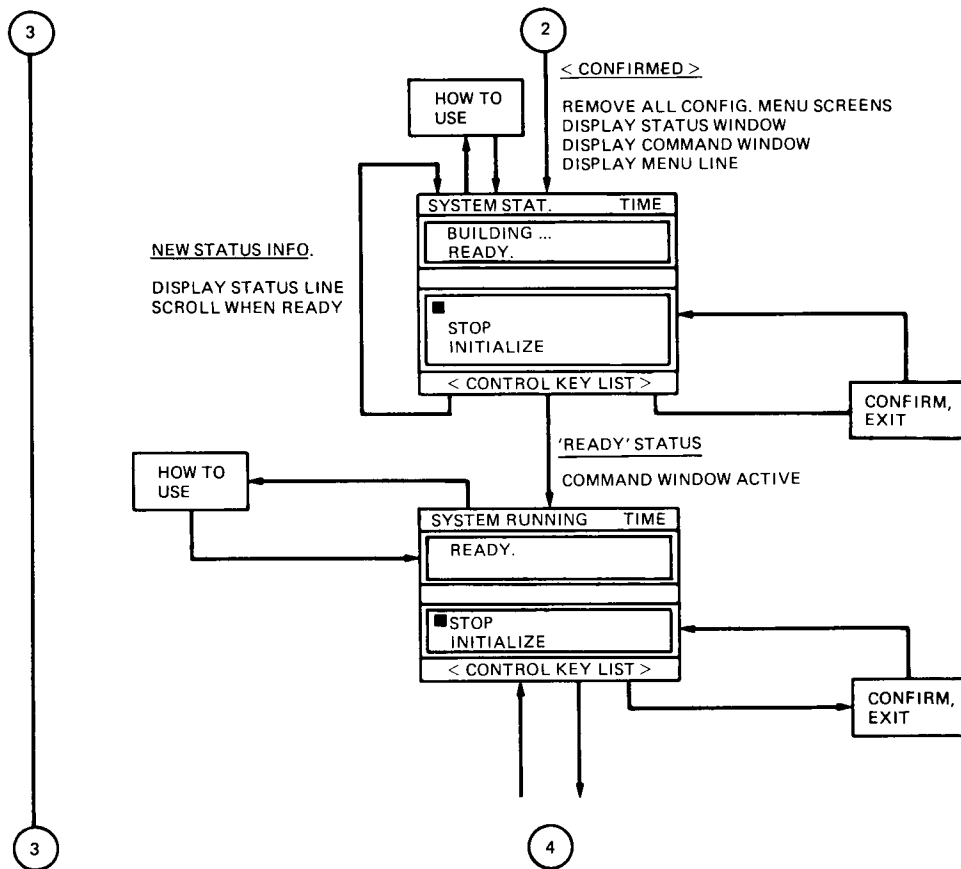


Fig. 3 (contd)

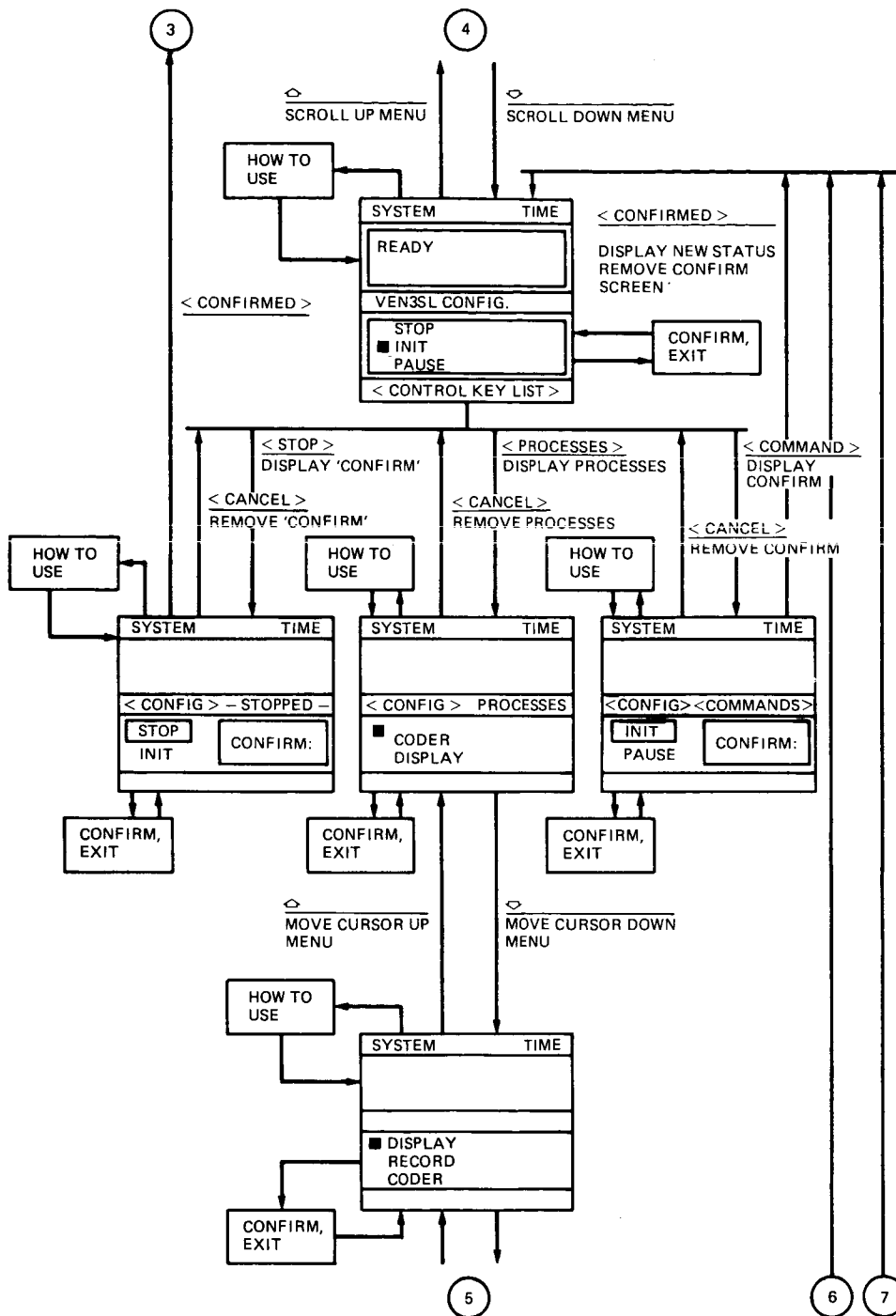


Fig. 3 (contd)

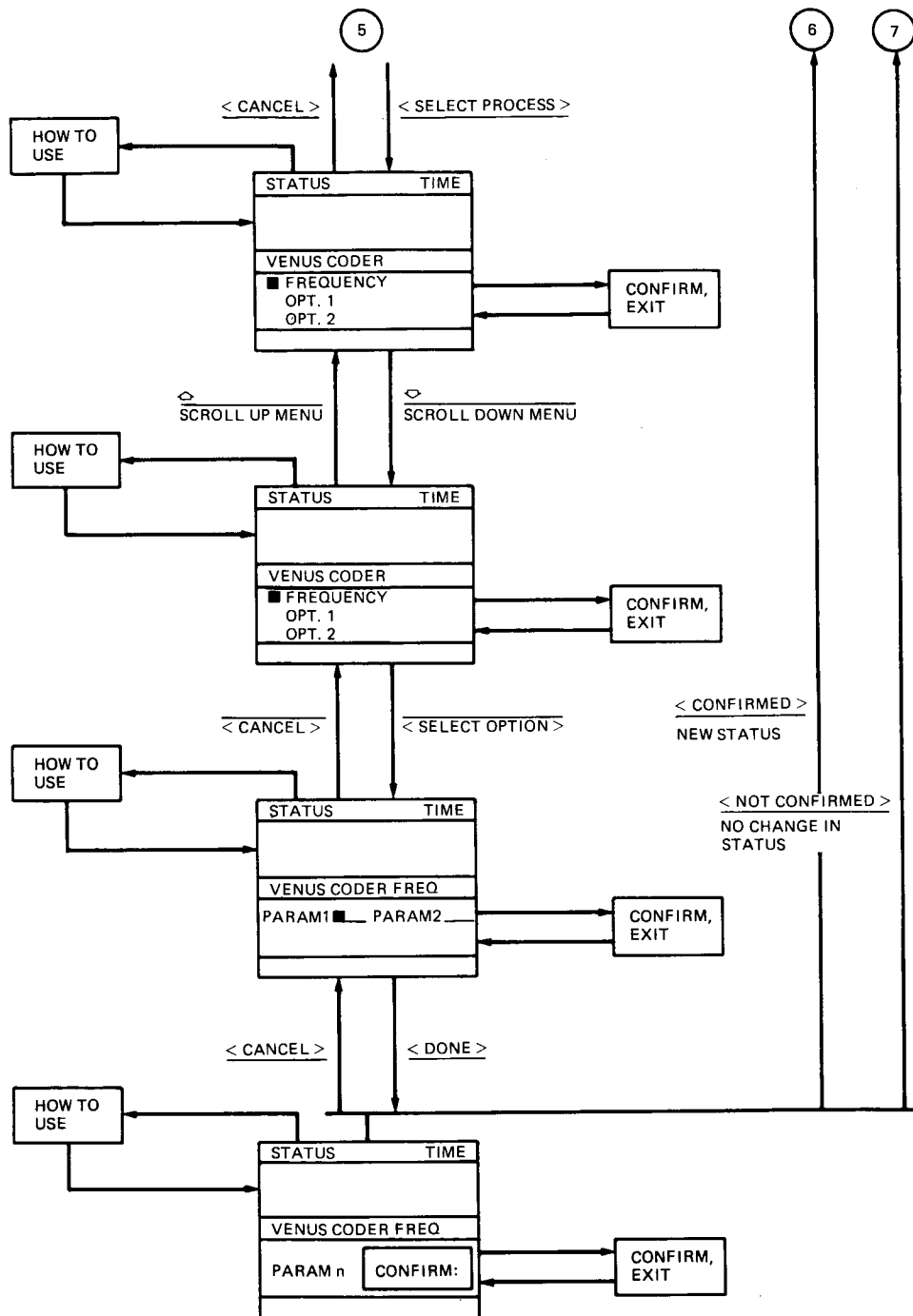


Fig. 3 (contd)

DSS 63 64-Meter Antenna S- and X-Band Efficiency and System Noise Temperature Calibrations, July 1986

S. D. Slobin

Radio Frequency and Microwave Subsystems Section

The DSN 64-m antenna in Spain (DSS 63) has been calibrated prior to its upgrading to a 70-m High Efficiency configuration in preparation for the Voyager Neptune encounter in August 1989. The S-band (2285-MHz) and X-band (8420-MHz) effective area efficiency and system noise temperature calibrations were carried out during July 1986 to establish a baseline system performance for this station. It is expected that the 70-m upgrade will result in at least a 1.9-dB G/T improvement at X-band relative to the 64-meter baseline reference. This article is the first in a series which will document 64-m and High Efficiency 70-m and 34-m antenna performance improvements due to size increase, high-precision surface panel installation, dual-shaped reflector profiles for uniform illumination, microwave holographic surface panel adjustment, or combinations of the above elements.

I. Introduction

The DSN 64-m antenna network (DSS 14, 43, 63) is being upgraded in preparation for the Voyager Neptune encounter, and also to enable acceptable performance at frequencies higher than X-band. In particular, the antenna diameter is being increased to 70 meters, the main reflector and subreflector profiles are being shaped (in contrast to standard paraboloidal and hyperboloidal forms), high-precision shaped main reflector panels are being installed, and an extensive series of focusing and panel setting operations are being undertaken. The measurements reported here were made at the S- and X-band frequencies of 2285 MHz and 8420 MHz, respectively.

The existing 34-m High Efficiency antennas (DSS 15, 45, 65), which already have shaped reflector surfaces, will have their panels set using microwave holographic techniques recently developed at JPL and elsewhere.

This article is the first in a series which will document the performance of the 64/70-m antennas in the pre-70-m (1986/87) and post-70-m (1987/88) configurations, as well as the performance of the 34-m High Efficiency antennas. At the present time, calibration efforts will concentrate on the High Efficiency antennas; however, the older 34-m Ha-Dec antennas will be re-calibrated at the conclusion of the present efforts. The results of these calibrations will be used to update DSN/Flight Project Interface Design documents and telecommunication prediction and performance analysis computer programs.

The antenna calibration technique was performed using a computer-based method commonly referred to as the MDA/NAR technique. The Metric Data Assembly Noise Adding Radiometer (MDA/NAR) is used to measure system noise temperatures when the antenna is alternately pointed at a calibra-

tion radio source and then at a nearby cold-sky location. The entire gain and noise temperature calibration methodology is embodied in three software packages: RADIOMETRY, MDA/NAR, and AGA/9600. RADIOMETRY generates source location predictions that drive the antenna during the radio source observation. MDA/NAR generates on- and off-source noise temperature estimates during a radio source observation period. AGA/9600 determines antenna pointing corrections, corrections for source size, and estimates of antenna efficiency at each particular observation point. The entire antenna gain calibration procedure is described elsewhere.¹

A major factor during the July 1986 DSS 63 64-m calibration was the choice of the Madrid station-developed MDA/NAR methodology over the JPL-developed BP-80 NAR technique, a similar noise-adding radiometer antenna calibration method. Both techniques were extensively evaluated in parallel use. This choice has effectively cemented the MDA/NAR technique into the DSN antenna calibration program for the duration of the antenna testing period for the next several years. What was desired was an accurate radiometric system, capable of quasi-automatic data acquisition (gain and pointing) at any DSN complex. The MDA/NAR proved slightly more accurate due to the method of handling typical small receiver nonlinearities. The BP-80 NAR, an earlier development, included a method for handling small detector nonlinearities, but not receiver nonlinearities. Hence, the MDA/NAR technique resulted in improved overall accuracy. Also, the MDA/NAR provided the desired quasi-automatic data acquisition, whereas the BP-80 did not. On the other hand, the MDA/NAR, while fulfilling the dedicated application for which it was designed, falls short in related applications where the BP-80 proves versatile and occasionally necessary. For example, initial antenna RF alignment tasks (lateral and axial focusing, and sidelobe-level checks) are conveniently accomplished using the BP-80 manual and real-time data reduction necessary to proceed with on-site measurements. The MDA/NAR, requiring a separate data reduction process (using the same computer previously utilized for data acquisition), proves cumbersome and time consuming for any real-time decision-dependent work cycle. Error analysis of the MDA/NAR is discussed in Section IV of this article.

A typical MDA/NAR-supported observation process is as follows: A natural radio source is chosen for at least several hours of observation. The antenna moves to an off-source position near the radio source (typically 0.240 degree) so that the measured system noise temperature represents the contribution of ground and atmosphere only (in addition to

the constant hardware contribution). For a period of about 4 minutes, the radio source is scanned in the azimuth and elevation directions. From measurements of noise temperature and antenna position, the antenna efficiency and pointing error can be determined, with suitable small corrections made for source size and pointing error.

The radio-source calibrators used at DSS 63 (and their S/X-band flux densities, Janskys) were 3C274 (140.00/46.00), 3C123 (32.00/10.15), 3C286 (11.78/5.435), 3C218 (27.7/8.34), and 3C161 (13.05/4.075). These sources are considered to exhibit stable flux levels with time and are therefore suitable for use as standard gain calibrators. The DSN has adopted standard radio source flux densities for the calibration sources. (A description of previous efficiency measurements at 8420 MHz and the radio sources used is given in [1].) For a 100-percent area-efficient antenna, the expected increase in system noise temperature from a natural radio source is given by

$$\Delta T_s = S A_p / 2k$$

where

S = flux density of the radio source, W/m²-Hz

A_p = physical area of the antenna, m²

k = Boltzmann's constant (1.380622E-23), W/Hz-K

The actual gain of the antenna (for 100-percent area efficiency) is given by

$$G(\text{ratio}) = 4\pi A_p / \lambda^2$$

where

A_p = physical area of antenna

λ = wavelength

For a 64-m-diameter antenna, at 8420 MHz (X-band), the 100-percent efficient gain is 75.04 dBi. At 2285 MHz (S-band), the 100-percent efficient gain is 63.71 dBi.

To the extent the 100-percent area-efficient system noise temperature increase is not achieved, the measured area efficiency of the antenna may thus be determined. Included in the measured area efficiency is the attenuating effect of the atmosphere, resulting in an estimate of efficiency that is too low. This can be accounted for by atmospheric modeling or by actual measurements of atmospheric parameters at the time of the calibration.

¹Antenna Gain Calibration Procedure, 70-Meter Upgrade Project, JPL Document Number D-3794 (internal document), Jet Propulsion Laboratory, Pasadena, Calif., November 15, 1986.

Efficiency and noise temperature curves are presented both with and without atmospheric effects included. It is recommended that for all telecommunications link analyses, the "atmosphere-free" antenna parameters be used. In this way the *total* real or postulated atmospheric attenuation and noise temperature can be included in the analysis. (Existing design documents present antenna gain and system noise temperature *including* atmospheric effects—a confusing situation.)

II. Antenna Area Efficiency

Figures 1 and 2 show the measured S-band antenna efficiencies both with and without the atmospheric attenuation effect, respectively. The S-band atmospheric model is based on the accepted [2] zenith attenuation of 0.03 dB, corresponding to a standard clear atmosphere. At 30-degree elevation angle (2 airmasses in the flat-earth approximation) the attenuation is doubled to 0.06 dB. (An attenuation loss of 0.03 dB corresponds to an effective loss of efficiency of 0.688 percent for a perfect antenna.) For antennas with less than 100-percent efficiency, this loss of efficiency is not entirely experienced. The actual area efficiency without atmospheric attenuation is determined by

$$\text{efficiency (w/o atm)} = \text{efficiency (w/atm)} \times L$$

where

$$L = 10^{A(\text{dB})/10}, \geq 1$$

$$A(\text{dB}) = \text{attenuation at elevation angle of interest}$$

Therefore, because of the inherent nonperfect antenna efficiency, the entire effect of atmospheric removal is not realized. In other words, the removed atmospheric attenuation is not simply added to the antenna efficiency. In the manner described above, the measured antenna efficiencies with atmospheric loss were modified at each elevation angle to calculate the inherent antenna efficiency as though no atmosphere were present. By using the no-atmosphere efficiency curves, without the confusing compensations for included atmospheric loss, the effects of varying atmospheric conditions (large at higher frequencies) can be accounted for more readily in later determinations of overall telecommunications link performance.

Second-order curves were fitted to the data shown in Figs. 1 and 2. These curves are of the form

$$\text{efficiency} = a_0 + a_1\theta + a_2\theta^2$$

where

$$\theta = \text{elevation angle, degrees}$$

The coefficients of this expression for the S-band efficiency curves are given in Table 1.

In a similar manner, the X-band efficiency curves were calculated both with and without the standard clear-atmosphere attenuation effects. For X-band, the atmospheric model uses an accepted [2] zenith attenuation of 0.04 dB, which corresponds to a total signal loss of 0.917 percent for a perfect antenna. Figures 3 and 4 show the X-band efficiencies both with and without atmospheric effects included. The coefficients of the efficiency curve-fits are also given in Table 1. Included in Table 1 are the peak values of efficiency, the elevation at which these peak values occur, and the standard deviation of the curve fit.

It should be appreciated that the simple atmospheric modeling used at S- and X-bands is quite appropriate. Heavy cloud cover and/or rain precludes calibration measurements. For future work at higher frequencies (e.g., Ka-band) it is envisioned that the technique of measuring off-source system noise temperature as a function of elevation angle will be used to obtain better estimates of the atmospheric loss during specific measurement sessions.

It is seen that in the X-band efficiency curves, the efficiency falls off rather rapidly at angles away from the peak angle. DSS 63 is unique in that structural braces were added with the goal of reducing antenna gain change due to main reflector distortion. However, original bracing which was to have been removed to provide the final configuration was intentionally retained for an interim period due to scheduling problems. Since the DSS 63 subreflector *y-z* focusing movement was developed for a slightly differently configured antenna, it is felt that the gain fall-off results from incorrect subreflector movement in attempting to compensate for main reflector distortion and quadripod sag. The DSS 63 results at both S- and X-band should be considered atypical. Indeed, measurements on the other 64-m antennas do not show this large change of efficiency with elevation angle. (The subreflector *y-z* focusing curves which were operational during the measurements reported here are defined elsewhere.²)

III. System Noise Temperature

Part of the antenna efficiency determination is a measurement of off-source system noise temperature. Figures 5 and 6 show raw data determinations of S- and X-band system noise temperatures as a function of elevation angle for several radio

²JPL Software Specification Document No. DFA-5222-OP, *Antenna Mechanical Subsystem—Subreflector Controller for 64 m Antennas* (internal document), Jet Propulsion Laboratory, Pasadena, Calif., March 21, 1986.

sources on two different days. For X-band, the "prime" and "backup" maser preamplifier curves include different waveguide noise temperature contributions due partially to different path lengths in the receiving system. The 12-inch-longer path length of the prime maser contributes approximately 1 K, and the prime maser has approximately 1-K higher noise temperature. This accounts for the 2-K difference between system noise temperatures for the two systems. The prime X-band maser is designated as X-TWM1 (S/N 2006). The backup X-band maser is X-TWM2 (S/N 2003). Both are Block II masers. The S-band maser is designated S-TWM1 (S/N 4001).

Figure 7 shows solid-curve approximations to the experimental data. These curves are not extrapolated below a 10-degree elevation angle, the lower limit of the experimental data. Because of the large number of airmasses below 10-degree elevation (greater than 6 airmasses), care should be taken in obtaining noise temperature estimates in the 0- to 10-degree elevation region. The horizontal inhomogeneity of the atmosphere makes extrapolation in elevation a source of significant error in noise temperature modeling.

As with the efficiency determinations, the atmospheric noise temperature effects can be removed from the raw data by suitable atmospheric models. At S-band, the 0.03-dB zenith attenuation corresponds to a noise temperature contribution of 1.93 K; the 0.04-dB X-band zenith attenuation corresponds to 2.57-K noise temperature. These models assume an effective atmospheric physical temperature of 280 K. The noise temperature contribution that is removed is determined from

$$T_{\text{atm}} = 280 \times \left(1 - \frac{1}{L}\right)$$

where L = atmospheric loss factor (described earlier). Figure 8 shows the three noise temperature curves with the atmospheric noise, as modeled, removed. Table 2 indicates the fourth-order curve fit coefficients and standard deviations of curve fit for the curves shown in Figs. 7 and 8. Both sets of X-band backup maser data have been combined into one curve.

IV. Error Analysis

Despite extensive and continuing error analysis of both the BP-80 and MDA/NAR radiometers from July 1986 through the present, a full accuracy statement is not yet possible. It must be remembered that all raw measured values are of system noise temperature, and thus depend on the initial calibration of the noise diode, the noise diode stability, receiver linearity, and a knowledge of maser noise contribution—a value which may have changed slightly since initial construc-

tion and testing. These are the major sources of instrumental systematic errors.

As a matter of perspective, however, it is unlikely that instrumental systematic errors exceeding ± 0.2 dB (± 5 percent) with 3σ confidence are present. Random errors in the determination of antenna efficiency (cf. Figs. 1 and 3) are estimated to be ± 0.15 dB at S-band, and ± 0.2 dB at X-band (3σ). The largest source of inaccuracy in the measurement of X-band antenna system efficiency remains the basic radio astronomical flux density absolute accuracy, which is estimated to be ± 0.5 dB (3σ) ($\pm 4\%$, 1σ [1]). At S-band, it is estimated that there exists a flux density accuracy of somewhat less than ± 0.3 dB with similar 3σ confidence [3]. Assuming these estimated error sources to be independent, it is seen that the radio source flux density is the largest contributor to uncertainty in the rms estimate of antenna efficiency. The absolute accuracy in the determination of antenna efficiency for the DSS 63 antenna can thus be stated as:

S-band: ± 0.4 dB (3σ)

X-band: ± 0.6 dB (3σ)

Continued refinement of noise temperature measurement techniques will not significantly alter these values, as the present limiting factor in efficiency determination is the knowledge of radio source flux density.

As radio source flux density is not a factor in system noise temperature determination, this large error source may be neglected in this analysis. Random errors in the determination of off-source noise temperature may be somewhat less than those seen in antenna efficiency, as the noise temperature is a raw data measurement and not subject to random pointing errors and corrections. It is estimated that for both S- and X-band, the random noise temperature determination errors are less than 0.1 dB (3σ). Thus the remaining uncertainties, systematic and random, yield the following estimates of noise temperature tolerances:

S/X-band: ± 0.22 dB (3σ)

The corresponding uncertainties at a nominal 25-K system noise temperature are:

S/X-band: ± 1.5 K (3σ)

The two main sources of error in the data analysis phase (as opposed to experimental errors in data gathering) are curve fitting and atmospheric correction.

Standard deviations of curve fits are stated in Tables 1 and 2 for the efficiency and noise temperature curves. These values are essentially the random errors quoted earlier. For the

efficiency curves, the standard deviations are less than 1 efficiency-percent. For noise temperatures, the standard deviations are better than 0.25 K for the curves shown in Fig. 8. Extrapolations for noise temperature below about a 10-degree elevation angle (the lowest experimental point) should be made with care.

The source of clear-sky atmospheric models is [2]. As the atmospheric conditions during the calibration measurements are not known beyond the fact that there existed a clear sky, some amount of atmospheric modeling error exists. It is estimated, based on experience, that zenith atmospheric model errors of less than 20 percent (1σ) exist, which would result in efficiency errors not exceeding 0.1 percent (1σ) at zenith for a 50-percent efficient antenna.

A comprehensive error analysis covering the entire antenna calibration process, including important systematic error estimation and radiometer accuracy analysis, will be published in a later *TDA Progress Report*.³

V. Comparison of Measured and Expected Antenna Efficiencies

In this section, the elements contributing to the net X-band area efficiency of the DSS 63 64-m antenna are given and discussed. A comparison with measured efficiencies is made using models developed from physical optics (PO) analysis and geometrical theory of diffraction (GTD) analysis, modified by other losses as described below. As the theoretical models do not include an atmospheric effect, the comparison is made with the X-band no-atmosphere best-fit curve shown in Fig. 4.

The existing PO analysis program⁴ does not consider the effect of main reflector distortion and subreflector focusing as a function of elevation angle. It does, however, allow a detailed analysis of feed system parameters affecting overall antenna efficiency. The gain/efficiency effects of large-scale (tens of meters, laterally) ordered distortions of the main reflector are calculated using the GTD program⁵ using the surface specified by structural analysis. The effects of small-scale distortions (centimeters to meters, laterally) due to main and subreflector surface roughness and panel manufacturing and

setting tolerance are given by the so-called Ruze loss [4]. This Ruze loss can be applied to results of both the PO and GTD programs. Thus both programs are capable of describing antenna performance at 45-degree elevation (or whatever rigging angle results in a "perfect" antenna shape); however, only the GTD program yields efficiency determinations over the entire range of elevation angles.

The physical optics program assumes perfect antenna shape and subreflector position, and hence is equivalent to calculations made for an actual antenna at an elevation angle of 45 degrees where the main reflector is designed and set to have a perfect paraboloidal shape. The feed system analyzed here uses a dual hybrid mode horn. Table 3 lists the expected feed system losses. In addition, hardware losses are given, including those arising from reflector panel manufacturing and setting tolerances. The subreflector and panel tolerances total 1.06 mm, rms. It is seen that feed system losses (items 2 through 7) reduce the 100-percent area efficiency by 1.02 dB, to a net effective antenna gain of 74.02 dBi. This value is compared with the equivalent GTD-calculated gain of 74.13 dBi. For the purposes of this article, these gain values are deemed to be identical, and both methods are regarded as equivalently predicting antenna performance. Further losses (a total of 0.82 dB) show the effect of the non-feed components such as waveguide loss, dichroic plate loss, VSWR, quadripod blockage, and the Ruze loss components described above. An rms surface tolerance of 1.06 mm results in a Ruze loss of 0.61 dB.

The efficiency value of 0.569 has not been achieved at 45-degree elevation by any 64-m antenna in the DSN, although the Goldstone antenna, DSS 14, has achieved 52 percent, 0.39 dB below the 56.9-percent expectation given by the PO program. DSS 14 64-m efficiency measurements will be made in late 1987 and will be reported in a later *TDA Progress Report*.

Figure 9 shows a comparison of measured antenna area efficiency (without atmosphere, Fig. 4) and expected values of efficiency as given by GTD calculations of antenna gain, reduced by known or postulated hardware losses. The PO-equivalent losses (Table 3, items 2-7) are not determined separately by GTD, but are accounted for internally. Additional loss (a total of 0.821 dB) from waveguide (0.070 dB), dichroic plate (0.035 dB), VSWR (0.039 dB), and quadripod blockage (0.677 dB) reduces the GTD-calculated antenna gain. Also, an efficiency loss due to small-scale surface roughness is considered, and the level of roughness expected is that given in Table 3 (i.e., 1.06 mm, rms). The net efficiency factor due to this loss is given by the Ruze formula

$$\eta = \exp\left[-\left(\frac{4\pi\epsilon}{\lambda}\right)^2\right]$$

³R. Riggs, Jet Propulsion Laboratory, private communication, May 1987.

⁴A. Cha, *Physical Optics Analysis of NASA/JPL Deep Space Network 70-m Antennas*, JPL D-1853 (internal document), Jet Propulsion Laboratory, Pasadena, Calif., November 1984.

⁵T. Veruttipong, D. Rochblatt, W. Imbriale, and V. Galindo, *Dual Shaped and Conic GTD/Jacobi-Bessel Analysis Programs, A User Manual*, JPL D-2583 (internal document), Jet Propulsion Laboratory, Pasadena, Calif., July 30, 1985.

where

ϵ = small-scale surface roughness

λ = wavelength

It is seen that although the shapes of the two curves are similar, there exists a substantial difference between expected and measured curves. The measured efficiency for DSS 63 is 1.12-dB lower than the expected efficiency. Figure 10 shows similar curves which will help explain these results. The five curves shown include the Fig. 9 curves, plus three additional curves of GTD-calculated efficiency for Ruze surface roughness of 1.5, 1.8, and 2.0 mm, rms. The measured (Fig. 4) data shown in Figs. 9 and 10, when compared with the GTD-calculated efficiency curves, give quite good performance agreement if one accepts a 1.7- to 1.8-mm rms level of small-scale surface roughness, which is certainly reasonable for a well-used and aged 64-m antenna. The K-band (11.45-GHz) holography measurements with 0.4-m resolution made in May 1985 with the extra antenna brace installed, indicate an rms surface error, measured normal to the best-fit paraboloid, of 1.53 mm at a 40-degree elevation angle. This rms surface error includes the Ruze loss plus a small gravity-induced distortion. This is entirely consistent with the 1.7- to 1.8-mm Ruze tolerance described above. It was predicted⁶ that panel adjustment would reduce the rms surface error to 0.86 mm. Thus, it is seen that this type of analysis confirms the use of

GTD to predict antenna performance, and also puts upper limits on the tolerances of the assumed and/or measured values of the losses described earlier.

In summary, it is seen that PO and GTD programs agree within about 0.1 dB at the point the computations can be compared with one another. At that point, a reasonable assumption of small-scale surface roughness virtually identically matches the experimental data defining antenna efficiency vs. elevation angle.

We consider the DSS 63 64-m July 1986 S/X-band calibrations to be very successful. As discussed, absolute area efficiency accuracies are clearly limited by radio source flux accuracies, and when flux and instrumental systematic errors are combined with random measurement errors, we obtain area efficiency error estimates of ± 0.4 dB (3σ confidence) at S-band and ± 0.6 dB (3σ) at X-band. Absolute noise temperature accuracies, an equally important parameter in SNR-limited telecommunication links, are found to be ± 0.22 dB (3σ) at both bands. This translates, for a nominal 25-K system, to ± 1.5 -K (3σ) accuracy.

⁶M. P. Godwin, et al., "Final Report on Holographic Tests at S-band and K-band on the DSS-63 64 Metre Antenna", Report No. A087, Job No. 50/042, Eikontech Limited, Sheffield, England, February 1986.

ORIGINAL PAGE IS
OF POOR QUALITY

Acknowledgment

The calibration of the entire group of DSN 64-m, 70-m, and 34-m antennas is a significant effort of worldwide scope involving many people. Although the author is responsible for the final data analysis, publication, and transferral to flight project planning documentation, his is a small but unifying part of the entire task.

The following people among others should be acknowledged for their contributions to the calibration work: at the Madrid Station, where the MDA/NAR techniques were developed over the past several years, A. Rius, J. Calvo, A. Chamarro, J. Gimeno, G. Pasero, J. Galvez, and J. Munoz; at the Canberra Station, G. Baines, A. Bailey, and R. Livermore; at the Goldstone Station, W. Wood, D. Girdner, and J. McCoy; at JPL, K. Bartos, D. Bathker, R. Riggs, M. Franco, C. Stelzried, A. Freiley, and B. Seidel.

References

- [1] J. A. Turegano and M. J. Klein, "Calibration radio sources for radio astronomy: Precision flux density measurements at 8420 MHz," *Astronomy and Astrophysics*, vol. 86, pp. 46-49, 1980.
- [2] E. K. Smith, "Centimeter and millimeter wave attenuation and brightness temperature due to atmospheric oxygen and water vapor," *Radio Science*, vol. 17, No. 6, pp. 1455-1464, November-December 1982.
- [3] A. J. Freiley, P. D. Batelaan, and D. A. Bathker, "Absolute flux density calibrations of radio sources: 2.3 GHz," *JPL Technical Memorandum 33-806*, Jet Propulsion Laboratory, Pasadena, Calif., December 1, 1977.
- [4] J. Ruze, "Antenna tolerance theory—A review," *Proceedings of the IEEE*, vol. 54, No. 4, pp. 633-640, April, 1966.

Table 1. Coefficients of second-order curve fits for antenna area efficiencies

$$\text{efficiency} = a_0 + a_1\theta + a_2\theta^2$$

where θ = elevation angle, degrees

Coefficient/Parameter	S-Band (2285 MHz)	X-Band (8420 MHz)
	With Atmosphere (cf. Fig. 1)	With Atmosphere (cf. Fig. 3)
a_0	54.25744	32.69687
a_1	8.635463E-02	0.4869833
a_2	-6.788819E-04	-4.959421E-03
Peak efficiency, %	57.004	44.652
Peak angle, deg	63.601	49.097
Standard deviation, %	0.676	0.767
	Without Atmosphere (cf. Fig. 2)	Without Atmosphere (cf. Fig. 4)
a_0	56.30269	34.80555
a_1	3.554052E-02	0.4332722
a_2	-2.862227E-04	-4.540844E-03
Peak efficiency, %	57.406	45.141
Peak angle, deg	62.085	47.708
Standard deviation, %	0.679	0.822

ORIGINAL PAGE IS
OF POOR QUALITY

Table 2. Coefficients of fourth-order curve fits for S- and X-band system noise temperatures

$$T_{\text{system}} = a_0 + a_1\theta + a_2\theta^2 + a_3\theta^3 + a_4\theta^4$$

where θ = elevation angle, degrees

Coefficient/Parameter	S-Band (2285 MHz) ^a	X-Band (8420 MHz) ^b , Prime Maser	X-Band (8420 MHz) ^c , Backup Maser
	With Atmosphere (cf. Fig. 7)	With Atmosphere (cf. Fig. 7)	With Atmosphere (cf. Fig. 7)
a_0	5.652297E+01	6.267107E+01	6.146491E+01
a_1	-1.618135E+00	-2.483746E+00	-2.613738E+00
a_2	3.732890E-02	6.249823E-02	6.721768E-02
a_3	-3.992906E-04	-7.002778E-04	-7.637453E-04
a_4	1.607969E-06	2.884866E-06	3.171873E-06
Zenith noise temperature, K	27.671	24.143	22.028
Standard deviation, K	0.198	0.390	0.389
	Without Atmosphere (cf. Fig. 8)	Without Atmosphere (cf. Fig. 8)	Without Atmosphere (cf. Fig. 8)
a_0	3.670053E+01	3.638264E+01	3.507050E+01
a_1	-4.414013E-01	-9.301171E-01	-1.046979E+00
a_2	6.952927E-03	2.255099E-02	2.677656E-02
a_3	-5.212648E-05	-2.452661E-04	-3.015780E-04
a_4	1.566596E-07	9.880078E-07	1.239911E-06
Note: If $\theta \geq 80^\circ$, $T_{\text{system}} = 21.192$ K			
Note: If $\theta \geq 85^\circ$, $T_{\text{system}} = 19.056$ K			
Zenith noise temperature, K	25.571	21.192	19.056
Standard deviation, K	0.071	0.231	0.135

^aS-band (2285 MHz) specifications: maser S-TWM1; S/N 4001; and 2.5 K noise temperature.

^bX-band (8420 MHz) specifications: prime maser; X-TWM1; S/N 2006; and 3.7 K noise temperature.

^cX-band (8420 MHz) specifications: backup maser; X-TWM2; S/N 2003; and 2.03 K noise temperature.

Table 3. Design expectations for 64-m antenna with dual hybrid mode feedhorn at 8420 MHz and 45-degree elevation angle using physical optics analysis

Item	Loss, dB	Net Gain, dBi
1. 100% Area Efficiency		75.04
2. Illumination Amplitude	-0.454	
3. Illumination Phase	-0.146	
4. Forward and Rear Spillover	-0.210	
5. Subreflector Blockage	-0.170	
6. $m \neq 1$ modes	-0.035	
7. Cross polarization	-0.0004	74.02
8. Waveguide loss	-0.070	
9. Dichroic plate loss	-0.035	
10. VSWR	-0.039	
11. Quadripod Blockage	-0.677	
12. Main reflector panels		
Manufacturing (0.035 inches)	-0.430	
Setting (0.019 inches)	-0.127	
13. Subreflector		
Manufacturing (0.012 inches)	-0.051	72.59 (= 0.569 efficiency)

Note: The rms panel and subreflector tolerance = 0.04159 in. (1.06 mm)

ORIGINAL PAGE IS
OF POOR QUALITY

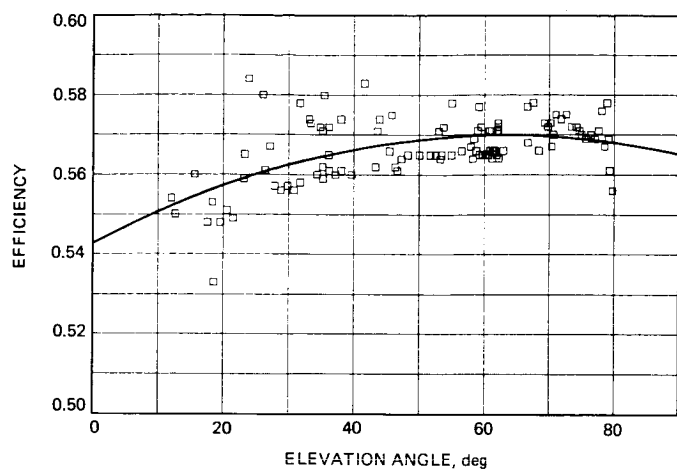


Fig. 1. DSS 63 64-m S-band (2285-MHz) area efficiency with atmospheric attenuation included

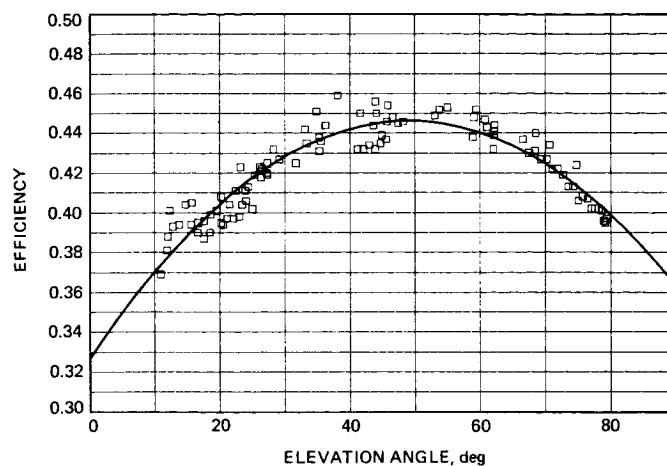


Fig. 3. DSS 63 64-m X-band (8420-MHz) area efficiency with atmospheric attenuation included

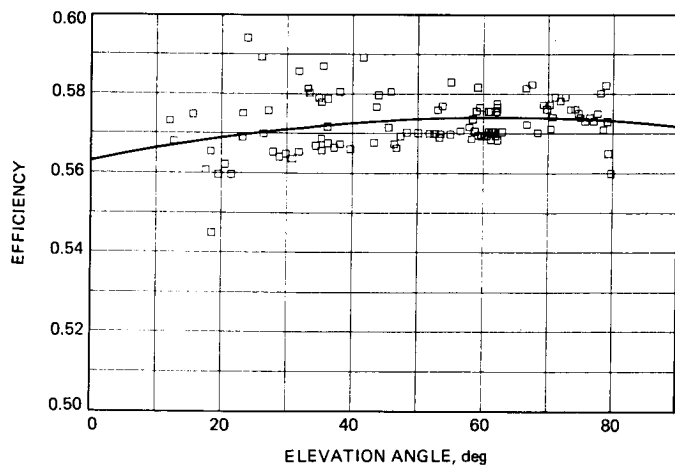


Fig. 2. DSS 63 64-m S-band (2285-MHz) area efficiency without atmospheric attenuation

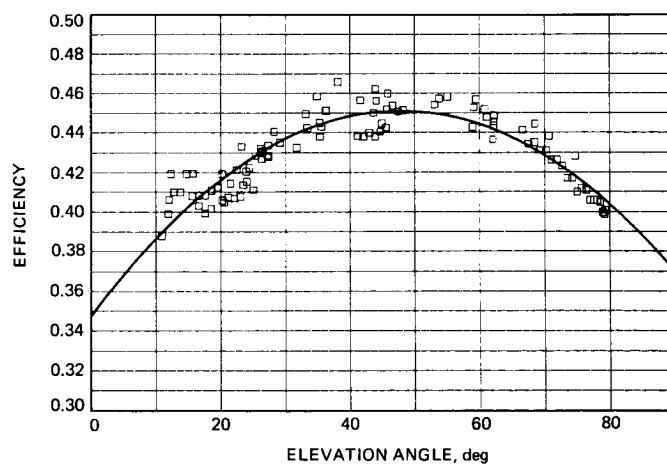


Fig. 4. DSS 63 64-m X-band (8420-MHz) area efficiency without atmospheric attenuation

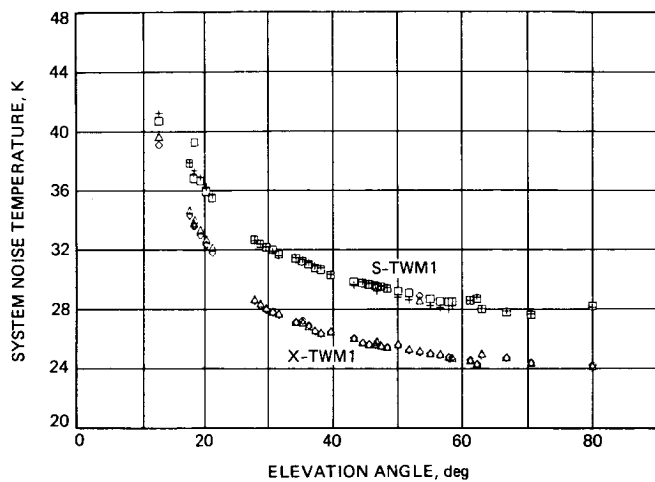


Fig. 5. DSS 63 64-m system noise temperature raw data, S-band (2285-MHz) and X-band (8420-MHz) prime maser, including atmospheric contribution

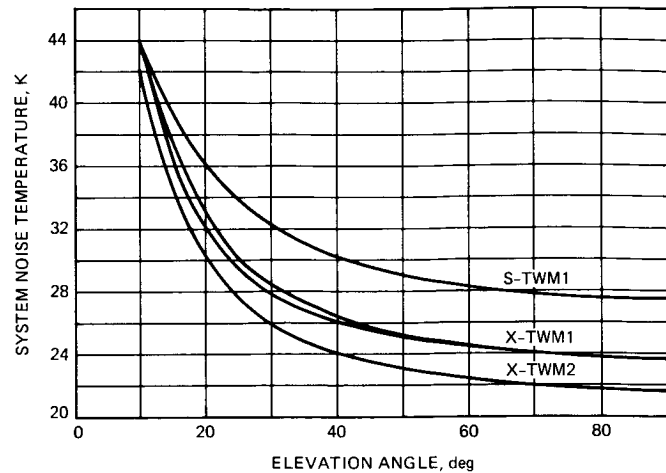


Fig. 7. DSS 63 64-m system noise temperature solid-curve approximations to raw data, S-band (2285 MHz) and X-band (8420 MHz), including atmospheric contribution

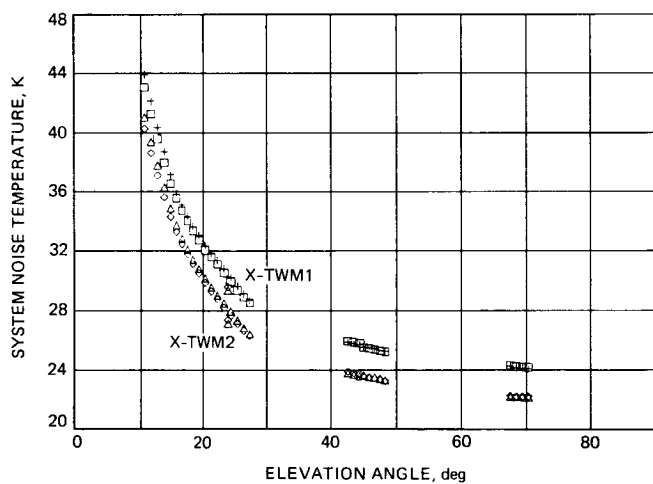


Fig. 6. DSS 63 64-m system noise temperature raw data, X-band (8420-MHz) prime maser and X-band backup maser, including atmospheric contribution

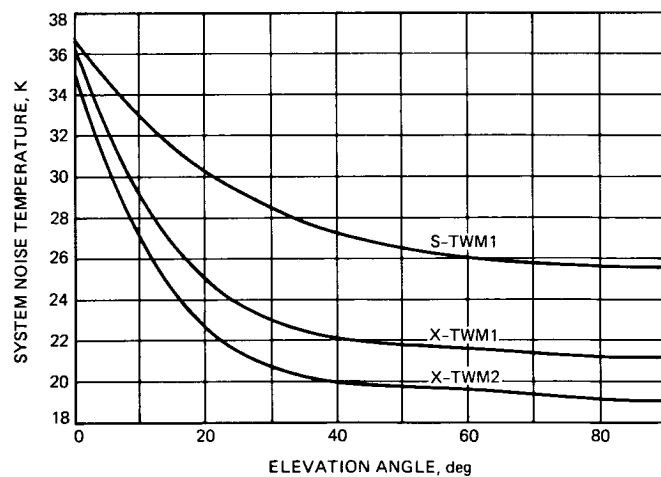


Fig. 8. DSS 63 system noise temperature models, S-band (2285 MHz) and X-band (8420 MHz), without atmospheric contribution

ORIGINAL PAGE IS
OF POOR QUALITY

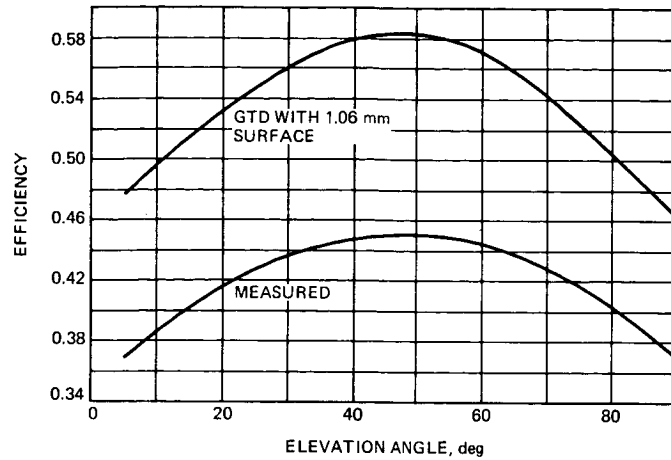


Fig. 9. Comparison of DSS 63 64-m GTD-calculated efficiency (with 1.06-mm-rms Ruze surface tolerance) and measured efficiency

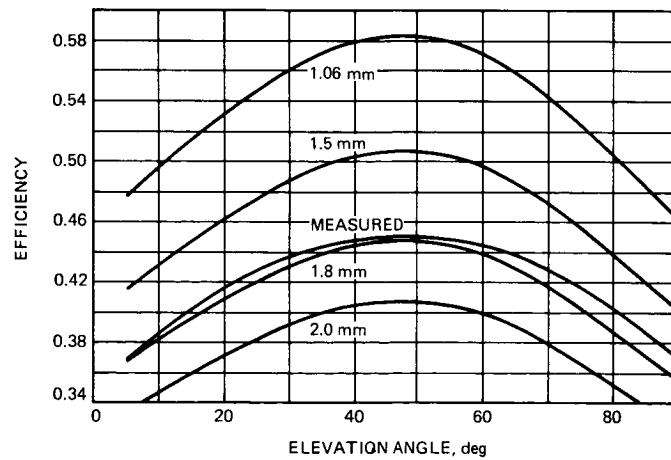


Fig. 10. Comparison of DSS 63 64-m GTD-calculated efficiency and measured efficiency for various Ruze surface tolerance values

DSS 43 64-Meter Antenna S- and X-Band Efficiency and System Noise Temperature Calibrations, January 1987

S. D. Slobin

Radio Frequency and Microwave Subsystems Section

The DSN 64-m antenna in Australia (DSS 43) has been calibrated prior to its upgrading to a 70-m High Efficiency configuration in preparation for the Voyager Neptune encounter in August 1989. The S-band (2285-MHz) and X-band (8420-MHz) antenna area efficiency and system noise temperature calibrations were carried out during December 1986 and January 1987 to establish a baseline system performance for this station. This article is the second in a series documenting 64-m and High Efficiency 70-m and 34-m antenna performance improvements for the NASA/JPL Deep Space Network. The agreement between theory and measurement is excellent.

I. Introduction

This article is the second in a series documenting the performance of the 64-/70-m antennas in the pre-70-m (1986/87) and post-70-m (1987/88) configurations, as well as the performance of the 34-m High Efficiency antennas. The article on the 64-m station in Spain (DSS 63) is presented elsewhere in this issue [1]. Much of the general description of the antenna calibration methodology and data reduction techniques is given in that reference. The descriptions given in this article will therefore not be as detailed.

Antenna calibration measurements were taken during the months December 1986 and January 1987 on five separate days. Because of weather conditions documented in the reports as "storm cloud," "mid-level cloud-like thick fog," and "shower-type cloud," data from days 1986/339 and 349 and 1987/012 were not used. The remaining two days, 1987/

018 and 020, appear to have had good weather, and those days provided the data for the antenna calibration. The radio sources observed were 3C274, 3C218, and 0521-365. The sources 3C274 and 3C218 are regarded as DSN standard calibrators, but it was found that both 3C218 and 0521-365 needed adjustments of their accepted values of 100-percent area-efficiency antenna temperature in order to obtain agreement with the 3C274 measurements. The largest correction was 14 percent, applied to source 0521-365 at X-band. A correction of this size undoubtedly arises from the use of an incorrect value of flux density in the antenna gain analysis (AGA) data reduction program. All other corrections were in the range of 1 to 3 percent. This aspect of the calibration will be discussed later. For reference, the 100-percent area-efficient gain of a 64-m-diameter antenna at S-band (2285 MHz) is 63.71 dBi. At X-band (8420 MHz), it is 75.04 dBi. A comprehensive description of the adjustments made to the theoretical X-band gain values to predict actual antenna performance is given in [1].

Efficiency and noise temperature curves are presented both with and without the atmospheric effects included. The measurements, of course, were made with the antenna immersed in the earth's atmosphere. At a 10-deg elevation angle, the antenna looks through nearly six zenith-equivalent atmospheres, and radio source noise temperature contributions are attenuated by nearly 0.25 dB at X-band. The effective efficiency [2] is thus somewhat lower than the real antenna efficiency. This atmospheric effect must be removed to determine the true inherent quality of the antenna itself. It is recommended that for all telecommunications link analyses, the atmosphere-free antenna parameters be used. In that way, any known or postulated atmospheric effect (noise temperature and attenuation) can be added fully and directly into the link calculations.

II. Antenna Area Efficiency

Figures 1 and 2 show the S-band antenna efficiencies both with and without the atmospheric attenuation effect, respectively. It was found when looking at the raw AGA data (cf. [1]) that there was some inconsistency in comparisons of antenna efficiency as determined by two different radio sources at the same elevation angle. For the complete set of data, it was found at S-band that source 3C218 yielded efficiencies which were high compared to those determined by source 3C274. Conversely, source 0521-365 yielded efficiencies which were too low compared to those determined by source 3C274. At X-band, both sources yielded efficiencies that were too high. Since it is unknown at the present time where the uncertainty lies (either in flux density or source size correction factor), the efficiency correction is adjusted, equivalently, by modifying the value of 100-percent area-efficient antenna temperature (M. J. Klein, personal communication and [2]). Included in this value are the unknown source characteristics, to be more accurately determined at a later date. Thus, if efficiency values are measured to be too high (by some determination), then the *expected* noise temperature increase from that radio source is modified *upward*. It must be remembered that this adjustment is made relative to a well-known, strong radio source, 3C274, which is one of the DSN standard calibrators. Radio source 3C218 is substantially weaker than 3C274 (one-fifth as strong) and subject to larger measurement error; thus, its determination of antenna efficiency was modified in deference to the 3C274 values. This technique is valid and is commonly used. It allows antenna efficiency values to be obtained at elevation angles where no standard calibration sources can be found. Clearly, this bootstrapping technique allows interim calibrations of new radio sources for use with other antennas *at the same frequency and with the same beamwidth*. The adjustments made to the observed radio sources are listed in Table 1. These adjustments are made to the AGA-calculated efficiency values, not

to the expected antenna temperature increases. They should not be regarded as a definitive DSN calibration of those radio sources.

The atmosphere adjustment is made according to the description given in [1]. The values used for S- and X-band zenith atmospheric attenuations are 0.03 and 0.04 dB, respectively.

Second-order curves were fitted to the data shown in Figs. 1 and 2. These curves are of the form

$$\text{efficiency} = a_0 + a_1\theta + a_2\theta^2$$

where

θ = elevation angle, degrees

The coefficients of this expression for the S-band efficiency curves are given in Table 2.

Similarly, Figs. 3 and 4 show the X-band efficiency determinations for the conditions with and without atmosphere. The coefficients of the efficiency expression are also given in Table 2.

A comparison of Figs. 3 and 4 of this article with the similar figures in the DSS 63 calibration report [1] will show that the X-band efficiency curves for DSS 43 are much flatter than for DSS 63. This is due to the main reflector bracing difference between the two antennas. The DSS 43 antenna had the same bracing upgrade as the DSS 63 antenna, but in the case of the DSS 63 antenna, the original braces were not removed as intended. The DSS 43 and DSS 14 (Goldstone) 64-m antennas existed in their proper configurations before the 70-m upgrade, and the subreflector focusing movement¹ needed to compensate for main reflector and quadripod deformation was optimum for that configuration. Since identical subreflector focusing was maintained for DSS 63, it is felt that this is one cause of the large efficiency fall-off, the other being the compromised bracing situation at DSS 63, which existed for a short interim period, including the July 1986 tests.

III. System Noise Temperature

Figures 5 and 6 show the S-band system noise temperatures (with and without atmospheric effect) obtained on days 1987/018 and 020. These measurements are the off-source back-

¹JPL Software Specification Document No. DFA-5222-OP, "Antenna Mechanical Subsystem - Subreflector Controller for 64M Antennas" (internal document), Jet Propulsion Laboratory, Pasadena, Calif., March 21, 1986.

ground reference temperatures, and thus do not depend on any of the characteristics of the radio sources such as flux density or source size correction. The S-band measurements show two distinct sets of results. This is felt to be due to a possible error in calibration of the noise-adding radiometer noise diode. No weather-dependent cause of noise temperature variation appears to explain the data. Also, no information exists which might enable a choice of data sets. A closer look at the efficiency curves (Figs. 1 and 2) shows a hint of this problem at elevation angles below about 40 degrees. Again, no choice of data sets was possible, and the accuracy of these data must be regarded as somewhat compromised by a long-period varying systematic error. (This error type will be regarded as random for the sake of analysis in this article.) Fortunately, the S-band telecommunications data are generally less critical to the DSN than are X-band data, and the large S-band uncertainties will not severely compromise link performance.

Figures 7 and 8 show the X-band off-source system noise temperatures on days 1987/018 and 020, for the conditions with and without atmospheric contribution, respectively. These data are well behaved in contrast to the S-band noise temperatures, although there also may be a hint of systematic error seen in the 1-K mismatch of noise temperatures in the 55- to 60-degree elevation angle region. These data were taken 5 hours apart, and it is possible a changing noise diode contribution or a clear-air atmosphere change may have contributed to the difference. More frequent noise diode calibration (possibly several times per hour) may assist in reducing further problems in this area. Table 3 lists the fourth-order curve-fit coefficients and standard deviation of curve fit for the curves shown in Figs. 5 through 8. In addition, certain maser preamplifier information (serial number and noise temperature) is also given.

IV. Error Analysis

As stated in [1], a comprehensive error analysis of the entire antenna calibration project will be forthcoming. In the case of the DSS 43 64-m antenna calibration, the ± 1 percent S-band efficiency variation and the ± 2 -K S-band noise temperature variation over the 10- to 30-degree elevation angle range give a clue to the size of the long-term random errors (several hours to 1 day) that may be encountered. The data taken over the 10- to 30-degree elevation angle range appear to consist of two distinct sets, one taken on each day. It is possible that on one day the noise diode contribution varied and on the other it did not. At X-band, however, the efficiency values show a spread at low elevation angles, without a corresponding spreading of the noise temperature values. It is possible then, that an error source independent of noise tem-

perature measurement (pointing correction, for example) may have contributed to this problem. It is not possible at this time to fully resolve pointing correction errors, if any, which may exist in the data. To do this would require an extremely precise measurement of X-band antenna beam shape in the region out to 10 millidegrees from beam peak and down to 1 dB below peak antenna gain.

It should also be noted that in general there may not be an easily observed correspondence between noise temperature variation (interpreted as a random error) and antenna efficiency measurement. For example, if a 0.05-dB (1.2-percent) source of atmospheric attenuation were to obscure the observing region, one would see both an on- and off-source noise temperature increase of about 3 K, a system noise temperature increase of about 10 percent. The derived antenna efficiency would show a variation of about 0.6 efficiency-percent for a 50-percent efficient antenna. This efficiency variation might not be easily separated from other random errors, and the observer would be puzzled as to why such a large change in off-source noise temperature did not significantly affect the calculated efficiency value.

As stated in the DSS 63 calibration report [1], it is unlikely that instrumental systematic errors exceeding ± 0.2 dB (± 5 percent) with 3σ confidence are present. These errors are primarily due to receiving system nonlinearities and result in a more or less constant miscalibration of the noise-adding radiometer noise diode. The determination of the linearity correction, however, is also subject to random errors. The measurable result of this is an incorrect system noise temperature determination and hence an incorrect estimate of antenna efficiency. In the AGA program, these nonlinearities are measured and analytically removed, but not perfectly. For the purpose of the error analysis done here, any long-term variability (hours to days) in noise diode contribution or linearity change are assumed to exist as random errors, and as such they are included in the standard deviation of curve fits as presented in Tables 2 and 3.

Typical random errors, as determined from curve-fit standard deviation, appear to be ± 0.1 dB (3σ) for S-band efficiency and ± 0.15 dB (3σ) for X-band efficiency. The radio source flux density accuracies are estimated to be ± 0.3 dB and ± 0.5 dB (3σ) [1] for S- and X-band, respectively. Thus, it may be stated that the absolute accuracy in the determination of antenna efficiency for the DSS 43 antenna is

S-band: ± 0.4 dB (3σ)

X-band: ± 0.6 dB (3σ)

The radio source flux uncertainty is the major contributor to the error in determination of antenna efficiency. Until radio

source flux density is more accurately defined, further work to reduce instrumental systematic errors will not materially change the present overall accuracy of antenna efficiency.

For noise temperature accuracy, only the systematic and random errors need be considered. For Figs. 5 and 7, the S- and X-band noise temperature curves, the curve-fit random errors are 0.4 dB and 0.2 dB (3σ), respectively. Thus, in conjunction with the systematic error of 0.2 dB, it is stated that the error in determination of system noise temperature is

S-band: ± 0.5 dB (3σ)

X-band: ± 0.3 dB (3σ)

corresponding to ± 3.1 K at S-band and ± 1.8 K at X-band, 3σ , for a nominal 25-K system noise temperature.

V. Comparison of Measured and Expected Antenna Efficiencies

In a manner entirely similar to that presented in [1], a comparison was made among the X-band antenna performance expectations as given by physical optics (PO) and geometrical theory of diffraction (GTD) programs, with modifications to the GTD curves to account for varying levels of small-scale surface irregularity due to main reflector panel manufacturing and setting tolerances, and subreflector manufacturing tolerance. The GTD program gives efficiency determination as a function of elevation angle. This varies, due primarily to gravity-induced main reflector distortion. Since the main reflector is not a perfect paraboloid away from the rigging angle (and hence has only a best-fit focus), subreflector focusing is accomplished only in a best-fit sense.

Table 4, reproduced directly from [1], shows the expected feed system losses (calculated by the PO program) and hardware losses which reduce theoretical 64-m antenna performance. A full description of the elements of this table appears in [1]. It is found that the PO and GTD analyses predict nearly identical antenna performance (within 0.1 dB at the 74.02-dBi point in Table 4). Again, it is noted in the table that the expected small-scale (Ruze) surface tolerance is 1.06 mm for a newly manufactured and very well-adjusted 64-m antenna.

Figure 9 shows a comparison of measured antenna area efficiency (without atmosphere, Fig. 4) and expected values of efficiency as given by GTD calculations of antenna gain, reduced by known or postulated hardware losses. In this

figure, GTD calculations with adjustments of 0.821 dB for known loss and a Ruze loss corresponding to an rms surface error of 1.06 mm appear as the top curve, with a maximum efficiency of 0.584. The measured efficiency curve appears with a maximum value of 0.454, which is 1.09 dB lower than theoretical. This difference is explainable to a large extent by the examination of Fig. 10. Similar GTD calculations, but with additional Ruze rms surface tolerances of 1.5, 1.8, and 2.0 mm, are shown. It is seen, as in the DSS 63 case, that the acceptance of a 1.7- to 1.8-mm rms level of small-scale surface roughness gives excellent agreement with the measured curve. It should also be noted that the peak experimental efficiencies (without atmosphere) of DSS 43 and DSS 63 are virtually identical (0.454 for DSS 43 vs 0.451 for DSS 63).

The S-band holographic tests² carried out on this antenna in January 1985 indicate an rms surface error (for 0.4-m resolution) of 2.09 mm for a 64-m-diameter surface, and 1.74 mm for a 57-m-diameter surface, excluding the outer ring of panels. It was predicted that potential rms surface errors of 1.33 and 1.06 mm, respectively, would result after panel readjustment. Although panels were reset in August 1985, substantial improvement obviously did not result. The fact that both DSS 43 and DSS 63 show a 1.7- to 1.8-mm surface (as deduced by X-band GTD/Ruze calculations and experiment) supports the January 1985 holography measurements. The fact that the X-band efficiency measurements were made *after* the August 1985 panel reset indicates that there may exist some reflector surface irregularity (or a holography limitation) which is not allowing surface adjustment below the 1.7-mm rms level.

Holography produces a data type which optimizes reflector efficiency at the measurement angle, unless special measures are used to shift that data to a different elevation "rigging" angle. For DSS 43, the holography data were not shifted, and the measurement angle was 34 degrees. Had the holography measurement been carried out at 45 degrees and panels reset to optimize efficiency at that elevation angle, one would expect a rightward shift of the experimental curve in Fig. 9. This would improve the already good fit to the 1.8-mm theoretical curve seen in the figure.

The agreement between theoretical expectations and the DSS 63 and DSS 43 measurements is judged to be excellent.

²M. P. Godwin, et al., "Final Report on S-Band Holographic Tests on DSS-43 64 Metre Antenna," Report No. A079, Job No. 50/041, Eikontech Limited, Sheffield, England, September 1985.

Acknowledgment

The author wishes to thank the engineers at the Canberra DSCC, in particular G. Baines, A. Bailey, and R. Livermore, for their efforts in obtaining the data needed for this article. D. Bathker and K. Bartos at JPL provided many useful suggestions for additional analysis, especially regarding the comparison of PO, GTD, and experimental data.

References

- [1] S. D. Slobin, "DSS 63 64-meter antenna S- and X-band efficiency and system noise temperature calibration," *TDA Progress Report 42-90* (this issue), vol. Apr.-June 1987, Jet Propulsion Laboratory, Pasadena, Calif., August 15, 1987.
- [2] J. A. Turegano and M. J. Klein, "Calibration radio sources for radio astronomy: Precision flux density measurements at 8420 MHz," *Astronomy and Astrophysics*, vol. 86, pp. 46-49, 1980.

Table 1. Adjustments to 100-percent area efficiency for calibration radio sources, DSS 43 64-m calibration, January 1987

Frequency	Radio Source	Adjustment Factor
S-Band (2285 MHz)	3C274	1.000
	3C218	0.975
	0521-365	1.01
X-Band (8420 MHz)	3C274	1.000
	3C218	0.98
	0521-365	0.86

Note: Source 0521-365 is not a DSN standard calibrator, and thus a large adjustment is not unexpected.

Table 2. Coefficients of second-order curve fits for antenna area efficiencies

$$\text{Efficiency} = a_0 + a_1\theta + a_2\theta^2$$

where θ = elevation angle, degrees

Coefficient/Parameter	S-Band (2285 MHz)	X-Band (8420 MHz)
	With Atmosphere (cf. Fig. 1)	With Atmosphere (cf. Fig. 3)
a_0	0.547454	0.3945515
a_1	8.882707E-04	2.388105E-03
a_2	-7.774209E-06	-2.639022E-05
Peak efficiency	0.57283	0.44858
Peak angle, deg	57.129	45.246
Standard deviation	0.00357	0.00506
	Without Atmosphere (cf. Fig. 2)	Without Atmosphere (cf. Fig. 4)
a_0	0.5705453	0.4185152
a_1	2.678935E-04	1.722039E-03
a_2	-2.833061E-06	-2.079413E-05
Peak efficiency	0.57688	0.45417
Peak angle, deg	47.280	41.407
Standard deviation	0.00359	0.00506

Table 3. Coefficients of fourth-order curve fits for S- and X-band system noise temperatures

$$T_{\text{system}} = a_0 + a_1\theta + a_2\theta^2 + a_3\theta^3 + a_4\theta^4$$

where θ = elevation angle, degrees

Coefficient/Parameter	S-Band (2285 MHz) ^a	X-Band (8420 MHz) ^b
	With Atmosphere (cf. Fig. 5)	With Atmosphere (cf. Fig. 7)
a_0	5.666247E+01	7.358913E+01
a_1	-2.363757E+00	-3.812552E+00
a_2	6.504466E-02	1.105952E-01
a_3	-8.282610E-04	-1.436480E-03
a_4	3.928624E-06	6.909606E-06
	Note: If $\theta \geq 75^\circ$, $T_{\text{system}} = 20.138$ K	Note: If $\theta \geq 70^\circ$, $T_{\text{system}} = 21.814$ K
Zenith noise temperature	20.138 K	21.814 K
Standard deviation	0.934 K	0.377 K
	Without Atmosphere (cf. Fig. 6)	Without Atmosphere (cf. Fig. 8)
a_0	3.770463E+01	4.703577E+01
a_1	-1.226025E+00	-2.124297E+00
a_2	3.422649E-02	6.186806E-02
a_3	-4.503180E-04	-7.958403E-04
a_4	2.211606E-06	3.778312E-06
	Note: If $\theta \geq 70^\circ$, $T_{\text{system}} = 18.234$ K	Note: If $\theta \geq 70^\circ$, $T_{\text{system}} = 19.233$ K
Zenith noise temperature	18.234 K	19.233 K
Standard deviation	0.905 K	0.313 K

^aS-band (2285 MHz) specifications: Maser S-TWM1; Block IV; RCP; S/N 4004; 3.01-K noise temperature.

^bX-band (8420 MHz) specifications: Maser X-TWM2; Block IIA; RCP; S/N 2010; 3.61-K noise temperature.

Table 4. Design expectation for 64-m antenna with dual hybrid mode feedhorn at 8420 MHz and 45-degree elevation angle using physical optics analysis.

Item	Loss, dB	Net Gain, dBi
1. 100% Area Efficiency		75.04
2. Illumination Amplitude	-0.454	
3. Illumination Phase	-0.146	
4. Forward and Rear Spillover	-0.210	
5. Subreflector Blockage	-0.170	
6. $m \neq 1$ modes	-0.035	
7. Cross polarization	-0.0004	74.02
8. Waveguide loss	-0.070	
9. Dichroic plate loss	-0.035	
10. VSWR	-0.039	
11. Quadripod Blockage	-0.677	
12. Main reflector panels		
Manufacturing (0.035 inches)	-0.430	
Setting (0.019 inches)	-0.127	
13. Subreflector		
Manufacturing (0.012 inches)	-0.051	72.59 (= 0.569 efficiency)

Note: The rms panel and subreflector tolerance = 0.04159 in. (1.06 mm)

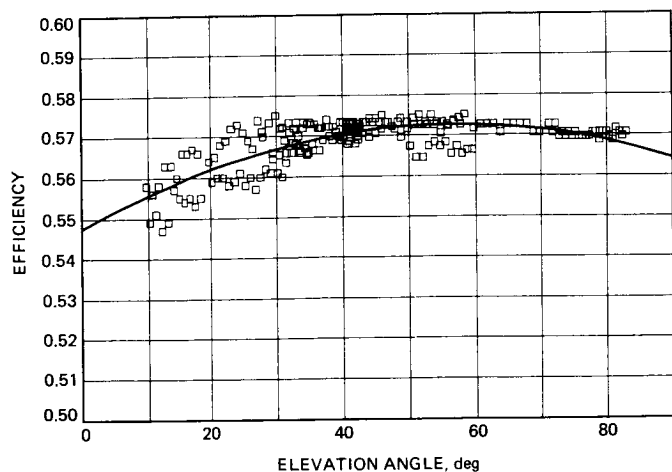


Fig. 1. DSS 43 64-m S-band (2285-MHz) area efficiency with atmospheric attenuation included

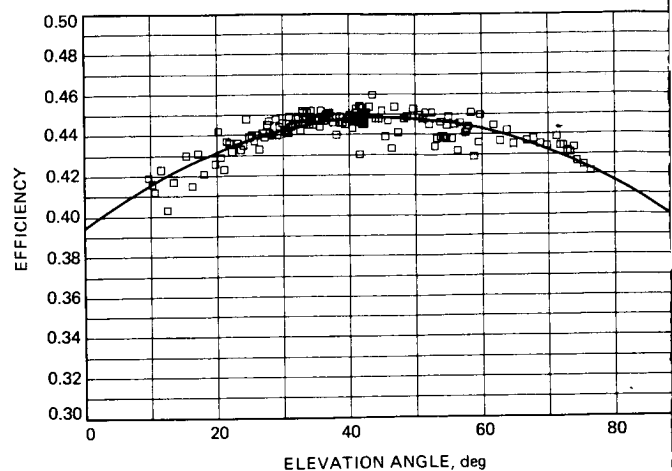


Fig. 3. DSS 43 64-m X-band (8420-MHz) area efficiency with atmospheric attenuation included

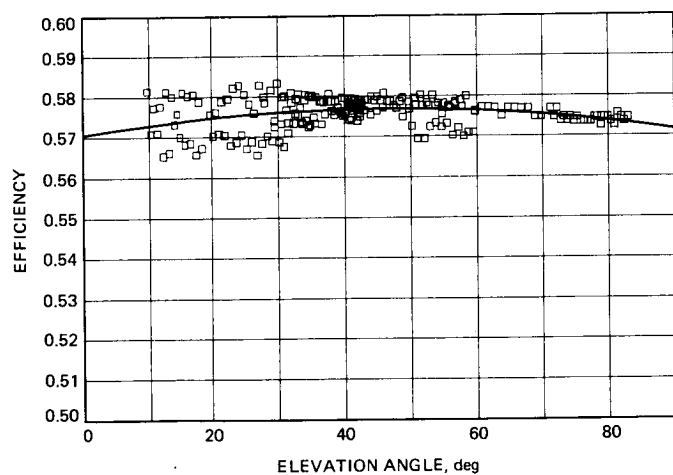


Fig. 2. DSS 43 64-m S-band (2285-MHz) area efficiency without atmospheric attenuation

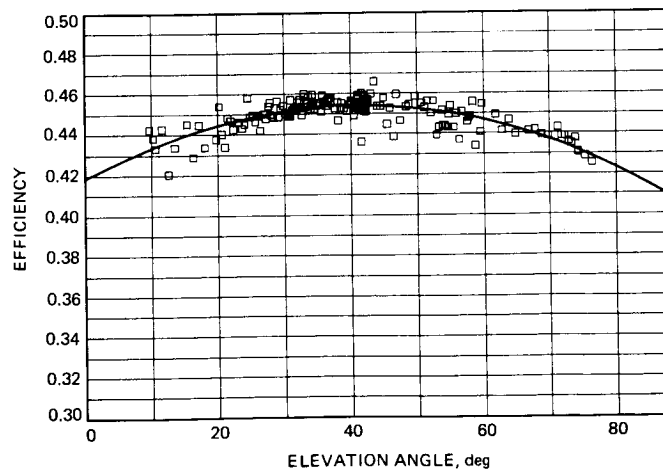


Fig. 4. DSS 43 64-m X-band (8420-MHz) area efficiency without atmospheric attenuation

ORIGINAL PAGE IS
OF POOR QUALITY

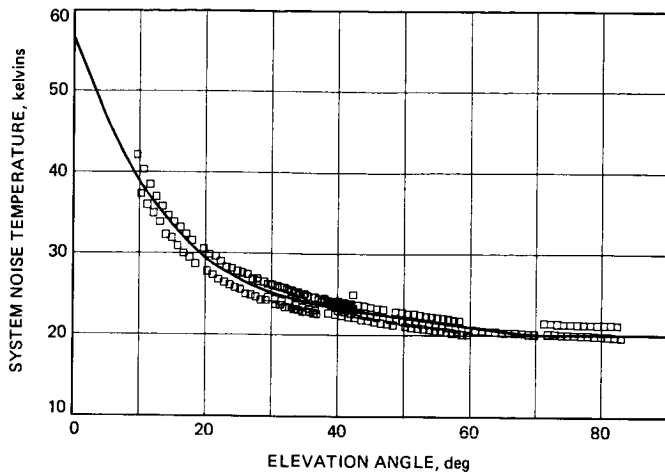


Fig. 5. DSS 43 64-m S-band (2285-MHz) system noise temperature, including atmospheric contribution

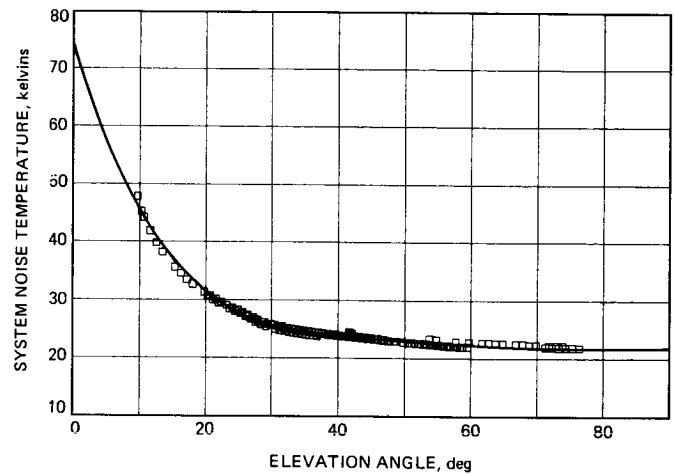


Fig. 7. DSS 43 64-m X-band (8420-MHz) system noise temperature, including atmospheric contribution

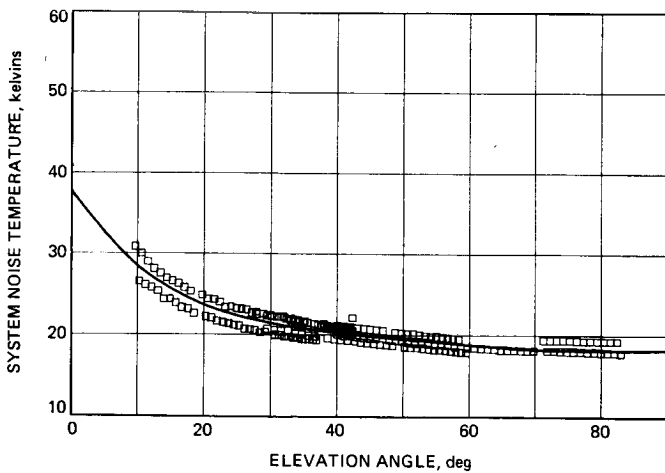


Fig. 6. DSS 43 64-m S-Band (2285-MHz) system noise temperature, without atmospheric contribution

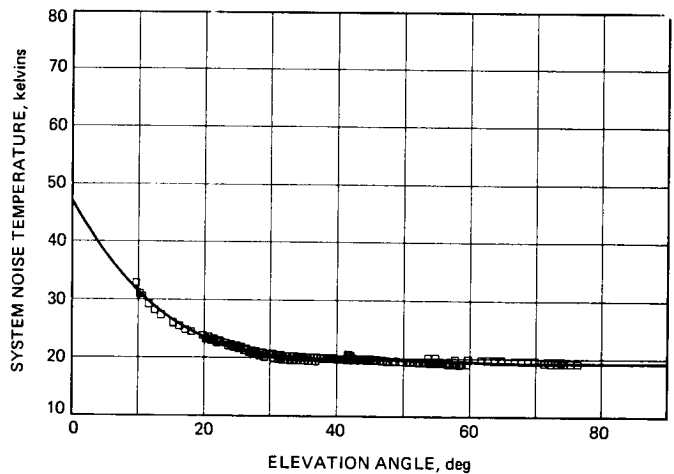


Fig. 8. DSS 43 64-m X-band (8420-MHz) system noise temperature, without atmospheric contribution

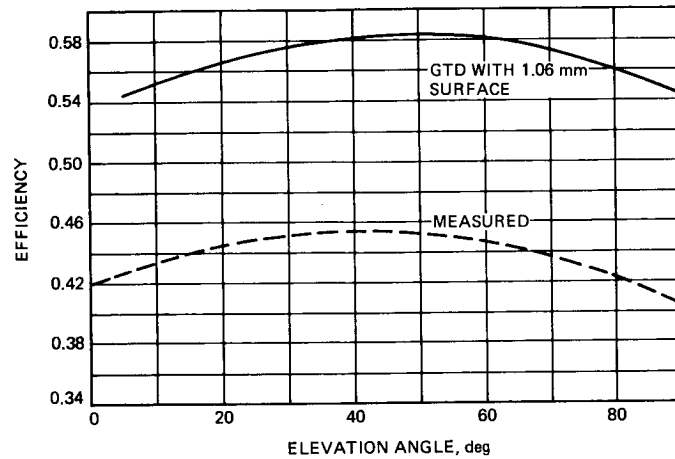


Fig. 9. Comparison of DSS 43 64-m GTD-calculated efficiency (with 1.06-mm rms Ruze surface tolerance) and measured efficiency

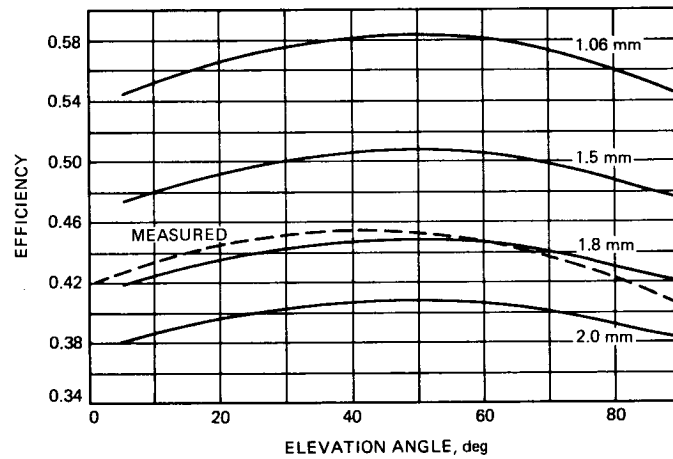


Fig. 10. Comparison of DSS 43 64-m GTD-calculated efficiency and measured efficiency for various Ruze surface tolerance values

ORIGINAL PAGE IS
OF POOR QUALITY

DSS 43 Antenna Gain Analysis for Voyager Uranus Encounter: 8.45-GHz Radio Science Data Correction

S. D. Slobin and W. A. Imbriale

Radio Frequency and Microwave Subsystems Section

A malfunction of the DSN 64-meter antenna in Australia forced the antenna to operate with a mispositioned subreflector during the Voyager Uranus encounter period (January 24, 1986). Because of changing main reflector shape and quadripod position as a function of elevation angle, the antenna gain and pointing were not as expected, and the 8.45-GHz received signal level changed during the pass. The study described here used Geometrical Theory of Diffraction (GTD) analysis to determine actual antenna gain and pointing during that period in an attempt to reconstruct the radio science data. It is found that 1.4 dB of signal variation can be accounted for by antenna geometry changes and pointing error. Suggested modifications to the values measured during the pass are presented. Additionally, an extremely useful tool for the analysis of gravity-deformed reflectors was developed for use in future antenna design and analysis projects.

I. Introduction

A series of DSS 43 64-m antenna system failures during the Voyager Uranus encounter on January 24, 1986, affected the quality of radio science data taken during the occultation phase of the encounter. In particular, an antenna elevation angle encoder failed and was removed from service (disconnected). This failure, in turn, caused the subreflector controller (SRC) to command the subreflector to move as though it were operating in its normal gain-peaking mode, although at a much faster rate. After about 12 minutes, the subreflector movement was automatically stopped because of a previously planned decision to turn off the SRC. The antenna continued to track the spacecraft for the rest of the pass, but the antenna had a mispositioned subreflector, which affected both antenna gain and pointing. All calculations described here were carried out for a frequency of 8.45 GHz.

This article presents the results of a study undertaken to analyze antenna performance using JPL-developed GTD (geometrical theory of diffraction) computer programs and other programs¹ to determine antenna shape as a function of gravity loading at different elevation angles. These programs define the geometry of the problem, taking into consideration quadripod sag and subreflector position, in order to determine antenna gain and pointing with respect to spacecraft location.

It was planned that during the encounter sequence, the gain-peaking would be turned off, because the subreflector motion required to make the correction would introduce unwanted

¹T. Veruttipong, D. Rochblatt, W. Imbriale, V. Galindo, *Dual Shaped and Conic GTD/Jacobi-Bessel Analysis Programs, A User Manual*, JPL D-2538 (internal document), Jet Propulsion Laboratory, Pasadena, Calif.

phase error in the received signal. It was determined that normal tracking would continue until the antenna reached an elevation angle of 64 degrees. Previous to this time, both y (vertical) and z (axial) subreflector movements were made to continuously peak the gain during the track. In addition, antenna pointing correction (squint correction) was made to reposition the beam on the spacecraft, since the y - z subreflector motion moved the beam continuously. Above 64 degrees elevation, the subreflector would remain fixed and pointing would be optimized by previous conscan use (discontinued a half-hour earlier). It was expected that the gain loss due to the lack of subreflector focusing would be acceptable.

The resultant condition of the antenna in its "failed" mode was this: (1) An initial step-function pointing error occurred due to the subreflector movement, not entirely compensated for by squint correction; (2) the pointing error changed throughout the pass as the antenna elevation approached or departed from the elevation angle corresponding to the failed subreflector position; (3) an initial step-function gain loss occurred because of a misfocused subreflector; and (4) this gain loss changed as the antenna elevation approached or departed from the elevation angle corresponding to the failed subreflector position.

II. Physical Description of Antenna Deformations

The gravity loading on large antennas causes quite large (up to 1 inch) deformations of surface shape, and causes movements of the quadripod structure that misposition the subreflector. The accepted coordinate system description for an azimuth-elevation antenna is that with the antenna pointing at the southern horizon, and an observer looking into the face of the dish, the $+y$ direction is at the top of the dish, $+x$ is toward the east/right edge of the dish, and the $+z$ axis comes out from the center of the dish toward the observer. Typically, the origin of this coordinate system is the center of the dish surface. This is not a requirement, however, as the dish shape can be defined in any coordinate system.

At a 45-degree elevation angle, the DSS 43 64-m antenna structure is designed and set to be "perfect," i.e., the main reflector is a perfect paraboloid, and the quadripod structure is located so that with the subreflector at some reference point, its virtual focus (on the concave side of the hyperboloidal subreflector) is coincident with the focus of the paraboloid. Thus, antenna gain is maximized and the resultant antenna beam is located precisely on the $+z$ axis. The DSN 64-m antennas have been designed to take into account structural deformations so that antenna pointing is maintained under gravity loading at elevation angles differing from 45

degrees [1]. In other words, when the antenna elevation changes from 45 to 60 degrees, the beam moves up to 60 degrees, not 59.9 degrees. Unfortunately, this design results in a slightly degraded antenna gain. To overcome the gain loss, the subreflector is repositioned in z and y axes to place its focus coincident with the best-fit focus of the distorted main reflector. The resulting pointing error is taken out by means of antenna movement known as "squint correction."

At angles higher than 45 degrees, the main reflector dish flattens out, its focal length increases, and the quadripod sags in both the $+y$ and $-z$ directions. The $-z$ movement can probably be explained by the base of the quadripod legs being pulled downward by the sagging backup structure. The distortions in the main reflector alone cause the beam to swing upward in the $+y$ direction. The sagging quadripod (also in the $+y$ direction) moves the subreflector, and this motion moves the beam back down toward the $-y$ direction. These effects nearly cancel out (to better than 0.010 degrees over the 35- to 75-degree elevation range). To recapture gain, the subreflector is moved (for this example) in the $+z$ and $-y$ directions. The resultant beam moves in the $+y$ direction, and this requires a downward (negative) squint correction. At 80-degree elevation angle, the subreflector movements for z and y are, respectively, 0.34 and -2.57 inches. The squint correction is -0.0938 degrees. For comparison, the 3-dB beam width of a 64-m antenna operating at X-band is approximately 0.036 degrees.

For antenna elevations of less than 45 degrees, the top edge falls forward, the dish deepens, the focal length is reduced, and the quadripod falls downward toward the ground and outward away from the main reflector. The dish movement pushes the beam down, and the quadripod movement brings it back. The required subreflector movement to peak the gain is inward ($-z$) and up ($+y$). At 10-degree elevation, the z and y movements are -0.57 and +1.34 inches, and the squint correction is +0.0488 degrees.

III. Computational Methods

All calculations used in this study began with a description of the main reflector. The x , y , and z coordinates of 275 points on one-half the dish surface (the $+x$ half-plane) were obtained from the JPL Ground Antenna Engineering Section.² The other half of the dish was developed, and the x , y , and z coordinates of the dish under gravity loading were calculated at elevation angles of interest using structural deformation values also obtained from that Section. The GTD technique requires

²R. Levy and M. S. Katow, Ground Antenna and Facilities Engineering Section, Jet Propulsion Laboratory, Pasadena, Calif., personal communication, July 1986.

what is known as a "global" description of the main reflector surface using Jacobi-Fourier polynomials [2]. The resulting coefficients are used in the GTD program itself in order to calculate the field scattered by the main reflector. In this analysis, it is assumed that the subreflector is hyperboloidal in shape and does not change shape due to gravity loading.

The GTD program uses a geometrical theory of diffraction analysis to compute the scattered near fields from the subreflector and a physical optics analysis (Jacobi-Bessel algorithm) to compute the scattered far fields from the main reflector using the subreflector fields as input. The program can handle arbitrarily shaped surfaces for both the subreflector and main reflector with respect to the main reflector system. A complete description of the program is given elsewhere.³

Inputs to the GTD program include geometric descriptions of the feed system. In particular, the feedhorn (dual-mode hybrid horn) is located in the upper left feedcone (of three) as seen looking into the dish. The subreflector coordinate system is located at the phase center of the feedhorn at a 45-degree antenna elevation angle. Under sagged conditions, the subreflector coordinate system and feedhorn are considered to move with the quadripod structure. This movement must be given as input, along with Euler angle rotation of the subreflector coordinate system itself in the main reflector coordinate system. Under sagged conditions, the feedhorn must be moved in the subreflector coordinate system to locate it back in the feedcone (assumed not to move as a function of elevation angle change and gravity loading). An Euler angle rotation of the feedhorn is necessary to adjust the polarization of the far-field pattern.

Thus, with the global surface description of the main reflector, and geometric inputs of subreflector and feedhorn position, the far-field Jacobi-Bessel coefficients can be calculated and the far-field gain and pointing for the antenna can be determined. By defining a center of expansion for the far-field coefficients, computational time may be reduced if one can quickly locate the antenna beam and examine its structure with fine resolution of the far-field coordinates.

IV. Results

The results of this study are given in the set of curves presented here. These curves show DSS 43 antenna performance during the Voyager Uranus occultation period (1986 024/2100 to 025/0300 GMT).

Figure 1 shows antenna elevation angle during the pass. Meridian transit is at 23:07:41 GMT at an elevation angle of

77.78 degrees. The actual spacecraft occultation occurred between about 23:20 and 00:40 GMT.

Figure 2 shows what the gain during normal operation of the antenna would have been with proper subreflector y and z focusing and perfect antenna pointing. The gains shown in these figures include only losses due to aperture illumination, feed and subreflector spillover, phase error, and cross-polarization. Other loss sources from small-scale surface roughness (Ruze loss), quadripod blockage, dissipative loss, and VSWR are not included. These losses are constant as a function of elevation angle and do not affect the results of the study presented here. Actual gain is approximately 2-dB less than shown in the figure. All curves of antenna gain show the inherent quality of the antenna as a function of main reflector shape and subreflector position only. They may be interpreted as the operational gain of the antenna when the beam is pointed perfectly at a spacecraft. Note that antenna gain is maximum at an elevation angle (Fig. 1) of 45 degrees.

Figure 3 is a combination of Figs. 1 and 2 and again shows a peak gain at an elevation angle of 45 degrees. Again, this is antenna performance with subreflector y - z focusing to peak up the gain. Because of computational resolution, the gain appears to be maximum over the range 45 to 50 degrees.

Figure 4 shows the position of the antenna beam relative to the main reflector z axis in the y - z plane. Note that y - z focusing to peak the gain causes relatively large movement of the beam. When the antenna is moved above 45-degree elevation, the beam ends up high. The opposite occurs below 45-degree elevation. The squint correction tables, which command antenna pointing to compensate for this beam movement, take their inputs from subreflector y and z position, and not from antenna elevation angle. In other words, the squint correction is not made as a function of elevation angle, but from subreflector position. In the DSS 43 problem being investigated here, the rapid subreflector movement over a 12-minute period caused a large and rapidly changing squint correction, even though the actual antenna elevation change was only 2 degrees. The beam movement predicted from GTD calculations differed slightly from that which was actually made using the squint correction tables. This is the source of the pointing error, resulting in a loss of received signal level (or equivalently, operational gain). The details of the squint correction error will be discussed later.

Figures 5-7 duplicate Figs. 2-4, differing only in the fact the GTD calculations were carried out with the subreflector fixed in a position corresponding to an elevation angle of 64 degrees. This is the position of the subreflector during a Voyager track 2 weeks before encounter, and was considered to be the "baseline reference signal level" with which actual encounter data would be compared.

³T. Veruttipong, et al., *op. cit.*

Figure 6 shows the gain versus elevation angle for the subreflector fixed at a position corresponding to the 64-degree elevation angle. Note the significant gain change, which is normally corrected with subreflector y - z focusing.

Figure 7 shows pointing versus elevation angle for the case with the subreflector fixed at 64-degree elevation. Note how pointing is maintained nearly constant when compared to the y - z focused case shown in Fig. 4.

Figures 8-10 are similar to Figs. 5-7, differing only in the fact that the subreflector is now in its failed position corresponding to an antenna elevation angle of 34 degrees. Figure 8 (gain versus time) shows the large loss experienced at meridian transit when the antenna elevation angle was 77.78 degrees.

Figure 9 shows gain versus elevation with the subreflector fixed at its 34-degree position.

Figure 10 shows antenna beam movement with elevation angle for a subreflector fixed at its 34-degree position. Note that the slope of this curve is the same as in Fig. 7. The beam position difference between the two curves is 0.063 degrees (approximately), almost two beamwidths of a 64-m antenna. This is the amount of beam movement that would be experienced during the uncontrolled subreflector movement if the antenna squint correction had been inoperative.

Figure 11 shows Figs. 2, 5, and 8 plotted on the same scale. Note that antenna gain with the subreflector fixed at the 64-degree position would have given performance nearly equal to the y - z focused subreflector for most of the pass. Only near the end of the pass, when the antenna was pointed at the lower elevation angles, would performance have been worse. The 34-degree subreflector case shows markedly degraded performance, except at the end of the pass, when its position was more nearly optimum for the low elevation antenna. All curves assume perfect antenna pointing and indicate the inherent gain of the antenna without regard to the spacecraft.

Figure 12 shows the gain advantage of y - z subreflector focusing compared to fixing the subreflector at a position corresponding to an antenna elevation of 64 degrees.

Figure 13 shows the gain advantage of y - z subreflector focusing compared to fixing the subreflector at a position corresponding to an antenna elevation of 34 degrees.

Figure 14 shows the gain loss (assuming perfect pointing) that would have been experienced under actual encounter conditions compared to performance measured 2 weeks

previously with the subreflector fixed at 64 degrees. This curve is the difference between the 64-degree and 34-degree curves in Fig. 11. Because there is an additional loss due to pointing errors, this curve is not sufficient to adjust the Uranus encounter radio science data.

Figure 15 shows the pointing error resulting from incorrect squint correction. Before the encounter sequence period, up until 20:35 GMT, the spacecraft was tracked using conscan. This ensured virtually perfect pointing and maximum gain with the subreflector y - z focusing in operation. After conscan was turned off, 35 minutes elapsed before the elevation encoder failed and uncontrolled subreflector movement began. It is assumed that pointing remained perfect for this time period. During the subreflector movement period (21:09:54 to 21:22:07 GMT), the SRC was still operational, and the antenna squint correction very nearly kept up with the changing antenna beam position derived by the GTD analysis. At 21:22:07 GMT, the damage had been completed. For purposes of this analysis it is assumed that a step-function beam position error occurred. It was determined that the actual beam movement as derived by GTD was 0.0589 degrees. The antenna squint correction (which responded to the moving subreflector) corrected for 0.0625 degrees, leaving a step-function pointing error of 0.0036 degrees at 21:22:07 GMT, the time of SRC shutoff. In the figure, pointing error from 21:09 to 21:22 should be considered unreliable. Before 21:09, the pointing should be considered perfect. At 03:00 GMT, conscan was again turned on and it was found that the pointing residuals were approximately 0.001 degrees. For the purposes of this study, it was assumed that perfect pointing was achieved at this time.

Figure 16 shows the signal loss expected from bad pointing (incorrect squint correction) only. The values are calculated using a method presented in the DSN/Flight Project Interface Design Document.⁴

Figure 17 shows the final result of this study. The curve shows the actual signal loss during encounter compared to the track 2 weeks previous (with the subreflector at its fixed 64-degree elevation position). It is assumed that perfect pointing, using conscan or otherwise, was achieved during the previous track. This curve contains all items affecting loss of spacecraft signal, including antenna main reflector distortion, subreflector mispositioning, and gain loss due to errors in

⁴Deep Space Network/Flight Project Interface Design Document 810-5, Rev. D, TCI-10, Rec. C (internal document), Jet Propulsion Laboratory, Pasadena, Calif., 1977 and 1983.

squint correction. The losses presented in this curve are calculated from those in Fig. 14, added to those given in Fig. 16. It is suggested that this curve be used to upwardly modify measured values during the actual encounter sequence by the losses given in this curve. The resulting curve should be compared to the values measured during the 2-week earlier Voyager pass. Any differences in the two should be attributed to planetary ring structure, planetary atmosphere, or other phenomena.

Another adjustment to the radio science data should be made to account for the attenuating effect of the earth's atmosphere. This problem has not been addressed in this study. A nominal 8.5-GHz clear-air attenuation of 0.04 dB per airmass could be used if real-time estimates of the effect are unavailable.

V. Conclusion

The study presented here shows the efficacy of using GTD analysis to sort out the effects of rather complex antenna geometrical conditions due to gravitationally deformed main reflector surface and nonoptimum subreflector position. Both inherent gain degradation and signal loss due to pointing error can be determined for a variety of situations, planned and unplanned. The analysis technique was applied to the problem arising from an incorrectly positioned subreflector during the Voyager Uranus encounter of January 1986. The study concludes that 1.4 dB of received signal level variation can be accounted for, 1.15 dB from antenna deformation and subreflector misfocusing, and 0.25 dB due to pointing error loss. These results can be applied to the Voyager radio science data to eliminate the antenna-dependent loss of the received signal data.

Acknowledgment

The authors wish to thank the following persons for their assistance in this study. R. Levy and M. S. Katow of the Ground Antenna Engineering Section provided the main reflector surface description for the DSS 43 antenna under the effect of gravity loading. A. G. Cha and T. Veruttipong provided much needed aid in sorting out the intricacies of the GTD software. E. M. Andres was invaluable in providing computational assistance using the JPL Univac computer.

References

- [1] M. S. Katow and M. Mori, *Computation of RF Boresight Direction From Reflector Distortions*, JPL Technical Report 32-1526, vol. XVII, pp. 78-82, Jet Propulsion Laboratory, Pasadena, Calif., 1973.
- [2] V. Galindo-Israel, et al., "Interpolation methods for GTD analysis of shaped reflectors, *TDA Progress Report 42-80*, October-December 1984, pp. 62-67, Jet Propulsion Laboratory, Pasadena, Calif., February 15, 1985.

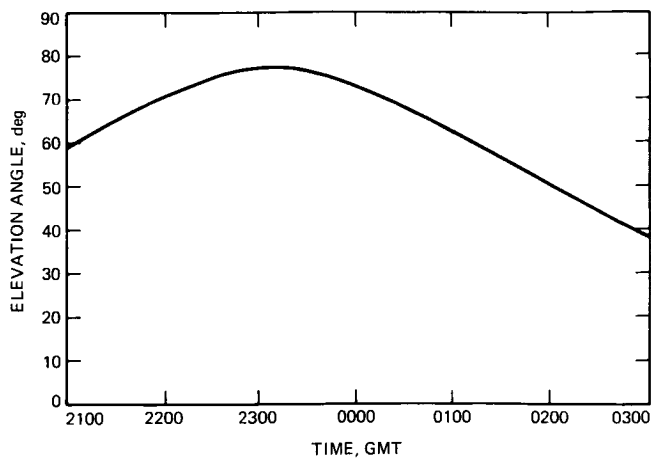


Fig. 1. DSS 43 antenna elevation angle vs time during Voyager Uranus encounter period

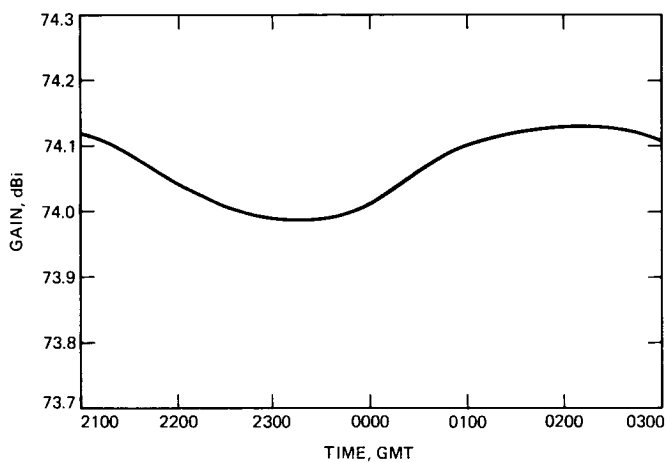


Fig. 2. Gain vs time with subreflector y and z focusing

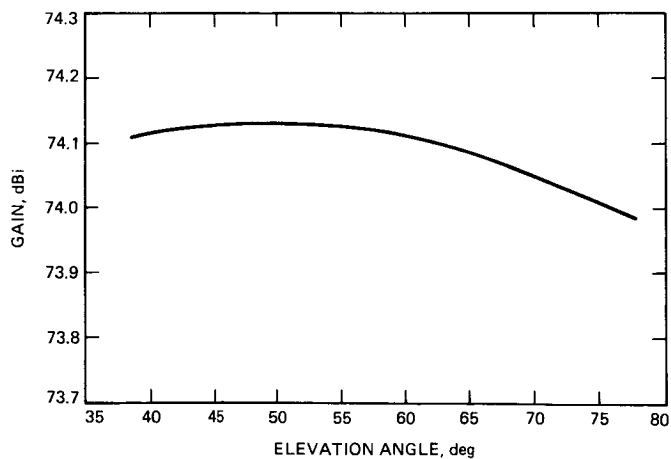


Fig. 3. Gain vs elevation angle with subreflector y and z focusing

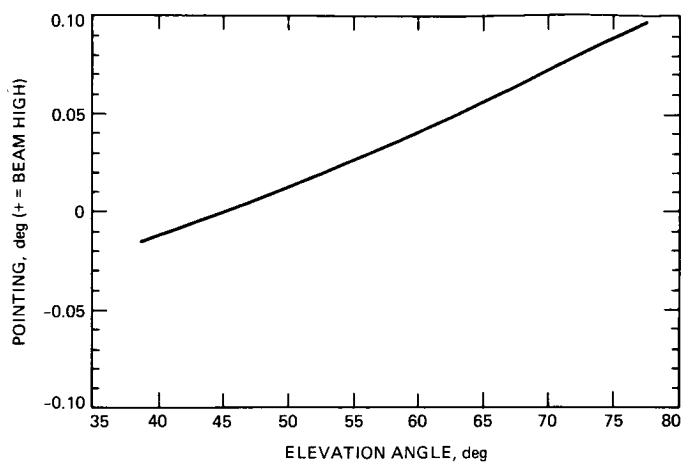


Fig. 4. Beam pointing vs elevation angle with subreflector y and z focusing

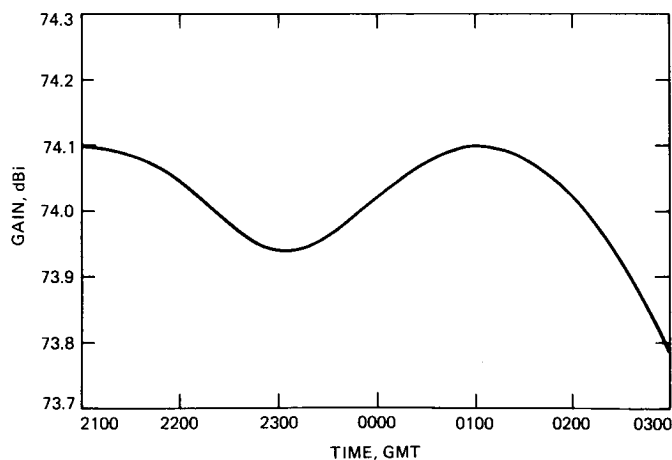


Fig. 5. Gain vs time with subreflector fixed at 64-degree elevation angle position

ORIGINAL PAGE IS
OF POOR QUALITY

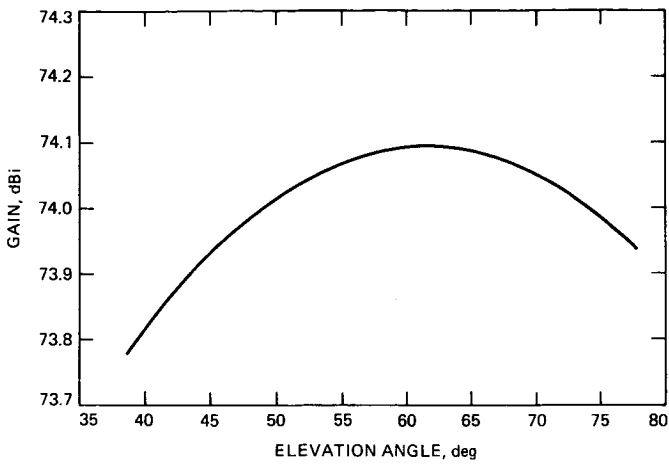


Fig. 6. Gain vs elevation angle with subreflector fixed at 64-degree elevation angle position

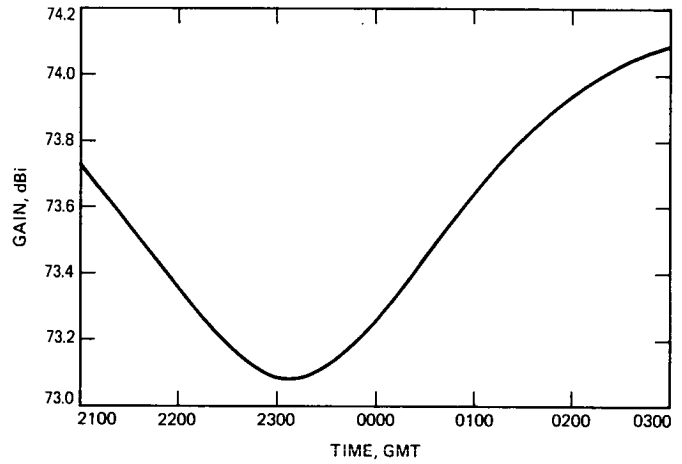


Fig. 8. Gain vs time with subreflector fixed at 34-degree elevation angle position

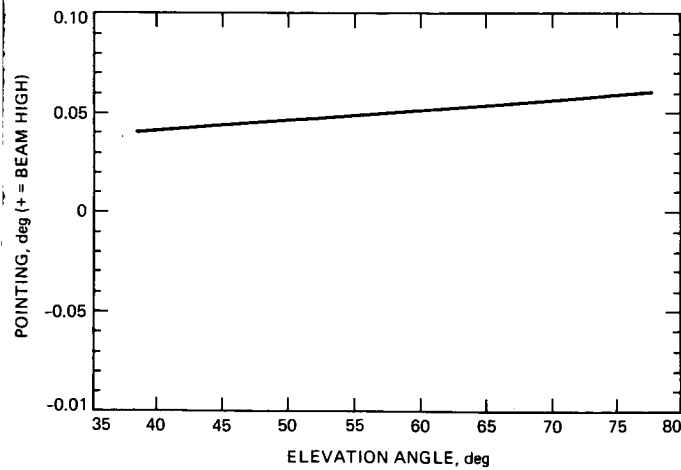


Fig. 7. Beam pointing vs elevation angle with subreflector fixed at 64-degree elevation angle position

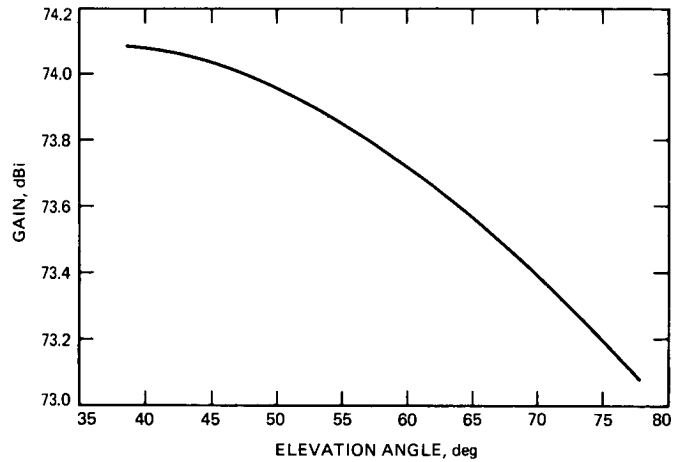


Fig. 9. Gain vs elevation with subreflector fixed at 34-degree elevation angle position

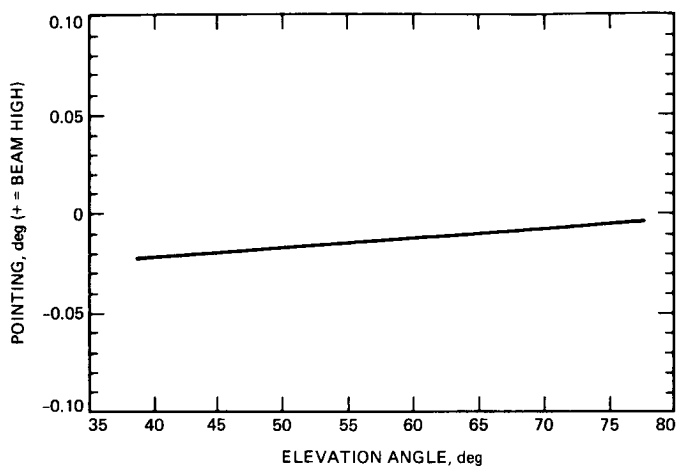


Fig. 10. Beam pointing vs elevation angle with subreflector fixed at 34-degree elevation angle position

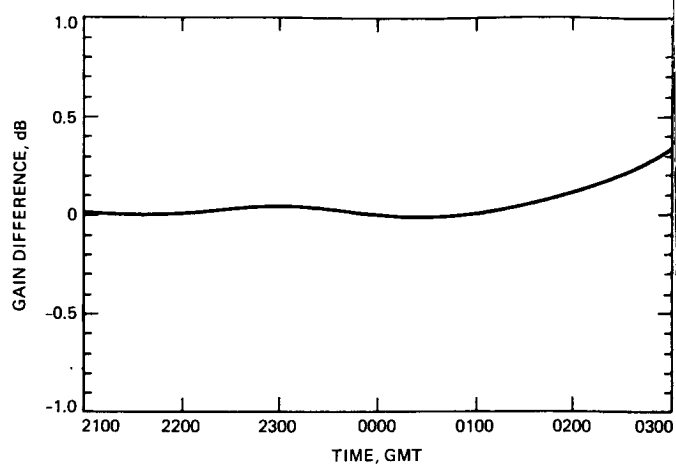


Fig. 12. Gain advantage of subreflector y-z focusing during encounter compared to subreflector fixed at 64-degree position

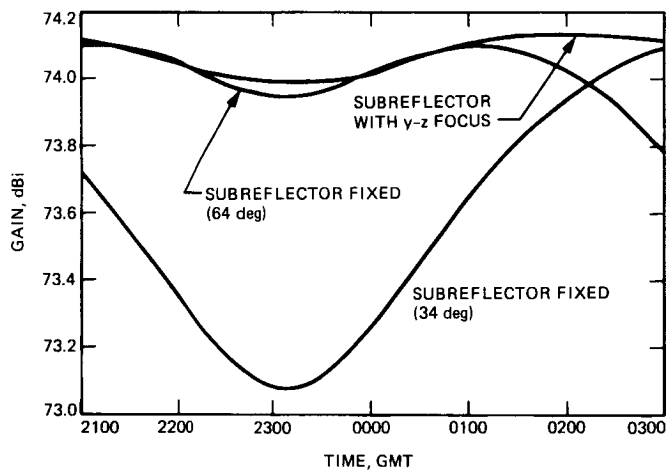


Fig. 11. DSS 43 antenna gain curves for different subreflector conditions, assuming perfect antenna pointing

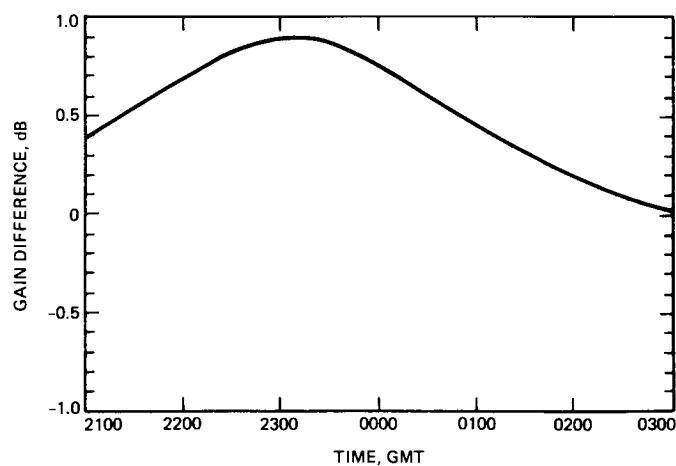


Fig. 13. Gain advantage of subreflector y-z focusing during encounter compared to subreflector fixed at 34-degree position

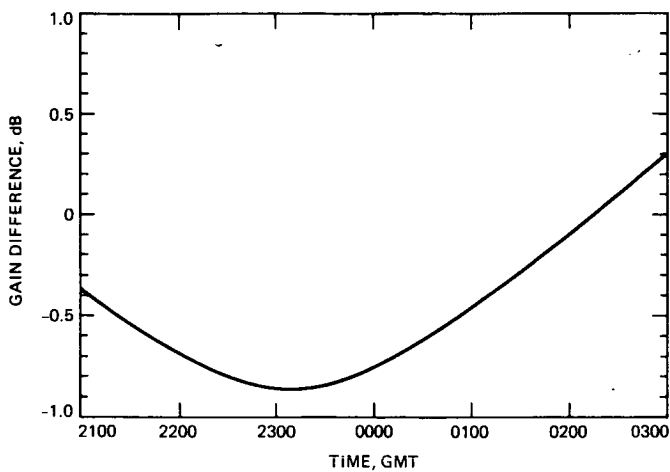


Fig. 14. Gain loss during encounter compared to 2-weeks previous performance, assuming perfect pointing ("—" equals loss)

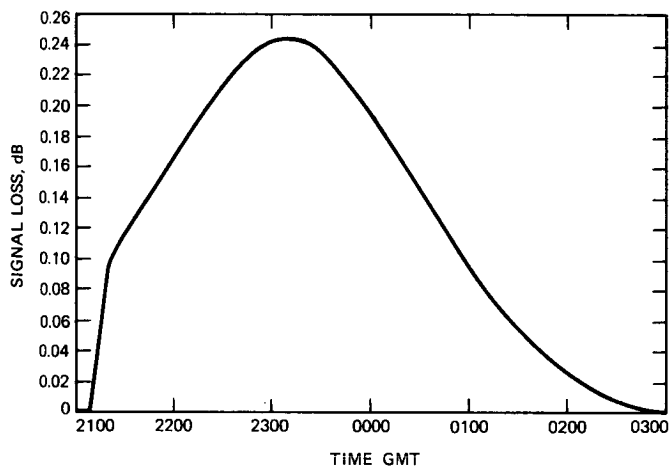


Fig. 16. Signal loss during encounter due to incorrect squint correction

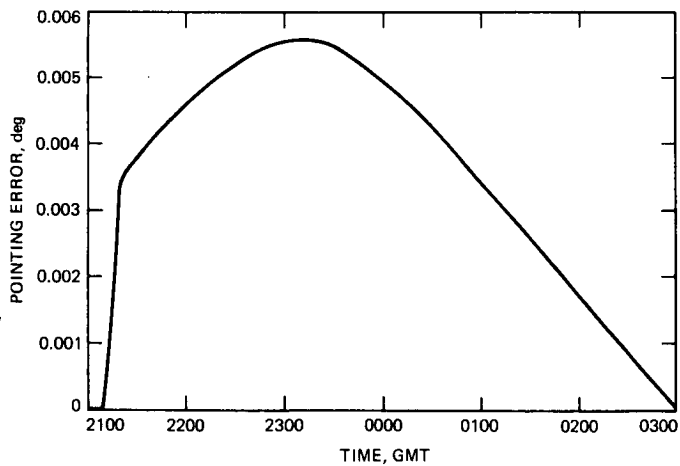


Fig. 15. Pointing error during encounter due to incorrect squint correction

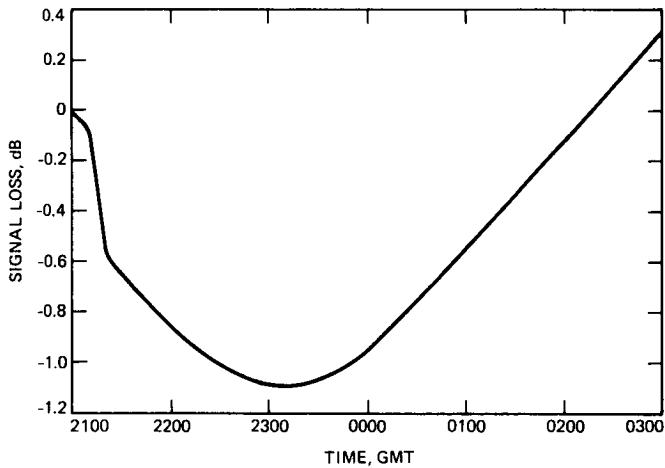


Fig. 17. Signal loss during encounter compared to earlier performance, due to both antenna gain loss and pointing error ("—" equals loss)

ORIGINAL PAGE IS
OF POOR QUALITY

A New Linear Quadratic Optimal Controller for the 34-Meter High Efficiency Antenna Position Loop

J. A. Nickerson

Ground Antenna and Facilities Engineering Section

This article explores the design of a new position loop controller for the 34-m High Efficiency Deep Space antennas using linear quadratic (LQ) optimal control techniques. The LQ optimal control theory is reviewed, and model development and verification are discussed. Families of optimal gain vectors were generated by varying weight parameters. Performance specifications were used to select a final gain vector. Estimator dynamics were selected and the corresponding gain vectors were computed. Final estimator selection was based on position, commanded rate, and estimator error responses.

I. Introduction

This article investigates the application of linear quadratic (LQ) optimal control technique for designing a new position loop tracking controller for the 34-m high efficiency ground based antenna. Most antenna controllers consist of an analog rate loop and a position loop closed with a computer. Two different types of control algorithms typically used for antenna position control are proportional-integral (PI) controllers and state feedback controllers.

Proportional-integral control is accomplished by applying gains to position error and the integral of position error. The summed result is used as a commanded rate for the rate loop. Zero steady state error to a ramp input (a type II system) is realized with a PI controller. This type of controller, however, can not arbitrarily specify the eigenvalues of the closed position loop.

A more sophisticated controller which can arbitrarily specify the eigenvalues of the closed position loop is state

feedback. This requires representing the control system as a set of first order differential state equations and multiplying each state by a gain. The summed results are used as a commanded rate for the rate loop. State feedback is more difficult to implement than PI control because PI controllers need only have knowledge of the position error while state feedback requires knowledge of all states. Unfortunately, many states are inaccessible to measure or state measurement is cost prohibitive. The use of a dynamic estimator, which estimates the value of each state based on a plant model and measurable states, solves this problem. The gains for implemented state controllers are often calculated based on designer selected eigenvalues.

The new approach explored in this article uses linear quadratic (LQ) optimal control to calculate families of gain vectors. Final gain selection is based on meeting desired performance criteria. After the control-gain design is completed, another design procedure is required for the estimator. Several estimator gains are designed and simulated with the

final control gain. Estimator gain selection is based on system performance specifications, minimal estimator error, and insensitivity to encoder and digital to analog (D/A) quantization.

II. Theory

The plant can be linearly modeled by a set of first order differential equations of the form:

$$\begin{aligned}\dot{\mathbf{x}} &= \mathbf{A}\mathbf{x} + \mathbf{B}\mathbf{u}; \mathbf{x}(0) = \mathbf{x}_0 \\ \mathbf{y} &= \mathbf{C}\mathbf{x}\end{aligned}\quad (1)$$

where \mathbf{x} is an $n \times 1$ state column vector; \mathbf{u} is a $1 \times m$ input row vector; \mathbf{y} is a $1 \times m$ output column vector; \mathbf{A} , \mathbf{B} , and \mathbf{C} are coefficient matrices of appropriate dimensions. A commonly used control design is state variable feedback:

$$\mathbf{u} = -\mathbf{K}\mathbf{x} \quad (2)$$

where \mathbf{K} is a feedback gain vector, not necessarily producing an optimum controller. Substituting Eq. (2) into Eq. (1) yields:

$$\begin{aligned}\dot{\mathbf{x}} &= \mathbf{A}\mathbf{x} - \mathbf{B}\mathbf{K}\mathbf{x} \\ \dot{\mathbf{x}} &= (\mathbf{A} - \mathbf{B}\mathbf{K})\mathbf{x}\end{aligned}\quad (3)$$

Equation (3) suggests that plant dynamics are modified by the feedback gain vector \mathbf{K} . State feedback is attractive because the closed loop eigenvalues of the system are arbitrarily specified by the proper selection of the feedback vector \mathbf{K} . Numerical procedures exist which calculate \mathbf{K} for a desired set of eigenvalues (see [4]). Although a designer can iterate a pole selection until the closed loop system meets performance criteria, there are no guarantees that the design is optimal.

The LQ optimal control technique for a linear system uses a quadratic performance index as an optimality criterion. Given the system description in Eq. (1) the quadratic performance index J is of the form:

$$J = \int_0^\infty (\mathbf{x}^T \mathbf{Q} \mathbf{x} + \rho \mathbf{u}^T \mathbf{R} \mathbf{u}) dt \quad (4)$$

where \mathbf{Q} is a positive semi-definite matrix, \mathbf{R} is a positive definite matrix, and ρ is a positive non-zero scalar. The first term penalizes transient deviation of the state from the origin. The second term penalizes the amount of control effort used to control the states. Terms \mathbf{Q} , \mathbf{R} , and ρ are weighting terms

which adjust penalties for transient deviation and control effort. The solution for the standard LQ problem is given elsewhere [1], [3], [4]; therefore, only the results are summarized below. The optimal steady state solution yields the control law:

$$\mathbf{u} = -\mathbf{K}\mathbf{x} \quad (5)$$

where

$$\mathbf{K} = \mathbf{R}^{-1} \mathbf{B}^T \mathbf{P} \quad (6)$$

\mathbf{P} is a symmetric positive semi-definite solution to the Riccati equation in matrix form:

$$\mathbf{A}^T \mathbf{P} + \mathbf{P} \mathbf{A} + \mathbf{Q} - \mathbf{P} \mathbf{B} \mathbf{R}^{-1} \mathbf{B}^T \mathbf{P} = 0 \quad (7)$$

The steady state solution exists if the following conditions are met:

- (1) the controlled plant is controllable or can be stabilized,
- (2) the final time is $t = \infty$, and
- (3) $(\mathbf{A}, \mathbf{Q}^{1/2})$ is observable.

Numerical procedures are used to solve the Riccati equation and calculate \mathbf{K} knowing the system and weighting matrices (see [4]).

The LQ optimal design technique for state feedback control guarantees an infinite gain margin and a greater than 60 degree phase margin for continuous (analog) systems. The final implementation of this controller is a time-discretized (digital) form. Stability for the time-discretized case is degraded from the continuous case because of finite sampling time. Tomizuka [1] investigated gain and phase margin for the discretized controller using:

$$\begin{aligned}\text{Gain Margin} &> \frac{1}{1 - \sqrt{\frac{\mathbf{F}}{\mathbf{F} + \mathbf{\Gamma}^T \mathbf{H} \mathbf{\Gamma}}}} \\ \text{Phase Margin} &> 2 \sin^{-1} \left\{ \frac{1}{2} \sqrt{\frac{\mathbf{F}}{\mathbf{F} + \mathbf{\Gamma}^T \mathbf{H} \mathbf{\Gamma}}} \right\}\end{aligned}\quad (8)$$

where \mathbf{H} is the solution to the discrete version of the Riccati equation, \mathbf{F} is the product $\mathbf{R}\rho$, and $\mathbf{\Gamma}$ is the discretized version of \mathbf{B} . A complete discussion of the discretized case may be found in [1].

Implementation of state feedback requires knowledge of the entire state vector. When states are unmeasured they must be estimated. A closed-loop estimator is based on a plant

model and the weighted difference between the estimated and actual output. Figure 1 describes state feedback implementation using an estimator. The estimator equation takes the form of:

$$\dot{\hat{\mathbf{x}}} = \mathbf{A}\hat{\mathbf{x}} + \mathbf{B}\mathbf{u} + \mathbf{L}(\mathbf{y} - \mathbf{C}\hat{\mathbf{x}}); \hat{\mathbf{x}}(0) = \hat{\mathbf{x}}_0 \quad (9)$$

where \mathbf{L} is the estimator error gain vector and \mathbf{x} represents the estimated state vector. Rewriting Eq. (9) yields:

$$\dot{\hat{\mathbf{x}}} = (\mathbf{A} - \mathbf{L}\mathbf{C})\hat{\mathbf{x}} + \mathbf{B}\mathbf{u} + \mathbf{L}\mathbf{y} \quad (10)$$

Subtracting Eq. (10) from Eq. (1) produces the equation describing the estimator error dynamics.

$$\dot{\mathbf{e}} = (\mathbf{A} - \mathbf{L}\mathbf{C})\mathbf{e} \quad \mathbf{e} = (\mathbf{x} - \hat{\mathbf{x}}) \quad (11)$$

Equation (11) is similar to Eq. (3). The error dynamics can be shown to depend on the selection of \mathbf{L} . Therefore, error dynamics are selected and a pole placement algorithm is used to calculate the estimator gain vector.

The closed-loop system dynamics depend on the combined eigenvalues of the controller and the estimator. However, the controller design is independent of the estimator design because estimator gains do not alter controller dynamics and controller gains do not alter estimator dynamics.

III. Modeling

Before LQ design techniques were applied, a plant model was developed. Figure 2 presents the linear model of the rate loop for the 34-m high efficiency AZ-EL antenna. Simplifying the model by eliminating fast dynamics (i.e., using large negative eigenvalues) and normalizing yielded the transfer function:

$$G(s) = \frac{Y(s)}{U(s)} = \frac{491.2(0.94s + 1)}{s^2 + 46.18s + 491.2} \quad (12)$$

where $U(s)$ is the input rate in degrees per second and $Y(s)$ is output rate in degrees per second. The simplified model in Eq. (12) represents a rigid antenna without structural dynamics.

Verification of the simple rate loop model of Eq. (12) was accomplished by using an HP dynamic signal analyzer, model 3562A, to measure the swept-sinusoid frequency response of the elevation rate loop at DSS (Deep Space Station) 15. Figures 3 and 4 present the measured gain and phase responses, respectively. The gain and phase responses were curve fit to produce a transfer function model for comparison with the simplified theoretical model. Curve fit results are shown in Figs. 5 and 6. Goodness-of-fit is shown by com-

paring measured and curve fit data in Figs. 3 and 5 for gain response and Figs. 4 and 6 for phase response. The transfer function description of the curve fit is:

$$G(s) = \frac{472.1(0.12s + 1)(s^2 + 0.667s + 188.0)}{(s^2 + 55.4s + 472.1)(s^2 + 1.11s + 187.3)} \times \frac{(s^2 + 0.534 + 440.2)}{(s^2 + 0.610s + 422.6)} \quad (13)$$

Eliminating polynomials due to structural resonances in Eq. (13) yields:

$$G(s) = \frac{472.1(0.12s + 1)}{s^2 + 55.4s + 472.1} \quad (14)$$

Comparing Eq. (12) with Eq. (14) suggests the model simplification of Eq. (12) was reasonable in the frequency range between 0.1 to 10 Hz.

Optimal control techniques require a state representation of the plant model. Transforming Eq. (12) into a diagonal canonical set of state equations of the form in Eq. (1) yielded:

$$\dot{\mathbf{x}} = \begin{bmatrix} -29.56 & 0 \\ 0 & -16.62 \end{bmatrix} \mathbf{x} + \begin{bmatrix} 8.217 \\ 4.62 \end{bmatrix} \mathbf{u} \quad (15)$$

$$\mathbf{y} = [8.217, -4.619] \mathbf{x}$$

where u is input rate and y is output rate. The state equations were then augmented to include position and integral of position states. Augmenting required increasing the dimension of \mathbf{A} from 2×2 to 4×4 , the dimension of \mathbf{B} from 2×1 to 4×1 , and the dimension of \mathbf{C} from 1×2 to 1×4 .

$$\begin{pmatrix} x_1 \\ x_2 \\ x_3 \\ x_4 \end{pmatrix} = \begin{bmatrix} 0 & 1 & 0 & 0 \\ 0 & 0 & 8.217 & -4.619 \\ 0 & 0 & -29.56 & 0 \\ 0 & 0 & 0 & -16.62 \end{bmatrix} \begin{pmatrix} x_1 \\ x_2 \\ x_3 \\ x_4 \end{pmatrix} + \begin{bmatrix} 0 \\ 0 \\ 8.217 \\ 4.619 \end{bmatrix} u \quad (16)$$

The new states are integral of position, x_1 , and position, x_2 , the input u is a rate command. The augmented state equations with state feedback produce a type II position controller. A diagonal canonical form of the state equation was used to reduce computations for implementation and to ensure reasonable matrix numerical conditioning.

Equation (16) describes a regulator. Once a gain vector, K , was calculated, implementation required altering the regulator equations to track reference inputs. The position state became position error and integral of position became integral of position error.

IV. LQ Controller Design

The LQ design approach depends on weighting matrix selection. Relative magnitude of weighting determines the optimal result. Coefficient selection, however, is not intuitive and guidelines are helpful. Bryson and Ho [3] suggest the simple rule:

$$Q = \text{diag} \frac{1}{\|x_{i_{\max}}\|} \quad (17)$$

where $x_{i_{\max}}$'s are the maximum values allowed for the i th state. Off diagonal terms are zero. A unit step response suggests $x_{11} = 1$ (position error). Weighting position error and rate loop dynamics equally yielded:

$$Q_{22} = Q_{33} = Q_{44} = 1 \quad (18)$$

Assuming a 0.5 second rise time, $Q_{11} = 4.0$. Q_{11} will be less than 4.0 for longer rise times. R and ρ are scalars for a single input single output (SISO) system. Thus, R was set equal to 1 and only ρ was parameterized to vary control effort penalties. A continuous LQ formulation was used to calculate the control gain vector K . The sampling time for the controller was selected as 50 Hz because of the high rate loop bandwidth. The fast sampling time allowed computed continuous gain vectors to be used with the discretized system.

The optimal control gains were calculated for different Q_{11} and ρ combinations. Several families of gain vectors were computed for each Q_{11} by varying ρ . Table 1 lists the results of several control gain computations. The table contains calculated gains and resulting closed-loop eigenvalues for each $Q_{11} - \rho$ combination.

Each control gain design iteration was simulated using the model in Eq. (16). Figures 7, 8, 9, and 10 represent simulated 50 millidegree step responses for several control gain vectors. Each figure shows a family of curves based on gains resulting

from a constant Q matrix but with different ρ values. The figures show that smaller values of ρ , which reduce control effort penalties, produced a greater control effort and thereby reduced system overshoot and settling time. Larger values of Q_{11} increased step response overshoot and reduced settling time. System overshoot, as a function of Q_{11} is obtained from the corresponding closed-loop eigenvalues in Table 1. Increasing Q_{11} reduced system damping.

Performance specifications for this LQ controller require: (1) the closed position loop response have less than 40 percent overshoot for small position steps and (2) a minimum position loop bandwidth of 0.25 Hz. The step responses in Figs. 7, 8, 9, and 10 have overshoots less than 20 percent, and hence are acceptable. Bandwidth is limited by the presence of structural resonances. Rate loop structural resonances are as low as 2.3 Hz. The position loop bandwidth must be at least an octave below the first structural resonance; otherwise the position loop may excite the structural resonances. Therefore, the position loop bandwidth should remain below 0.43 Hz. Figures 11, 12, 13, and 14 are closed-loop frequency responses using gain vectors obtained from Table 1 which best satisfy the 0.43 Hz position loop bandwidth goal. The bandwidths range from 0.39 to 0.43 Hz. The four Q and ρ combinations which satisfy the bandwidth criterion are:

$$K_A : Q_{11} = 4 \quad \rho = 1.5 \quad \text{bw} = 0.43 \text{ Hz}$$

$$K_B : Q_{11} = 2 \quad \rho = 1.0 \quad \text{bw} = 0.41 \text{ Hz}$$

$$K_C : Q_{11} = 1 \quad \rho = 0.6 \quad \text{bw} = 0.40 \text{ Hz}$$

$$K_D : Q_{11} = 0.5 \quad \rho = 0.4 \quad \text{bw} = 0.39 \text{ Hz}$$

Final gain vector selection was based on a performance index. The integral of time multiplied by absolute error (ITAE) index, I , was chosen because it places emphasis on errors occurring later in time [2]. The general form of the performance index is:

$$I = \int_0^T t |e(t)| dt \quad (19)$$

where T is the study period, t represents time, and $e(t)$ is the position error. The ITAE index was calculated for the four possible gain vectors with T equal to 5 seconds. K_A produced the lowest index value relative to K_B , K_C , and K_D and was selected as the final control gain.

Consequently, stability margins were calculated for control gain K_A using Eq. (8). The steady state discrete Riccati equation solution was calculated based on gain vector K_A . The gain

margin for the discretized system is 14.6 dB with a phase margin of 48 degrees. Gain and phase margin values indicate K_A is a robust controller design for the discrete system.

V. Estimator Design

The estimator design procedure consisted of selecting estimator dynamics and computing the estimator gain vector. The integral-of-position error is easily obtained in real time by numerical integration. Therefore, a third order estimator was designed. A discretized version of the third order plant model for 50 Hz implementation was used to calculate estimator gains. Equation (20) is the discretized third order model.

$$\mathbf{x}(k+1) = \begin{bmatrix} 1 & 0.1268 & -0.7922 \\ 0 & 0.5437 & 0 \\ 0 & 0 & 0.7150 \end{bmatrix} \mathbf{x}(k) + \begin{bmatrix} 0.01167 \\ 0.0979 \\ 0.0679 \end{bmatrix} u(k) \quad (20)$$

where k represents discrete time. Eight sets of dynamic parameters were selected and an estimator gain vector calculated for each set. Table 2 presents the pole locations and calculated gain vectors for each design iteration. Estimator and controller gains were simulated using the curve fit rate loop with structural dynamics as the actual plant. Plant output rate was integrated to calculate position. Encoder and D/A quantizing effects were also simulated. Estimator performance was based on position response, command rate, and estimator error. The position response should display the same performance as discussed under controller design. Command rate is equivalent to the output of the D/A converter. Local monotonicity of the command rate response is desirable to eliminate the position controller exciting structural resonances. (Local monotonicity suggests that within a limited time frame the command rate is either steadily increasing or steadily decreasing.) Therefore, the command rate should be a smooth function. Estimator error (actual position minus estimated position) should be much less than one least significant bit of the encoder (0.0003433 degrees) for the 20-bit encoder. Satisfying this error criterion will maintain precision pointing and reduce possible limit cycling due to the accumulation of large estimator errors.

The results of the position, commanded rate, and estimator error responses were used to judge estimator dynamics. Figures 15, 16, 17, and 18 show position and commanded rate response simulations for estimators 2, 3, 4, and 7, respectively. The position response curves for all estimators are similar. Selecting the "best" estimator based on position response is difficult. Commanded rate responses were next analyzed.

Estimators 2, 4, and 7 produced commanded rate responses which do not have "good" local monotonicity; the commanded rate in Figs. 19, 21, and 22 oscillated between D/A quantization levels. Estimator 3 (Fig. 20) had between 60 percent and 84 percent fewer oscillations than the other estimators and produced the smoothest commanded rate response.

Local monotonicity is a function of estimator dynamics. Each new position quantization level causes a step in estimator error. Estimators respond to steps in error as a function of their eigenvalues. Estimators 2 and 4 have eigenvalues which cause overshoot in the estimator error response. The overshooting increased the estimator error and caused the loss of local monotonicity. On the other hand, estimator 7 has heavily damped eigenvalues. Estimator 7's error response could not respond quickly to changing position. Thus, sluggish response of estimator 7 reduced local monotonicity. Estimator 3 has the best response; the error response has no overshoot to changes in position yet its dynamics were fast. The fast, critically damped estimator response also has the smallest overall error. The selected control design uses the control gain vector K_A and the estimator gain vector L_3 .

VI. Summary

Linear quadratic (LQ) optimal control techniques were applied to developing a new type II, state feedback, antenna position controller. A simplified experimental transfer function model was developed and verified by curve frequency response data. The model was mapped into a diagonal canonical set of state equations which were augmented to include position and integral-of-position states. Weighting matrices were selected and families of optimal gains were calculated based on the augmented model. The closed-loop system was simulated with each gain vector and the "best" gain was selected based on meeting given performance specifications. The integral-of-position state was eliminated and the third order model was used to design a new state estimator. Estimator dynamics were selected and estimator gain vectors calculated. The selected control gain vector was simulated with each estimator gain vector using a high order plant model with model mismatch, structural resonances, and quantization affects. An estimator gain vector was selected which minimized quantizing effects and estimator error.

This article described LQ optimal controller and estimator design techniques for an antenna position controller. Final design selection was based on satisfying performance specifications. The performance specifications, however, are not necessarily optimal. Investigations are needed which will determine the optimal performance requirements for this system. Once new performance criteria are determined, the LQ optimal controller and the estimator can be redesigned.

Acknowledgements

The author thanks Dallas Cox, Hugh Smith, and John Engel for their help in system modeling and theoretical discussions.

References

- [1] M. Tomizuka, ME 232 Advanced Control Systems I, Class Notes, Univ. of Berkeley, CA, Dept. of Mechanical Engineering, 1984.
- [2] R. C. Dorf, *Modern Control Systems*. 3rd ed., Reading, Mass.: Addison-Wesley Publishing Co., 1983.
- [3] A. E. Bryson, Jr. and Y. Ho, *Applied Optimal Control*. Waltham, Mass.: Blaisdell Publishing Co., 1969.
- [4] G. F. Franklin and J. D. Powell, *Digital Control of Dynamic Systems*. Reading, Mass.: Addison-Wesley Publishing Co., 1980.

Table 1. Calculated control gain vectors and eigenvalues

Q_{11}	ρ	K_1	K_2	K_3	K_4	Eigenvalues (rad/s)
4	4	1.000	1.513	0.442	-0.6694	$-0.964 \pm j 0.789, -17.052, -30.298$
	2	1.414	1.854	0.563	-0.4246	
	1.5	1.633	2.024	0.628	-0.4472	
	1	2.000	2.300	0.740	-0.4772	
	0.5	2.828	2.903	1.009	-0.5175	
2	2	1.000	1.605	0.498	-0.3613	$-0.935 \pm j 0.663, -17.243, -30.672$ $-0.962 \pm j 0.670, -17.304, -30.797$
	1	1.414	2.008	0.665	-0.4037	
	0.9	1.491	2.081	0.697	-0.4091	
	0.5	2.000	2.559	0.923	-0.4310	
1	1	1.000	1.773	0.605	0.3435	$-0.912 \pm j 0.497, -17.468, -31.157$ $-0.951 \pm j 0.493, -17.582, -31.478$
	0.7	1.195	2.015	0.719	-0.3555	
	0.6	1.291	2.133	0.777	-0.3588	
	0.5	1.414	2.284	0.854	-0.3607	
	0.1	3.162	4.443	2.164	-0.2187	
0.5	1					$-0.95 \pm j 0.157, -17.940, -32.382$
	0.5	1.000	2.068	0.800	-0.3046	
	0.4	1.118	2.261	0.906	-0.3006	
	0.3	1.291	2.544	1.069	-0.2081	
	0.1	2.236	4.111	2.887	-0.1287	

Table 2. Calculated estimator gain vectors and eigenvalues

Estimator No.	L_α	L_1	L_2	L_3	Eigenvalues	
1	L_A	0.6645	3.409	0.3549	-10	$-50 \pm j 50$
2	L_B	0.9086	4.194	-4.396	-15	$-80 \pm j 80$
3	L_C	0.7253	-0.8109	-0.7709	-15	-25 -80
4	L_D	0.9387	1.109	-2.554	-10	-80 -100
5	L_E	0.0879	2.448	0.1223	-10	$-25 \pm j 25$
6	L_F	-0.1140	1.755	0.0189	-10	$-20 \pm j 5$
7	L_G	-0.1140	1.954	0.0312	-10	$-20 \pm j 10$
8	L_H	-0.1140	2.743	0.0796	-10	$-20 \pm j 20$

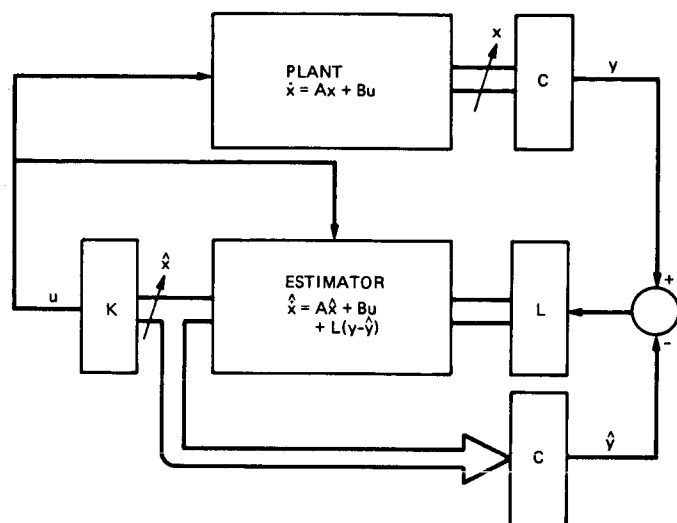


Fig. 1. State feedback with an estimator for a continuous time regulator

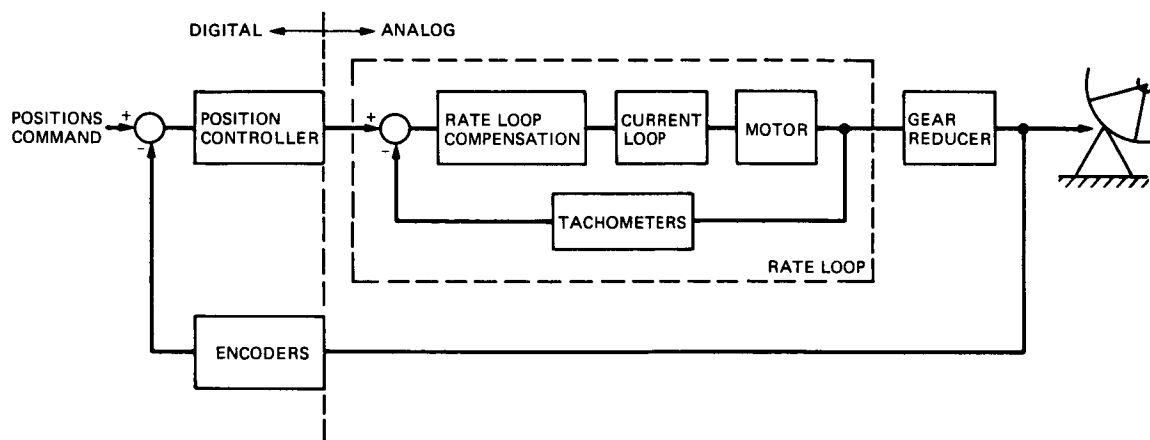


Fig. 2. Rate loop model

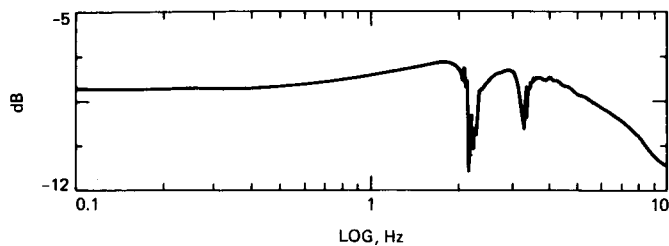


Fig. 3. DSS 15 elevation rate loop gain response

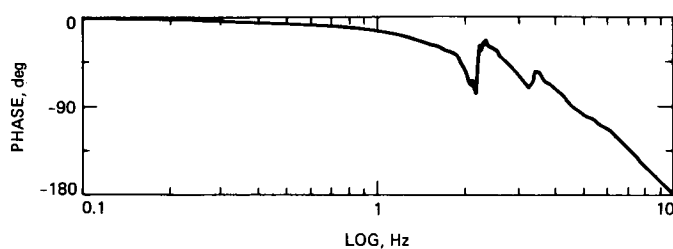


Fig. 4. DSS 15 elevation rate loop phase response

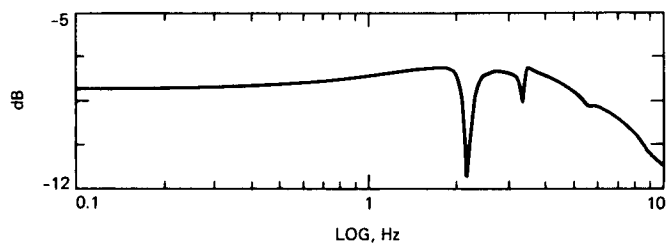


Fig. 5. Curve-fit gain response

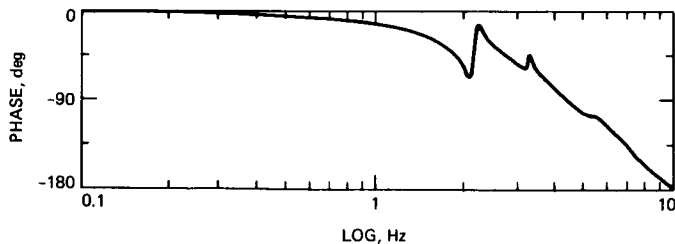


Fig. 6. Curve-fit phase response

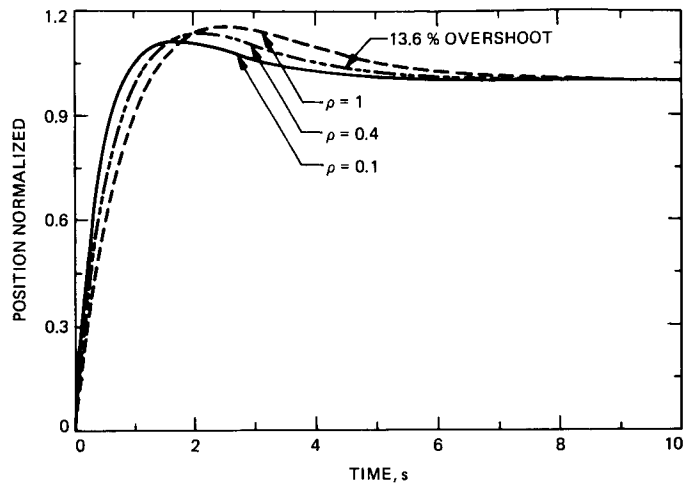


Fig. 7. Normalized step responses for $Q = 0.5$

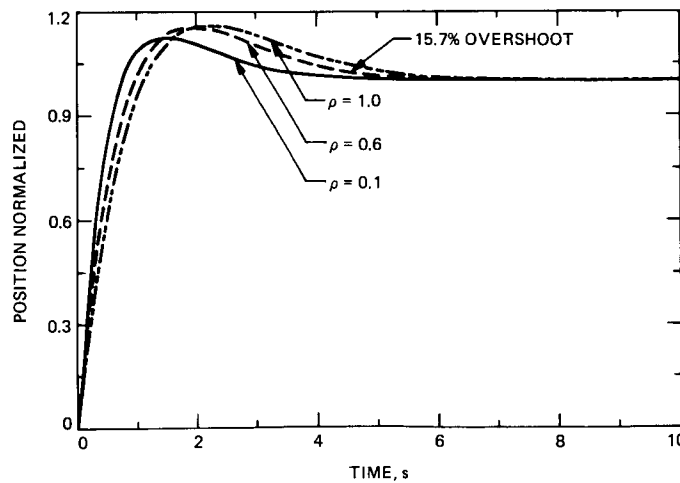


Fig. 8. Normalized step responses for $Q = 1.0$

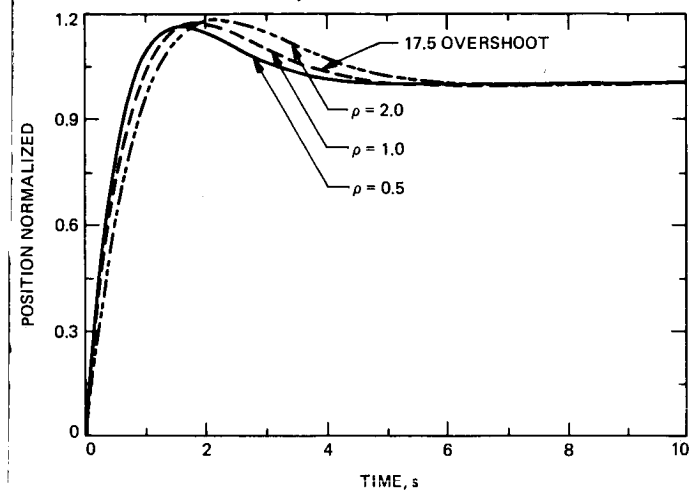


Fig. 9. Normalized step responses for $Q = 2.0$

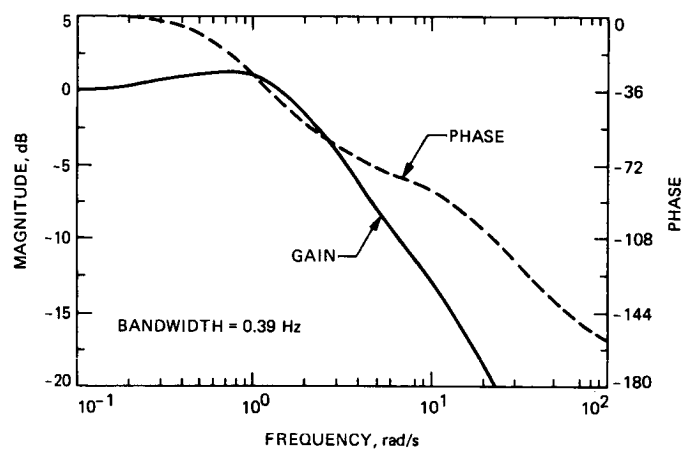


Fig. 11. Frequency response for $Q = 0.5$, $\rho = 0.4$

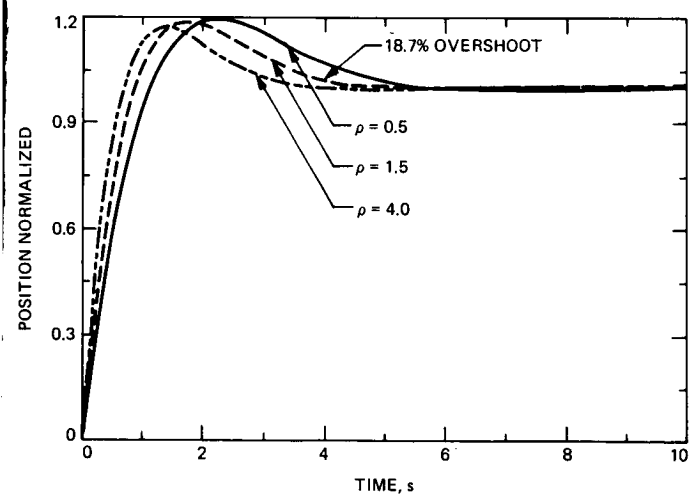


Fig. 10. Normalized step responses for $Q = 4.0$

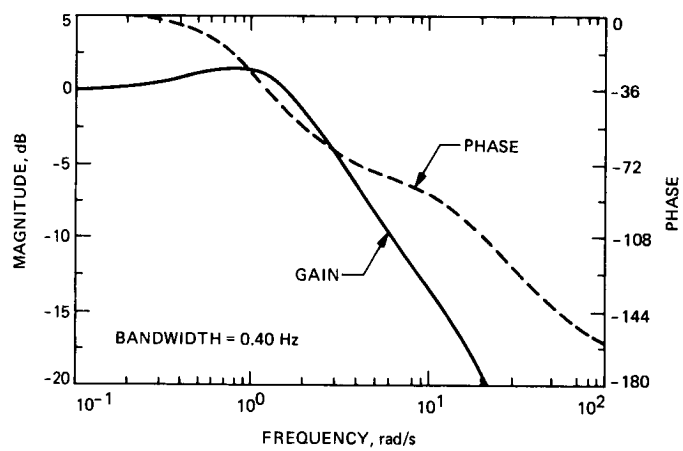


Fig. 12. Frequency response for $Q = 1.0$, $\rho = 0.6$

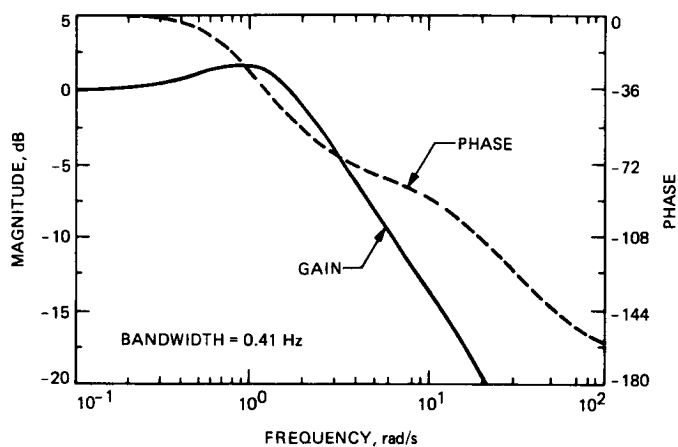


Fig. 13. Frequency response for $Q = 2.0$, $\rho = 1.0$

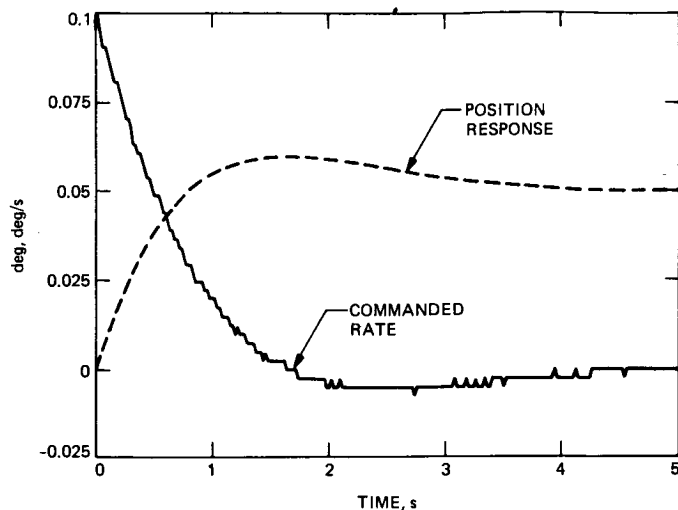


Fig. 15. Position and commanded rate responses for estimator 2

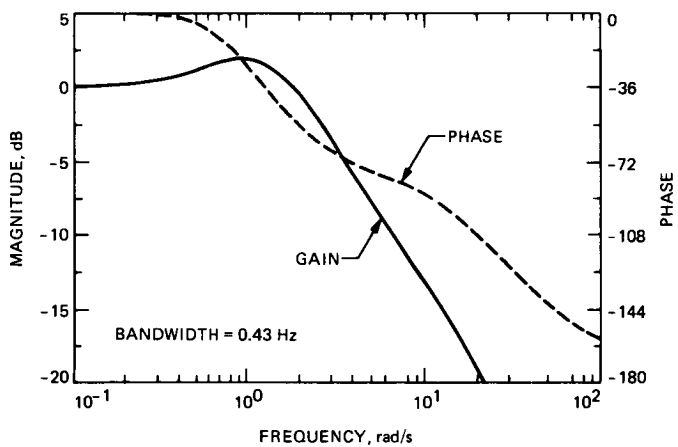


Fig. 14. Frequency response for $Q = 4.0$, $\rho = 1.5$

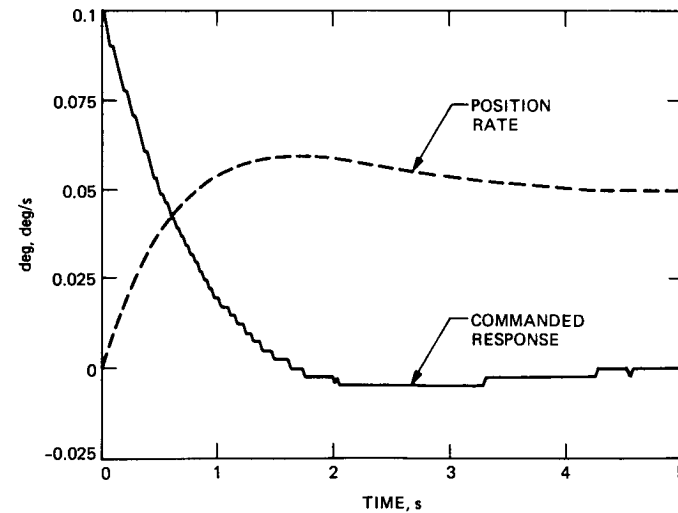


Fig. 16. Position and commanded rate responses for estimator 3

ORIGINAL PAGE IS
OF POOR QUALITY

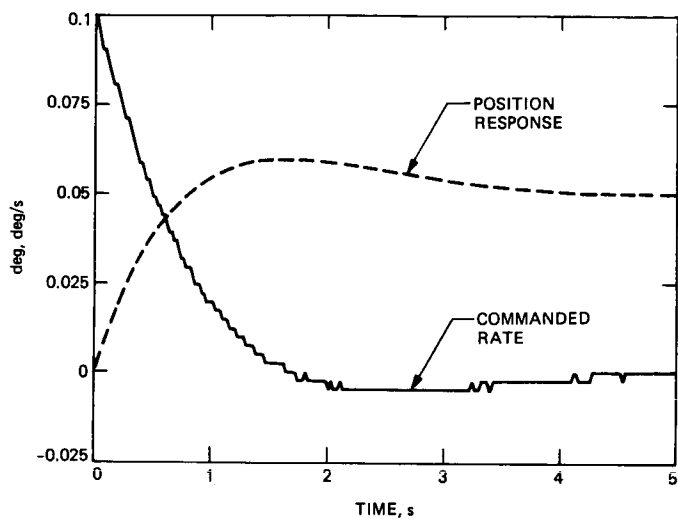


Fig. 17. Position and commanded rate responses for estimator 4

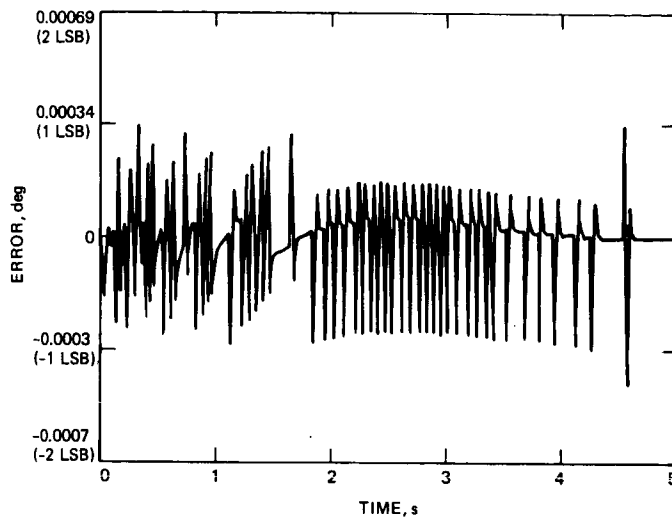


Fig. 19. Estimator 2's error response

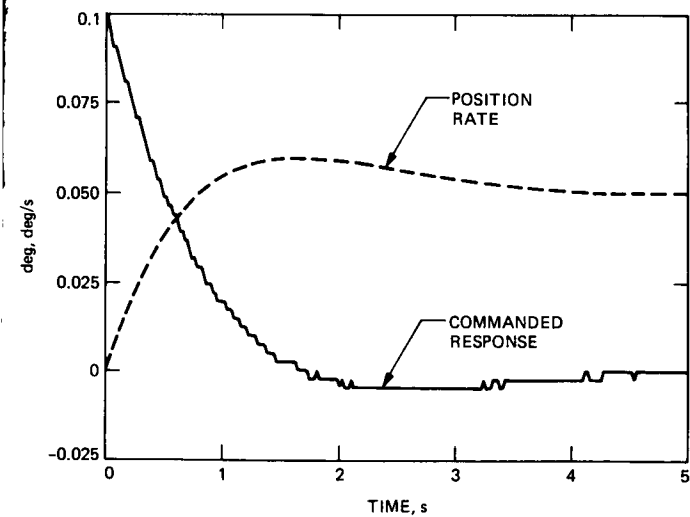


Fig. 18. Position and commanded rate responses for estimator 7

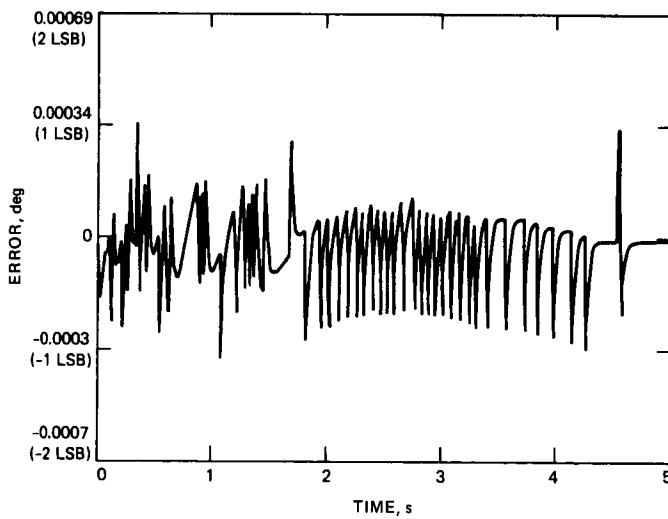


Fig. 20. Estimator 3's error response

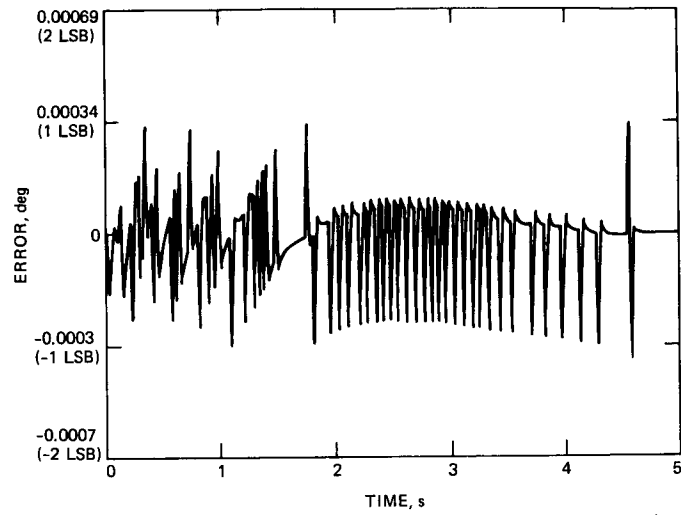


Fig. 21. Estimator 4's error response

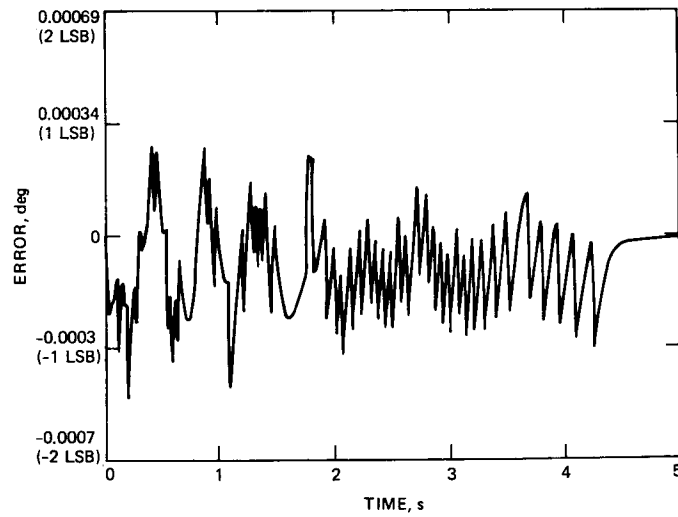


Fig. 22. Estimator 7's error response

A Method for Using a Time Interval Counter to Measure Frequency Stability

C. A. Greenhall

Communications Systems Research Section

This article shows how a commercial time interval counter can be used to measure the relative stability of two signals that are offset in frequency and mixed down to a beat note of about 1 Hz. To avoid the dead-time problem, the counter is set up to read the time interval between each beat note upcrossing and the next pulse of a 10 Hz reference pulse train. The actual upcrossing times are recovered by a simple algorithm whose outputs can be used for computing residuals and Allan variance. A noise-floor test yielded a $\Delta f/f$ Allan deviation of $1.3 \times 10^{-9}/\tau$ relative to the beat frequency.

I. Beat-Frequency Method

In the beat-frequency or single-mixer method of frequency stability measurement, the two sources to be compared must have a small frequency offset, typically in the neighborhood of 1 Hz. The two sources at frequency f_0 are mixed down to a sinusoidal beat note at the offset frequency f_b . This sine wave is passed through a zero-crossing detector, which produces a square wave at the same frequency. The relative time deviation or fractional frequency deviation of the two sources is equal to f_b/f_0 times that of the square wave or, more precisely, its stream of upcrossings, which are spaced approximately one second apart [1]. The improvement to be discussed below deals only with the measurement of these upcrossing times; the analog front end of the system remains the same.

II. Current Measurement System

In the current system used at the JPL Interim Frequency Standards Test Facility (IFSTF), the square wave beat note goes to a custom-built digital module, the Stevens-Sydnor

Machine, which latches the readings of a free-running 1 MHz 30-bit counter at the upcrossings and writes them to a 7-track tape, which is processed off-line by a Univac 1100 computer at the Information Processing Facility (Fig. 1). Actually, each Stevens-Sydnor Machine can handle three independent input channels and multiplex them onto the tape. Of course, the Univac software has to correct for the counter rollover, which happens about every 17.9 minutes. In this way, the upcrossing times are captured with a resolution of 1 μ s. Otoshi and Franco [2] have been using a system similar to the IFSTF's, but with a 10 MHz counter, to measure Deep Space Station stability.

Although the IFSTF system has given good service, it has several disadvantages. The counter resolution is too coarse for certain applications whose f_b/f_0 ratio is not small enough to put the quantization noise floor below the frequency instabilities to be measured. The 7-track incremental tape drives are obsolete, expensive to rent, and unreliable. (The author had to write a special software routine to recover from unreadable tape blocks.) The Stevens-Sydnor Machines have a problem

with input crosstalk; consequently, only one channel at a time can be used. The cumbersome off-line tape processing and graph plotting causes a turnaround time of several hours between running a test and seeing graphical results.

III. An Improved System—The Picket Fence

Because the frequency stability test operation is soon to be moved to the new Frequency Standards Laboratory, this is a good time to find a better way to carry out the tests and get timely results. High-quality commercial equipment for the job is already at hand; namely, a Hewlett Packard 1000 computer and several HP 5334A universal counters, which can measure time intervals with a 1 ns resolution and interface with the computer on an IEEE-488 bus. The problem has been that these are interval counters with dead time between measurements; unaided, such a counter can measure at most every other period of the stream of beat-note upcrossings. This dead-time limitation has now been overcome by the introduction of one more element, a 10 PPS (pulses per second) reference signal, called the Picket Fence, provided by a frequency standard and a divider.

A. Test Setup and Procedure

The new setup is shown in Fig. 2. The beat note square wave goes into Input A of the counter, the picket fence into Input B. The same frequency standard should drive both the counter and the divider to keep the picket fence coherent with the counter. In a multichannel system, each beat note has its own counter and there is only one picket fence signal going into all the B inputs.

To carry out a test, the Period A function of the counter is used to make a preliminary measurement of the period p of the square wave. It is permissible to use an increased gate time or the 100-reading average function when doing this measurement. Having measured the nominal period, the counter is switched to its Time Interval A to B function, and records all subsequent readings. Each reading is the time interval between an upcrossing and the next picket fence pulse. As long as the periods are not too short, the counter has time to reset itself between readings, and hence no upcrossing is missed. From these raw data, the actual upcrossing times are recovered in software by an algorithm discussed below. Figure 3 shows the time evolution of the measurement process.

B. Data Processing

Let d be the picket fence period (100 ms), p the initial period measurement, and v_0, v_1, v_2, \dots the sequence of time interval data. Let t_0, t_1, t_2, \dots be the actual upcrossing times relative to some time origin, perhaps one of the picket fence pulses (Fig. 3). Each t_n differs from the corresponding $-v_n$ by

an unknown integer multiple of d , and we would like to resolve the ambiguities.

Let Δ denote the backward difference operator, e.g., $\Delta t_n = t_n - t_{n-1}$. The following assumptions are made about the beat note:

- (1) The first period Δt_1 differs from p by less than $d/2$. Any two successive periods $\Delta t_{n-1}, \Delta t_n$ differ by less than $d/2$. This guarantees that the 100 ms ambiguities can be uniquely resolved.
- (2) Each period Δt_n is greater than $d + g$, where g is the maximum dead time of the counter. This just guarantees that no upcrossing is missed.

Since the t_n increase quickly and may contain important information in their least significant bits, they are awkward to compute, store, and use. Accordingly, the algorithm actually computes the sequence of time residuals defined by

$$x_n = t_n - t_0 - np, \quad n = 0, 1, 2, \dots \quad (1)$$

Figure 4 shows the relationship between the t_n and the x_n . The core of the algorithm is the signed residue function $\text{Smod}(x, m)$, which is defined to be x minus the closest integer multiple of m to x . For example,

$$\text{Smod}(3, 5) = \text{Smod}(-7, 5) = -2$$

If x is halfway between two integer multiples of m , then it doesn't matter whether $\text{Smod}(x, m)$ is defined to be $m/2$ or $-m/2$.

The algorithm that generates the x_n is given in Fig. 5. This version incorporates a mild error check (lines 10 and 13) to prevent one bad input from spoiling all the subsequent outputs. Appendix A gives a proof that the numbers defined by Eq. (1) are identical to the outputs x_n generated by the basic version of the algorithm, that is, with lines 10 and 13 removed. This is accomplished by forcing the second difference $\Delta^2 x_n$ to be less than $d/2$ in absolute value (in accordance with assumption 1) and also equal to $-\Delta^2 v_n$ modulo d . Nevertheless, experience has shown that some protection against bad data is needed. Table 1 shows what can happen to the basic version if there is one error with magnitude slightly greater than $d/4$. The starred value of ddx ($n=3$) has been converted by Smod from $-0.52d$ to $0.48d$. As a result, the x_n start to increase linearly. This can cause computational problems for a program that analyzes the x_n . The error check with threshold $d/4$ anchors the current bad data to the last good data. If Δx_m is the anchor dx_a at time n , and the condition in line 10 is satisfied at times n and $n+1$, then Δx_{n+1} is within $d/2$ of Δx_m . In the example, the anchor stays at

Δx_1 for $n = 2$ and 3. At $n = 4$, it is pulled up again. As a result, the x_n values go back to 0 after time 2. Time will tell whether this simple expedient is adequate in practice.

IV. Noise-Floor Test

In order to evaluate the technique, a single-channel hardware and software system was set up (Fig. 2). The HP 1000 collects the data in real time and stores the outputs of the unfolding algorithm on disk. At the same time, a user can process any portion of the test into residuals and Allan deviation. Results can be printed, plotted on screen, or plotted on a pen plotter.

To measure the ultimate noise floor of the technique and to test the integrity of the measurement system, an almost perfect beat note square wave was simulated by a low-rate pulse generator, which was stable at the nanosecond level, and whose period could also be programmed to the nearest nanosecond. The chosen period was

$$0.938196601 \text{ s} = (10 - r)d$$

where $d = 0.1 \text{ s}$, the picket fence period, and r is the Golden Ratio, $(\sqrt{5} - 1)/2$. This period guarantees a good mix of counter readings v_n [3, pp. 510, 511, 543]. If a conveniently available 1 PPS signal had been used, the counter would have always been reading the same value. The same frequency source, a cesium standard, was used for driving the counter, the picket fence, and the pulse generator. Thus, the results include instabilities and errors of the pulse generator, picket fence divider, and counter, but not of the measurement time base that drives these components.

A test of duration of 108,600 s was carried out. The accumulated time residuals, with the mean frequency offset removed (about 0.3 ns/s), remained within a 6 ns band over the entire run. The Allan deviation, shown in Fig. 6, is approximately $1.3 \times 10^{-9}/\tau$ for τ between 0.94 s and 11,500 s. This shows that all the equipment maintained time coherence at the nanosecond level and that the counter met its specifications.

To see what this means for an actual test of frequency sources, recall that these numbers must be scaled down according to the source and beat frequencies. For example, if two 1 MHz sources with a 1 Hz offset were being tested, the digital part of the measurement system would contribute a $\Delta f/f$ Allan deviation of $1.3 \times 10^{-15}/\tau$.

V. Conclusions

The technique described in this article is a method for measuring the stability of the square wave produced by mixing two offset frequency sources and passing the low-frequency sine wave through a zero-crossing detector. In contrast to the current IFSTF system, which uses custom digital hardware and has microsecond resolution, this technique uses commercial hardware of moderate cost (under \$3000 per counter) with an IEEE-488 interface, and offers nanosecond accuracy.

The author has recently learned of the existence of a unit that can latch the readings of a free-running counter with a precision of 1 ns for several input channels. The counter rolls over every 2^{24} ns, about 16.8 ms, so that in effect the counter makes its own picket fence with that period, and the same unfolding algorithm applies. A multichannel frequency stability measurement system built around this unit might be smaller and less expensive than one built around several interval counters in separate chassis.

Acknowledgment

I would like to give credit to G. J. Dick and R. E. Taylor for conversations that led to the ideas used in this article.

References

- [1] C. A. Greenhall, "Frequency stability review," *TDA Progress Report 42-88*, October-December 1986, pp. 200-212, Jet Propulsion Laboratory, Pasadena, Calif., February 15, 1987.
- [2] T. Y. Otoshi and M. M. Franco, "DSS frequency stability tests performed during May 1985 through March 1986," *TDA Progress Report 42-86*, April-June 1986, pp. 1-14, Jet Propulsion Laboratory, Pasadena, Calif., August 15, 1986.
- [3] D. E. Knuth, *The Art of Computer Programming*, vol. 3. Reading, MA: Addison-Wesley, 1973.

Table 1. State of the unfolding algorithm after line 9 ($d = 1$) with one bad input and no error handling

n	v	$v1$	$x1$	dua	dxa	du	ddx	dx	x
0	0			line 9 not applicable					0
1	0	0	0	10	0	0	0	0	0
2	-0.26	0	0	0	0	0.26	0.26	0.26	0.26
3	0	-0.26	0.26	0.26	0.26	-0.26	0.48*	0.74	1.00
4	0	0	1.00	-0.26	0.74	0	0.26	1.00	2.00
5	0	0	2.00	0	1.00	0	0	1.00	3.00
6	0	0	3.00	0	1.00	0	0	1.00	4.00

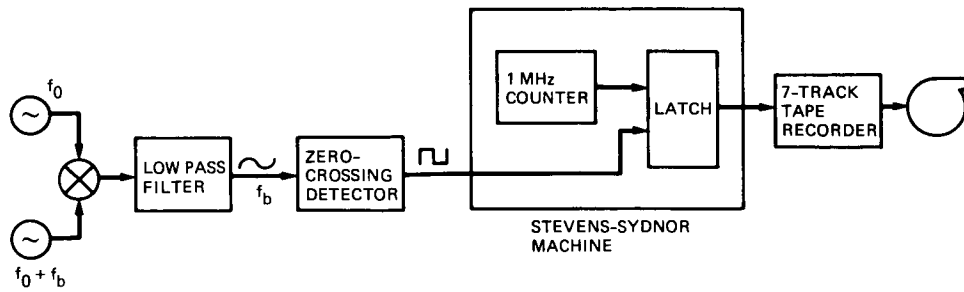


Fig. 1. Current IFSTF frequency stability measurement system

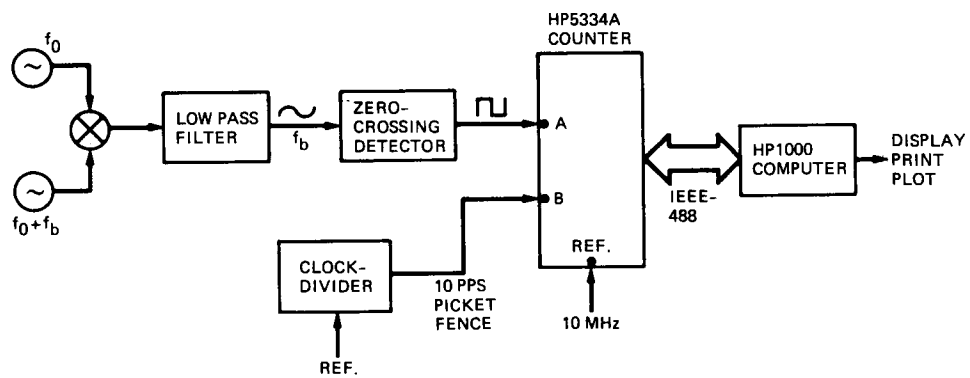


Fig. 2. Picket fence measurement system

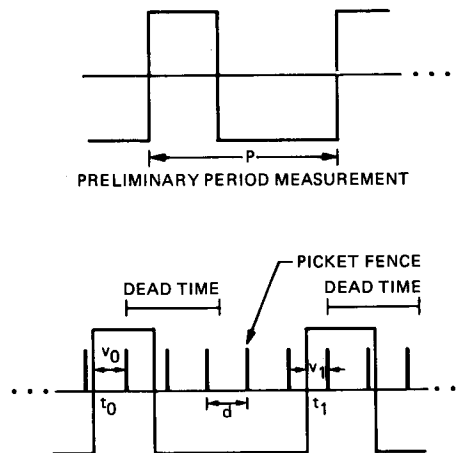


Fig. 3. Time evolution of the measurement process

ORIGINAL PAGE IS
OF POOR QUALITY

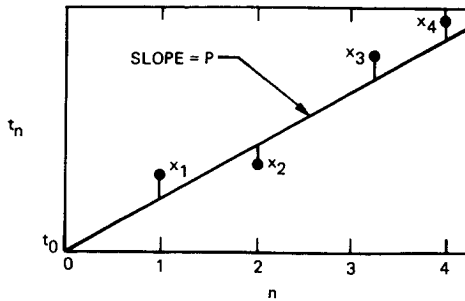


Fig. 4. Zero-crossing times and residuals

```
! Global parameters: p, d
Do for n = 0, 1, 2, ...
  Read v_n
  Call Unfold (n, v_n, x_n)
  Output x_n
Enddo

Subroutine Unfold (n, v, x)
! Inputs: n, v
! Output: x
! Local variables
! du : current du = -dv
! dx : current dx
! dua: du anchor
! dxa: dx anchor
! ddx: current dx - dxa or second difference
! v1 : previous v
! x1 : previous x
1. If n = 0 then
  ! Initialize
2.   dua = p
3.   dxa = 0
4.   x = 0
5. Else
6.   du = v1 - v
7.   ddx = Smod (du - dua, d)
8.   dx = dxa + ddx
9.   x = x1 + dx
  ! Error handling
10.  If |ddx| < d/4 then
    ! Data OK, drag anchor along
11.    dxa = dx
12.    dua = du
13.  Endif
14. Endif
15. x1 = x
16. v1 = v
17. Return
```

Fig. 5. Unfolding algorithm

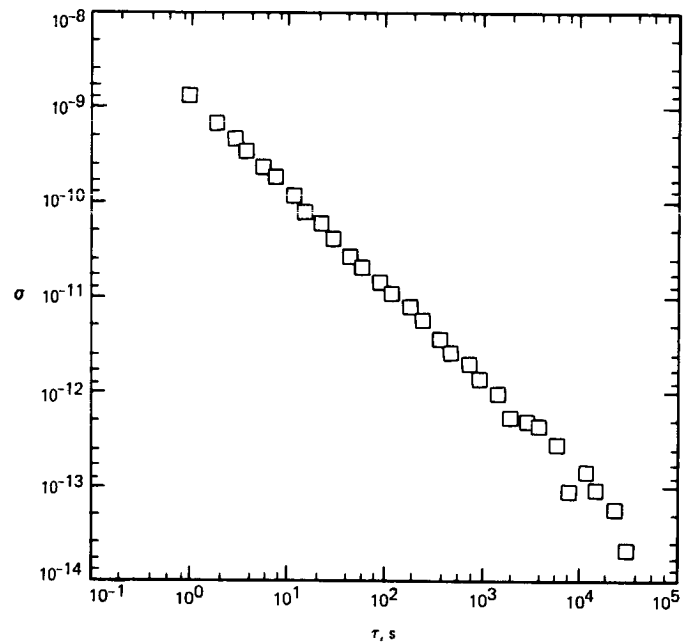


Fig. 6. Allan deviation for a noise floor test on a pulse train with period 0.94 s

Appendix A

Proof of Correctness of the Unfolding Algorithm

To avoid confusion let the output of the algorithm be denoted by X_n , while x_n is still defined by Eq. (1). The error correction lines 10 and 13 are deleted. We shall prove by induction that $X_n = x_n$ for all n . For $n = 0$, both quantities are zero. For $n = 1$ we have

$$\begin{aligned} du &= -\Delta v_1 \equiv \Delta t_1 \pmod{d}, \\ ddx &= \text{Smod}(\Delta t_1 - p, d) = \Delta t_1 - p \text{ (assumption 1)} \\ &= x_1. \end{aligned}$$

Therefore, $X_1 = x = x_1$ since $dx a = x 1 = 0$. For $n > 1$ assume the algorithm is correct up to $n - 1$. Then

$$\begin{aligned} dua &= -\Delta v_{n-1} \equiv \Delta t_{n-1} \pmod{d}, \\ du &= -\Delta v_n \equiv \Delta t_n \pmod{d}, \\ ddx &= \text{Smod}(\Delta^2 t_n, d) = \Delta^2 t_n \text{ (assumption 1)} \\ &= \Delta^2 x_n, \\ dxa &= \Delta x_{n-1}, \quad x 1 = x_{n-1}, \\ dx &= \Delta x_{n-1} + \Delta^2 x_n = \Delta x_n, \\ X_n &= x = x_{n-1} + \Delta x_n = x_n. \end{aligned}$$

Referees

The following people have refereed articles for *The Telecommunications and Data Acquisition Progress Report*. By attesting to the technical and archival value of the articles, they have helped to maintain the excellence of this publication during the past year.

H. A. Ali	S. J. Dolinar, Jr.	C. R. Lahmeyer	G. M. Resch
D. G. Bagby	D. M. Enari	F. L. Lansing	R. Sadr
D. A. Bathker	M. J. Grimm	G. S. Levy	B. L. Schumaker
B. Benjauthrit	R. Hartop	L. Maleki	M. Shahshahani
A. Cha	H. Hemmati	F. Manshadi	H. Shao
K. -M. Cheung	R. L. Horttor	Col. W. T. McLyman	J. G. Smith
C. T. Chian	I. -S. Hsu	A. Mileant	R. Stevens
C. Christensen	R. S. Hughes	D. Morabito	E. Stone
R. C. Clauss	W. J. Hurd	S. Petty	E. W. Stone
B. Crow	W. A. Imbriale	F. Pollara	R. L. Sydnor
F. Davarian	C. W. Johnson	E. C. Posner	T. W. Veruttipong
G. J. Dick	D. Johnson	L. E. Primas	C. C. Wang
R. M. Dickson	A. V. Kantak	W. Rafferty	
D. Divsalar	A. Kliore	M. S. Reid	